Study of the bacterial microenvironment in a bioleaching stirred tank bioreactor : transport phenomena and kinetic modelling in three-phase flow

Jonathan Chéron

École doctorale 608 : Sciences et Ingénierie des Molécules, des Produits, des Procédés et de l'Énergie

THÈSE

Présentée et soutenue publiquement pour l'obtention du grade de

Docteur de l'Université de Lorraine

Spécialité Génie des Procédés, des Produits et des Molécules

Par

Jonathan Chéron

le 8 octobre 2021

Study of the bacterial microenvironment in a bioleaching stirred tank bioreactor: transport phenomena and kinetic modelling in three-phase flow

Directeur de thèse : **Pr. Eric Olmos**
Co-encadrants de thèse : **Dr. Anne-Gwénaëlle Guezennec & Pr. Stéphane Delaunay**

Jury

Pr. Sue Harrison,	University of Cape Town	Rapportrice
Pr. Caroline Gentric,	Université de Nantes	Rapportrice
Pr. Laurent Cassayre,	LGC Toulouse	Examinateur
Pr. Eric Olmos,	Université de Lorraine	Examinateur
Dr. Anne-Gwénaëlle Guezennec,	BRGM Orléans	Examinatrice
Pr. Stéphane Delaunay,	Université de Lorraine	Examinateur / Président de jury
Dr. Céline Loubière,	CHRU Nancy	Invitée

Université de Lorraine
Laboratoire Réactions et Génie des Procédés (LRGP)
UMR CNRS 7274, Nancy, FRANCE

Acknowledgement / Remerciements

Les remerciements, sûrement la meilleure partie de la thèse ! Il y en a du beau monde à remercier, de belles choses à dire, des évènements notoires à partager et j'en passe. Je vais tenter de faire ça de manière synthétique et de n'oublier personne.

Je souhaite tout d'abord dédier ma thèse à mon père, Philippe. Pour l'anecdote, je lui avais promis quand j'étais bien plus petit de le surpasser question études, lui étant ingénieur. Me voilà officiellement docteur, et une promesse enfin tenue après toutes ces années. Il y a beaucoup de choses que j'aimerais te dire, mais je pense que de simples mots ne suffiraient pas pour te remercier pour ce que tu as fait pour moi au long de ma vie. Je n'ai jamais été délaissé, jamais été dans le besoin et toujours été soutenu. C'est en grande partie grâce à toi que j'en suis là. Merci !

Evidemment, comme il y a souvent l'un avec l'autre, je tiens aussi à remercier profondément ma mère, Véronique. Entre l'apprentissage des bêtises, du fonctionnement glorieux de l'administratif, des révisions de BAC de philo au cinéma et des batailles de boules de neiges dans la maison, je pense qu'on a du quasiment tout fait et on n'est pas prêt de s'arrêter !

Quand on y pense, la thèse reste une sacrée aventure, parsemée de lieux, de rencontres et d'expériences. Cette aventure a commencé au BRGM et c'est pour cela que je tiens à remercier l'équipe qui m'y a accueilli pendant 1 an et qui m'a appris tant de choses. Et plus particulièrement, un grand merci à Anne-Gwénaëlle pour ton enseignement et surtout ta patience qui m'a énormément aidé pour progresser. Même si beaucoup ont évolué dans leurs carrières respectives depuis, je tiens à remercier d'autres anciens (et deux actifs) de l'équipe. Merci à Fred, ou devrais-je dire Grand Aigle, pour ta sagesse infinie. Merci à Anthony pour tous les conseils que tu as pu me donner quand je débutais. Merci à Agathe pour ton aide et tes conseils. Merci à Marion pour ton assistance sur le côté expérimental et tous les bons moments à la halle. Merci à Elia pour les fous rires dans le laboratoire. Merci à Cindy pour tous les moments incroyables en biomol, les visages bizarres aux hublots, les chaises qui tournent, les gants qui parlent, les bières et j'en passe ! Merci à Jérémy pour la quantité astronomique de discussions sur tout et n'importe quoi, c'est impossible de s'ennuyer avec toi !

Et dire, tout ça n'était que la première année... C'est là que l'anarchie commence, l'arrivée au LRGP. Quand on y pense, j'y étais avant même le début de la thèse, soit presque 5 ans là-bas. Je vais commencer par remercier l'équipe BioPromo : Eric, Stéphane, Manu, Manu, Isabelle, Catherine, Latifa, Fabrice, Yann, Bruno et Mohammed (c'est dans ces moments-là que j'ai peur d'oublier quelqu'un). Merci pour tous ces moments passés ensemble et pour les échanges qu'on a pu avoir, scientifiques comme informels.

Eric, tu savais que ce moment arriverait un jour dans ta vie, le moment où j'allais devoir dire des choses sur toi. Je suis dans le regret de devoir d'annoncer que je me dois de... te remercier énormément ! Je félicite ton courage pour m'avoir pris en thèse après avoir vu un échantillon de moi durant plusieurs mois en stage. Je ne suis pas prêt d'oublier les soirées à galérer sur des UDF, les réflexions sur les TD que tu pourrais donner aux Saiens, les soirées bières dans des bars obscurs qui ne servent que du rhum pur, les enchaînements nuit-jour de correction de publis, les matrices de la mort et tant d'autres choses. Encore merci à toi.

Forcément, je n'ai jamais été seul dans cette galère et je dois mentionner les personnes étranges que j'ai croisé dans les couloirs de BioPromo... Je vais commencer par remercier les spécimens presque normaux, à savoir Laureline, Eusèbe, Amani, Chafik, Liliane, Delphine (j'ai dit presque...), Fanny, Laure, Mélodie et Ibrahima. Ensuite, il me faut aborder les spécimens particuliers :

En premier lieu, un grand merci à Caroline, ma compère de thèse, du début à la fin, qu'il vente, qu'il pleuve, qu'il neige ou qu'il fasse beau (quoique le dernier est plutôt un mythe qu'on transmet aux enfants lorrains qui veulent pas dormir...), autour d'une bière ou du 17e café de la journée. Je pense qu'entre l'administration, les posters, les stagiaires, les réunions, les formations de l'école doctorale, les dessins, mon humour incroyable, les pétages de plombs et les dimanches soir au labo, on aura vraiment tout vécu. Merci pour ton soutien incroyable !

Un second grand merci à Charlotte pour m'avoir soutenu dans cette quête d'apport continuel de clarté, de sérieux et de sagesse dans le laboratoire. Il n'y avait pas de travail sans passage sur le site de la SPA à revoir à quel point Mako est adorable. Il n'y avait pas de pause sucrée sans commencer la construction d'un palace de smarties avec plan à l'appui. Il n'y avait pas de sorties sans tentative de meurtre dans une randonnée 12 strates au-dessus de ma condition physique. Il n'y avait pas de café sans discuter avec la tasse licorne. Et enfin, il n'y avait pas de moments de haute concentration sans recevoir, par le plus grand des hasards, 20 images trop mimis. Je suis content de voir que grâce à toi, c'est la #TeamChien qui a gagné !

Merci à Aurélia pour l'omniprésence des chenilles, les vidéos de hamsters, les clubs bières à l'ENSIC et les soirées Crouqui. Merci à Julien pour tous les super moments passés avec toi, en randonnée comme autour d'une bière. Merci à Céline pour avoir inventé une toute nouvelle catégorie d'humour, basée sur la mécanique des fluides et qui finit en général en floating point exception quand tentée pour briller à l'apéro... Merci à Xavier pour les pauses café de 8h à 18h. Merci à Anne pour les soirées MTT au labo, les BK improvisés et les demi-demi. Merci à Adrien (hey mais t'es pas du labo toi) pour ton enseignement précieux sur les transferts de fichiers et les idées de numéros de cirque à apprendre à mon futur chien. Merci à Emile pour ta réinvention de la mécanique des fluides. Merci à Mélina pour réussir avec succès à contenir la folie de Xavier journalièrement et pour ta présence de temps à autre en randonnée avec les chiens.

Et évidemment, je dois aussi citer et remercier tous mes potes de SAIA. Un grand merci à Géraldine, Noémie, Benoît, Anthony, Laura et Bob. C'est toujours un plaisir incroyable de vous revoir de temps en temps quand on en trouve l'occasion, sur un WE réservé souvent 1 à 2 ans à l'avance pour être sûr de ne pas se manquer. Je ne préfère même pas mentionner trop de choses à votre égard, il y a beaucoup trop à dire, et dans 300% des cas ça risque de me retomber dessus. Merci à vous tous !

Certains diraient que je suis un geek, même si je me soigne. Et depuis plus de 15 ans que je parcoure la toile, j'en ai rencontré du monde. C'est pour ça que je tiens aussi à les remercier et particulièrement ceux que j'ai souvent croisé pendant ma thèse, à savoir Biboulinet, Flora, Pefel, Kayu, Vivi et Qilin. A special mention to Julien and Mea : thank you for everything, for your unconditional support, for listening to me even in my darkest moments, for sharing many things with me and reminding me what it is to make people happy. I hope to have the opportunity to visit you one day, I still owe you so much for all you did and I want to see Mea's coffee empire. Of course, I'll take an astronomical amount of cheese as payment. A thousand thanks to you both !

Je souhaite aussi remercier le Parc Animalier de Sainte Croix, qui a été mon havre de paix sur les dernières années. Là-bas, j'ai pu pleinement vivre mes passions, la nature et la photographie, et ce dans un contexte où mon travail et mes connaissances n'ont pas d'importance, où je peux pleinement me reposer et discuter librement de mes passions avec le staff comme les visiteurs. Je tiens à remercier tous les photographes du parc et particulièrement Cindy, Corinne, Philippe, Ben et Pierre. Merci aussi aux membres du staff et surtout à Nicolas et Anthony pour toutes les choses que vous m'apprenez et les faits incroyables que vous relatez à chaque fois que j'ai l'occasion de vous croiser !

Je tiens aussi à remercier deux très bonnes amies, Enora et Lison, avec qui je partage moulte discussions depuis un paquet d'années. J'espère que cela continuera.

Enfin, ces remerciements ne seraient pas complets sans inclure un certain nombre d'individus importants. Et c'est pour ça que je souhaite remercier du fond du cœur Charlie, Minnie, Shaman, Swally, Aniu, Crios, Thorgal, Milak, Siut, Gaïa, Nuna, Masak, Thor, Falcon, Thanos, Namor, Stark, Loki, Bolt, Gump, Gépéto, Gaou, Holly, Pep's, Paf, Rouky, Riki, Ranger, River, Rhéa, Raven, Ravage, Orion, Star, Ouragan, Oggy, Oreo, Oups, Obélix, Pearl, Polux, Polochon, Rye, Rasta, Shadow, Pépito, Carlito, Ron, Mulder, Pam, Naali, Harry, Qilak, Freyja, Ruska, Nassak, Styx, Eros, Floki, Silva, Ilana, Bao, Ying Tao, Cha Hua, Taïga, Malou, Sally, Mako, Angus, Meije, Jay'z, Noum, Moon, Shadow, Kayo, Nox, Falko, Ficelle, Hertta, Lara, Kinaï, Crouqui, Pixel, Angus, Hina, Nouki et j'en oublie sûrement quelques-uns. J'ai foi en le fait qu'ils apprendront un jour à lire !

Contents

List of Figures

List of Tables

Nomenclature

Variables

a	Interfacial area per unit volume	$\mathrm{m^2\,m^{-3}}$
C	Impeller off bottom clearance	m
$c_{\mathrm{g,l}}$	Dissolved gas concentration	$\mathrm{mol\,l^{-1}}$
c_{g}^*	Equilibrium concentration	$\mathrm{mol\,l^{-1}}$
C_w	Impeller torque	$\mathrm{N\,m^{-1}}$
D	Impeller diameter	m
D_{l}	Diffusivity of gas in liquid	$\mathrm{m^2\,h^{-1}}$
d_{p}	Particle diameter	m
E	Electric potential	V
E_a	Activation energy	$\mathrm{J\,mol^{-1}}$
E_c	Energy of a particle-particle collision	J
F	Force per unit volume	$\mathrm{N\,m^{-3}}$
$f(C)$	Chemical function	$-$
$f_g(T)$	Impact function of temperature on microbial growth	$-$
G	Local velocity gradient	$\mathrm{s^{-1}}$
g	Gravitational acceleration	$\mathrm{m\,s^{-2}}$
$g(1-X_{c,\mathrm{s}})$	Topological function	$-$
G_{s}	Initial sulfide mineral grade	$\mathrm{mol\,kg^{-1}}$
G_k	Turbulent production	$-$
H	Henry's law constant	$\mathrm{mol\,l^{-1}\,Pa^{-1}}$
H_{l}	Liquid height	m
H_{s}	Suspension quality	$-$
K	Constant used in the Monod equation	$\mathrm{mol\,l^{-1}}$
k	Turbulent kinetic energy	$\mathrm{m^2\,s^{-2}}$
$K(T)$	Temperature-dependant rate constant	$-$
K_{ls}	Interphase exchange coefficient between liquid and solid phases	
$k_{\mathrm{l}}a$	Mass transfer coefficient	$\mathrm{s^{-1}}$
k_D	Death rate	$\mathrm{h^{-1}}$
l_K	Kolmogorov length scale	m
M	Molecular mass	$\mathrm{kg\,mol^{-1}}$
m	Microbial maintenance	$\mathrm{h^{-1}}$
N	Agitation rate	$\mathrm{s^{-1}}$
$n(l)$	Bubble size distribution	$-$
P	Power	W
p	Pressure	Pa
P_{g}	Partial pressure of the gas	Pa
Q	Flow rate	$\mathrm{m^3\,s^{-1}}$
q	Specific rate of consumption or formation	$\mathrm{g\,g^{-1}\,l^{-1}\,h^{-1}}$
Q_p	Impeller pumping capacity	$\mathrm{m^3\,s^{-1}}$

r	Rate of consumption or formation	$\mathrm{g\,l^{-1}\,h^{-1}}$
r_0	Radial distribution function	–
SF	Sheared fraction	–
T	Tank diameter	m
T	Temperature	K or °C
t_K	Characteristic time	h
u	Velocity	$\mathrm{m\,s^{-1}}$
u_{l_K}	Velocity scale	$\mathrm{m\,s^{-1}}$
V	Volume	$\mathrm{m^3}$
W_s	Solid-liquid mass ratio	–
$X_{c,\mathrm{s}}$	Mineral conversion	–
Y	Yield	$\mathrm{g\,g^{-1}}$
CTR	Carbon Transfer Rate	$\mathrm{g\,l^{-1}\,h^{-1}}$
CUR	Carbon Uptake Rate	$\mathrm{g\,l^{-1}\,h^{-1}}$
OTR	Oxygen Transfer Rate	$\mathrm{g\,l^{-1}\,h^{-1}}$
OUR	Oxygen Uptake Rate	$\mathrm{g\,l^{-1}\,h^{-1}}$

Greek letters

α	Volume fraction	–
δ	Film thickness	m
γ	Diffusion coefficient	–
γ_a	Anodic transfer coefficient	–
γ_c	Cathodic transfer coefficient	–
$\gamma_{\theta_\mathrm{s}}$	Collisional dissipation of energy	$\mathrm{m^2\,s^{-2}}$
μ	Specific growth rate	$\mathrm{h^{-1}}$
μ_l	Liquid viscosity	$\mathrm{Pa\,s}$
$\mu_{\mathrm{t,l}}$	Turbulent viscosity of the liquid phase	$\mathrm{Pa\,s^{-1}}$
ν_l	Liquid kinematic viscosity	$\mathrm{m^2\,s^{-1}}$
ρ	Mass density	$\mathrm{kg\,m^{-3}}$
$\overline{\overline{\boldsymbol{\tau}}}$	Phase stress strain tensor	Pa
σ	Surface tension	$\mathrm{N\,m}$
σ_p	Particle stress	Pa
θ_s	Granular temperature	$\mathrm{m^2\,s^{-2}}$
θ_m	Mixing time	s
ε	Turbulent energy dissipation	$\mathrm{m^2\,s^{-3}}$
φ	Topological parameter	–
φ_g	Gas holdup	–

Dimensionless number

Fr	Froude number	–
N_A	Aeration number	–
N_p	Power number	–
N_Q	Pumping number	–
N_Q	Pumpung / Flow number	–
N_js	Just-suspended agitation rate	–
Re	Reynolds number	–

Subscripts

a	Anode
adj	Adjusted

c	Cathode
c	Conversion
col	Collisional
D	Drag
diss	Dissipated
g	Gas
gl	Action between gas and liquid
ini	Initial
js	just-suspended
kin	Kinetic
l	Liquid
ls	Action between liquid and solid
m	Mixed
max	Maximum
min	Minimal
opt	Optimal
p	Particle
ref	Reference
s	Solid
t	Turbulence
TD	Turbulent dispersion
tot	Total
v	Volume
w	Weight

Abbreviations

At.	*Acidithiobacillus*
L.	*Leptospirillum*
S.	*Sulfobacillus*
A310	Lightnin A310 impeller
AMD	Acid Mine Drainage
BSD	Bubble Size Distribution
CAD	Computer-Aided Design
CAPEX	CApital EXpenditure
CFD	Computational Fluid Dynamics
CM	Compartment Model
DO	Dissolved Oxygen
EEd	Elephant-Ear down impeller
EPS	Extracellular Polymeric Substance
ETRMD	Emerging Technologies Raw Material Demand
EU	European Union
HTPGd	HTPG down impeller
IM	Inner Membrane
MSPD	Mixed Side-Pore Diffusion
OM	Outer Membrane
OPEX	OPerating EXpenditure
PBM	Population Balance Model
PS	Periplasmic Space
R600	R600 spiral backswept impeller
RT4B	4-bladed Rushton turbine

RT6B	6-bladed Rushton turbine
sp. or spp.	Species
STR	Stirred Tank Reactor
UNEP	United Nations Environment Program
WEEE	Waste from Electrical and Electronic Equipment
X	Biomass

Introduction

In recent years, the increasing number of new exploration and resource evaluation programs has shown a significant revival in the activity of reuse of primary and secondary mineral resources (mining waste). At the same time, the treatment processes of these resources remain a major issue. Deposits are now indeed increasingly complex, with resources that feature unusual characteristics due to their mineralogical complexity or high sulphur content. They become also smaller in size and with limited valuable metal content. Mining wastes, often responsible for acid mine drainage, are also increasingly accumulating and remain of limited interest for exploitation because of their low metal content. For these types of resources, conventional treatment processes, such as pyrometallurgy, are indeed unsuitable from both economic and environmental points of view. In this context, hydrometallurgy which presents milder conditions (lower temperature and sustainability) is thus a viable alternative. Among hydrometallurgical processes, bioleaching considers the use of microorganisms in aqueous solution, which reduces production and operating costs while being more environmentally friendly.

More particularly, bioleaching in agitated mode using large-scale stirred tank reactors is seen as a process of interest as it may allow a better control of different operating conditions and parameters such as physicochemical (temperature, pH, aeration, agitation), biological (microbial consortium) and geometrical parameters (tank, impellers, sparger, baffles). Thus, this process offers an interesting technical alternative to static heap applications that may present limitations for the treatment of these new unconventional resources. However, till now, due to the large operational and capital expenditures of large-scale bioreactors, bioleaching in agitated mode remains mainly limited to the few cases with sufficient high metal value. The generalization of bioleaching stirred tank reactor requires thus further technical optimization to reach its economic viability. Nonetheless, recent advances showed that this may be a more generalizable technology to answer the ecological concerns related to resources extraction.

Bioleaching thus involves particles (ore), liquid phase (water-like), a gaseous phase (aeration / carbon feed) and microorganisms to ensure the biological reactions. Consequently, the bioleaching process is based on the coupling between a complex gas-liquid-solid hydrodynamics (generated by rotating impellers), chemical and biological reactions. On one hand, kinetic modelling was widely reviewed in the literature but the dedicated studies focused on reaction rates modelling and considered perfectly mixed

systems. On the other hand, the description of multiphase hydrodynamics in bioleaching tanks remains scarce and still needs more intense developments. For this purpose, even if experimental data should still be generated, process modelling and especially computational fluid dynamics has proven to be a powerful tool for describing complex hydrodynamics. It allows indeed to access to yet unmeasurable data (particle stress, local turbulent dissipation rates in dense multiphase flows) or to avoid costly experimental campaigns (such as screening of system designs). In static conditions, the coupling of mass transfer and transport was successfully applied with the development of the HeapSim model, that represents the underlying phenomena of heap bioleaching [1].

In this context, this PhD thesis work was the main component of the **MODELIX** project, which aimed at the development of an integrated model describing the transport phenomena within a bioleaching tank and their impact on chemical and biochemical activities.

The achievement of this general goal was carried out along four parts:

- A literature review of bioleaching process characteristics, its operation and the models used to simulate its chemical and biological performances was first presented in **Chapter 1**. Considering the importance of hydrodynamics description in this work, a particular focus was put on expected transport phenomena encountered in the stirred tank reactor, such as gas-liquid mass transfer and hydromechanical stress.

- Then, **Chapter 2** sets the building blocks necessary for the structuring and validation of the bioleaching model. For this, an extended experimental study of a laboratory-scale bioleaching stirred tank reactor was carried out to describe the evolution of chemical and biological kinetics over time. Along this study, the microorganisms diversity and their distribution (respectively in the liquid and on solid phases) were obtained using molecular biology tools. Additionally, abiotic studies of the tank were also performed to determine essential hydrodynamics parameters, namely the just-suspended agitation rate and the gas-liquid mass transfer coefficient and to propose models linking these variables to process operating conditions.

- One key phenomenon identified was the particle suspension and possibly the hydromechanical stress encountered by these particles when transported in the liquid phase. To produce new knowledge on the couplings between bioreactor design and operation and these hydrodynamic characteristics, the work proposed in **Chapter 3** quantifies the impact of impeller design, agitation rate and solid

concentration on particle suspension and particle stress by using 50 solid-liquid CFD simulations. Scale-up criteria for particle stress and suspension homogeneity were especially looked for by comparing 2-liter laboratory- and 800-liter pilot-scales results.

- Lastly, as gas-liquid mass transfer is also expected to be one key limitation for bioleaching process intensification, the **Chapter 4** of this PhD aimed at developing a CFD-based compartmental hydrokinetic model to enhance the knowledge of the local phenomena impact, at the bioreactor scale. To this end, a CFD gas-liquid model of a bioleaching stirred tank reactor was presented and used to determine and validate the gas-liquid mass transfer coefficient model. To ensure its ease of use, this approach was simplified and combined with results from kinetic modelling to establish a compartmental model, focused here on the description of oxygen transport within the bioreactor, in presence of biological and chemical consumptions. Lastly, a scaling study was carried out to predict the distribution of oxygen in the bioreactor from pilot- to industrial-scale.

This project was funded by an Inter-Carnot collaboration between the Institut Carnot BRGM in Orléans, represented by the BRGM (French geological and mining research center) and the Institut Carnot Icéel in Nancy, represented by the LRGP (Reactions and process engineering laboratory). The scientific collaboration is represented on one hand by the BRGM, with an expertise in the development and operation of bioleaching stirred tank reactors at laboratory-, pilot- and industrial-scale. On the other hand, the LRGP constitutes an important pole in process engineering and has developed numerous applications for the description of cellular microenvironments in reactors. In addition, the team strongly relies on heavily on computational fluid dynamics tools and on the design of setups dedicated to the development and validation of advanced models.

Bibliography

[1] J. Petersen and D. G. Dixon. Modeling and Optimization of Heap Bioleach Processes. In D. E. Rawlings and D. B. Johnson, editors, *Biomining*, pages 153–176. Springer, Berlin, Heidelberg, 2007.

Chapter 1

State of the Art

Contents

1.1 Global state of metal-based resources

1.1.1 Increase of global metal consumption

Over the past few decades, the demand for metals has promptly increased due to the growing needs of the modern society, thus increasing the pressure on natural resources. These needs are first related to the surge of global population, which, despite the slowdown in its growth, is estimated to reach 8.5 billion in 2030 [1]. Moreover, the developing countries are expected to follow the trend of the industrialized countries in terms of needs and it is expected that the global metal demand will increase three to nine-fold [2]. As example, China entered an intensive, steel-dependent, phase of growth between 2000 and 2010 which resulted in a 9.1% increase of global iron extraction [3] and a 68.5% increase of the global crude steel production (from 850 to 1433 million tons) [4]. The trend of global steel crude production is shown on Fig. 1.1.

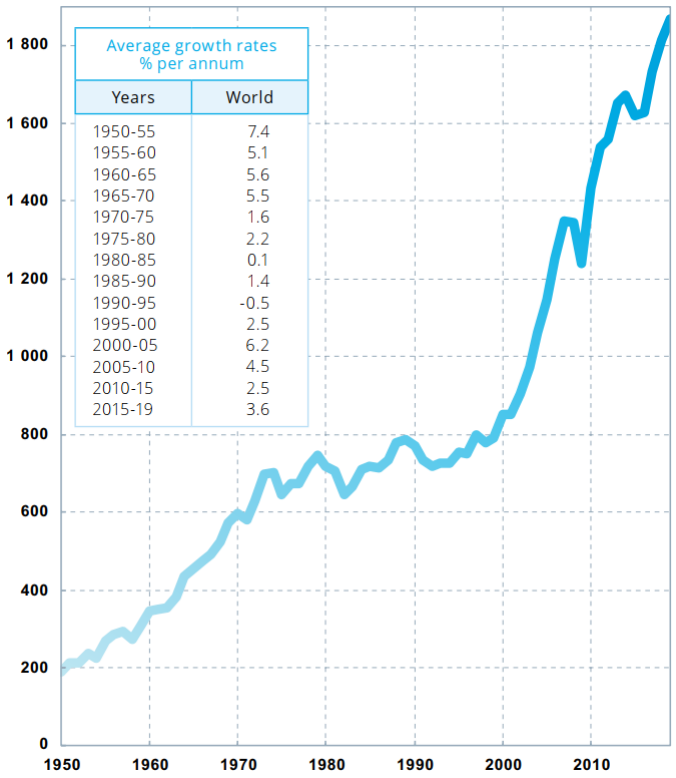

Figure 1.1: World crude steel production since 1950, in million tons [4].

On the other hand, metal raw materials are essential basic resources for manufacturing most of the products used in everyday life applications. This is explained by the multiple properties of metals such as conductivity, ductility, hardness, heat resistance and even appearance. These particularities are increasingly used along technological progress and are crucial for high tech products and emerging innovations, as shown in Table 1.1 with the projected evolution of raw materials used [2, 5]. In contrast, the number of metals needed for the production of an average mobile phone went from 10 in 1980 to more than 60 nowadays [6, 7]. Among them are particular metals of

various qualifications, such as “energy metals” [8] or “high-tech metals” [9], because of the unique capabilities and combination of properties they offer as alloys and their relevance in the renewal energy sector. To give a few examples, neodymium magnets are the strongest magnets on earth and can be easily used in many applications such as medical imaging or computer hard drives due to its versatility ; gold is used in wiring due to its high conductivity capabilities and cobalt is commonly utilized for the production of high-performance alloys because of its high durability.

Table 1.1: Growth in raw material used today and predicted for 2030 [2]. Data given in tons.

Raw material	Production	ETRMD 2006	ETRMD 2030
Gallium	152	28	603
Indium	581	234	1911
Germanium	100	28	220
Neodymium	16800	4000	27900
Platinum	255	very small	345
Tantalum	1384	551	1410
Silver	19051	5342	15823
Cobalt	62279	12820	26860
Palladium	267	23	77
Titanium	7211000	15397	58148
Copper	1509300	1410000	3696070
Ruthenium	29	0	1
Niobium	44531	288	1410
Antimony	172223	28	71
Chromium	19825713	11250	41900

ETRMD = Emerging Technologies Raw Material Demand

In 2010, the European Commission defined a list of critical raw materials represented by their economic importance and potential supply risk [10]. Over the years, this list was updated and, considering the criteria and the 61 raw materials screened, 30 of them were identified as critical raw materials, as shown in Fig. 1.2 [11, 12].

With the current economic development of the world and the state of technological progress, the interest for these so-called critical raw materials will grow increasingly in the coming years.

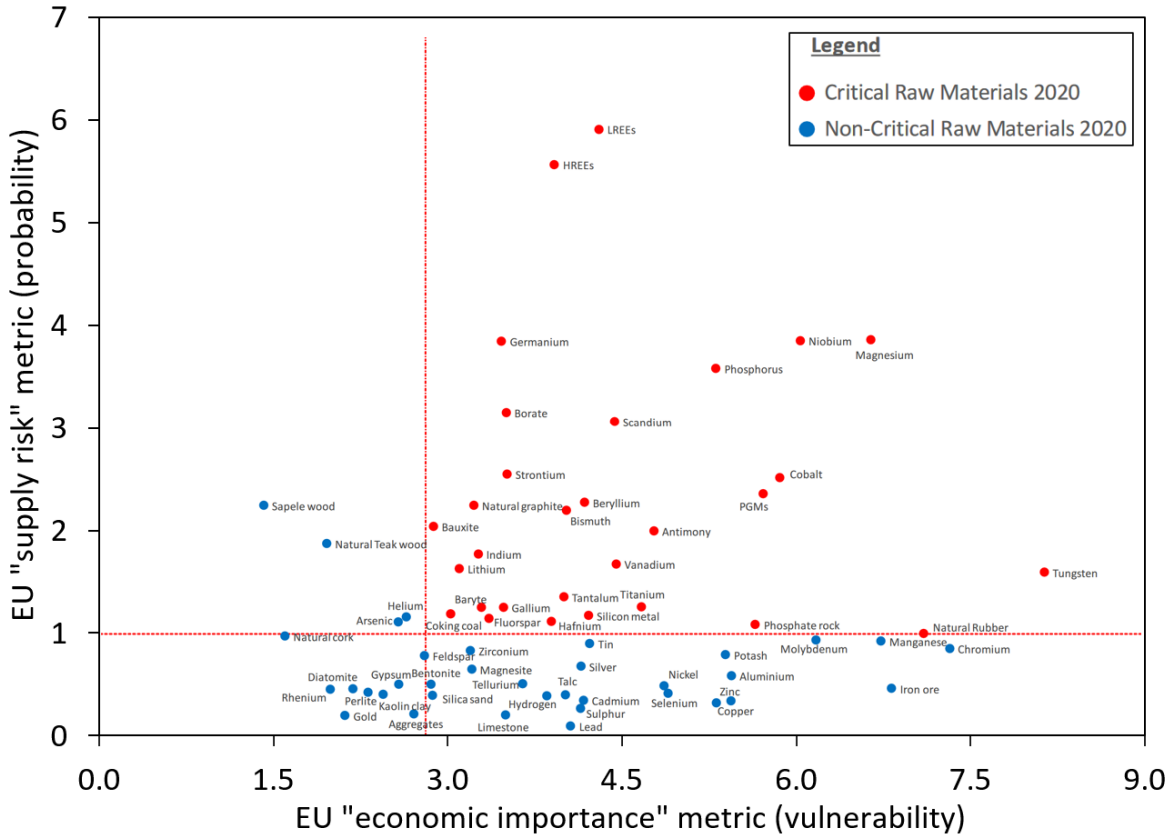

Figure 1.2: Identification of the critical raw materials. The broken red line represents the limit set by the European Commission (2018) [5]. Figure from the European Commission (2020) [12, 13].

1.1.2 Metal-based resources depletion

The global use of metal-based resources is expected to double between 2010 and 2030 [14]. The direct consequence is the additional pressure put on natural resources due to mining intensification, which leads to a decrease of recoverable resources reserves. Whereas the scarce of resources has not yet been reached, the reserves are definitely limited and, for the moment, can only be predicted based on the resources considered recoverable and on the known natural stocks, as shown on Table 1.2.

Table 1.2: Recoverable reserves of key resources [3].

	Recoverable resources from known reserves $\times 1 \times 10^9$ t	**Global extraction in 2010** $\times 1 \times 10^6$ t
Oil	233	3.573
Coal	1.318	7.025
Natural gas	176	2.609
Iron ore	190	2.634
Copper ore	100	1.877
Bauxite and alumina	28	226

The pressure on natural resources also appears through the steady decline of the average ore grade over the years. The average ore grade over the time is obtained using the data given by the mining companies. Calvo et al. (2016) reported it over 38 mines analyzed, which corresponded in 2016 to $5.26\,\mathrm{g\,t^{-1}}$ for gold ore, 9.6 % w/w for zinc ore, 3.4 % w/w for lead ore and 1.48 % w/w for copper ore [15]. Mudd (2009) carried out a complete study over the mines in Australia and, among others, determined the evolution of the average ore grade over the years, as shown on Fig. 1.3 [16].

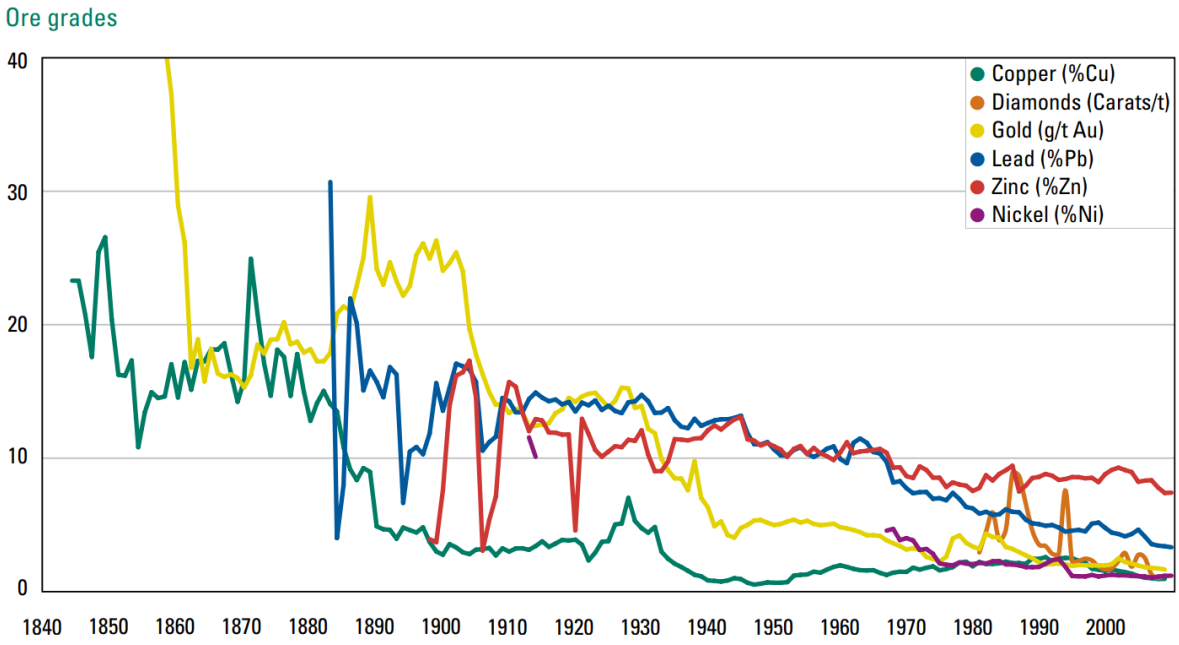

Figure 1.3: Ore grades of mines in Australia between 1840 and 2005. Figure from UNEP (2011) [14] and data from Mudd (2009) [16].

While the mining industry has focused on the richest deposits, ensuring profitability at lower cost, these deposits tend to thin out, forcing the focus on other deposits of lower grade to cover the increasing material demand. This arises the issue of operating cost (OPEX) on less rich deposits as their exploitation will require the extraction of more raw material to obtain a similar extraction yield to the richer deposits. Processing steps between the ore extraction and the metal production (transport, grinding, separation, etc.) have to be applied to a larger ore quantity, leading to a rise of energy consumption. Even with the technological improvements of the metallurgical processes, the growth of energy consumption is still higher than the increase of metal production, as shown in Fig. 1.4 [15].

Another phenomenon induced by the intensification of metal-containing resources is the accumulation of wastes, mostly consisting of overburden, tailings and slag, that are often little or not used and hold a potential negative environmental effect.

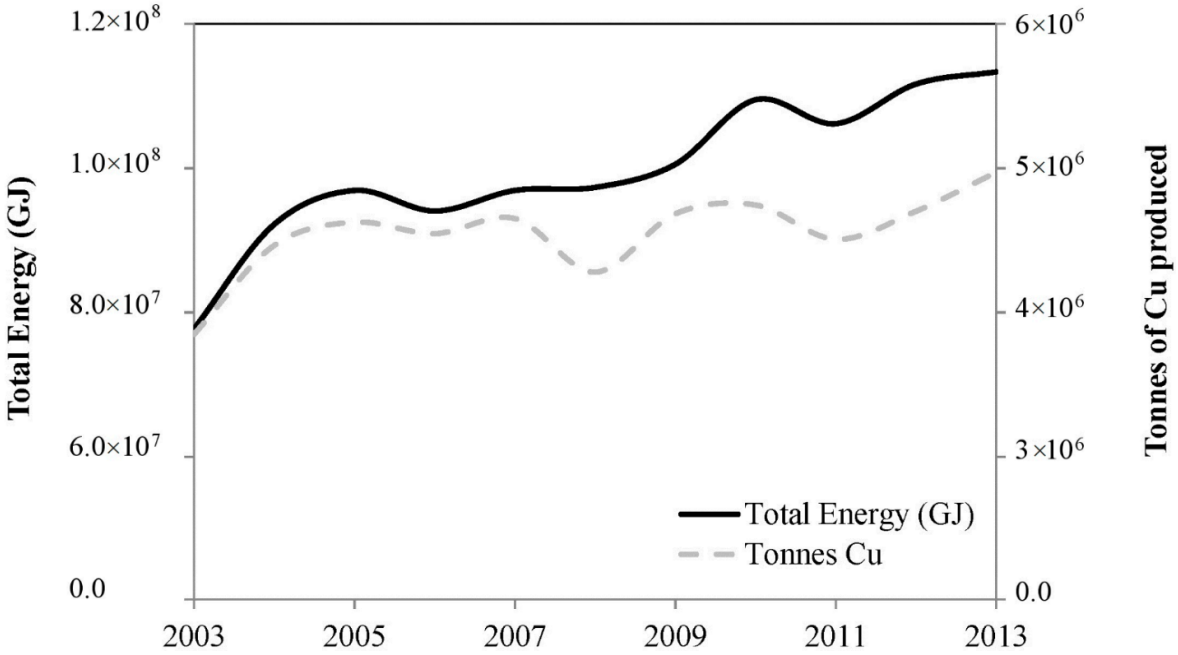

Figure 1.4: Comparison of the total energy consumed (GJ) with the copper produced (t) in the Chilean mines between 2003 and 2013. Figure from Calvo et al. (2016) [15].

1.1.3 Expansion of the range of resources used

During the last decades, the mining and metallurgy sectors thus entered a challenging phase due to limitations of raw material availability and quality. Moreover, growing concerns of the ecological impacts of mining add new insights about the value chain of metals. In this regard, new ways of extracting the resources were found and developed around the world in order to maintain sufficient supply of critical resources. For example, in 2015, the European Commission adopted a Circular Economy package that redesigned the value chain in a sustainable way [5]. This included the valorization of resources previously seen as waste through recycling. Similar policies of regulations and waste management were developed in the USA, South Africa and even globally, as reviewed by Matinde et al. (2018) [17].

Wastes are generated throughout the process from the raw material extraction to the processing of a metal, such as overburden, tailings and slags, as shown on Fig. 1.5. Similarly for end-of-life metal-base products, because of the pace of technological improvements, wastes from electrical and electronic equipments (WEEE) coming from the so-called ”urban mine” are accumulating at an alarming rate and were estimated at around 50 millions tonnes in 2018 [18]. This waste holds a potential detrimental environmental impact as they may exhibit one or more hazardous properties such as toxicity, corrosivity, ignitability and reactivity [19, 20].

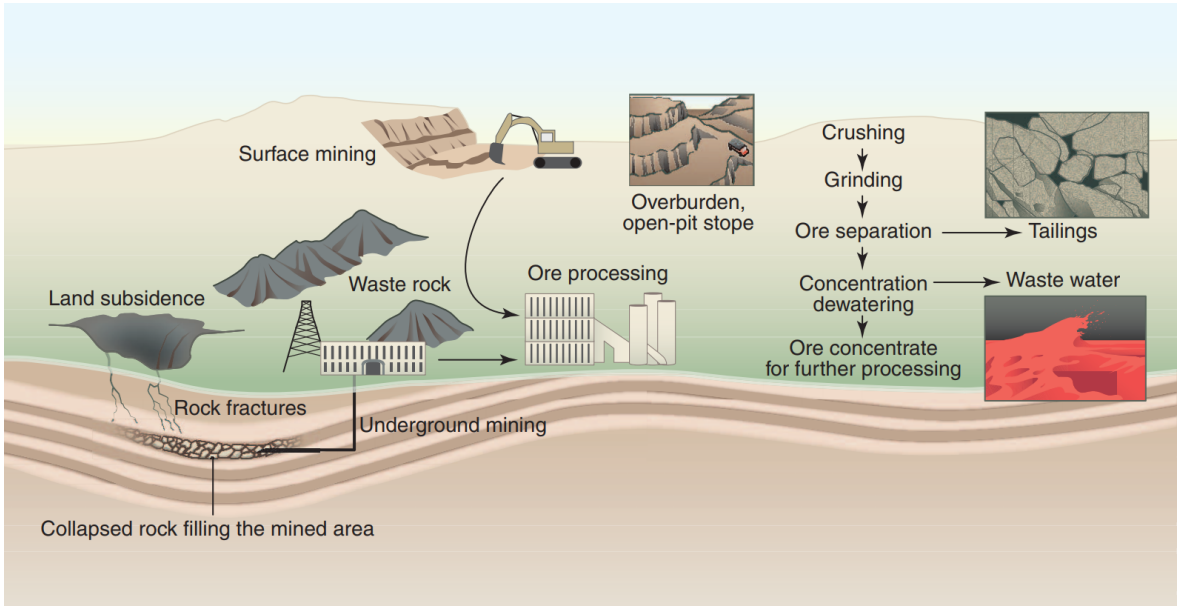

Figure 1.5: Generation of wastes and environmental effects during the mining process. Figure from Bian et al. (2012) [21].

In a sustainable development system, waste takes on the role of a new resource because it contains valuable and potentially exploitable materials. However, these resources could also be qualified as "unconventional" as they present unusual features in terms of range of shape, size and physicochemical properties [21]. On one hand, tailings consist of very low grade of metals and can show a complex mineralogy or a high sulfur content. On the other hand, WEEE contains a wide variety of metals present in high concentrations but also non-metallic materials such as plastic, ceramic, wood, etc. [22]. The valorization of these resources requires the adaptation of the metallurgical processes to these specific characteristics in order to limit investment and operating costs while maintaining a high extraction efficiency.

1.2 Extractive processes using metal-based resources

The evolution of processes linked to metal extraction evolved through the ages. Nevertheless, the major technical and scientific advances of these processes were during the Industrial Revolution when the importance and versatility of metal were discovered, leading to an explosive development of their extraction [23]. Nowadays, most of the progress are tied to the optimization of existing methods.

1.2.1 Mineral beneficiation

Beside mining, which is the extraction of ore, the recovery of metal from raw material follows a succession of operations from the ore to usable metal. The first step is known as mineral beneficiation or mineral processing and consists in the size reduction of the ore and the concentration of minerals of interests. It includes mechanical, physical and physicochemical treatments that can be classified in 4 types of unit operations:

- **Comminution:** Particle size reduction of the ore through a succession of crushing and grinding operations (Fig. 1.6(a-b)). This operation has two main objectives: (i) to increase the specific surface area of the particles and (ii) to increase the degree of liberation by releasing the wanted minerals from the ore matrix. The final size of the ore depends on the downstream process and varies from the centimeter scale down to less than 100 microns.

- **Sizing:** Separation of the particles according to their size by screening or classification. This operation can also remove undesired materials.

- **Concentration:** Separation of the particles using their physical and chemical properties. The aim of concentration is to increase the relative concentration of the valuable part (concentrate) by separating it from the gangue or undesired minerals (tailing). Multiple methods exist to concentrate the particles depending on the properties of both the wanted and discarded minerals. For example, gravity concentration will separate the particles based on their relative velocity in a force field (gravity, centrifugal, magnetic or buoyant forces) [24].

- **Dewatering/Drying:** Removal of moist contained in the concentrate or tailing using solid-liquid separation. This last operation facilitates the transportation of the concentrate/tailing and also allows to meet the regulatory specifications for safe deposition [25].

During the past decades, few improvements were done to the main principles of mineral beneficiation aside from the evolution and optimization of existing machinery. One of the biggest issue of mineral processing is the energy consumption and mostly of the comminution part, which accounts for 50-70 % of the total energy consumption [26, 27]. This is explained by the exponential increase of energy used inversely proportional to the targeted particle diameter as the surface area of particles that needs to be treated also increases exponentially with a decreasing particle size. Considering the treatment of "unconventional resources", this energy consumption is even more important as smaller particles may be required to attain the desired materials that may be contained in more complex substrates, such as WEEE [28]. For this, a pretreatment step has become common practice to weaken the ore before comminuting them, such as heating, chemical addition or electrical impulses [29].

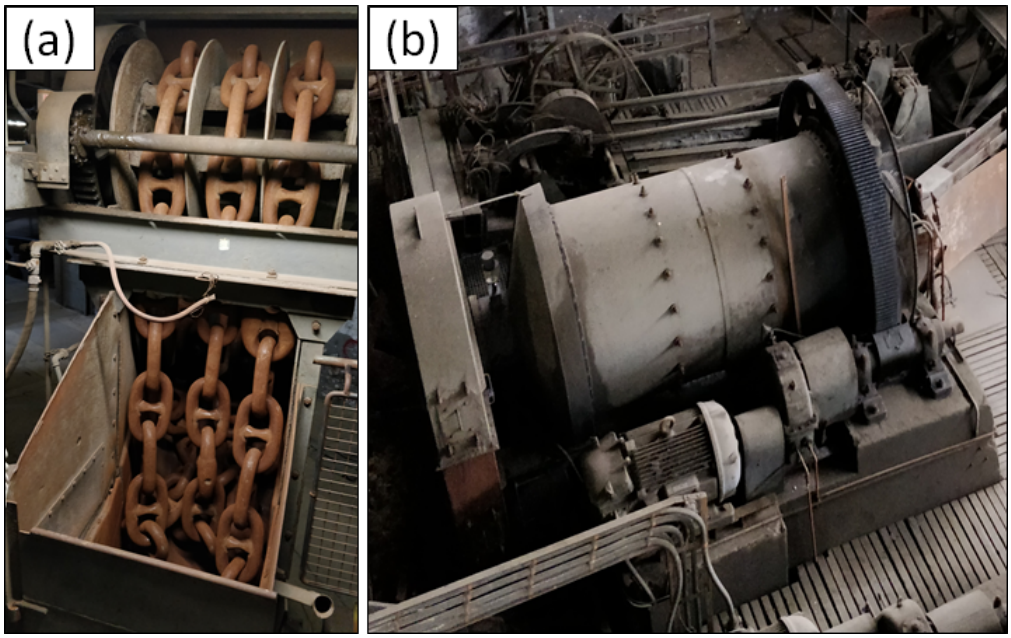

Figure 1.6: Photographs of communition in the Rammelsberg Mine in Germany. (a) Chain crusher used to break large particles and (b) ball mill to grind small particles.

1.2.2 Extractive metallurgy processes

These steps are followed by extractive metallurgy, which consists in chemical operations to extract the metal from the particle-state ores. Various methods are being used for extractions, such as hydrometallurgy and pyrometallurgy. Branches of these methods exist, like electrometallurgy and ionometallurgy but remains in minority compared to the other two. The choice of most suitable extractive metallurgy operation depends on the properties of the material used and may be combined, as shown on Fig.1.7 [30, 31].

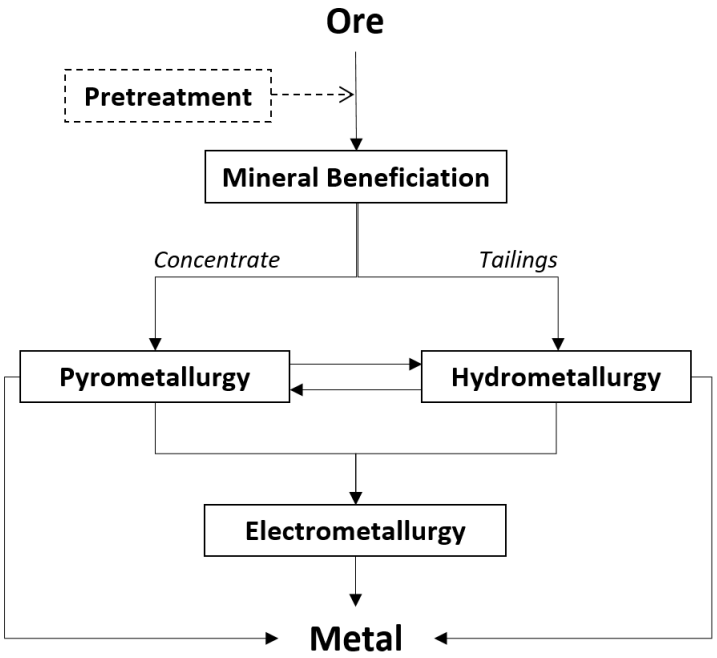

Figure 1.7: Example of a typical extracting metallurgy process.

Most of these processes are also applicable to the urban mine. However, due to the nature of the materials, additional steps of dismantling and separation are to be expected.

Pyrometallurgy

Pyrometallurgy is the oldest extractive metallurgical process and consists in the extraction or refinement of valuable materials using high temperatures. Many technologies are used for pyrometallurgy, which depend on the base material and the metal extracted. As example, copper and nickel may be extracted using the following unit operations:

- Copper can be recovered from copper iron-sulfide or copper-sulfide minerals such as chalcopyrite $CuFeS_2$ or chalcocite Cu_2S. A typical process for recovery is through smelting and refining of an ore concentrate [32]. Using secondary resources, copper may be extracted from slags or scraps (electronic wires or electronic wastes) following the same process as for copper ore [22, 33].

- Nickel is extracted from sulfide ores, mostly from concentrates containing pentlandite $(Ni, Fe)_9 S_8$, chalcopyrite $CuFeS_2$ and pyrrhotite Fe_7S_8, but can also be recovered from furnace dust, slags or Ni-Cd batteries [34, 35]. Nickel production processes include roasting, smelting and converting steps.

In the past two decades, pyrometallurgy became the main process to recover metals from electronics wastes due to the surge of WEEE wastes [22]. The recovery methods using pyrometallurgy were forced to follow the regulations on sustainable development. As such, these methods evolved to complex processes including multiple operations (incineration, smelting, drossing, sintering, melting and reactions in a gas phase) and were included with other processes of metallurgical extraction. These changes allowed to limit negative environmental impacts due to noxious gases emission and wastes accumulation, as shown by Fig. 1.8 with the evolution of the zinc extraction process [30, 36]. For comparison, the old process on Fig. 1.8a lacked means of recycling of all wastes, which was improved, as shown on Fig. 1.8b, by hydrometallurgical technologies to extract the remaining iron contained in the residues. Moreover, with the addition of an electrolysis step, the zinc purity was improved and the remaining dilute sulfuric acid was recycled into a leaching step to replace the carbon reduction.

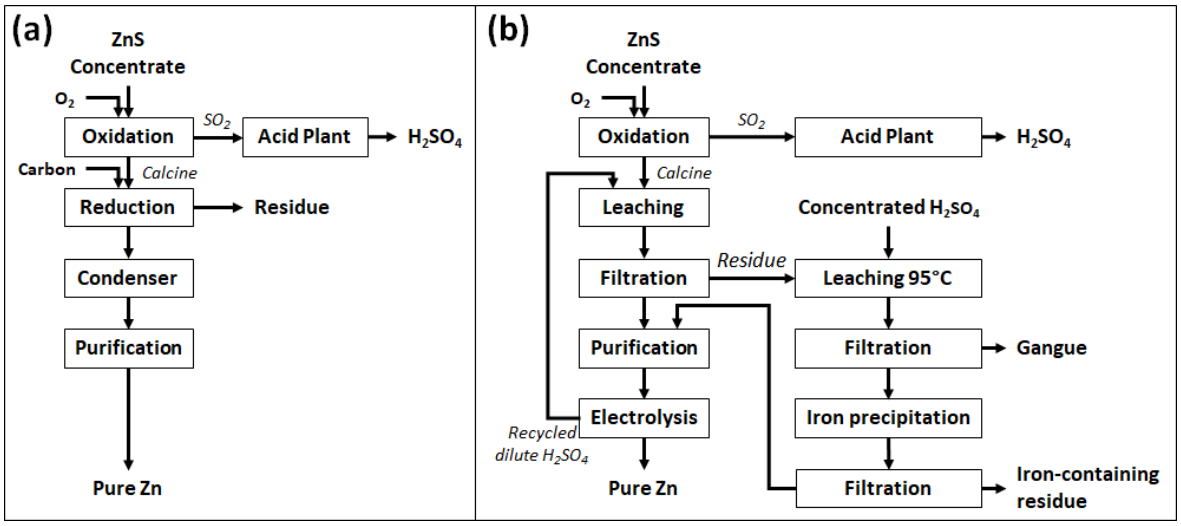

Figure 1.8: Evolution of the process for zinc extraction from sulfide concentrates. (a) Old pyrometallurgical route considering sphaleric oxidation by roasting followed by a zinc oxide reduction and (b) new technology using pyro-, hydro- and electrometallurgical route. Figure from Habashi et al. (2009) [30].

Hydrometallurgy

Hydrometallurgy is a multi-step process that uses aqueous solutions for metal extraction. It involves the extraction of metal via a leaching step allowing the liberation or solubilization of the metal. Then, the metal recovery is performed through a combination of unit operations such as solvent extraction, electrowinning or cementation.

The leaching step uses diverse reagents. Due to the oxidative nature of the reactions, these media will feature acidic compounds including H_2SO_4, HNO_3, HCl and aqua regia, and are combined with oxidants such as H_2O_2, O_2, I_2, Cl_2 or Fe^{3+} [37–39]. The main issue of the leaching step is the regeneration of the oxidant in order to sustain the reaction. This regeneration may be done using chemical means, such as oxidation using potassium permanganate, but was found to be slow nonetheless. The other option is to used biological methods and, for comparison, the maximal biological oxidation rate was found to be 10 to 20 times faster than the chemical methods [40].

Biohydrometallurgy is a branch of hydrometallurgy that considers the use of microorganisms to interact directly or indirectly with the mineral. The main advantages of biohydrometallurgy compared to the traditional abiotic methods are the decrease of operational costs (OPEX) and capital costs (CAPEX) due to the use of lower temperatures, and the sustainability of the process because of more environmental friendly methods. Many applications can be considered using biohydrometallurgy to recover metal from different resources, such as bioleaching, bioflotation, bioaccumulation, biocomplexation, etc.. Among these applications, this study focuses on bioleaching.

1.3 Bioleaching among the metallurgical processes

1.3.1 Bioleaching and biomining

Biomining, as defined by Johnson (2014), is a term describing the technologies that utilize biological systems to facilitate the extraction and recovery of metals from ores and waste materials [41]. It includes the bioleaching processes, that solubilize the target metal and biooxidation processes, that release the occluded target metal from the mineral. Both processes of biomining share the same reactions and microorganisms. Although the use of biomining is fairly recent in mining industry, historical record shows that natural occurrences of bioleaching have been observed for centuries [42]. For instance, acid mine drainage (AMD) containing metals (Fig. 1.9a) were observed by ancient civilizations such as the Romans and Phoenicians. Similar observations were made and exploited centuries ago in the Rio Tinto Mines in Spain (Fig. 1.9b) and in the Falun Mines in Sweden [43, 44]. In 1922, this natural phenomenon was linked to the presence of unidentified sulfur-oxidizing microorganisms [45]. In 1947, *Acidithiobacillus ferrooxidans* (formerly *Thiobacillus ferrooxidans*) was the first bioleaching microorganism to be isolated from an AMD of bituminous coal [46, 47]. The usefulness of these microorganisms for extractive metallurgy led to many researches and developments of processes that could use this potential. For this purpose, the first microorganisms-assisted process was patented in 1955 and was used later on in 1964 for copper and uranium extraction in the United States [48].

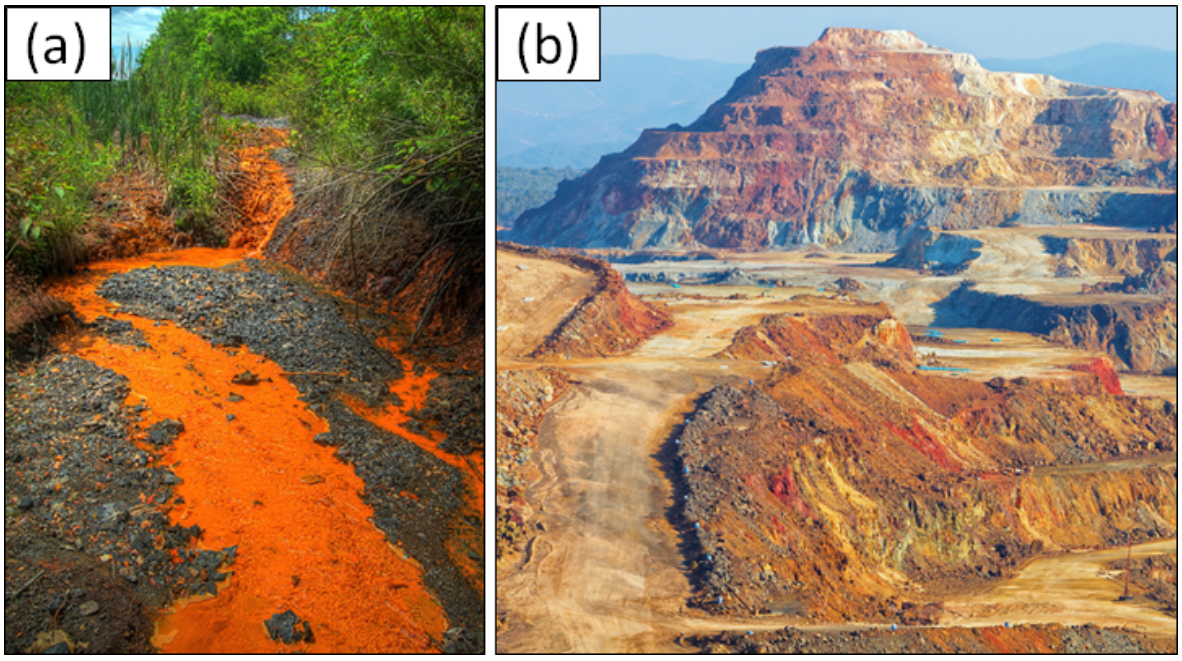

Figure 1.9: Photographs of (a) acid mine drainage in Pittsburgh and (b) the Rio Tinto Mines in Spain.

Following the first industrial bioleaching process, the technology has been widely and increasingly reviewed and refined for a better understanding of its physical, biochemical and microbial mechanisms, as shown in Fig. 1.10 [49]. Nowadays, the technology is used in dozens of large scale processes to recover metals from sulphide matrix (or ores), mainly from refractory gold concentrates and from low-grade copper ore. Recently, new developments have been carried out to widen its use to new resources [50–53] such as oxidised ores (laterites) [54, 55], industrial and urban wastes (WEEE) [22, 56] but, until now, they have not been applied at industrial scale yet. This research work is focused on bioleaching applied to sulfide matrix.

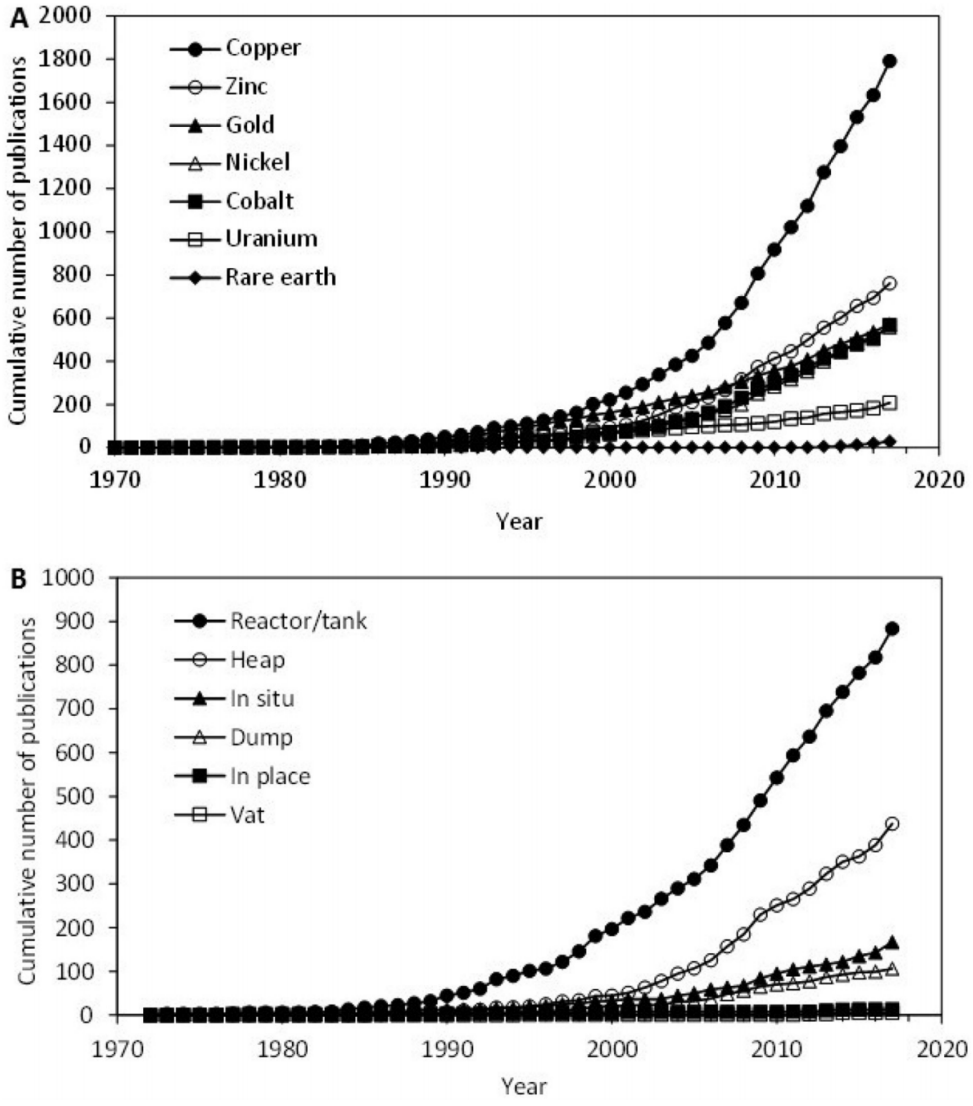

Figure 1.10: Cumulative number of publications listed on Scopus and referring in their abstract to biomining, using words such as bioleaching, biooxidation or biosolubilisation for (A) the metal of interest and (B) the specific applications used for extraction. Figure from Kaksonen et al. (2018) and data from Scopus [49].

1.3.2 Common bioleaching applications

Industrially, two main techniques of bioleaching currently exist: static (percolation) (Fig. 1.11a) and dynamic (agitation) (Fig. 1.11b) [43].

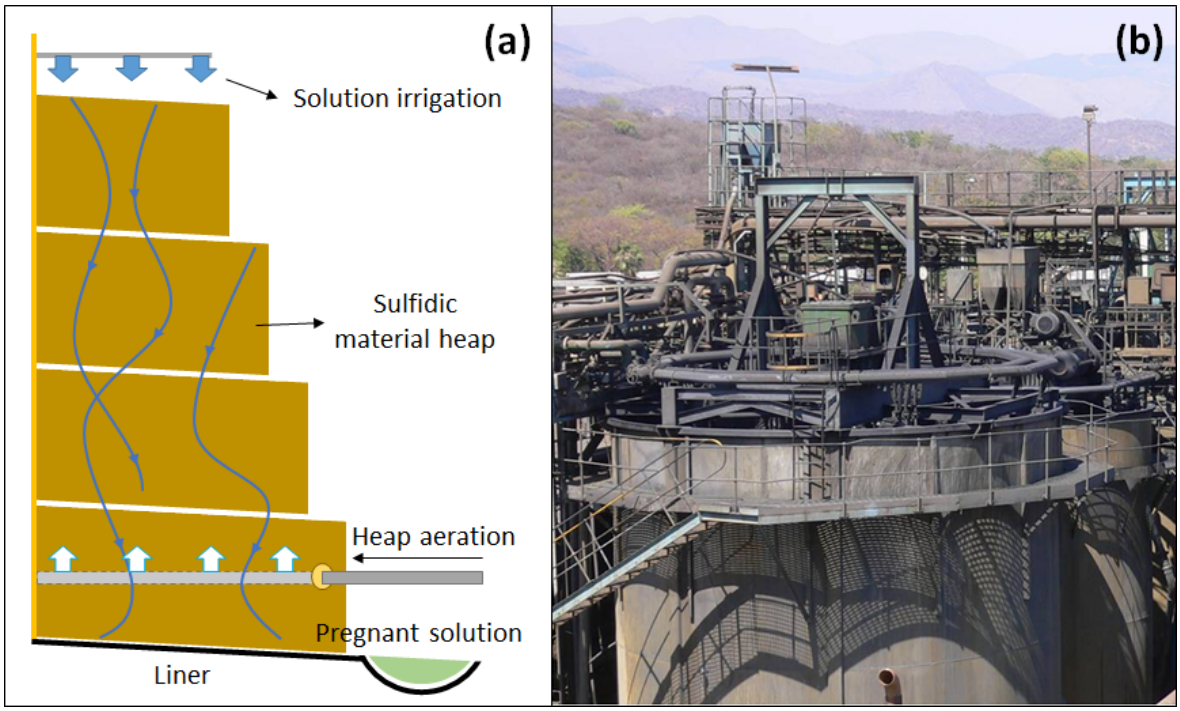

Figure 1.11: Representation of the main bioleaching principles. (a) Schematic representation of the static heap leaching process and (b) Photograph of a stirred tank reactor in the Fairview gold mine, in South Africa.

Percolation leaching is represented by four technologies: dump leaching, heap leaching, in-situ leaching and vat leaching [57, 58]. The main technologies, dump and heap leaching, consist in the irrigation of a heap with an acidic solution that may contain microorganisms. The solution will percolate through the heap and as the heap rests on an impermeable liner, the pregnant solution can later be collected at the base for metal recovery [49]. Furthermore, the heap may be aerated to assist the permeability and the microorganisms growth. Dump or heap leaching are essentially used for low grade ores where concentration is usually not economy viable for common resources, such as low grade copper sulfide [59]. Besides, the process is slow (several months or years) with a poor yield, but is interesting due to its low OPEX [60]. Dump and heap leaching are being used by dozens of commercial applications and produce 16% of global primary copper [61].

Leaching in agitated mode uses stirred tank reactors in combination with microorganisms for metal solubilization or liberation. On the contrary to percolation leaching, it shows high CAPEX and OPEX. Because of this, bioreactors are mostly used for high value ores and concentrates, containing metals such as gold, nickel or cobalt. The extraction process is fast (several days) and the global yield is usually high (more than

90%) [62]. The main interest of bioleaching stirred tank is the possibility to control precisely the different parameters such as the physicochemical parameters (temperature, pH, aeration, agitation), the biological parameters (microbial consortium) and the mass and energy transfers [63, 64].

As seen in the previous part, bioleaching is evolving towards the exploitation of 'unconventional' resources caused by the declining trend in mean ore grades. If heap bioleaching has been the main process option for their treatment until now, it may not be systematically the best solution. The main reasons that preclude heap process are the composition of the materials to be treated (presence of carbonate causing heap clogging, or high concentrations of sulphides that lead to uncontrolled and excessive temperature increase in the heap) and the lack of sufficient space, especially in densely populated areas like in Europe. In such cases, bioleaching STR might be a technical alternative but is mostly too expensive except in very few cases when the metal value is high enough (e.g. such as in Uganda for the cobalt recovery in flotation tailings [65] or in Finland for the valorization of nickel from talc mining residues [66, 67]). Further technical optimization is still needed for this technology to reach an economic viability. Nonetheless, recent advances showed that this may be a fitting technology to answer the ecological concerns related to resources extraction. Bioleaching processes were proven to be used in integrative processes, such as for the CEReS and ASPIRE projects that relate industrial symbiosis between wastes streams to enhance resource efficiency with waste reuse [68, 69]. Khaing et al. (2019) showed that the technology is also adaptable to environmental-friendly lixiviant, with the use of iodide-iodine mixture as an alternative to gold cyanidation [70]. Lastly, as water scarcity is becoming an issue while still being essential for resources extraction, Boxall et al. (2017) demonstrated that saline and brackish water could be used in bioleaching processes as an alternative to fresh water in water scarce regions, such as Australia and Chile [71].

1.3.3 Mechanisms of mineral dissolution

Bioleaching mechanisms have been widely reviewed in the literature to understand the complexity lying behind the mineral dissolution and the role of the microorganisms in this process [72–74]. The process was formerly described as "direct" and "indirect" bioleaching depending on the role of the microorganisms in the leaching part [75, 76]. Direct leaching is represented by a direct electron transfer from the metal sulfide to the attached microorganisms, as shown in the following reaction for direct leaching of pyrite FeS_2:

$$FeS_2 + 3.5\,O_2 + H_2O \xrightarrow{bacteria} Fe^{2+} + 2\,{SO_4}^{2-} + 2\,H^+ \tag{1.1}$$

However, no direct electron transfer through enzymes, nanowires, etc. were demonstrated yet, and kinetics and electrochemical studies disproved the existence of such transfers [77–79]. Because of this, a direct mechanism does not seem to exist. Recently, new terms were suggested to better fit the actual process: ”contact” and ”non-contact” leaching [77, 80]. Both terms are related to the indirect leaching where the metal sulfide is oxidized by ferric iron (Fe^{3+}) which comes from ferrous iron (Fe^{2+}) oxidation by iron-oxidizing bacteria, as shown on Fig.1.12. Contact or non-contact leaching respectively correspond to attach or planktonic cells.

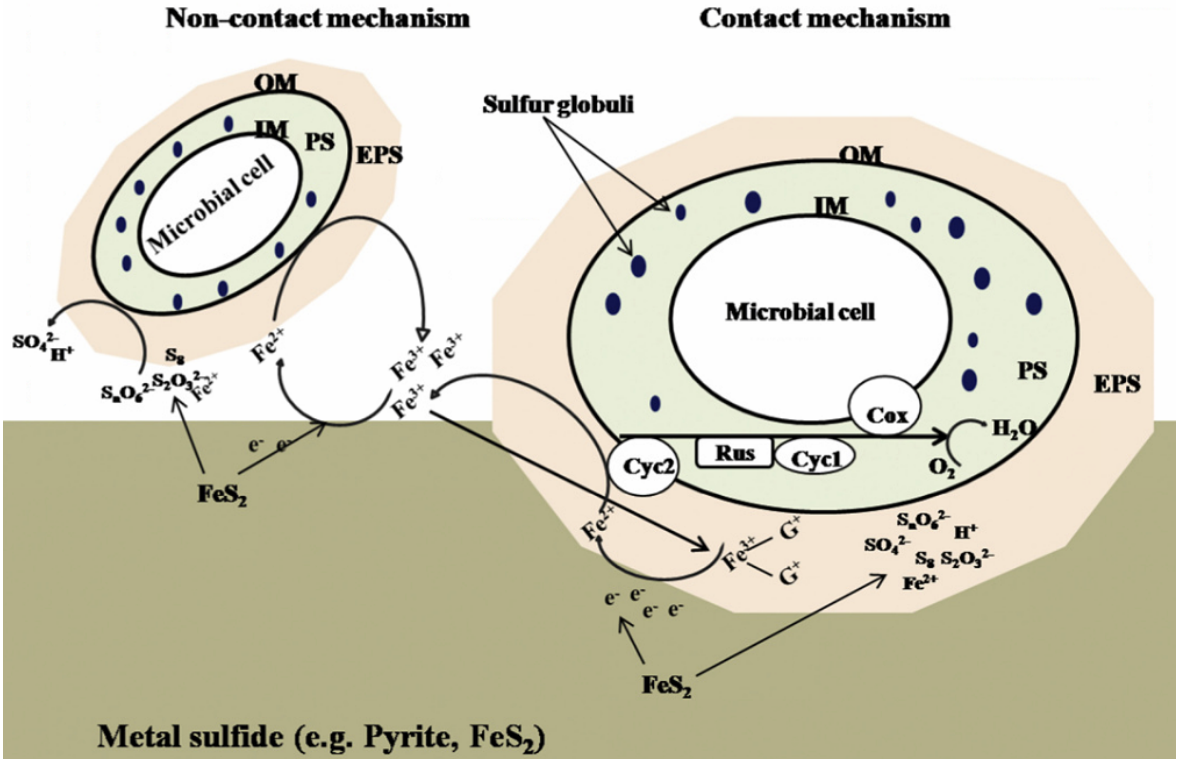

Figure 1.12: Description of contact and non-contact bioleaching mechanisms by planktonic and attached cells, respectively. The different layers are the extracellular polymeric substance (EPS), inner membrane (IM), periplasmic space (PS) and outer membrane (OM). Figure reprinted from Srichandan (2019) [81].

The regeneration of Fe^{3+} takes place in an extracellular polymeric substance (EPS) layer, secreted by the microorganisms on the mineral surface and containing these microorganisms [82, 83]. EPS are composed of polysaccharides, proteins and lipids that are secreted by acidophilic microorganisms and adhere to the cell walls [84]. This layer seems to play an essential role in metal dissolution as its properties allow an increase in cell adhesion to metal sulfide and a reaction space for Fe^{3+} [85–87]. It was indeed shown, using atomic force microscopy, that the removal of EPS on the surface of chalcopyrite led to a decrease of attached cells on the particle surface [88].

Attached cells on the particle surface assist both mechanisms and release sulfur colloids, sulfur intermediates and minerals fragments. These compounds are managed by the planktonic cells in the non-contact mechanisms and the combination of both processes was qualified as "cooperative leaching" [80, 89]. These mechanisms describe the role of microorganisms in the process and their interaction with the mineral sulfides but fail to describe the chemical reactions that take place in the liquid broth. For this, the work of Schippers et al. (1996) identified two different pathways: the thiosulfate and the polysulfide pathways, as shown on Fig.1.13 [73, 90, 91]. These different pathways result from the existence of two groups of metal whose respective atomic properties, make them soluble or insoluble in acid media [92].

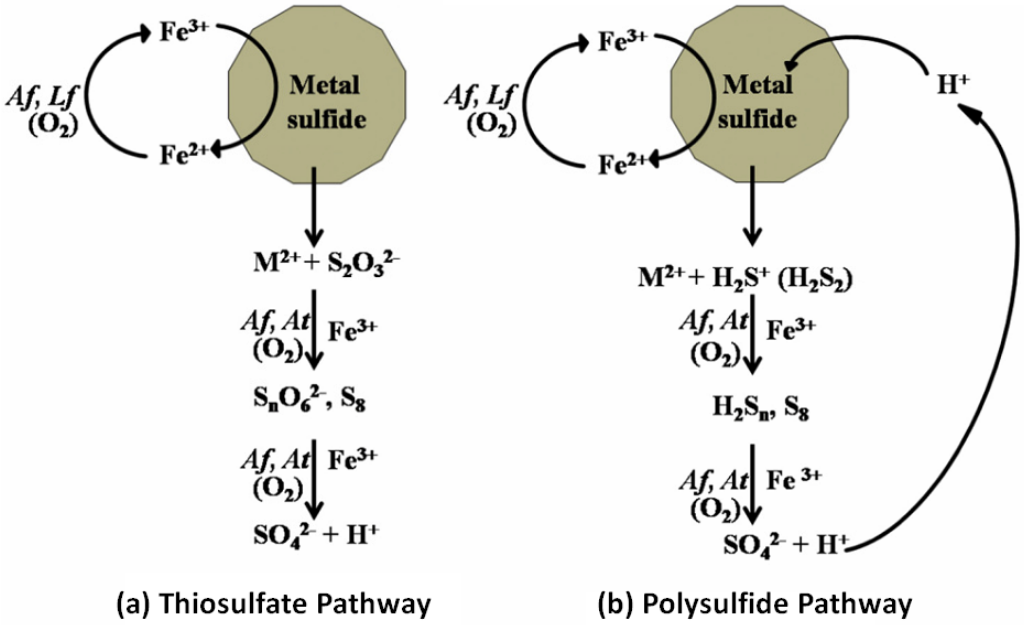

Figure 1.13: Schematic representation of (a) the thiosulfate and (b) polysulfide mechanisms during the bioleaching of a metal sulfide. *Af*, *Lf* and *At* represent *Acidithiobacillus ferrooxidans*, *Leptospirillum ferriphilum* and *Acidithiobacillus thiooxidans*, respectively. Figure from Srichandan et al. (2019), modified from Schipper and Sand (1999) [91, 93].

Thiosulfate Pathway

The thiosulfate pathway is the reaction mechanisms for acid-insoluble metals, represented by pyrite (FeS_2), molybdenite (MoS_2) and tungstenite (WS_2) (Fig. 1.13a). This pathway consists in an oxidation of the metal sulfide through an attack of Fe^{3+}, leading to a soluble sulfur oxyanion ($S_2O_3^{2-}$) and a ferrous iron ion (Eq. 1.2). The thiosulfate is highly unstable in acid conditions and is oxidized to tetrathionate, which will be degraded into differents compounds, such as elemental sulfur, sulfite, trithionate and pentathionate. Finally, due to the composition of the medium and the presence of sulfur-oxidizing microorganisms, most of these compounds will be oxidized to sulfate (Eq. 1.3) [41, 94].

$$FeS_2 + 6\,Fe^{3+} + 3\,H_2O \longrightarrow 7\,Fe^{2+} + {S_2O_3}^{2-} + 6\,H^+ \tag{1.2}$$

$${S_2O_3}^{2-} + 2\,O_2 + H_2O \longrightarrow 2\,{SO_4}^{2-} + 2\,H^+ \tag{1.3}$$

As seen previously, ferric iron is regenerated by the iron-oxidizing microorganisms (Eq. 1.4). This reaction requires oxygen as it is the final electron acceptor in the cell, as seen in Fig. 1.12. An abiotic oxidation of ferrous iron is also possible but is very slow in acidic and low temperature media and, as such, is negligible compared to the microbial oxidation. Using microbial oxidation of sulfur-oxidizing species, elemental sulfur can also be oxidized into sulfuric acid using Eq. 1.5.

$$14\,Fe^{2+} + 3.5\,O_2 + 14\,H^+ \longrightarrow 14\,Fe^{3+} + 7\,H_2O \tag{1.4}$$

$$S_0 + 2\,O_2 + 2\,H^+ \longrightarrow H_2SO_4 \tag{1.5}$$

Polysulfide Pathway

The dissolution of most metal sulfides, which are acid-solubles, such as sphalerite (ZnS), galena (PbS), arsenopyrite (FeAsS), chalcopyrite ($CuFeS_2$) and hauerite (MnS_2), is done according to the polysulfide pathway (Fig. 1.13b). In this mechanism, the metal-sulfur bond of the metal sulfide is cleaved by proton attack [73] (Eq. 1.6, with a monosulfide as example). The resultant sulfidic sulfur is then frequently dimerized into hydrogen disulfide which is oxidized into elemental sulfur via polysulfides using ferric iron [93] (Eq. 1.7). It is interesting to note that this oxidation does not necessarily need ferric iron as dioxygen could act as the electron acceptor. Nonetheless, due to the low efficiency of this reaction, the presence of ferric iron is preferable [91]. Lastly, the elemental sulfur is further oxidize to sulfuric acid by the sulfur-oxidizing microorganisms (Eq. 1.8). In the absence of these microorganisms, elemental sulfur is usually stable enough to remain in the medium.

$$MeS + Fe^{3+} + H^+ \longrightarrow Me^{2+} + 0.5\,H_2S_2 + Fe^{2+} \tag{1.6}$$

$$0.5\,H_2S_2 + Fe^{3+} \longrightarrow 0.125\,S_8 + Fe^{2+} + H^+ \tag{1.7}$$

$$0.125\,S_8 + 1.5\,O_2 + H_2O \longrightarrow {SO_4}^{2-} + 2\,H^+ \tag{1.8}$$

1.3.4 Complementary mechanisms

Bioleaching liquors contain a wide variety of species in solution, necessary for microbial maintenance. For example, the 0Km medium contains $(NH_4)_2SO_4$, H_3PO_4, $MgSO_4 \cdot 7\,H_2O$ and KOH in non-negligible quantities [95]. In addition to the reactive species mentioned above, extreme physicochemical conditions are encountered in bioleaching liquors, such as low pH and high redox potential, which may be responsible for additional reactions that can go against the bioleaching mechanisms, such as passivation, precipitation or cementation.

Precipitation is one of the most common complementary mechanism in bioleaching and may be used to remove iron from the medium as with jarosite formation using ferric iron. However, it could also have a detrimental effect as ferric iron is necessary for metal sulfide dissolution. Jarosite formation occurs at low pH, usually between 1.7 and 2.1 (Fig. 1.14), and requires a monovalent cation, such as potassium (K^+), sodium (Na^+), ammonium (NH_4^+) or hydronium (H_3O^+) [96–98]:

$$A^+ + 3\,Fe^{3+} + 2\,SO_4^{2-} + 6\,H_2O \longrightarrow AFe_3(SO_4)_2(OH)_6 + 6\,H^+ \tag{1.9}$$

where A^+ represents the monovalent cation.

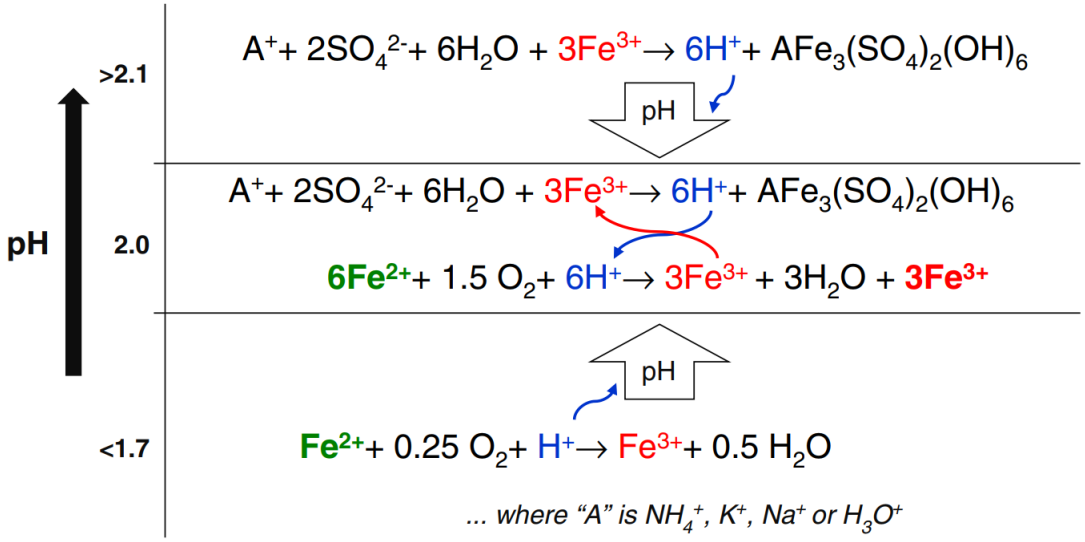

Figure 1.14: Schematic representation of the jarosite formation depending on the pH. Figure from Kaksonen et al. (2014) [97].

Between pH 2 and 4, ferric iron may also precipitate into schwertmannite where there is a deficit of monovalent cations using the mechanism presented in Eq. 1.10. Schwertmannite can further be converted to jarosite through ageing and decomposition processes [99].

$$8\,Fe^{3+} + SO_4^{2-} + 14\,H_2O \longrightarrow Fe_8O_8(OH)_6(SO_4) + 22\,H^+ \tag{1.10}$$

1.3.5 Diversity of microorganisms involved in bioleaching

Since the discovery of microorganisms in AMD and the awareness of their roles in mineral dissolution processes, microorganisms have been used extensively in many applications. They have indeed key functions in biomining mechanisms thanks to their robustness, capabilities and diversity, as shown in Table 1.3. As described previously, their main interest is their ability to oxidize ferrous iron and elemental sulfur, allowing the constant regeneration of the leaching oxidant and maintaining a low pH, which is beneficial for the metal sulphide dissolution [61]. Even if most researches were focused on *At. ferrooxidans* as the first microorganism to be discovered and isolated, a wider range of microorganisms with similar physiological characteristics exists, including *Archaea*. These microorganisms were identified by many studies that followed the discovery of *At. ferrooxidans* on the basis of their interest in biohydrometallurgy, as shown in Fig. 1.15 [100]. In general, a consortium contains several bacterial and archaeal species of each oxidizing types (iron- or sulfur-oxidizing). Consortia can either be found naturally (indigenous consortium) or artificially created (designated consortium) [64]. A common example of laboratory-used consortium is the BRGM-KCC consortium [101]. It is an indigenous consortium that combines several species including *Leptospirillum ferriphilum* (iron-oxidizing), *Acidithiobacillus caldus* (sulfur-oxidizing), *Sulfobacillus benefaciens* (iron- and sulfur-oxidizing), *Sulfobacillus thermosulfidooxidans* (iron- and sulfur-oxidizing) and *Ferroplasma acidiphilum* (iron-oxidizing). In biomining operations and especially for stirred-tank reactors, each process has its own consortium as the microbial composition is expected to depend on the operating conditions (mineral, temperature, pH, aeration) [102, 103].

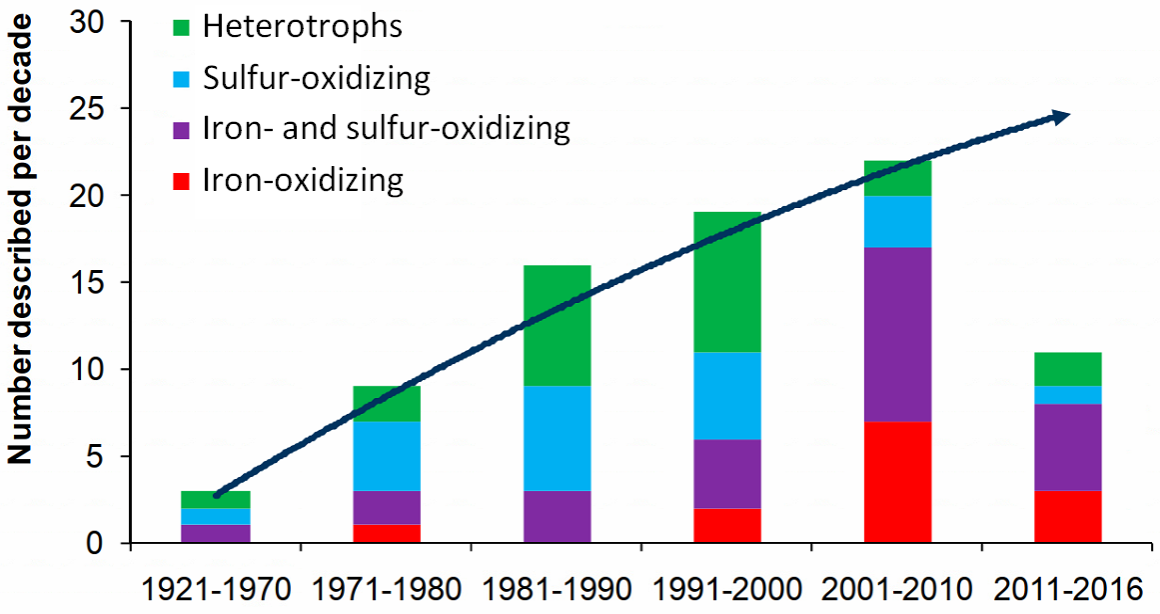

Figure 1.15: Number of acidophilic microorganisms (*Bacteria* and *Archaea*) isolated following the discovery of *At. ferrooxidans*. Figure from Watling (2016) [100].

Table 1.3: Phylogeny, range of growth for pH and temperature and oxidizing abilities of common acidophilic microorganisms. Data from Schippers et al. (2013) and Johnson (2014) [41, 77]

Species	Phylum	Temperature characteristics	Temperature range (°C)	pH range	Metabolism	Iron-oxidizing	Sulfur-oxidizing
Mesophilic and moderately thermophilic bacteria							
Acidiferrobacter thiooxydans	Proteobacteria	M/MT	>5-47	>1.2	Autotroph	+	+
Acidimicrobium ferrooxidans	Actinobacteria	MT	30-55	na	Mixotroph	+	-
Acidithiobacillus ferrooxidans	Proteobacteria	M	10-37	1.3-4.5	Autotroph	+	+
Acidithiobacillus caldus	Proteobacteria	MT	32-52	1.0-3.5	Mixotroph	-	+
Acidithiobacillus thiooxidans	Proteobacteria	M	10-37	0.5-5.5	Autotroph	-	+
Alicyclobacillus tolerans	Firmicutes	MT	<20-55	1.5-5.0	Mixotroph	+	+
Ferrimicrobium acidiphilum	Actinobacteria	M	<37	>1.4	Heterotroph	+	-
Leptospirillum ferriphilum	Nitrospira	MT	<45	0.5-3.5	Autotroph	+	-
Leptospirillum ferrooxidans	Nitrospira	M	na	1.3-4.0	Autotroph	+	-
Sulfobacillus benefaciens	Firmicutes	MT	<47	>0.8	Mixotroph	+	+
Sulfobacillus thermosulfidooxidans	Firmicutes	MT	20-60	1.5-5.5	Mixotroph	+	+
Sulfobacillus thermotolerans	Firmicutes	MT	20-60	1.2-5.0	Mixotroph	+	+
Thiomonas cuprina	Proteobacteria	MT	20-45	1.5-7.2	Mixotroph	-	+
Mesophilic and moderately thermophilic archaea							
Acidiplasma cupricumulans	Euryarchaeota	MT	22-63	0.4-1.8	Mixotroph	+	+
Ferroplasma acidiphilum	Euryarchaeota	M/MT	15-45	1.3-2.2	Mixotroph	+	-
Extremely thermophilic archaea							
Acidianus brierleyi	Crenarchaeota	T	45-75	1.0-6.0	Mixotroph	+	+
Acidianus infernus	Crenarchaeota	T	65-96	1.0-5.5	Autotroph	+	+
Acidianus sulfidivorans	Crenarchaeota	T	45-83	0.8-1.4	Autotroph	+	+
Metallosphaera hakonensis	Crenarchaeota	T	50-80	1.0-4.0	Mixotroph	na	+
Sulfolobus metallicus	Crenarchaeota	T	55-75	1.0-4.5	Autotroph	+	+
Sulfurococcus yelowstonensis	Crenarchaeota	T	50-86	1.0-5.8	Mixotroph	+	+

M = Mesophilic ; MT = Moderately thermophilic ; T = Extremely thermophilic ; na = data not available.

Most of bioleaching microorganisms were discovered in harsh environment, where the conditions could be considered toxic to the vast majority of lifeforms. Amend et Shock (2000) reported some of these discoveries, such as *Thermocrinis ruber*, discovered in the alkaline hot spring in the Lower Geyser Basin if Yellowstone National Park in USA, *Methanococus jannaschii* hosted by deep-sea hydrothermal systems at a depth of 2600 m on the East Pacific Rise or *Acidianus infernus*, found in the Solfatara fields of Naples in Italy [104]. Considering these environments, temperature is a good parameter to classify the different microorganisms in three main groups: mesophilic bacteria (20-40°C), moderately thermophilic bacteria (40-60°C) and extremely thermophilic *Archaea* (60-80°C), depending on their optimal growth temperatures [74, 100, 105]. This parameter is important in applications such as heap leaching because of the exothermicity of metal sulphide dissolution that may dramatically increase the temperature of the heap [106, 107]. As example, the oxidation of pyrite and chalcopyrite produces 2.578 and 2.883 $\mathrm{kJ\,mol^{-1}}$, respectively [104]. Brierley (2003) demonstrated that increasing the temperature of a heap column for gold-recovery containing mesophilic, moderately thermophilic and extremely thermophilic microorganisms led to important variation of microbial consortia depending on the temperature and position in the heap, which led to various degrees of sulfur oxidation [108]. Moreover, while the different microorganisms have shown similar efficiency for metal recovery in heap leaching, extreme thermophile microorganisms have proven to be slightly more beneficial, with the example of *Sulfolobus* spp. which was found to be persistent in heap that can maintain a high temperature for a long time, as in Escondida heap, in Chile [100, 109, 110].

Apart from the high temperatures, these environments also feature low pH (< 3) because of the oxidation of sulfur components into sulfuric acid, leading to an acidification of the surrounding medium. Bioleaching microorganisms are acidophiles in nature because of their ability to thrive in these environments. They are able to maintain a neutral internal cellular pH, which is essential for their energy intake mechanisms as species such as ferrous iron are weak reductant [111, 112]. As such, pH is closely related to bacterial growth and efficiency, as shown by Plumb et al. (2008) for various bioleaching organisms in stirred tank reactor [113]. The growth diversity of microorganisms can be showed by comparing optimal growth pH and temperature (Fig. 1.16) [100].

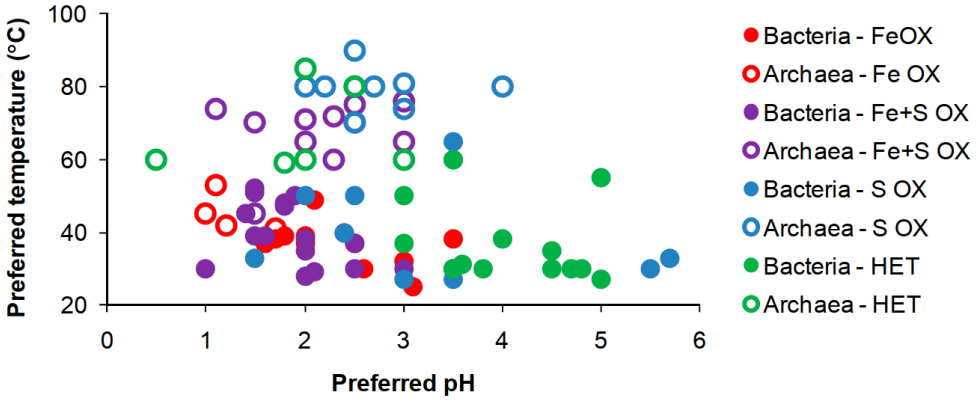

Figure 1.16: Optimal growth pH and temperature of most microorganisms associated with biohydrometallurgy. The microorganisms are represented by their metabolism, namely iron-oxidizing (Fe OX), iron- and sulfur-oxidizing (Fe+S OX), sulfur-oxidizing (S OX) and heterotroph (HET). Figure from Watling (2016) and data from commercial culture-collection database [100].

Lastly, the substrate composition and concentration have a particular interest in biomining processes considering their respective influence on microorganisms. The leaching of a substrate will inevitably lead to the solubilization of components that may have a detrimental effect on the microorganisms. Two phenomena are thus commonly observed: inhibition and toxicity.

- **Inhibiting components** can be products, substrates in high concentration or even biological-based components that will slow-down or limit the microbial activity via fixing mechanisms on the enzyme responsible for this activity. In biomining processes, these inhibitions may alter the microorganisms ability to fix or process ferrous iron or elemental sulfur. For example, Nurmi et al. (2009) demonstrated that, for cultures of *Leptospirillum ferriphilum*, ferric iron had an inhibiting effect on ferrous iron oxidation [114].

- **Toxic components** will directly affect vital functions such as enzyme inactivation, cell damage or formation of precipitates with essential metabolites, which may lead to cellular death [115]. While some metals are usually necessary for basic cellular mechanisms, they are considered toxic at high concentration. As biomining operations feature such conditions, it is often necessary to adapt the strains used to high metal concentrations. However, it was shown that a higher metal tolerance is not related to bioleaching efficiency, as shown by Watkin et al. (2008) for a copper-tolerant thermophilic consortium in a copper sulfide heap [116].

Recently, researches in biohydrometallurgy made consistent progresses in prospecting of new microorganisms that may be suited for various processes. Considering the current issues raised in the previous parts of this work, some focus were made to find suitable consortia in order to reach a sustainable approach. Kaksonen et al. (2018) predicted the requirement of chloride-tolerant acidophilic microorganisms that could allow

the use of seawater in arid regions [49]. In a different approach, consortia with high resistance to multiple metals are sought for e-waste bioleaching due to their polymetallic composition and high metal concentrations [117].

1.4 Improvement of bioleaching processes through modelling

1.4.1 Towards the digital evolution of bioleaching processes

Biohydrometallurgy and its underlying technologies were vastly improved for the past decades. Many researches were made to understand the complex mechanisms that compose these processes and to optimize them. This effort was dependent on an important interdisciplinary engagement including the work of geologists, chemists, metallurgists, microbiologists and chemical engineers [118, 119].

The digital revolution is beginning to offer powerful tools to assist the mining industry, such as modelling, artificial intelligence and machine learning. These tools have the potential to use the knowledge of a technology in order to optimize a process, limiting greatly the necessity of costly and lengthy experimental campaign.

Bioleaching, among the biohydrometallurgy processes, was focused by modelling tools to improve some aspects of its operation. As a biochemical engineering process, existing models were modified and apply to represent phenomena such as microbial growth, oxygen transfer, ore oxidation, energy balance and transport phenomena [120, 121]. These models were adjusted to account for their correlation with physicochemical parameters of the system considered, as reviewed by Mahmoud et al. (2017) [122]. For example in stirred tank reactor bioleaching, the couplings between microbial, mineralogical, physicochemical and geometrical factors need to be taken into account to optimize the process design and efficiency (Fig. 1.17).

As of today, the most comprehensive model is the HeapSim model of Petersen and Dixon (2007), which is an approach to represent the underlying phenomena of heap bioleaching [123]. The model was used to a great extend to establish and optimize multiple heap processes, for example van Staden et al. (2017) used it to model a high temperature heap bioleaching in Mintek, South Africa [124]. Based on the HeapSim model, Ahmadi et al. (2012) established a kinetic model for complex copper sulfide ores bioleaching in stirred tank reactor, adapted for multiple minerals and microorganisms [125]. However, this model lacked the physical modelling description of the complex hydrodynamics observed in STR.

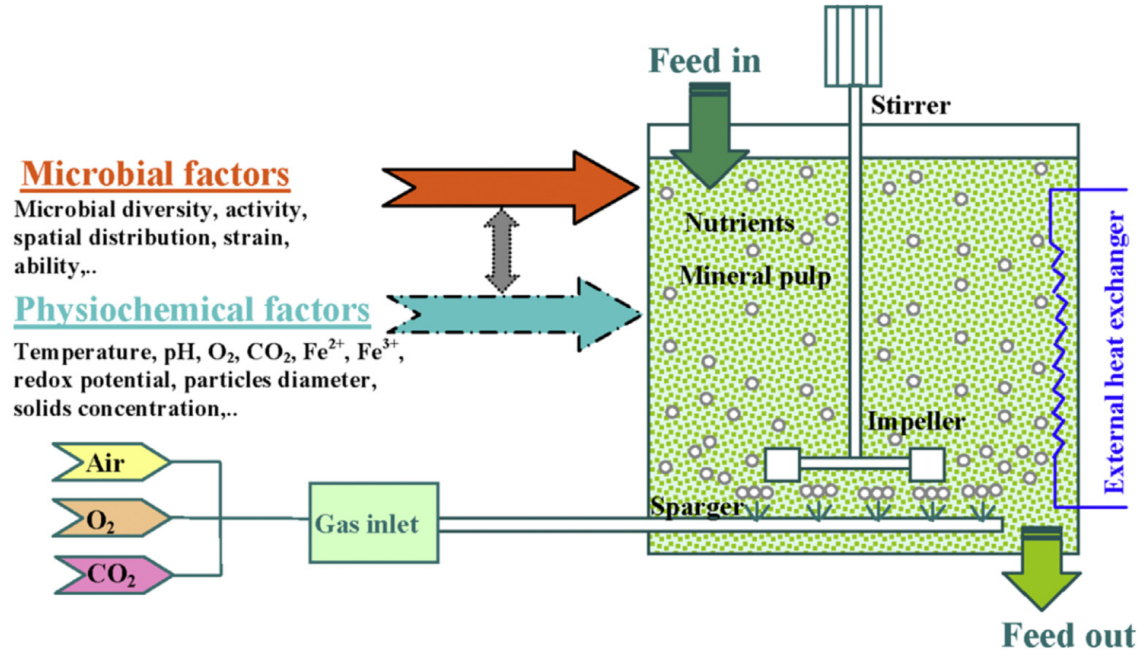

Figure 1.17: Factors influencing bioleaching in STR. Figure reprinted from Mahmoud et al. 2017 [122].

1.4.2 Sulfide mineral oxidation

In mineral leaching, the mechanism of dissolution of a sulfide ore is an oxidative-reduction reaction. Thus, the kinetics of dissolution is tied to the chemical and electrochemical conditions of the environment [126]. Moreover, due to the particulate nature of sulfide mineral in bioleaching processes, the size variation of the particle during dissolution also plays an important role. For this, Bouffard et al. (2006) represented the rate of dissolution r_s ($\mathrm{mol\,kg^{-1}\,h^{-1}}$) as a function of 3 parameters [127]:

$$r_\mathrm{s} = G_\mathrm{s} \cdot \frac{\mathrm{d}X_{c,\mathrm{s}}}{\mathrm{d}t} = G_\mathrm{s} \cdot K(T) \cdot f(C) \cdot g(d_{\mathrm{p},0}, X_{c,\mathrm{s}}) \tag{1.11}$$

where G_s ($\mathrm{mol\,kg^{-1}}$) is the initial sulfide mineral grade, $X_{c,\mathrm{s}}$ ($-$) is the mineral conversion, $K(T)$ a temperature-dependent rate constant, $f(C)$ a chemical function depending on the media composition and $g(d_{\mathrm{p},0}, X_{c,\mathrm{s}})$ a topological function representing the size variation of a sulfide ore of initial particle size $d_{\mathrm{p},0}$ (m) during leaching.

Thermal function $K(T)$

The thermal function $K(T)$ can be expressed by the Arrhenius equation:

$$K(T) = K_\mathrm{ref} \cdot \exp\left[-\frac{E_a}{R}\left(\frac{1}{T} - \frac{1}{T_\mathrm{ref}}\right)\right] \tag{1.12}$$

where K_ref ($\mathrm{h^{-1}}$) and T_ref (K) represent the reference temperature and kinetic constant value respectively, E_a ($\mathrm{J\,mol^{-1}}$) is the activation energy and R (=8.314 $\mathrm{J\,mol^{-1}\,K^{-1}}$) is the ideal gas constant.

Chemical function $f(C)$

The chemical function $f(C)$ represents the impact of the solution composition on the rate equation. Over the years, dozens of empirical functions were established based on the assumption of a rate-limiting reaction [127]. For this, experimental measurements were carried out to determine the order of reaction of the sulfide ore, relatively to the component of the solution, as shown in Table 1.4 for pyrite.

Holmes and Crundwell (2000) assessed the issue through the electrochemistry of the reaction [126]. As the leaching mechanism is an oxidative-reduction reaction, the chemical function is the kinetics result of two half-cell reactions. For example using pyrite, the first reaction is given by the oxidation of pyrite (Eq. 1.13) and the second is the reduction of ferric iron and oxygen (Eq. (1.14-1.15)).

$$\mathrm{FeS_2} + 8\,\mathrm{H_2O} \longrightarrow \mathrm{Fe_2}^{+} + \mathrm{SO_4}^{2-} + 16\,\mathrm{H}^{+} + 14\,\mathrm{e}^{-} \tag{1.13}$$

$$\mathrm{Fe_3}^{+} + \mathrm{e}^{-} \longrightarrow \mathrm{Fe_2}^{+} \tag{1.14}$$

$$\mathrm{O_2} + 4\,\mathrm{H}^{+} + 4\,\mathrm{e}^{-} \longrightarrow 2\,\mathrm{H_2O} \tag{1.15}$$

Crundwell (2013) explained that these reactions occur at all points on the mineral surface and at the same potential, the mixed potential, at which the net production of electron is zero [79]. Thus, the necessary condition for dissolution occurrence is that the net rate between anodic and cathodic reactions is also zero. Furthermore, the Butler-Volmer equation can be used to describe the rates of the respective half-reactions, where the anodic half reaction is considered irreversible and the cathodic half-reaction is considered reversible:

$$r_{\mathrm{a}} = k_{\mathrm{a}} \times \exp\left(\frac{\gamma_{\mathrm{a}} F E_{\mathrm{m}}}{RT}\right) \tag{1.16}$$

$$r_{\mathrm{c}} = k_{\mathrm{c}}\left[Fe^{3+}\right] \times \exp\left(\frac{(\gamma_{\mathrm{c}} - 1) F E_{\mathrm{m}}}{RT}\right) - k_{\mathrm{c}}^{1}\left[Fe^{2+}\right] \times \exp\left(\frac{\gamma_{\mathrm{c}} F E_{\mathrm{m}}}{RT}\right) \tag{1.17}$$

where k and k^1 $(-)$ are kinetic rate constants of the dissolution, γ $(-)$ is the transfer coefficient, F is the Faraday's constant and E_{m} (V) is the mixed potential. The transfer coefficient γ_{a} and γ_{c} were reported symmetrical by several studies and it can be assumed that $\gamma = \gamma_{\mathrm{a}} = \gamma_{\mathrm{c}}$ [126]. With the previous hypothesis that $r_{\mathrm{a}} = r_{\mathrm{c}}$, the following expression can be obtained:

$$E_{\mathrm{m}} = \frac{F}{RT} \times \ln\left(\frac{k_{\mathrm{c}}\left[Fe^{3+}\right]}{k_{\mathrm{a}} + k_{\mathrm{c}}^{1}\left[Fe^{2+}\right]}\right) \tag{1.18}$$

Table 1.4: Chemical function of pyrite oxidation and conditions of published experimental studies. Inspired and completed from Bouffard et al. (2006) [127]

Reactor	$d_{\mathbf{p}}$ **(µm)**	T (°C)	**Medium**	**Chemical rate function**	Reference
STR	74-150	33	0.0004-0.001 M Fe_{tot}	$f(C) = \left[Fe^{3+}\right]$	[128]
STR	125-250	25-30	0.0005-0.0032 M $Fe_3{}^+$ in Cl^-	$f(C) = \frac{\left[Fe^{3+}\right]^{0.58}}{[H^+]^{0.50}}$	[129]
Shake flask	10	30-70	0.02-0.09 M $Fe_3{}^+$ in $SO_4{}^{2-}$ or Cl^-	$f(C) = \frac{\left[Fe^{3+}\right]}{K+\left[Fe^{3+}\right]}$	[130]
CSTR	150-250	25	0.00001-0.003 M $Fe_3{}^+$ in Cl^-	$f(C) = K\left[Fe^{3+}\right]^{0.62}$	[131]
STR	44-105	40-100	0.1-1.0 M $Fe_3{}^+$ in Cl^-	$f(C) = \frac{\left[Fe^{3+}\right]}{\left(\left[Fe^{3+}\right]+K\left[Fe^{2+}\right]\right)^2}$	[132]
CSTR	105-250	no data	excess of $Fe_3{}^+$ in $SO_4{}^{2-}$	$f(C) = \frac{K_1-K_2\left(\left[Fe^{2+}\right]/\left[Fe^{3+}\right]\right)^{0.5}}{K_3+\left[Fe^{3+}\right]^{-0.50}+K_4\left(\left[Fe^{2+}\right]/\left[Fe^{3+}\right]\right)^{0.5}}$	[133]
STR	53-500	60-90	0.05-1.0 M $Fe_3{}^+$ in Cl^-	$f(C) = k_1\frac{\left[Fe^{3+}\right]^2}{\left[Fe^{2+}\right]\left(\left[Fe^{3+}\right]+K_1\left[Fe^{2+}\right]\right)} + k_2\frac{\left[Fe^{3+}\right]}{\left(\left[Fe^{3+}\right]+K_2\left[Fe^{2+}\right]\right)^2}$	[134]
STR	150-250	20-30	<0.003 M Fe_{tot} in $SO_4{}^{2-}$	$f(C) = \frac{\left[Fe^{3+}\right]^{0.30}}{\left[Fe^{2+}\right]^{0.47}[H^+]^{0.32}}$	[135]
STR	150-250	20-30	<0.003 M Fe_{tot} in $SO_4{}^{2-}$	$f(C) = \frac{\left[Fe^{3+}\right]^{0.93}}{\left[Fe^{2+}\right]^{0.40}}$	[135]
STR	45-53	35	0.001-0.270 M $Fe_3{}^+$ 0.0001-0.1 M $Fe_2{}^+$	$f(C) = \frac{1}{[H^+]^{0.5}}\left[\frac{\left[Fe^{3+}\right]}{K_1[H^+]^{-0.5}+K_2\left[Fe^{2+}\right]}\right]^{0.5}$	[136]
STR	53-75	30	0.04-0.4 M $Fe_3{}^+$ in $SO_4{}^{2-}$	$f(C) = \frac{\left[Fe^{3+}\right]}{\left[Fe^{3+}\right]+K\left[Fe^{2+}\right]}$	[137, 138]

STR = Stirred Tank Reactor ; CSTR = Continuous Stirred Tank Reactor.

This last expression can be injected into 1.16 to obtain the chemical function of the rate of dissolution:

$$f(C) = k_{\mathrm{a}} \times \left(\frac{k_{\mathrm{c}} \left[Fe^{3+} \right]}{k_{\mathrm{a}} + k_{\mathrm{c}}^{1} \left[Fe^{2+} \right]} \right)^{0.5} \tag{1.19}$$

Following this, two distinct types of leaching kinetics exist and relate the limiting form of the previous equation [139]:

> Type I for $k_{\mathrm{a}} \gg k_{\mathrm{c}}^{1} \left[Fe^{3+} \right]$, where ferric reduction is relatively slow:

$$f(C) \propto \left[Fe^{2+} \right]^{0.5} \tag{1.20}$$

> Type III for $k_{\mathrm{a}} \ll k_{\mathrm{c}}^{1} \left[Fe^{2+} \right]$, where ferric reduction is relatively fast:

$$f(C) \propto \left(\frac{\left[Fe^{3+} \right]}{\left[Fe^{2+} \right]} \right)^{0.5} \tag{1.21}$$

It was shown by Bouffard et al. (2006) that, for pyrite, the optimal value of k_{a} is zero and thus, pyrite oxidation is characterized by type III leaching [127].

Topological function $g(d_{\mathrm{p},0}, X_{c,\mathrm{s}})$

The topological function comes from the particulate nature of the leached mineral. The mineral available surface will decline during the dissolution, as shown in Fig. 1.18, which will affect the available reactive surface and thus, the reaction rate [140]. Moreover, the sulfide mineral may be contained in a non-soluble silicate matrix, which could complicate the estimation of the dissolution kinetics.

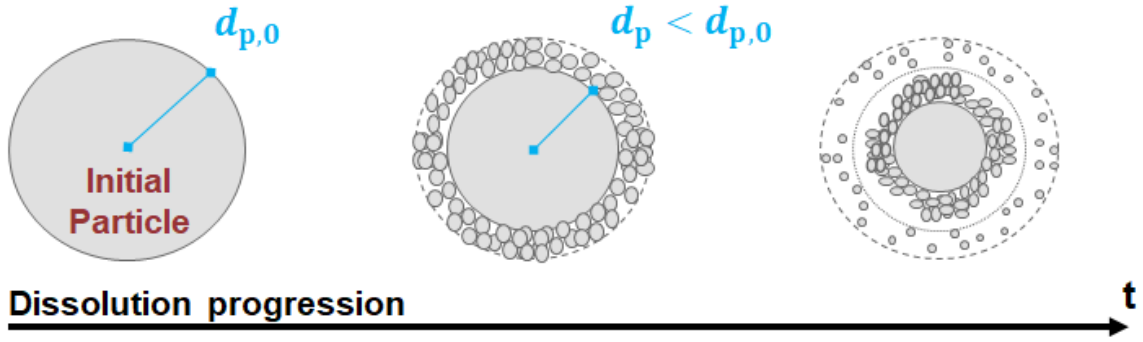

Figure 1.18: Schematic representation of the shrinking of a particle during dissolution.

The topological function is commonly represented using shrinking sphere or shrinking core type models, which will assume a constant, uniform size reduction of a spherical particle [141]. However, due to the observed variation of particle grade, size and shape, these models are often difficult to apply. A generalized model is given as the power-law expression proposed by Dixon and Hendrix [142]:

$$g(1 - X_{c,\mathrm{s}}) = (1 - X_{c,\mathrm{s}})^{\varphi} \tag{1.22}$$

where φ is a topological parameter that can be adapted depending on the particles characteristics. The parameter will be equal to 2/3 for spherical particles and was observed to be as high as 3 for a wide size distribution [142]. This parameter could be used dynamically, as the particle distribution will evolve during the leaching. Furthermore, multiple rate equations could be determined, each representing a specific size distribution with a particular φ.

Lastly, the topological function can further be improved by adding the initial particle size d_0 (m) and the solid molecular mass M_s ($\mathrm{kg\,mol^{-1}}$) and mass density ρ_s ($\mathrm{kg\,m^{-3}}$) as proposed by Bouffard (2003) [127, 140]:

$$g(1 - X_{c,\mathrm{s}}) = \frac{6M_\mathrm{s}}{\rho_\mathrm{s} d_0} (1 - X_c)^{\gamma} \tag{1.23}$$

Combining Eq. 1.11, 1.12, 1.21 and 1.23, the overall equation for spherical pyrite particles dissolution can be determined [125]:

$$r_\mathrm{s} = K_\mathrm{ref} \times \exp\left[-\frac{E_a}{R}\left(\frac{1}{T} - \frac{1}{T_\mathrm{ref}}\right)\right] \times \left(\frac{[Fe^{3+}]}{[Fe^{2+}]}\right)^{0.5} \times (1 - X_c)^{\gamma} \tag{1.24}$$

where

$$K = K_\mathrm{ref} \times \frac{6M_\mathrm{s}}{\rho_\mathrm{s} d_0} \tag{1.25}$$

This equation can be further improved by adding the impact of jarosite precipitation on the presence of Fe^{3+}. Bouffard and Dixon (2009) assumed a linear equilibrium between Fe^{3+} and H_2SO_4 to approximate the jarosite formation [143]:

$$K_\mathrm{jar} = \frac{[\mathrm{H_2SO_4}]}{[\mathrm{Fe^{3+}}]} = 0.3 \tag{1.26}$$

where K_jar is the equilibrium constant.

1.4.3 Microbial modelling

In bioleaching mechanisms, microbes are mainly responsible for the oxidation of ferrous iron (Eq. 1.4) and elemental sulfur (Eq. 1.5). A particular attention was given to the development of a rate equation for the oxidation of ferrous iron due to the importance of ferric iron for mineral dissolution. Most of these are unstructured kinetic models which represent growth and ferrous oxidation using simple mathematical models [144].

The rate of biomass growth r_X ($\mathrm{cell\,l^{-1}\,h^{-1}}$) can be modelled as the difference between microbial growth and death:

$$r_X = \frac{d\,[X]}{dt} = (\mu - k_D)\,[X] \tag{1.27}$$

where [X] ($\mathrm{cell\,l^{-1}}$) is the biomass concentration, k_D ($\mathrm{h^{-1}}$) the death rate and μ ($\mathrm{h^{-1}}$) the specific growth rate. The later can be modelled using various models that may consider one or multiple substrates consumption and inhibition from different sources. The most common model is the Monod equation, which is a simple empirical model representing the specific growth rate based on a limiting substrate utilisation [145]. For example, the specific growth rate for iron-oxidizing bacteria can be represented by the following Monod equation:

$$\mu = \mu_{max} \cdot \frac{\left[Fe^{2+}\right]}{K_{Fe^{2+}} + \left[Fe^{2+}\right]} \tag{1.28}$$

where μ_{max} ($\mathrm{h^{-1}}$) is the maximal specific growth rate and $K_{Fe^{2+}}$ ($\mathrm{mol\,l^{-1}}$) is the half-velocity constant, where $\mu/\mu_{max} = 0.5$. As the Monod equation is an empirical correlation, both μ_{max} and $K_{Fe^{2+}}$ are obtained experimentally and are dependent on the microbial species and the experimental conditions. Moreover, important differences are still observed from one strain to another [146]. Due to these facts, it is often difficult to obtain precise data for bioleaching microorganisms kinetic parameters as the microbes strive in various environments and often work in consortia, which highly impacts the values of the parameters. Nonetheless, average values are often taken to represent a specific class of bacteria based on their oxidizing type and temperature dependency. Bouffard and Dixon (2009) reviewed some of these values as shown on Table 1.5 [143].

Table 1.5: Growth parameters for bioleaching microorganisms [143].

Parameter	**Temperature**	**Iron-oxidizing**	**Sulfur-oxidizing**
μ ($\mathrm{h^{-1}}$)	M	0.11	0.007
	MT	0.11	0.009
	T	0.11	0.035
K ($\mathrm{mol\,l^{-1}}$)	–	0.1×10^{-3}	0.1

M = Mesophilic ; MT = Moderately thermophilic ; T = Extremely thermophilic.

Considering the common data available during experimental measurements, an alternative formulation in terms of ferrous iron consumption rate, via the Pirt equation, was proven better [147]. Furthermore, this formulation allows to take the microbial maintenance $m_{Fe^{2+}}$ ($\mathrm{h^{-1}}$) into account, representing the basic energy expenses of a microorganism to maintain its primary functions:

$$r_{\mathrm{Fe^{2+}}} = \frac{r_{\mathrm{X}}}{Y_{\mathrm{FeX}}^{max}} + m_{\mathrm{Fe^{2+}}} [\mathrm{X}] \tag{1.29}$$

where Y_{FeX}^{max} ($\mathrm{mol\,cell^{-1}}$) is the ferrous oxidation yield per unit of biomass.

Lastly, the previous formulation can be related to the biomass concentration using the specific ferrous iron consumption, as shown by the following equation:

$$q_{\mathrm{Fe^{2+}}} = \frac{r_{\mathrm{Fe^{2+}}}}{[\mathrm{X}]} \tag{1.30}$$

Review of literature rate equations

Over the last decades, the rate equation for the microbial oxidation of ferrous iron was widely reviewed, as shown by Table 1.6 [148]. Multiple assumptions were made to characterize the phenomena influencing microbial growth. While the kinetic constants will vary depending on the microbial strain considered, a general equation can still be established. Jones et al. (1983) observed an inhibition of *At. ferrooxidans* at high concentration of $\mathrm{Fe^{3+}}$, which they translated into an additional term on the Monod equation, as shown on Eq. 1.31 [149].

$$\mu = \frac{\mu_{\max} \left[\mathrm{Fe^{2+}}\right]}{K_{\mathrm{m}} \left(1 + \frac{\left[\mathrm{Fe^{3+}}\right]}{K_{\mathrm{i}}}\right) + \left[\mathrm{Fe^{2+}}\right]} \tag{1.31}$$

with K_{i} ($\mathrm{mol\,l^{-1}}$) an inhibition constant.

Similar observations were made by Nurmi et al. (2009) who observed a competitive inhibition of $\mathrm{Fe^{2+}}$ by $\mathrm{Fe^{3+}}$ for *L. ferriphilum* cultures in fluidized bed bioreactor [114]. Braddock et al. (1984) proposed to include a threshold value of $\mathrm{Fe^{2+}}$ which takes into account the absence of microbial growth at too low concentration (Eq. 1.32) [150].

$$\mu = \frac{\mu_{\max} \left(\left[\mathrm{Fe^{2+}}\right] - \left[\mathrm{Fe^{2+}}\right]_t\right)}{K_{\mathrm{m}} + \left(\left[\mathrm{Fe^{2+}}\right] - \left[\mathrm{Fe^{2+}}\right]_t\right)} \tag{1.32}$$

with $\left[\mathrm{Fe^{2+}}\right]_t$ ($\mathrm{mol\,l^{-1}}$) the ferrous iron concentration threshold value. The value was experimentally determined for *At. ferrooxidans* at $2.5 \times 10^{-4}\,\mathrm{mol\,l^{-1}}$.

Furthermore, Özkaya et al. noticed that, in batch bottles cultures of *L. ferriphilum*, this value linearly increased with the initial concentration of Fe^{2+} and Fe^{3+} [146]. Nikolov et al. (1992) represented the rate equation using a Haldane kinetics, which represents the impact of self-inhibition of the substrate, which was later proved to be adapted for cultures of *At. ferrooxidans* and *L. ferriphilum* [114, 146, 151]. Nurmi et al. (2009) also added the effect of multiple metal concentrations and their inhibiting effect on microbial growth as observed for *L. ferriphilum* cultures [114]. The work of Crundwell (1997) has shown that the model could be widen to multiple substrates and products such as H^+ or O_2 concentrations [152]. As O_2 supply is known to be one rate-limiting mechanisms in bioleaching, its importance as a substrate in the specific growth rate equation was used in multiple complete model such as the HeapSim model. For this, Bouffard and Dixon (2009) used a dual substrate equation to include the impact of dissolved oxygen concentration on growth, as shown by Eq. 1.33 [143].

$$\mu = \mu_{\max} \cdot \frac{\left[Fe^{2+}\right]}{K_{Fe^{2+}} + \left[Fe^{2+}\right]} \cdot \frac{[O_2]}{K_{O_2} + [O_2]} \tag{1.33}$$

where K_{O_2} is the half-velocity oxygen constant ($= 5 \times 10^{-5}\,\mathrm{mol\,l^{-1}}$).

The rate equation for the elemental sulfur oxidation may be obtained using similar equations. As sulfur-oxidizing bacteria growth is also limited by dissolved oxygen availability, a dual-limiting substrate equation is also often used to represent the growth, as shown by Eq. 1.34.

$$\mu = \mu_{\max} \cdot \frac{[S]}{K_S + [S]} \cdot \frac{[O_2]}{K_{O_2} + [O_2]} \tag{1.34}$$

Table 1.6: Rate equations for the microbial oxidation of ferrous iron of published experimental studies. Inspired from Ojumu et al. (2006) [148]

Reactor	T (°C)	pH	$\mathbf{Fe_{tot}}$ (mol)	**Ferrous oxidation model**	**Reference**
Specific growth rate based models					
CSTR	28	2.2	no data	$\mu = \frac{\mu_{\max}\left[Fe^{2+}\right]}{K_m+\left[Fe^{2+}\right]}$	[145]
CSTR	30	1.6	0.005-0.4	$\mu = \frac{\mu_{\max}\left[Fe^{2+}\right]}{K_m\left(1+\frac{\left[Fe^{3+}\right]}{K_i}\right)+\left[Fe^{2+}\right]}$	[149]
CSTR	22	1.8-1.9	0.009-0.022	$\mu = \frac{\mu_{\max}\left(\left[Fe^{2+}\right]-\left[Fe^{2+}\right]_t\right)}{K_m+\left(\left[Fe^{2+}\right]-\left[Fe^{2+}\right]_t\right)}$	[150]
CSTR	35	1.8	0.009-0.059	$\mu = \frac{\mu_{\max}\left[Fe^{2+}\right]}{K_m\left(1+K_i\left[Fe^{3+}\right]\right)+\left[Fe^{2+}\right]}$	[153]
CSTR	29	1.8	0.035-1.27	$\mu = \frac{\mu_{\max}\left[Fe^{2+}\right]}{\left[Fe^{2+}\right]+K_m+\frac{K_m}{K_{i,1}}\left[Fe^{3+}\right]+\frac{\left(\left[Fe^{2+}\right]\right)^2}{K_{i,2}}}$	[151]
Ferrous iron consumption based models					
CSTR	30	2.0	0.0003-0.015	$r_{Fe^{2+}} = K_1\left(\frac{p_{O_2}}{K_2+p_{O_2}}\right)\left(\frac{\left[Fe^{2+}\right]}{\left[Fe^{2+}\right]+K_m\left(1+\frac{\left[Fe^{3+}\right]}{K_i}\right)}\right)$	[154]
CSTR	Fitted to data from Huberts (1994) [154]			$r_{Fe^{2+}} = K_1\left(\frac{\left[Fe^{2+}\right]/\left[H^+\right]}{K_m+\left[Fe^{2+}\right]/[H^+]+K_i\left[Fe^{3+}\right]}\right)^{0.5}\left(\frac{p_{O_2}}{K_2+p_{O_2}}\right)^{0.5}$	[152]
CSTR	Unpublished data from Hansford et Rawlings (1997)			$q_{Fe^{2+}} = \frac{q^{max}_{Fe^{2+}}}{1+K_m\frac{\left[Fe^{3+}\right]}{\left[Fe^{2+}\right]}}$	[155, 156]
Shake Flask	30	2.0	0.008-0.56	$r_{Fe^{2+}} = \frac{K_1\times\exp(-Ea/RT)[X]\left[Fe^{2+}\right]}{\left(K_m+\left[Fe^{2+}\right]\right)\left(1+\frac{\left[Fe^{3+}\right]}{K_i}\right)}$	[157]
Oxygen consumption based models					
Shake Flask	29	1.8-2.0	0.00025-0.026	$r_{O_2} = \frac{K[X]\left[Fe^{2+}\right]}{\left[Fe^{2+}\right]+K_m\left[1+\frac{[X]}{K_{i,1}}+\frac{\left[Fe^{3+}\right]}{K_{i,2}}+\frac{[X]\left[Fe^{3+}\right]}{\alpha K_{i,1}K_{i,2}}\right]}$	[158]
CSTR	30	1.8-1.9	0.05-0.36	$q_{O_2} = \frac{q^{max}_{O_2}}{1+\frac{K_m}{\left[Fe^{2+}\right]-\left[Fe^{2+}\right]_t}+\frac{K_m}{K_i}\frac{\left[Fe^{3+}\right]}{\left[Fe^{2+}\right]-\left[Fe^{2+}\right]_t}}$	[147]

CSTR = Continuous Stirred Tank Reactor.

Modelling of the effect of pH and temperature on microbial growth

In microbial processes, it is known that microorganisms are sensible to environmental conditions, *viz.* medium composition, pH, temperature and oxygenation. As shown in the previous part of this work, each microorganism has an optimal range of pH and temperature for its growth (Table 1.3).

Ojumu and Petersen (2011) showed that the specific microbial oxidation rate for *L. ferriphilum* cultures follows a symmetrical bell-shaped curved with the variation of pH of the medium around the optimum of the microorganism considered [159]. As a matter of fact, a pH below the optimal value has a negative effect on bacterial growth due to the difficulty to maintain a neutral cytosolic pH. On the other hand, a pH higher than the optimal value limits the availability of protons, which are needed for ferrous iron oxidation [152]. Moreover, as seen in the previous section, precipitation phenomena occur at pH above 1.7, which restraints iron and monovalent cation availability and indirectly affects the growing efficiency [97, 98]. As shown by the model of Crundwell (1997), this variation can directly be represented in the rate equation as a function of H^+ concentration (Eq. 1.35) [152].

$$r_{Fe^{2+}} = K_1 \left(\frac{\left[Fe^{2+}\right] / \left[H^+\right]}{K_m + \left[Fe^{2+}\right] / \left[H^+\right] + K_i \left[Fe^{3+}\right]} \right)^{0.5} \left(\frac{[O_2]}{K_{O_2} + [O_2]} \right)^{0.5} \tag{1.35}$$

The effect of temperature on microbial growth can be described with a bell-curved below the optimal temperature but after this temperature, the growth decreases sharply to 0. It is explained by the absence of microbial activity observed at lower temperature and the cell destruction at higher temperature [148, 160]. Various models may be used to represent such impact. The most commonly seen in the literature is the Ratkowsky equation, that represents the impact of temperature on the maximal specific growth rate:

$$\mu_{max} = b \left(T - T_{min}\right) \left[1 - \exp\left(c \left(T - T_{max}\right)\right)\right] \tag{1.36}$$

where b (h^{-1}) and c ($°C^{-1}$) are constants that depend on the microbial strain. Franzmann et al. (2005) determined the value of these constants and growth temperature of several *Bacteria* and *Archaea*, as detailed in Table 1.7 [161].

Table 1.7: Value of growth temperatures and Ratkowsky model constants for various microorganisms. Reproduced from Franzmann et al. (2005) [161]

Organism	**Substrate**	$T_{\min}$ (°C)	T_{opt} (°C)	T_{max} (°C)	b (h^{-1})	c ($°C^{-1}$)
L. ferrooxidans	Fe_2^+	7.8 ± 1.4	36.7	44.6 ± 0.2	0.01117 ± 0.00088	0.27674 ± 0.03632
L. ferriphilum	Fe_2^+	10.7 ± 1.1	38.6	48.5 ± 1.0	0.01551 ± 0.00132	0.22061 ± 0.06207
Ferroplasma acidiphilum	Fe_2^+	12.7 ± 6.1	39.6	47.2 ± 0.7	0.00431 ± 0.0149	0.3453 ± 0.03546
Acidimicrobium ferrooxidans	Fe_2^+	7.4 ± 3.0	48.8	59.5 ± 0.3	0.01444 ± 0.00155	0.25323 ± 0.04458
Ferroplasma cyprexacervatum	Fe_2^+	15.0 ± 1.4	55.2	63.0 ± 0.1	0.00652 ± 0.00035	0.3453 ± 0.03546
S. thermosulfidooxidans	Fe_2^+	11.7 ± 5.3	51.2	63.5 ± 1.4	0.012 ± 0.0028	0.16324 ± 0.07199
Acidianus brierleyi	Fe_2^+	48.7 ± 2.6	71.5	81.5 ± 0.9	0.01732 ± 0.00521	0.14965 ± 0.07795
At. ferrooxidans	S_0	-40.4 ± 19.1	29.6	44.3 ± 2.6	0.00063 ± 0.00022	0.1747 ± 0.09516
At. thiooxidans	S_0	-4.2 ± 0.8	32.8	39.7 ± 0.1	0.00293 ± 0.0001	0.30891 ± 0.01506
At. caldus	S_0	-32.4 ± 11.0	48.8	53.6 ± 0.1	0.00109 ± 0.00018	0.89486 ± 0.27001
S. metallicus	S_0	26.3 ± 1.6	71.0	76.0 ± 0.1	0.00236 ± 0.00012	0.70422 ± 0.8867

Bouffard and Dixon (2009) also developed an alternative to the Ratkowski model to determine the impact of temperature, which can be used in specific microbial oxidation rate models [143]. This model characterized mathematically the asymmetrical, bell-shaped curve with the minimum, maximum and optimal temperature of microbial viability. This is represented by the function $f_g(T)$, which varies depending on the temperature, as shown by the following equations:

$$f_g(T) = \frac{B}{\exp(T) + \exp(-AT)} \tag{1.37}$$

where

$$B = A^{\frac{1}{1+A}} + A^{\frac{-A}{1+A}} \tag{1.38}$$

$$T = \ln(B\cosh\pi)\left[-\frac{1}{A} + \left(\frac{T - T_{\min}}{T_{\max} - T_{\min}}\right)\left(1 + \frac{1}{A}\right)\right] \tag{1.39}$$

Then, A can be evaluated using the implicit equation:

$$T_{\min} + (T_{\max} - T_{\min})\left[\frac{A}{(1+A)^2}\frac{\ln A}{\ln(B\cosh\pi)}\right] = T_{\text{opt}} \tag{1.40}$$

This function $f_g(T)$ can directly be included in the rate equation. It will act as a progressive switch depending on the medium temperature. For $T \approx T_{\text{opt}}$, $f_g(T)$ will be maximum and roughly equal to 1. For $T \leq T_{\min}$ or $T \geq T_{\max}$, $f_g(T)$ will be at its lowest and nearly equal to 0. As described by Fig. 1.19 for *L. ferriphilum*, both models produced equivalent results to show the impact of temperature on bacterial growth. While the adapted model failed to represent accurately the absence of microbial growth at both extremes, it offered the advantages of avoiding the necessity of the required constants of the Ratkowski model.

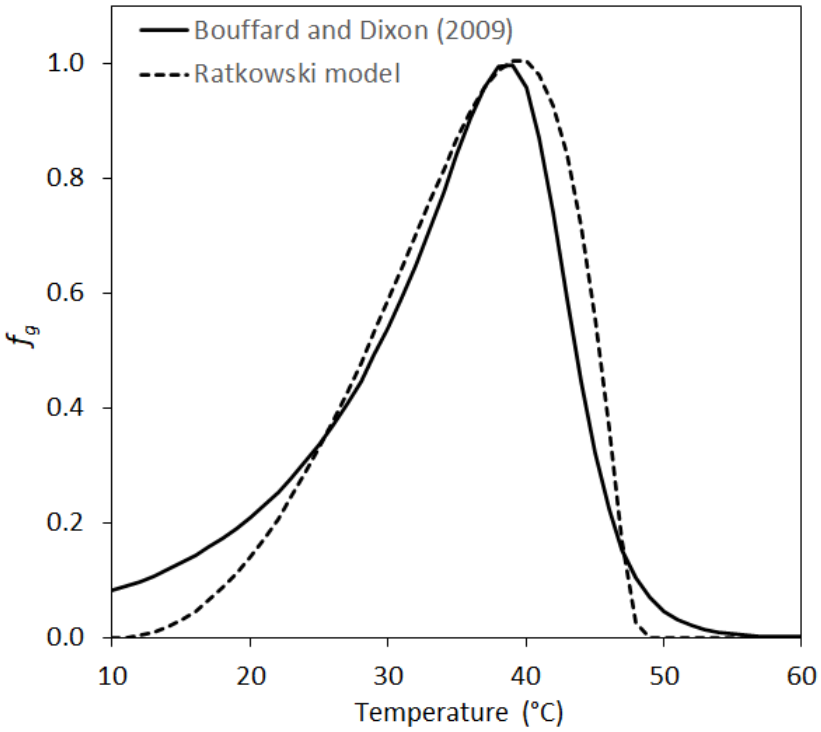

Figure 1.19: Impact of temperature on *L. ferriphilum* growth using the Ratkowski model and the adapted model of Bouffard and Dixon (2009) [143].

1.4.4 Transport phenomena modelling

As explained in the previous section, bioleaching is based on a chemical dissolution of a metal sulphide which is assisted by microorganisms. The biological and chemical models alone assume the homogeneity of biomass, substrates and dissolved gases throughout the system considered. This is nearly met for small scales system such as laboratory-scale set-up but is hardly reached when considering the usual industrial-scale bioleaching processes. As a matter of fact, static processes can extend up to millions of cubic meters and dynamic processes are often carried out in multiple tanks of size up to 1000 m^3. Whether this process is carried out using static or dynamic approaches, transport phenomena is thus expected to play an important role on the process efficiency.

Heap leaching is based on the irrigation of a heap with an acidic solution that percolates through flowing channels within solid particles that constitute the heap. Additionally, aeration of the heap is performed to assist permeability and bacterial growth. This leads to multiple flow domains that should be considered for transport phenomena modelling: solid, stagnant liquid, flowing liquid and gas. Prior to the creation of the HeapSim model, the transport phenomena within a heap were investigated by multiple authors, as pointed Bouffard and Dixon (2001) who further developed the models [120, 162]. Current models assume a plug flow behaviour of the flowing so-

lution through the heap and mass transfer phenomena between stagnant and flowing solutions using side-pore diffusion. The later is determined using mathematical models such as the mixed side-pore diffusion (MSPD) that considers solution concentration homogeneity of the pores (Fig. 1.20).

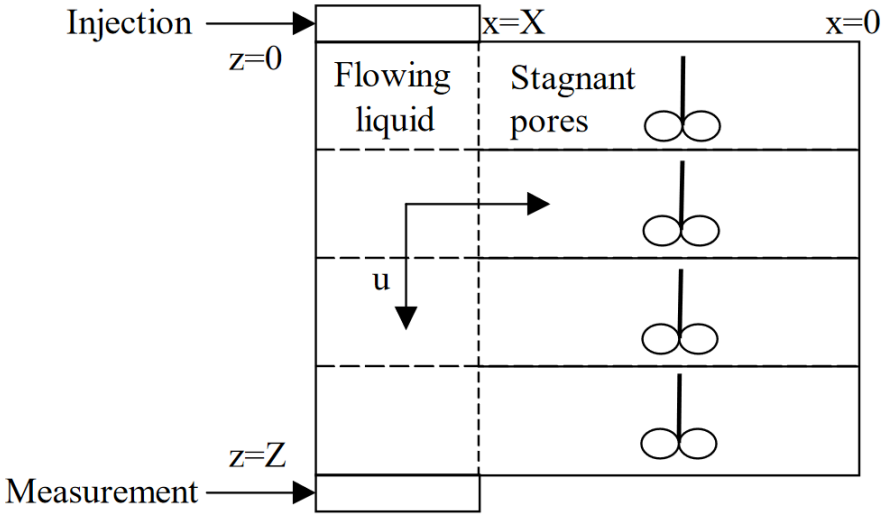

Figure 1.20: Representation of the MSPD model. Figure reprinted from Bouffard and Dixon (2001) [120].

In mechanically-mixed systems, kinetic models were translated from the existing static models as kinetics is mostly dependent on the substrates and microorganisms. Additionally, theoretical models of gas-liquid mass transfer can be used to represent the oxygen mass transfer into the solution [163]. However, the transport phenomena highly differ from the ”static” processes as the system is mechanically mixed. Various parameters have proven to be of influence on the distribution of the scalars transported in the flow, as shown on Fig. 1.21. A better control of these parameters is expected to enhance process efficiency [164].

Currently, experimental representation of the solid mixing efficiency in a STR exists, such as the determination of mixing indices using a mesh tank by Harrison et al. (2020) [164]. Furthermore, recent studies of Zheng et al. (2018) used CFD modelling to represent the three-phase hydrodynamics of a bio-oxidation STR [165, 166]. However, despite the availability of both kinetic and hydrodynamic studies, no model fully represents the coupling of these methods on STR, which is critical considering the complexity and size of industrial bioleaching STR. Hence, the importance of hydrodynamics in bioleaching STR processes will be looked for in the next section.

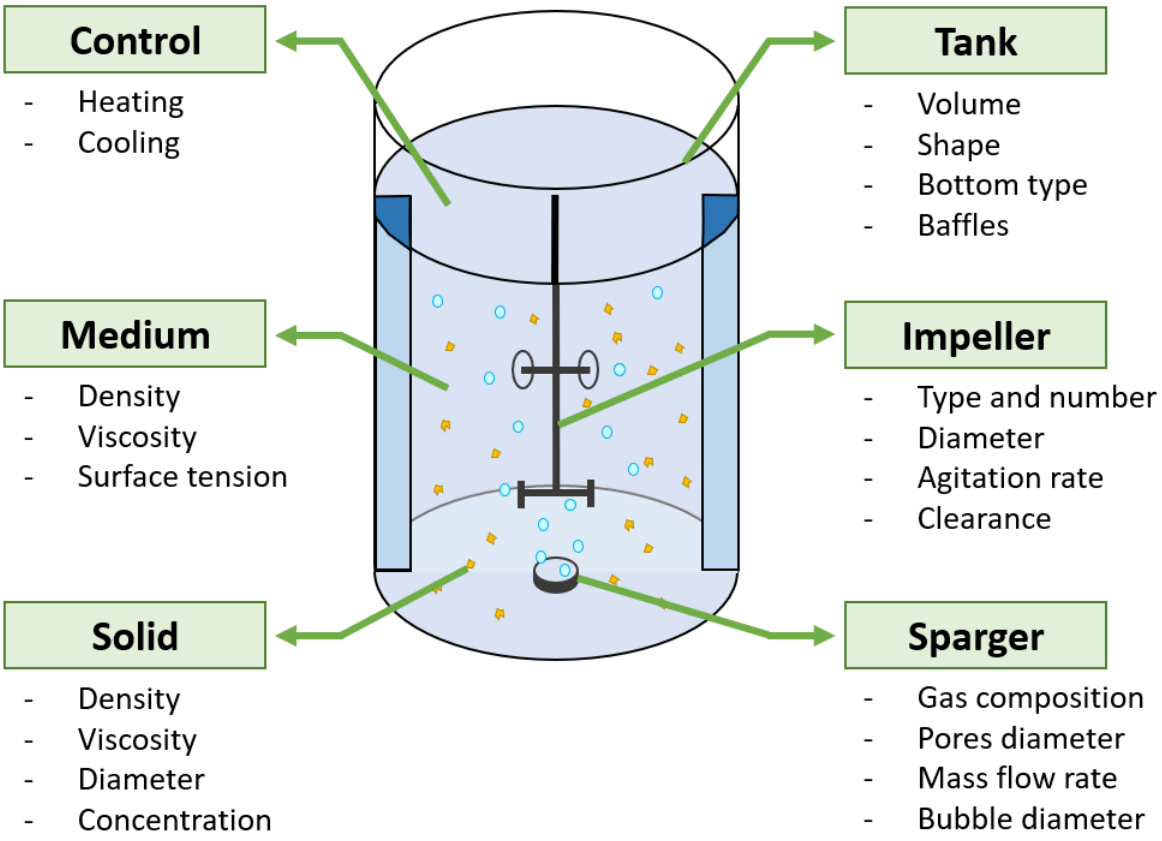

Figure 1.21: Representation of a bioleaching gas-liquid-solid STR and the components influencing scalars transport.

1.5 Importance of hydrodynamics in bioleaching STR processes

Bioleaching mechanisms were widely reviewed to represent the intricacy of both microbial growth and activity, and mineral dissolution. However, the modelling of these mechanisms and standard bioreactor scale-up rules generally assume the homogeneity of biomass, substrates and dissolved gases concentrations throughout the reactor. This is nearly met for laboratory scale reactors but hardly reached at the industrial scale due to higher circulation timescales.

1.5.1 Quality of mixing in STR

As in any chemical engineering process, the management of bioleaching stirred tank bioreactors is aimed at optimizing the reacting conditions to accelerate the oxidation processes of the sulphides and to maximize the solubilization or liberation efficiency of valuable metals. This optimization of the reacting conditions is probably closely related to the homogeneity of biomass, substrates and dissolved gases throughout the reactor in order to maximize the contact between these components [167, 168]. This is especially important considering that the interactions between the microorganisms

and sulphides (microbial attachment and biofilm formation) are considered as key parameters to improve bioleaching [61, 122]. To this end, improving mixing efficiency would result in a decrease of the mixing time, which will be translated by a better mass transfer and an improvement of the suspension quality [121, 169].

As previously presented in Fig. 1.21, a bioleaching stirred tank is described as a cylindrical baffled tank with a flat or dish bottom. The gases are distributed in the medium using a perforated sparger. Lastly, mixing is carried out by means of a stirring shaft containing one of multiple impellers. While the medium used in bioleaching is close to the composition of water, with similar viscosity and density, it also contains often high level of solid (up to 30% w/w) and must be well aerated due to the oxygen demand of the oxidation reactions. Due to these, the impellers are carefully chosen to ensure: (i) the homogenization of the solution component, (ii) the solid particles suspension and dispersion, (iii) the bubbles dispersion and breakages while avoiding impeller flooding to enhance gas-liquid mass transfer.

Mixing was focused by a large number of studies and, independently of the solid and gas phases dispersion, the relation between liquid mixing and impeller geometry was closely considered [170]. The common approaches to evaluate the impact of an impeller on blending fluids are to estimate the pumping capacity of the impeller and the mixing time. The pumping number N_Q can be used to represent the volumetric pumping capacity of an impeller relative to its diameter and rotational speed:

$$N_Q = \frac{Q_p}{ND^3} \tag{1.41}$$

with Q_p ($m^3\,s^{-1}$) the impeller pumping capacity, N (s^{-1}) the agitation rate and D (m) the impeller diameter. On the other hand, the mixing time θ_m represents the time needed to obtain a certain degree of homogeneity, which directly depends on the local turbulence, responsible for local mixing [171]. Nienow (1997) established a relation of θ_m for single impeller systems, which is related to the tank and impeller diameters, and the turbulent energy dissipation ε ($m^2\,s^{-3}$) but is independent on the impeller type [172]:

$$\theta_m = 5.9 \cdot \left(\frac{T}{D}\right)^{1/3} \varepsilon^{-1/3} T^{2/3} \tag{1.42}$$

with T the tank diameter (m). The mixing time is usually in order of magnitude of several seconds to several minutes to achieve a mixing efficiency of 95% [173].

Considering the various parameters impacting mixing, medium composition will have a negligible impact as most bioleaching media may be considered similar to water. The temperature can greatly vary on bioleaching processes depending on the

consortium and substrate used, which can significantly impact the liquid viscosity. Nevertheless, this factor is rather easily controlled in stirred tank reactor and remains fixed during the process. On the other hand, geometry, composition (liquid, solid and gas) and component parameters (particle and bubbles diameters) are essential for optimizing the mixing conditions [168, 174]. Significant power consumption of the process comes from mechanical mixing, which is partially related to the solid content (through sufficient agitation rate ensuring suspension and gas-liquid mass transfer efficiency) and its physical properties [175, 176]. Bioleaching in STR involves substantial power consumption to reach these mass transfer performance, which results in high OPEX that limit, until now, the use of this technology to the treatment of high added-value resources (mainly refractory gold ores). Besides these commodities, the expansion of bioleaching to 'unconventional' primary resources requires adapting the STR process to the characteristics of these resources in order to limit CAPEX and OPEX while maintaining high extraction efficiency [65, 177]. These resources present a wide range of shape, size and physical properties which makes difficult the establishment of generalized scale-up rules.

Power consumption

The power number N_p was the first and most widespread parameter used to link the power consumption to the geometric parameters of the tank and impellers [178]. Furthermore, it allows the determination of the power consumption per unit of volume P/V, which is considered as the best criterion for the scale-up of STR [179, 180] as it could be related to mass transfer capacities or mixing times [181, 182]. The power number N_p, initially depending on the Reynolds number Re, the Froude number Fr and the dimensionless geometric parameters of the tank, was refined over the year until the work of Rushton et al. (1950), which presented the following equation [178, 179]:

$$N_P = \frac{P}{\rho_l N^3 D^5} = f\left(Re = \frac{\rho_l N D^2}{\mu}, Fr = \frac{N^2 D}{g}\right) \tag{1.43}$$

with P (W) the power required for the impeller rotation, ρ_l ($\mathrm{kg\,m^{-3}}$) the fluid density and μ (Pa s) the liquid viscosity. As most bioleaching STR feature baffles to avoid the formations of a whirlpool, the impact of the Froude number is negligible in comparison with the Reynolds number impact. Furthermore, it is a well-known result that, for a turbulent regime ($Re > 10^4$) of baffled vessels, the power number is also independent of the Reynolds number and reaches a constant value that only depends on bioreactor design [179]. The impeller power number for various impellers is shown on Table 1.8. It is also important to emphasize that the required power P (which is related to the electric power consumption) should be preferentially minimized to limit the OPEX of the bioleaching process, which is antinomic with high hydrodynamic performance.

Table 1.8: Literature data of asymptotic impeller power numbers in turbulent regime.

Impeller	N_P	**Literature reference**
RT4B	4.0	[183]
RT6B	4.0 - 6.0	[180]
R600	4.2	[183]
HTPGd	0.67	[183]
EEd	1.7 - 2.1	[184, 185]
A310	0.3 - 0.5	[186]

RT4B = 4-bladed Rushton turbine ; RT6B = 6-bladed Rushton turbine ; R600 = R600 spiral backswept impeller ; HTPGd = HTPG down impeller ; EEd = Elephant-Ear down impeller ; A310 = Lightnin A310 impeller

1.5.2 Solid suspension

Although the power number was widely used in the literature to define standard designs of solid-liquid stirred tank, this parameter is not sufficient to describe the suspension quality, defined by the spatial distribution of the particles within the flow. Alternative parameters need to be considered in order to optimize the solid distribution [187, 188]. Experimentally, various approaches allowed to measure the influence of geometry or experimental conditions on solid distribution, such as sample withdrawal, conductivity, laser Doppler velocimetry, optical attenuation, magnetic resonance imaging and electrical resistance tomography [164, 168, 175, 176, 189–191]. These studies used different parameters to describe the homogeneity of the solid such as the cloud height, the just-suspended agitation rate and the suspension quality.

To describe a specific suspension state, the just-suspended agitation rate N_{js}, shown in Eq. 1.44, defines the minimal agitation rate ensuring the suspension of all solid particles [192–195]. This parameter also has the advantage of being the optimal condition to limit the hydromechanical stress in these bioreactors as it minimizes dissipated power, which makes it an interesting parameter to design tank operation. The following equation, called the Zwietering's equation, represents the just-suspended speed N_{js} as a function of geometrical and physicochemical parameters:

$$N_{\mathrm{js}} = S \cdot \nu_{\mathrm{l}}^{0.1} \cdot \left[\frac{g\left(\rho_{\mathrm{s}} - \rho_{\mathrm{l}}\right)}{\rho_{\mathrm{l}}}\right]^{0.45} \cdot W_{\mathrm{s}}^{0.13} \cdot d_{\mathrm{p}}^{0.2} \cdot D^{-0.85} \tag{1.44}$$

with ν_{l} ($\mathrm{m^2\,s^{-1}}$) the liquid kinematic viscosity, W_{s} ($-$) the solid-liquid mass ratio, d_{p} (m) the particle diameter, D (m) the impeller diameter and S ($-$) a function of various geometrical ratios of the tank and impeller.

However, despite the interest of determining the N_{js} and its wide use in recent works, it is insufficient to represent the distribution of particle suspension as it only

informs the state of the suspension at one particular point. Mak (1992) established a parameter, the suspension quality, that allows the determination of standard deviation of the local solid concentration as a way to characterize the solid distribution [196]. The suspension quality H_s can be calculated as the volume-averaged difference between the local and the mean concentration of solid particles [197–199]:

$$H_s = 1 - \sqrt{\frac{1}{V_{tot}} \cdot \iiint_{V_{tot}} (\alpha_s - \langle \alpha_s \rangle)^2 \, dV} \tag{1.45}$$

with V_{tot} (m^3) the total volume, α_s ($-$) the local volume fraction of the solid phase and $\langle \alpha_s \rangle$ the volume-averaged value of particle concentration in the vessel. However, the experimental set-up complexity makes difficult the use of this method to screen a high number of bioreactor designs. A previous study by Harrison et al. (2012) has proven a proper bioleaching system with a meshed tank could give enough data for this parameter to be experimentally determined [168]. Nonetheless, due to the difficulty of experimental implementation and measurement, the screening of suspension performance may advantageously also be reached through numerical means such as Computational Fluid Dynamics (CFD).

1.5.3 Gas-liquid mass transfer

Dissolved gases such as oxygen (O_2) and carbon dioxide (CO_2) play an important role in bioleaching mechanisms. As seen previously in the microbial oxidations, shown in Eq. 1.4 and 1.5, O_2 is the final electron acceptor for the renewal of essential substrates, such as ferric iron. Consequently, aeration must be carefully designed in bioleaching processes when using aerobic consortia as O_2 is one of the limiting components for iron and sulfur oxidation and bacterial growth [200, 201]. Moreover, it was shown that increasing dissolved oxygen (DO) leads to an increase of sulfide oxidation rate [202]. In all cases, it is preferable to optimize the gas-liquid mass transfer to ensure a sufficient supply of DO. From another perspective, the oxygen demand is related to the sulfide content. For example, the oxidation of 1.0 mol of pyrite requires 3.5 mol of oxygen [203]. Also, because of the high temperatures, low pH and the presence of soluble metals in bioleaching, reactive oxygen species can be formed, which were proven to be harmful to the process [204, 205].

Carbon dioxide is the carbon source for autotrophic microorganisms and may be used by some mixotrophic. Some researches investigated the impact of CO_2 on bioleaching efficiency with a shared result of an increase of efficiency when the air was supplemented with CO_2 [206–208]. Recently, Guezennec et al. (2018) provided more insight concerning the impact of CO_2 supplementation using a sulfidic copper concentrate and means to report the availability of CO_2 to the biomass [209]. From this

study, three main conclusions were drawn: (i) an increase of efficiency, up to 30%, was observed with CO_2-enriched air with a decreasing and nearly inhibiting result at higher concentration, (ii) the absence of CO_2 enrichment is responsible for a lag phase of the microbial activity due to carbon limitation and (iii) CO_2 enrichment impact both the concentration and composition of biomass, thus it is difficult to estimate the optimal CO_2 concentration. Nonetheless, the underlying mechanisms that are impacted by CO_2 enrichment are still being investigated as it is still unknown whether it is the mass transfer or the biological fixation that affects bioleaching efficiency.

A significant attention was put into gas-liquid mass transfer mechanisms in bioleaching processes, especially for STR. The gas-liquid mass transfer rate can be modelled using the following relation:

$$r_{\mathrm{gl}} = k_{\mathrm{l}}a(c_{\mathrm{g}}^{*} - c_{\mathrm{g,l}}) \tag{1.46}$$

where r_{gl} ($\mathrm{mol\,l^{-1}\,h^{-1}}$) is the gas-liquid mass transfer rate, $k_{\mathrm{l}}a$ ($\mathrm{h^{-1}}$) is the overall mass transfer coefficient, c_{g}^{*} ($\mathrm{mol\,l^{-1}}$) is the equilibrium concentration, $c_{\mathrm{g,l}}$ ($\mathrm{mol\,l^{-1}}$) is the dissolved gas concentration. The model is dependent on a wide number of parameters, mostly translated through the determination of $k_{\mathrm{l}}a$ and c_{g}^{*}.

Overall and local mass transfer coefficient

The overall mass transfer coefficient $k_{\mathrm{l}}a$ represents the resistance to the transfer encountered in the liquid and gas films between the gas and liquid bulk, as shown on Fig. 1.22. The resistance of the gas film is often considered negligible compared to the resistance of the liquid film. This parameter is dependent on the geometrical parameters of the tank (type, size and impeller, baffles and sparger design) and the physicochemical composition of the medium (gas, liquid and solid) [40, 210].

$k_{\mathrm{l}}a$ is the product of k_{l}, the mass transfer coefficient and a, the effective interfacial area per unit volume. k_{l} can be estimated from the surface renewal rates or the contact time between gas and liquid while a will mainly depend on the distribution of bubble sizes. Both of these parameters are difficult to measure and often approximated as a global $k_{\mathrm{l}}a$ using static or dynamic method. For this, various approaches were developed to estimate locally k_{l} and later reviewed by Kulkarni et al. (2007) [211]. The main used approaches are the two-fluid model and the penetration theory.

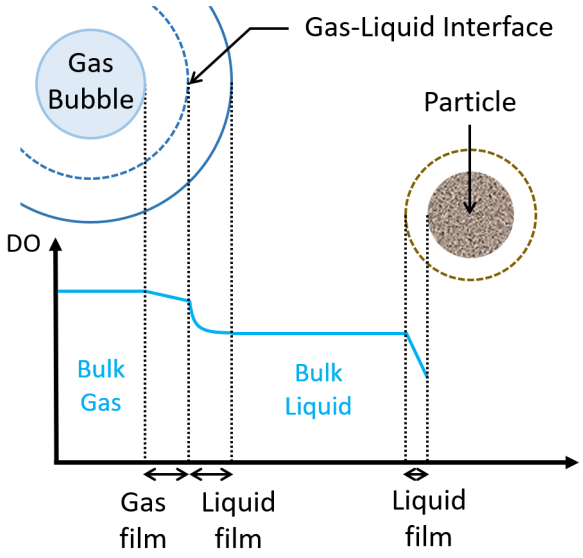

Figure 1.22: Schematic representation of gas-liquid mass transfer in a triphasic medium.

The two-fluid model of Whitman (1924) supposes that the gas-liquid interface is an interface between two stagnant fluids of different concentrations [212, 213]. Using Fick's law of diffusion, the mass transfer coefficient can be estimated:

$$k_{\mathrm{L}} = \frac{D_{\mathrm{l}}}{\delta} \tag{1.47}$$

where D_{l} ($\mathrm{m^2\,h^{-1}}$) is the diffusivity of gas in liquid and δ (m) is the film thickness.

The penetration theory of Higbie (1935) assumes that the mass transfer is an unsteady mechanism due to a brief contact time between phases [214]. Gas-liquid mass transfer will occur as long as there is contact between gas and liquid and each liquid element will be exposed to gas for the same period of time, as shown by the following equation.

$$k_{\mathrm{L}} = 2\sqrt{\frac{D_{\mathrm{l}}}{\pi t_K}} \tag{1.48}$$

where t_K (h) is a characteristic time in turbulent flow, equal to $\sqrt{\nu/\varepsilon}$. This uses the Kolmogorov's theory of isotropic turbulence which assumes that the gas-liquid interface is isotropic.

The interfacial area per unit volume a can be calculated using the gas fraction α_{g} and the mean bubble diameter, as shown in Eq. 1.50. As the bubbles can present various sizes and shapes, the mean bubble diameter has to be calculated using the bubble size distribution $n(l)$ (BSD). A common representation is the Sauter diameter d_{32} (m), which uses the BSD and corresponds to the ratio of the third moment of the distribution to the second moment:

$$d_{32} = \frac{\int_0^x l^3 n(l) dl}{\int_0^x l^2 n(l) dl} \tag{1.49}$$

As the interfacial area per unit of volume represents the total bubbles surface on the total volume V (m^3), it can be related to the Sauter diameter and the gas fraction by the following equation:

$$a = \frac{\int_0^x \pi l^2 n(l) dl}{V} = \frac{\pi \int_0^x l^2 n(l) dl}{V_g} \frac{V_g}{V_l + V_g} = \frac{\pi \int_0^x l^2 n(l) dl}{\frac{\pi}{6} \int_0^x l^3 n(l) dl} \alpha_g = \frac{6\alpha_g}{d_{32}} \tag{1.50}$$

The bubble size can also be determined using various empirical correlations which, depending on the approximation, can depend on the sparger geometry, the gas flow rate, the gas and liquid physicochemical parameters and the energy dissipation. In bioleaching applications, the presence of solid particles may impact the liquid effective density and viscosity. Recently, Davoody et al. (2016) suggested a correlation of the bubble diameter based on previous empirical formula, that can be adapted for slurry reactors [215, 216]:

$$d_b = 1.98 \varphi_g^{0.5} \rho^{-0.6} \varepsilon^{-0.4} \sigma^{0.6} + 0.0015 \tag{1.51}$$

where φ_g is the gas holdup and ρ ($kg\,m^{-3}$) the slurry density, equal to $\varphi_g \rho_g + \varphi_l \rho_l + \varphi_s \rho_s$, ε ($m^2\,s^{-2}$) the energy dissipation rate and σ ($N\,m$) the surface tension.

Equilibrium concentration c_g^*

According to Henry's law, the equilibrium concentration c_g^* is given by:

$$c_g^* = \frac{P_g}{H} \tag{1.52}$$

where P_g (Pa) is the partial pressure of the gas in the bubbles and H ($mol\,l^{-1}\,Pa^{-1}$) is Henry's law constant. Henry's law shows that an increase of P_g will lead to an increase of c_g^* and thus, to a rise of the driving force $(c_g^* - c_{g,l})$ in the equation describing the gas-liquid mass transfer rate (Eq. 1.46).

The solubility of a gas in a liquid is also affected by the composition of the medium, represented through Henry's law constant H. Due to the presence of ionic solutes in bioleaching media, solubility is negatively impacted by salting-out. The magnitude of this salting-out effect can be represented using Sechenov's equation [217]:

$$\log\left(\frac{c_w^*}{c_e^*}\right) = k_{Se,e} \times c_e \tag{1.53}$$

where c_w^* and c_e^* are the solubility of the gas in water and in the electrolyte respectively, $k_{Se,e}$ is the Setchenov's saline effect parameter of the electrolyte and c_e is

the electrolyte concentration in the medium. To determine the solubility of a gas in a solution with multiple electrolyte, the Schumpe's model can also be used [218]:

$$\log\left(\frac{c_{\mathrm{w}}^*}{c_{\mathrm{e}}^*}\right) = \sum_i h_i \times c_i \tag{1.54}$$

where h_i is an empirical parameter depending on the ion i. Few models exist for bioleaching media because of the wide variety and complexity of media used. For instance, Mazuelos and al. (2017) established an empirical relation to determine the oxygen solubility for copper-based sulphide mineral bioleaching:

$$c_{\mathrm{g}}^* = c_{\mathrm{w}}^* - 12.698 \times 10^{-\mathrm{pH}} - 0.0555 c_{Fe^{2+}} - 0.0290 c_{Fe^{3+}} - 0.0265 c_{Cu^{2+}} \tag{1.55}$$

Advantages of STR for gas-liquid mass transfer

As seen previously, dissolved gases are essential in bioleaching mechanisms due to the necessity of oxygen for mineral dissolution and microbial oxidations. STR processes offer great capabilities for gas-liquid mass transfer, which is related to the important gas mass flow rates used, the supplementation of air with carbon dioxide and the use of spargers that lowers the initial bubble size. Furthermore, most impellers are adapted for bubble breakage and dispersion throughout the tank, which increases the gas-liquid mass transfer. Because of these, higher oxygen transfer rates may be achieved in STR with a relative easy operability. For example, Guezennec et al. (2017) reported a maximum OUR of up to $1.8\,\mathrm{g\,l^{-1}\,h^{-1}}$ under oxygen-enriched atmosphere for the leaching of a pyritic tailings.

Despite these advantages, the aeration must be cautiously considered as power consumption is directly related to the gassing rate. This is shown using the aeration number N_A which translates the gassing rate Q_{g} ($\mathrm{m^3\,s^{-1}}$) on the impellers parameters:

$$N_A = \frac{Q_{\mathrm{g}}}{ND^3} \tag{1.56}$$

Taghavi et al. (2011) observed the ratio between gassed and ungassed power consumption P_{g}/P at different aeration number and showed that P_{g}/P was inversely proportional to N_A [219]. The power loss depends on the impeller and gassing rate used, with the Rushton impeller showing P_{g}/P below 0.4 [220, 221].

The power loss varied from 5 to 50% depending on the impeller and gassing rate used, which is explained by the formation of gas-filled cavities behind the blades at the highest gas flow numbers.

1.5.4 Hydromechanical stress

In most cases, the improvement of mixing efficiency is closely related to an increase of power dissipated by the impeller. However, from a physical point of view, the hydromechanical stress generated by the agitation may also prevent the microbial adhesion or even lead to lower process performances. This may be particularly detrimental for bioleaching processes due to the major importance of microbial attachment and biofilm formation [203, 222]. For instance, Xia et al. (2008) observed this detrimental effect with *At. ferrooxidans* cultures in shaking flasks [223]. Similar observations were made in STR during thermophilic cultures of *Sulfolobus sp.* [224, 225]. Moreover, it was shown by Wang et al. (2014) that, for moderately thermophiles cultures, the proportion of attached cells is higher than of planktonic cells [25]. Also, altering the capacity of the cells to attach on the mineral surface leads to a decrease of bioleaching efficiency [226]. Considering the effect of solid loading which can also induce physical stresses, it was demonstrated by Witne and Phillips (2001) that the increase of solid concentration in continuous STR induced an increase of the leaching rate until a point where it had a negative effect, which could be caused by the attrition of cells [206]. Similar results were observed by Raja (2005) in shaking bottles where a decrease in specific oxygen consumption rate and cell viability was observed at increasing quartzite concentrations [227]. In the same way, Nemati and Harrison (2000) observed that, if a partial suspension of the pulp was obtained for a concentration of 18% w/v (corresponding to 16% w/w with the hypothesis of $\rho_s = 2610\,\mathrm{kg\,m^{-3}}$), the rate of iron solubilization was reduced [228]. They concluded that, beyond a critical pulp concentration, cells were disrupted and their metabolic activity impaired. However, achieving complete particle suspension led to an apparent cell damage, as shown by a reduced cell count. More generally, it must be underlined that solid concentration has not the same influence on mesophilic and moderately thermophilic bacteria (such as *Leptosirillum* and *Acidithiobacillus* sp.), and extremely thermophilic archaea (such as *Acidianus*, *Metallosphaera*, and *Sulfolobus* sp.). STR bioleaching with archae cannot be operated at a solid concentration above 12.5% whereas solid concentration can reach 20% in bioleaching plants using mesophile and moderate thermophiles [61]. This difference is generally attributed to the shear sensitivity of archaea that have no rigid cell wall.

To understand the previous results, it is important to consider that, in bioleaching reactors, hydromechanical stresses may impact the process performance following three phenomena: (i) direct shear of the liquid phase on the microorganisms in suspension (Fig. 3.1a), (ii) shear stress on particles that potentially hold adhered microorganisms or biofilms (Fig. 3.1b), and (iii) particle-particle frictions and collisions (Fig. 3.1c).

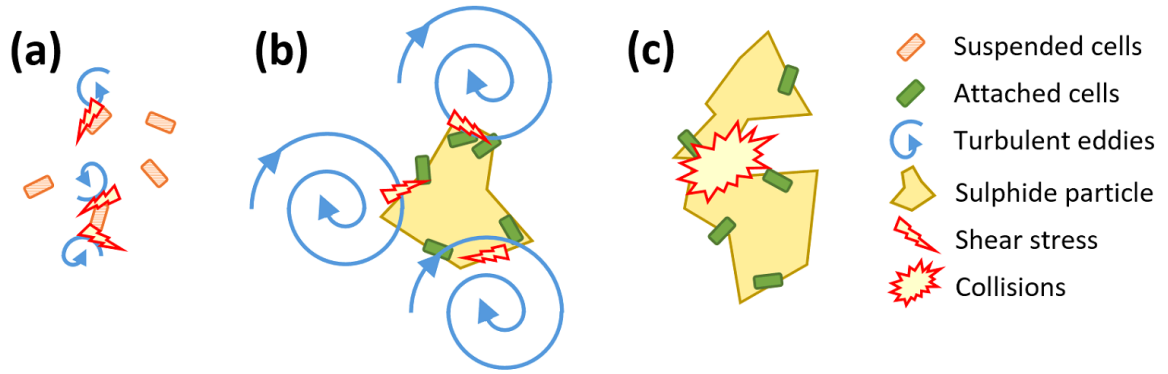

Figure 1.23: Description of the hydromechanical stress applied on microorganisms due to: (a) direct shear of the liquid; (b) shear stress on particles; (c) particle-particle frictions and collisions.

The occurrence of direct shear is still debated. It is generally assumed, but not completely demonstrated, that only the turbulent eddies of the same order of length or lower than the particle size are potentially detrimental to the particles and thus the microbial adhesion and biofilm formation [229]. In this case, namely some turbulent eddies are lower than approximately the particle diameter, particles are transported in the inertial subrange of turbulence and are subjected to turbulent stresses. To quantify the relationships between particle stress and hydrodynamics, Thomas (1964) provided the expression of particle stress σ_p (Pa) as related to the local mean square fluctuating liquid velocities $\overline{u_\mathrm{l}'}$ [230]:

$$\sigma_\mathrm{p} = \rho_\mathrm{l}\overline{u_\mathrm{l}'}^2 \simeq 0.7\rho_\mathrm{l}\left(\varepsilon d_\mathrm{p}\right)^{2/3} \propto \varepsilon^{2/3} \tag{1.57}$$

In isotropic and homogeneous turbulence, the local mean square fluctuating liquid velocities depend on the local turbulent dissipation rate ε ($\mathrm{m^2\,s^{-2}}$) and on particle diameter d_p (m). These researches were emphasized by the work of Kolmogorov (1941), who introduced microscales to represent the local isotropic state in turbulent flow [231, 232]. The Kolmogorov length scale $l_K = \left(\nu^3/\varepsilon\right)^{0.25}$ gives an estimation of the size of the smallest eddies in the flow. In this equation, ε is the power dissipation per unit of mass (or turbulent dissipation rate) and ν is the kinematic viscosity. Using this parameter and the previous assumption, hydrodynamics should have no impact on planktonic microorganisms if, locally, the Kolmogorov length scale is higher than the microorganism diameter [233]. This means that, if $d_\mathrm{p} < l_K$, the particles are transported in the viscous subrange of the turbulence and are mainly subjected to viscous stresses, which translates with the following equation:

$$\sigma_\mathrm{p} = \mu G = \mu\sqrt{\frac{\varepsilon}{\nu_\mathrm{l}}} \propto \varepsilon^{1/2} \tag{1.58}$$

with G ($\mathrm{s^{-1}}$) the local velocity gradient. Considering microorganisms of the micrometer scale, the maximal power dissipation necessary to induce direct cell damage

would be $\varepsilon \sim 1 \times 10^6\,\mathrm{W\,kg^{-1}}$, which is unlikely to be reached in standard stirred tank bioreactors. In comparison, the value of power dissipation that would induce hydrodynamic stress on particle with a diameter in the range 10 - 100 µm would be $\varepsilon \sim 0.01$ - $100\ \mathrm{W\,kg^{-1}}$, which is more likely to be observed with usual mixing conditions.

Lastly, particle-particle frictions frequency and intensity depend on the local volume fraction of particles and the relative velocity between particles, and consequently on the design of the bioreactor, the agitation rate and the mean particle concentration. Cherry and Papoutakis (1988) estimated that the energy of a particle-particle collision E_c could be approximated by the kinetic energy of a particle moving at the velocity of the smallest eddies, namely the velocity scale u_{l_K}, as defined by Kolmogorov [231, 234, 235]:

$$E_c = \frac{1}{2} \cdot m \cdot u^2 \propto \frac{1}{2} \cdot \left[\frac{4}{3} \pi \rho_\mathrm{p} \left(\frac{d}{2} \right)^3 \right] \cdot u_{l_K}^2 \tag{1.59}$$

$$u_{l_K} = (\varepsilon \cdot \nu)^{1/4} \tag{1.60}$$

However, as bioleaching uses small particle size, from 10 µm to 1 mm, and mostly solid concentration of less than 20% w/w, the resulting collision energy can be neglected compared to the other mechanical stresses impacting microorganisms. To summarize, the shear stress on particles is probably the most dominant phenomenon and should be closely observed.

1.5.5 Scaling-up of bioleaching processes in STR

Bioleaching stirred tank has been commercially implemented for decades, mostly using large tanks of working volume up to $1000\,\mathrm{m^3}$. As enlightened in the previous sections, the implementation and control of large industrial-scale processes requires upstream optimization due to the high CAPEX and OPEX. For this, the scale-up approach has been used as an experimental tool to answer these issues.

The scale-up procedure depends on the acquisitions of information on a small scale, typically laboratory scale (shake-flask, Erlenmeyer, stirred tanks, etc.), such as design rules and optimal operating conditions [236]. However, the complete physical extrapolation of a bioreactor is not possible, so the choice of optimization criterion must be carefully chosen. For mixing processes such as stirred tank reactor, the scaling factors are often determined through an overall equation [237]:

$$N^i D^j = constant \tag{1.61}$$

with i and j are process-dependent constants.

Furthermore, as defined through dimensional analysis by Zlokarnik (2006), most dimensionless parameters could be used as a basis of establishment of a scaling criterion [238]. For example, Nienow (2010) obtained the mixing parameters for the scale-up of a gas-liquid STR on the basis on a constant mass transfer coefficient $k_l a$ and gassing rate (Table 1.9).

Table 1.9: Influence of scaling on mixing parameters at constant $k_l a$ and gassing rate for a geometrical scaling ratio of 10. Reproduced from Nienow (2010) [236].

Parameter	**Large scale/Small scale ratio**
$P \propto N^3 D^5$	520
$\varepsilon \propto N^3 D^2$	0.52
N	0.17
Tip speed $u_{tip} \propto ND$	1.7
$Re \propto ND^2$	17
$\theta_m \propto N^{-1}$	5.9

In bioleaching processes, mixing efficiency is considered as a key parameter due to the necessity to disperse both solid particles and gases. Harrison et al. (2020) showed that P/V or ND could be used as optimization criteria for mixing efficiency in bioleaching STR (Table 1.10) [239].

Table 1.10: Influence of scaling on mixing parameters at constant P/V or ND for a scaling of factor 85. Reproduced from Harrison et al. (2020) [239]

Parameter	**Large scale/Small scale factor**	
	P/V constant	ND constant
P	85	19
P/V	1.0	0.2
N	0.4	0.2
D	4.4	4.4
ND	1.6	1.0
Re	7.2	4.4

1.5.6 CFD as a tool to characterize bioreactor hydrodynamics

Principles and applications of CFD

As seen previously, it is difficult to obtain a full description of the bioreactor hydrodynamics, such as the solid and/or the gas distribution, when relying only on experimental approaches. Computational Fluid Dynamics (CFD) can be used as an efficient approach to locally represent or calculate the hydrodynamics parameters of these processes. Among others, the local solid concentration, the liquid mean and fluctuating velocities and the impeller torque are representative parameters, as shown in Fig. 1.24 [216, 240]. Additionally, chemical reactions and their related parameters such as heat

and mass transfer may also be simulated using these tools [241]. As the numerical models are based on computer-aided design (CAD) geometries, design optimisation and/or scaling criteria are easily implemented, allowing the comparison of various designs and validation of experimental processes.

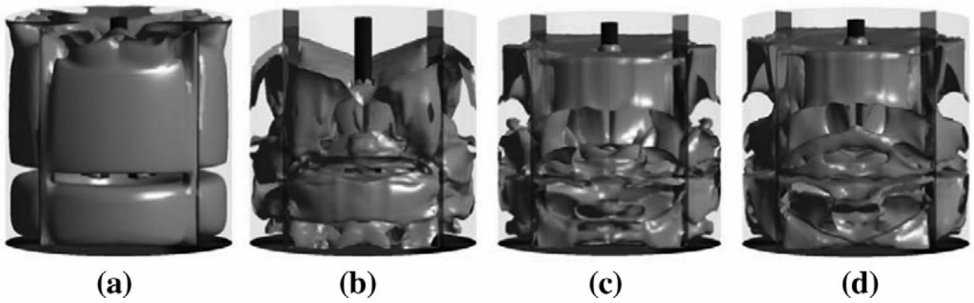

Figure 1.24: CFD simulation of the solid cloud height in STR. (a) $\alpha_s = 1\%$ w/v and $N = 1000$ rpm ; (b) $\alpha_s = 7\%$ w/v and $N = 600$ rpm ; (a) $\alpha_s = 7\%$ w/v and $N = 800$ rpm ; (a) $\alpha_s = 7\%$ w/v and $N = 1000$ rpm. Figure from Wadnerkar et al. (2012) [240].

The underlying principles of CFD are to model fluid dynamics of a system such as a STR, through the solving of multiple equations representing fluid flows, governed by the Navier-Stokes equations, and fluid-fluid or fluid-solid interactions. These equations include turbulence modelling to represent the fluctuating component of fluid flow in particular conditions. Moreover, additional parameters can be considered as the resultant of the flows, such as solid homogeneity and particle shear stress. As most CFD tools are combined with CAD software, the system can be adapted to any geometry modifications, namely the tank geometry and scale, and the number and type of impeller.

In bioleaching processes, the numerical simulation of hydrodynamics has been previously applied in heap applications. These works on heap bioleaching were recently thoroughly reviewed by McBride et al. (2018) [242]. Other works have observed the action of bioleaching conditions on local phenomena. Mousavi (2009) observed the impact of mass transfer and the flow behaviour around a single particle [243]. Metodiev (2006) characterized the flow and concentration profiles around a single cell of *At. ferrooxidans* [244]. However, the availability of other bioleaching applications by CFD is still lacking in the literature with only few studies available. Song et al. (2015) investigated the impact of various impellers speed on gas distribution in an industrial-scale gas-liquid STR [245]. The most complete model was established by Zheng et al. (2018) for a gas-liquid-solid biooxidation STR with integrated bubble size distribution and the impact of shear stress on microorganisms [216]. However, despite the lack of numerical studies on tank leaching applications, the description of a CFD model can be approximated using the wide literature of chemical processes representing liquid, solid-liquid, gas-liquid or gas-liquid-solid STR.

General approaches

The flow field generated in a stirred tank reactor may be approached using either the Eulerian or the Lagrangian specification (Fig. 1.25) [246]. The Eulerian approach represents the flow field at fixed locations and time. Thus the fluid properties are functions of space and time. This is the most common approach as process parameters are, most of the time, measured at a specific location of the process. On the other hand, the Lagrangian approach will model the flow as individual parcels that will be tracked over time. This approach is useful to obtain the streamlines of the flow which, applied to solid particle, may allow to obtain the evolution of location and physicochemical parameters of each solid particles through time.

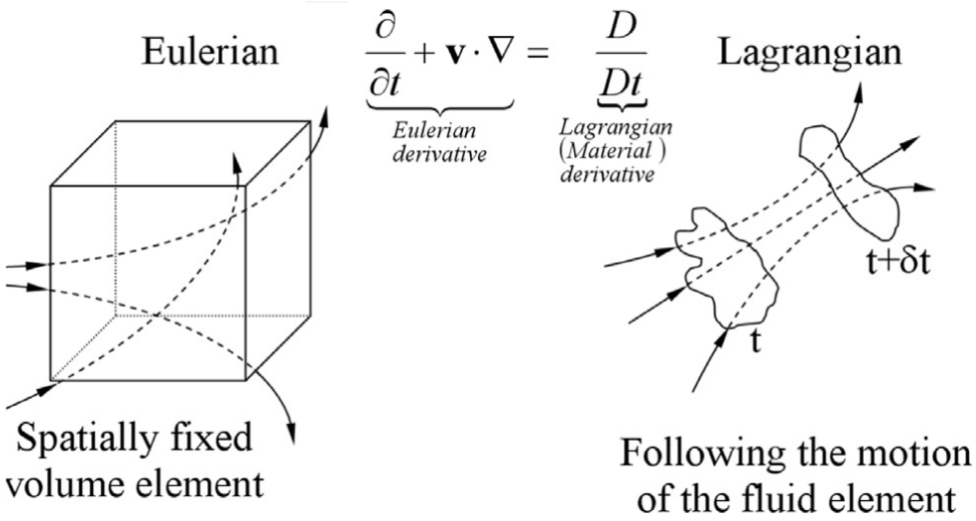

Figure 1.25: Eulerian (left) and Lagrangian (right) specification of the flow field. Figure from Shadloo et al. (2016) [246].

For multiphase flows, the governing equation are solved for each phase and, as such, multiple approaches may be used depending on the phase considered. The Eulerian-Eulerian approach models both the continuous and dispersed phases as interpenetrating continuum. The components of the dispersed phase, namely particles, droplets or bubbles, are averaged out to determine the local parameters such as the local velocity or volume fraction [247]. However, single mean size component distributions are often used because of the loss of that information during the local averaging. This may be negligible for small-sized solid distributions but have an important impact on bubbles for gas dispersion as breakage and coalescence phenomena induce a wide size distribution [248]. A common approach to include a particle size distribution is to couple the Eulerian-Eulerian specification with a population balance model (PBM). This model will represent the size segregation with the transport of both physical and internal variable space [248, 249]. Furthermore, the model may include additional phenomena that impact the component size variation such as coalescence, breakage, growth

and nucleation. Lastly, the Eulerian-Lagrangian approach depicts the continuous phase with an Eulerian approach and the dispersed phase with a Lagrangian framework [250].

Bioleaching applications in STR are carried out in a solid-liquid-gas flow, *i.e.* a continuous liquid phase and two dispersed, gas and solid phases. The Eulerian approach may be preferable to represent the three phases as the particle tracking is not needed for process optimization and the local properties may offer more information. A previous study by Zheng et al. (2018) used an Eulerian-Eulerian-Eulerian approach to represent the fluid flow and extrapolate the bubble diameter using local parameters [216]. Considering the impact of particle size, due to the small diameter of solid particles used in bioleaching (from 10 µm to 1 mm) compared to the scale of the process, the benefit of a particle size distribution is negligible compared to a mean diameter hypothesis. However, considering a bubble size distribution could be important due to the impact of gas-liquid mass transfer on bioleaching efficiency.

Hydro-biological coupling

Kinetics modelling of bioreactor assumes the homogeneity of biomass, substrates and dissolved gases throughout the tank. However, spatial heterogeneities are induced by the differences between the reaction timescale and the mixing timescale [251]. From a single cell point of view, this leads to a continuous change of the environment along time. The impact of these changes on cell metabolism is dependent of the cell reaction time to the environment, leading to two possibilities: (i) the cell reaction time is slower than the environmental changes and, as such, the mean concentration may be considered for the whole flow environment [252]; (ii) the cell reaction time is faster than the environmental changes and will suffer from periods of starvation, excess or limitation depending on the concentration field [253]. The first case may be validated for small, laboratory-scale bioreactors as the mixing time is usually short and kinetic models alone may be sufficient to simulate the environment. However, large scale bioreactors may present high concentrations gradients due to slower mixing time. These limitations impose the need to consider hydrodynamics in order to relate the biomass state to the local concentration field, as shown on Fig. 1.26 [254].

Using CFD models and Eulerian approaches, the local concentrations and velocity field may be obtained and transfered to a kinetic model that reacts to local substrate concentrations. This allows a reactive response of the bacterial environment to the local hydrodynamics.

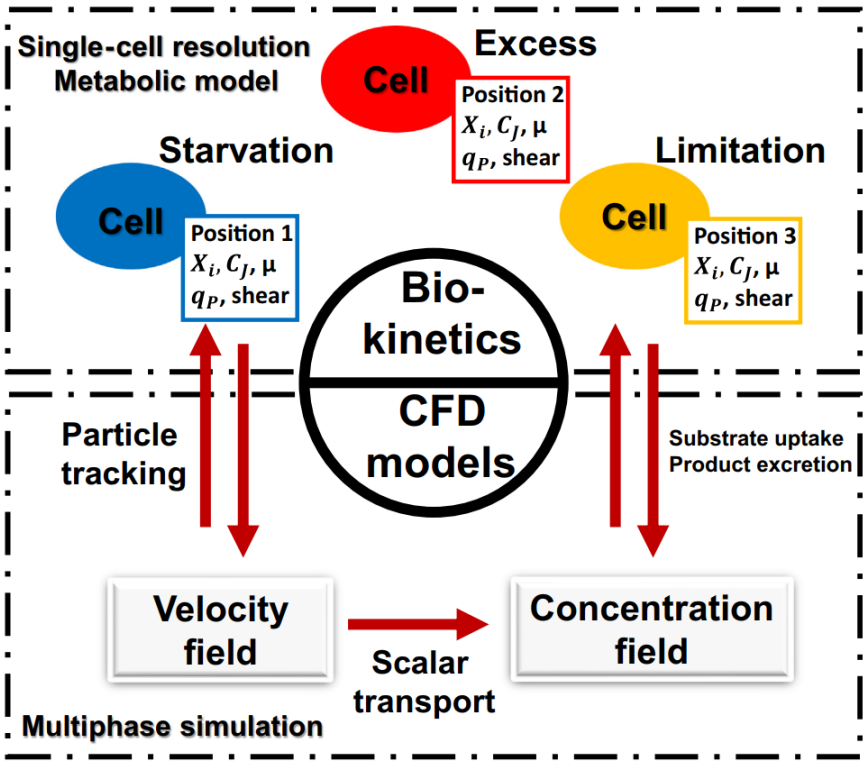

Figure 1.26: Representation of the coupled mechanisms between kinetics and hydrodynamics modelling. Figure reproduced from Wang et al. (2020) [254].

Compartment models

Despite the recent improvements in CFD, the solving methods and the computing power in hand, multiphase simulations are still difficult to implement [255]. The development of coupled hydro-kinetics models led high computing time as the implementation of kinetic reactions is responsible for the multiplication of the computing cost due to their resolution on each finite volume element [256]. Furthermore, for batch processes, the characteristic time of biological and chemical phenomena is much larger than of hydrodynamics. To address this concern, the compartment model (CM) approach was developed as an alternative to common CFD simulations and relies on the division of the flow model on multiple compartments, based on experimental evaluations, where flow properties, such as concentration, volume fraction and turbulence, are considered homogeneous [257, 258]. Each compartment of the model are interconnected through mass exchanges at the compartments interfaces, as shown on Fig. 1.27. This method enables a very significant reduction of computational cost but may reduce the simulation accuracy [259].

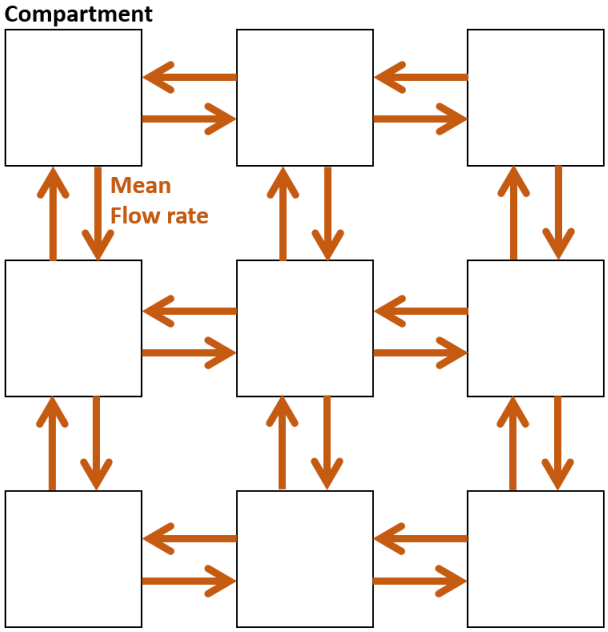

Figure 1.27: Interconnection between compartments in a compartment model approach. The compartments are represented by squares (□) and the mean flow rates between compartments are represented by arrows (⇆). Figure inspired from Delafosse et al. (2014) [255].

The CM method has been refined by coupling it with CFD modelling where the flow field is solved using CFD simulation and the properties are then averaged on a compartment description. The resulting simplified model may then be used to solve additional parameters such as chemical or biological reactions [260]. The advantages of this second approach is the ability to choose how the division of the flow field is done, because a specific split could be beneficial for the purpose of the model. For this, several compartmentalization algorithms exists that allow to split the flow field based on multiple flow variables accounting for mixing and other fluid properties [258].

1.6 Scientific approach and objectives

Bioleaching has been successfully implemented over the last decades to recover metal from sulfidic resources using static and dynamic processes. The knowledge of both physical and biological mechanisms was widely improved through a multitude of scientific works. Following the logical flow of the digital revolution, some part of bioleaching evolution have to be through modelling. This has allowed numerous process improvements while avoiding the multiplication of costly experimental pilot applications. For this, many models were developed to represent both the microbial kinetics and the sulfidic material dissolution. Furthermore, hydrodynamic studies added the effect of transport phenomena on the previous kinetics models, leading to complete models such as the HeapSim model. However, most of these researches focused on static processes and numerical studies on dynamic STR applications are scarce and incomplete. This project, named **MODELIX**, aimed at filling this gap by modelling and simulating the bacterial microenvironment / response through the development of a coupled bioleaching STR hydrokinetic model.

The kinetic models describing bioleaching applications are mostly seen separated and few works are using them in complete models, representing both microbial and chemical reactions function together. Furthermore, the kinetic parameters composing these models are often adapted to the study and generally for restricted conditions, which do not highlight the synergies observed on the complete process. To fill this lack, the **Chapter 2** describes an extended experimental study of a laboratory-scale bioleaching STR that related most parameters that may be obtained on a bioleaching study. Additionally, abiotic studies of this STR were also performed to determine essential hydrodynamics parameters.

Few studies addressed the hydrodynamics for bioleaching STR due to the complexity of the three-phase flow encountered. This work divided this issue into two stages: (i) solid-liquid flow modelling which allows to observe the impact of the tank and impeller geometry on particles dispersion, and (ii) gas-liquid flow modelling as a basis for gas-liquid mass transfer representation. Solid distribution and particle stress were widely reviewed in the literature. Despite the referenced studies, the identification of the impact of impeller geometry choice on bioleaching reactor hydrodynamics remains incomplete, especially in multi-stage bioreactors, which are the most commonly used at the industrial scale. Moreover, no study puts into evidence the coupling between power dissipation, solid homogeneity and occurrence of particle stress. For this, the **Chapter 3** uses multi-scales STR CFD models to simulate particle suspension and particle stress at different agitation rates and solid concentrations. The comparison of the effects of the impellers design on the hydrodynamics was assessed for the previously

stated parameters.

As seen in this chapter, gas-liquid mass transfer phenomena are essential in bioleaching applications. STR are well-adapted to achieve high oxygen transfer rates but must be carefully designed. Furthermore, these transfer rates are highly impacted by the bacterial presence due to constant consumption for the oxidations. **Chapter 4** describes the gas-liquid flow of a bioleaching STR through CFD modelling and uses the results to establish a compartment approach. In parallel, a bioleaching kinetic model was developed to represent the chemical dissolution, the biological oxidations and the oxygen gas-liquid mass transfer. This model was validated using the experimental values and used to validate the hypothesis of the previous gas-liquid CFD model. Lastly, the results of both model were used to develop a compartment model that considered only gas-liquid dispersion and mass transfer. This model was employed in a scaling-up study to predict the impact of bioreactor scale on its oxygenation.

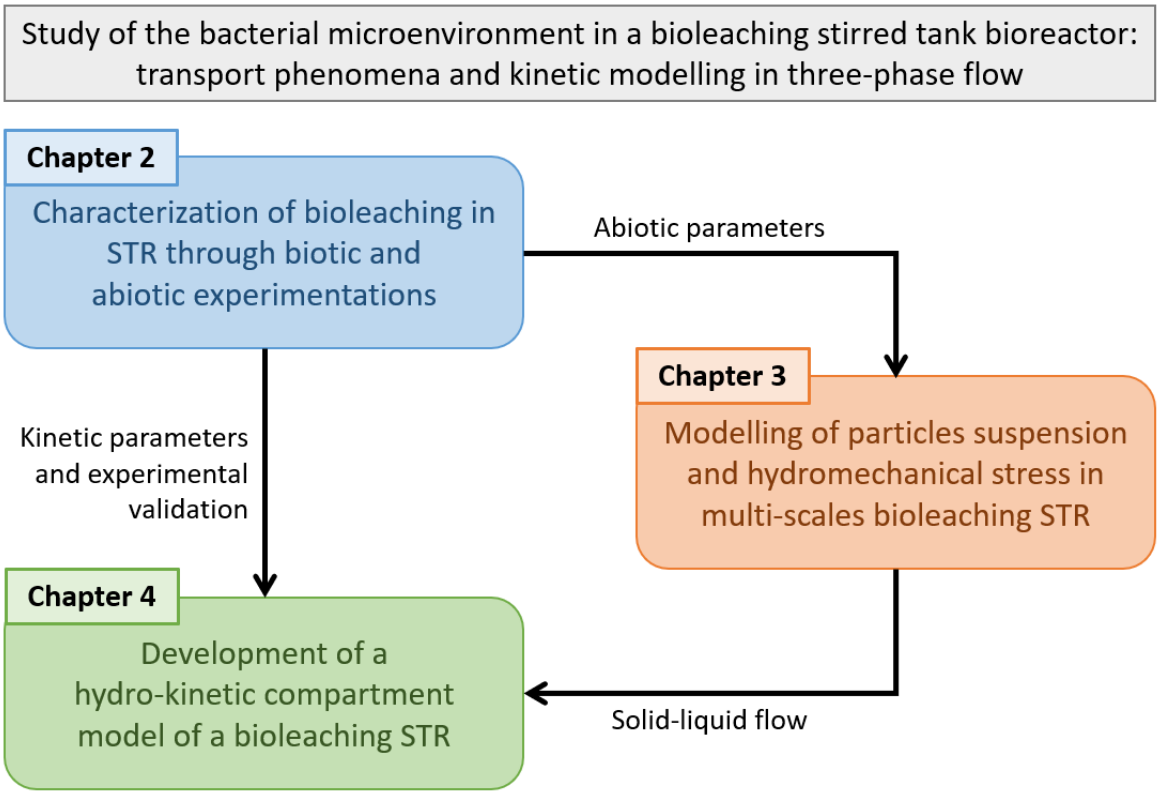

Figure 1.28: Global methodology of this work.

Bibliography

[1] United Nations. World Population Prospects: The 2019 Revision. *United Nations Econ Soc Aff*, page 46, 2019.

[2] UNEP, editor. *Metal Recycling: Opportunities, Limits, Infrastructure*. United Nations Environment Programme, Nairobi, Kenya, 2013.

[3] I. UNEP, M. Fischer-Kowalski, J. West, S. Giljum, M. Dittrich, N. Eisenmenger, A. Geschke, M. Lieber, H. Wieland, and A. Schaffartzik. Global material flows and resource productivity. *Assessment report for the UNEP international resource panel. United Nations Environment Programme, Nairobi*, 2016.

[4] World Steel Association. World Steel in Figures 2020. Technical report, World Steel Association 2020, 2020.

[5] European Commission. Report on critical raw materials and the circular economy. Website, European Commission, November 2018.

[6] National Research Council, D. o. E. a. L. Studies, B. o. E. S. and Resources, C. o. E. Resources, and C. o. C. M. I. o. t. U. S. Economy. *Minerals, Critical Minerals, and the U.S. Economy*. National Academies Press, March 2008.

[7] B. Rohrig. Smartphones: Smart Chemistry. *American Chemical Society*, April 2015.

[8] T. Graedel. On the Future Availability of the Energy Metals. *Annual Review of Materials Research*, 41(1):323–335, July 2011.

[9] M. Frenzel, R. Tolosana-Delgado, and J. Gutzmer. Assessing the supply potential of high-tech metals – A general method. *Resources Policy*, 46:45–58, December 2015.

[10] European Commission. Critical raw materials for the EU. Report of the Ad-hoc Working Group on defining critical raw materials. *Ad-hoc Working Group: July*, 2010:84, 2010.

[11] European Commission. Report on critical raw materials for the EU. *Report of the Ad hoc Working Group on Defining Critical Raw Materials. Brüssel*, 2014.

[12] European Commission. Critical raw materials resilience: Charting a path towards greater security and sustainability. *Report of the Ad hoc Working Group on Defining Critical Raw Materials. Brüssel*, 2020.

[13] M. Frenzel, J. Kullik, M. A. Reuter, and J. Gutzmer. Raw material 'criticality'—sense or nonsense? *Journal of Physics D: Applied Physics*, 50(12):123002, March 2017.

[14] UNEP, editor. *Decoupling Natural Resource Use and Environmental Impacts from Economic Growth*. Kenya, UNEP, 2011.

[15] G. Calvo, G. Mudd, A. Valero, and A. Valero. Decreasing Ore Grades in Global Metallic Mining: A Theoretical Issue or a Global Reality? *Resources*, 5(4):36, December 2016.

[16] G. M. Mudd. *The Sustainability of Mining in Australia: Key Production Trends and Environmental Implications*. Monash University, Department of Civil Engineering, Clayton, 2009.

[17] E. Matinde, G. S. Simate, and S. Ndlovu. Mining and metallurgical wastes: A review of recycling and re-use practices. *Journal of the Southern African Institute of Mining and Metallurgy*, 118(8):825–844, August 2018.

[18] F. O. Adeola. 2 - WEEE generation and the consequences of its improper disposal. In F. Vegliò and I. Birloaga, editors, *Waste Electrical and Electronic Equipment Recycling*, Woodhead Publishing Series in Electronic and Optical Materials, pages 13–31. Woodhead Publishing, January 2018.

[19] M. S. Sankhla, M. Kumari, M. Nandan, R. Kumar, and P. Agrawal. Heavy Metals Contamination in Water and Their Hazardous Effect on Human Health-A Review. SSRN Scholarly Paper ID 3428216, Social Science Research Network, Rochester, NY, September 2016.

[20] D. K. S. Devi, O. Sujana, and D. T. C. Singh. Hazardous Waste Management in India – A Review. 6(1):10, 2018.

[21] Z. Bian, X. Miao, S. Lei, S.-e. Chen, W. Wang, and S. Struthers. The Challenges of Reusing Mining and Mineral-Processing Wastes. *Science*, 337(6095):702–703, August 2012.

[22] J. Cui and L. Zhang. Metallurgical recovery of metals from electronic waste: A review. *Journal of Hazardous Materials*, 158(2):228–256, October 2008.

[23] F. Habashi. Fire and the art of metals: A short history of pyrometallurgy. *Mineral Processing and Extractive Metallurgy*, 114(3):165–171, September 2005.

[24] A. Das and B. Sarkar. Advanced Gravity Concentration of Fine Particles: A Review. *Mineral Processing and Extractive Metallurgy Review*, 39(6):359–394, November 2018.

[25] C. Wang, D. Harbottle, Q. Liu, and Z. Xu. Current state of fine mineral tailings treatment: A critical review on theory and practice. *Minerals Engineering*, 58:113–131, April 2014.

[26] D. Tromans. Mineral comminution: Energy efficiency considerations. *Minerals Engineering*, 21(8):613–620, July 2008.

[27] F. Musa and R. Morrison. A more sustainable approach to assessing comminution efficiency. *Minerals Engineering*, 22(7):593–601, June 2009.

[28] S. O. Adewuyi, H. A. M. Ahmed, and H. M. A. Ahmed. Methods of Ore Pretreatment for Comminution Energy Reduction. *Minerals*, 10(5):423, May 2020.

[29] V. Singh, P. Dixit, R. Venugopal, and K. B. Venkatesh. Ore Pretreatment Methods for Grinding: Journey and Prospects. *Mineral Processing and Extractive Metallurgy Review*, 40(1):1–15, January 2019.

[30] F. Habashi. Recent trends in extractive metallurgy. *Journal of Mining and Metallurgy, Section B: Metallurgy*, 45(1):1–13, 2009.

[31] C. A. Young. *SME Mineral Processing and Extractive Metallurgy Handbook*. Society for Mining, Metallurgy & Exploration, February 2019.

[32] W. G. Davenport, M. J. King, M. E. Schlesinger, and A. K. Biswas. *Extractive Metallurgy of Copper*. Elsevier, September 2002.

[33] P. Sarfo, A. Das, G. Wyss, and C. Young. Recovery of metal values from copper slag and reuse of residual secondary slag. *Waste Management*, 70:272–281, December 2017.

[34] P. Toscano and A. Utigard. Nickel, copper, and cobalt slag losses during converting. *Metallurgical and Materials Transactions B*, 34(1):121–125, February 2003.

[35] M. Assefi, S. Maroufi, Y. Yamauchi, and V. Sahajwalla. Pyrometallurgical recycling of Li-ion, Ni–Cd and Ni–MH batteries: A minireview. *Current Opinion in Green and Sustainable Chemistry*, 24:26–31, August 2020.

[36] E. Ma. Recovery of Waste Printed Circuit Boards Through Pyrometallurgy. In *Electronic Waste Management and Treatment Technology*, pages 247–267. Elsevier, 2019.

[37] M. T. Ochsenkühn-Petropoulou, K. S. Hatzilyberis, L. N. Mendrinos, and C. E. Salmas. Pilot-Plant Investigation of the Leaching Process for the Recovery of Scandium from Red Mud. *Industrial & Engineering Chemistry Research*, 41(23):5794–5801, November 2002.

[38] T. Chen, C. Lei, B. Yan, and X. Xiao. Metal recovery from the copper sulfide tailing with leaching and fractional precipitation technology. *Hydrometallurgy*, 147-148:178–182, August 2014.

[39] H. Cui and C. G. Anderson. Literature Review of Hydrometallurgical Recycling of Printed Circuit Boards (PCBs). *Journal of Advanced Chemical Engineering*, 6(1), 2016.

[40] M. Boon and J. J. Heijnen. Chemical oxidation kinetics of pyrite in bioleaching processes. *Hydrometallurgy*, 48(1):27–41, March 1998.

[41] D. B. Johnson. Biomining—biotechnologies for extracting and recovering metals from ores and waste materials. *Current Opinion in Biotechnology*, 30:24–31, December 2014.

[42] A. E. Torma. The role of Thiobacillus ferrooxidans in hydrometallurgical processes. In T. K. Ghose, A. Fiechter, and N. Blakebrough, editors, *Advances in Biochemical Engineering, Volume 6*, Advances in Biochemical Engineering, pages 1–37, Berlin, Heidelberg, 1977. Springer.

[43] H. L. Ehrlich. Past, present and future of biohydrometallurgy. *Hydrometallurgy*, 59(2):127–134, February 2001.

[44] L. U. Salkield. *A Technical History of the Rio Tinto Mines: Some Notes on Exploitation from Pre-Phoenician Times to the 1950s*. Springer Science & Business Media, December 2012.

[45] W. Rudolfs. Oxidation of iron pyrites by sulfur-oxidizing organisms and their use for making mineral phosphates available. *Soil Sci*, 14(2):135–145, 1922.

[46] A. R. Colmer and M. E. Hinkle. The Role of Microorganisms in Acid Mine Drainage: A Preliminary Report. *Science*, 106(2751):253–256, 1947.

[47] A. R. Colmer, K. L. Temple, and M. E. Hinkle. An iron-oxidizing bacterium from the acid drainage of some bituminous coal mines. *Journal of Bacteriology*, 59(3):317–328, March 1950.

[48] D. G. Lundgren, M. Valkova-Valchanova, and R. Reed. Chemical reactions important in bioleaching and bioaccumulation. (16):7–22, 1986.

[49] A. H. Kaksonen, N. J. Boxall, Y. Gumulya, H. N. Khaleque, C. Morris, T. Bohu, K. Y. Cheng, K. M. Usher, and A.-M. Lakaniemi. Recent progress in biohydrometallurgy and microbial characterisation. *Hydrometallurgy*, 180:7–25, September 2018.

[50] C. A. du Plessis, J. D. Batty, and D. W. Dew. Commercial Applications of Thermophile Bioleaching. In D. E. Rawlings and D. B. Johnson, editors, *Biomining*, pages 57–80. Springer, Berlin, Heidelberg, 2007.

[51] M. Gericke, J. W. Neale, and P. J. van Staden. A Mintek perspective of the past 25 years in minerals bioleaching. *Journal of the Southern African Institute of Mining and Metallurgy*, 109(10):567–585, October 2009.

[52] H. R. Watling. The bioleaching of nickel-copper sulfides. *Hydrometallurgy*, 91(1):70–88, March 2008.

[53] C. Joulian, V. Fonti, S. Chapron, C. G. Bryan, and A.-G. Guezennec. Bioleaching of pyritic coal wastes: Bioprospecting and efficiency of selected consortia. *Research in Microbiology*, September 2020.

[54] C. A. du Plessis, W. Slabbert, K. B. Hallberg, and D. B. Johnson. Ferredox: A biohydrometallurgical processing concept for limonitic nickel laterites. *Hydrometallurgy*, 109(3):221–229, October 2011.

[55] K. B. Hallberg, B. M. Grail, C. A. du Plessis, and D. B. Johnson. Reductive dissolution of ferric iron minerals: A new approach for bio-processing nickel laterites. *Minerals Engineering*, 24(7):620–624, June 2011.

[56] J. R. Dodson, A. J. Hunt, H. L. Parker, Y. Yang, and J. H. Clark. Elemental sustainability: Towards the total recovery of scarce metals. *Chemical Engineering and Processing: Process Intensification*, 51:69–78, January 2012.

[57] N. Pradhan, K. C. Nathsarma, K. Srinivasa Rao, L. B. Sukla, and B. K. Mishra. Heap bioleaching of chalcopyrite: A review. *Minerals Engineering*, 21(5):355–365, April 2008.

[58] L. W. John. The art of heap leaching - The fundamentals. page 26, 2011.

[59] J. A. Brierley and C. L. Brierley. Present and future commercial applications of biohydrometallurgy. *Hydrometallurgy*, 59(2):233–239, February 2001.

[60] J. Petersen. Heap leaching as a key technology for recovery of values from low-

grade ores – A brief overview. *Hydrometallurgy*, 165:206–212, October 2016.

[61] C. L. Brierley and J. A. Brierley. Progress in bioleaching: Part B: Applications of microbial processes by the minerals industries. *Applied Microbiology and Biotechnology*, 97(17):7543–7552, September 2013.

[62] D. E. Rawlings, D. Dew, and C. du Plessis. Biomineralization of metal-containing ores and concentrates. *Trends in Biotechnology*, 21(1):38–44, January 2003.

[63] C. S. Gahan, H. Srichandan, D.-J. Kim, and A. Akcil. Biohydrometallurgy and Biomineral Processing Technology: A Review on its Past, Present and Future. 1:15, 2012.

[64] D. E. Rawlings and D. B. Johnson. The microbiology of biomining: Development and optimization of mineral-oxidizing microbial consortia. *Microbiology*, 153(2):315–324, February 2007.

[65] D. H. R. Morin and P. d'Hugues. Bioleaching of a Cobalt-Containing Pyrite in Stirred Reactors: A Case Study from Laboratory Scale to Industrial Application. In D. E. Rawlings and D. B. Johnson, editors, *Biomining*, pages 35–55. Springer, Berlin, Heidelberg, 2007.

[66] K. D. Wakeman, P. Honkavirta, and J. A. Puhakka. Bioleaching of flotation by-products of talc production permits the separation of nickel and cobalt from iron and arsenic. *Process Biochemistry*, 46(8):1589–1598, August 2011.

[67] J. Neale, J. Seppälä, A. Laukka, P. Aswegen, S. Barnett, and M. Gericke. The MONDO Minerals Nickel Sulfide Bioleach Project: From Test Work to Early Plant Operation. *Solid State Phenomena*, 262:28–32, August 2017.

[68] S. King, M. Ayre, G. Simpson, D. Lusher, and J. Hopkins. Sustainable Regional Development Through Networks–the case of ASPIRE (Advisory System for Processing, Innovation and Resource Efficiency) to support industrial symbiosis for SMEs. In *Seventh Regional 3R Forum in Asia and the Pacific*. UNCRD Melbourne, 2016.

[69] C. G. Bryan, B. J. Williamson, J. Całus-Moszko, Q. van Haute, A. G. Guezennec, S. Gaydardzhiev, P. Wavrer, and R. Frączek. CEReS – co-processing of coal mine & electronic wastes: Novel resources for a sustainable future. *Hydrometallurgy*, 197:105444, November 2020.

[70] S. Y. Khaing, Y. Sugai, and K. Sasaki. Gold Dissolution from Ore with Iodide-Oxidising Bacteria. *Scientific Reports*, 9(1):4178, March 2019.

[71] N. J. Boxall, S. M. Rea, J. Li, C. Morris, and A. H. Kaksonen. Effect of high sulfate concentrations on chalcopyrite bioleaching and molecular characterisation of the bioleaching microbial community. *Hydrometallurgy*, 168:32–39, March 2017.

[72] D. B. Johnson. Development and application of biotechnologies in the metal mining industry. *Environmental Science and Pollution Research*, 20(11):7768–7776, November 2013.

[73] M. Vera, A. Schippers, and W. Sand. Progress in bioleaching: Fundamentals and

mechanisms of bacterial metal sulfide oxidation—part A. *Applied Microbiology and Biotechnology*, 97(17):7529–7541, September 2013.

[74] H. Zhao, Y. Zhang, X. Zhang, L. Qian, M. Sun, Y. Yang, Y. Zhang, J. Wang, H. Kim, and G. Qiu. The dissolution and passivation mechanism of chalcopyrite in bioleaching: An overview. *Minerals Engineering*, 136:140–154, June 2019.

[75] K. Bosecker. Bioleaching: Metal solubilization by microorganisms. *FEMS Microbiology Reviews*, 20(3-4):591–604, July 1997.

[76] H. L. Ehrlich. Geomicrobiology: Its significance for geology. *Earth-Science Reviews*, 45(1):45–60, November 1998.

[77] A. Schippers, S. Hedrich, J. Vasters, M. Drobe, W. Sand, and S. Willscher. Biomining: Metal Recovery from Ores with Microorganisms. In A. Schippers, F. Glombitza, and W. Sand, editors, *Geobiotechnology I*, volume 141, pages 1–47. Springer Berlin Heidelberg, Berlin, Heidelberg, 2013.

[78] F. Crundwell. How do bacteria interact with minerals? *Hydrometallurgy*, 71(1-2):75–81, October 2003.

[79] F. K. Crundwell. The dissolution and leaching of minerals: Mechanisms, myths and misunderstandings. *Hydrometallurgy*, 139(Supplement C):132–148, July 2013.

[80] H. Tributsch. Direct versus indirect bioleaching. *Hydrometallurgy*, 59(2):177–185, February 2001.

[81] H. Srichandan, R. K. Mohapatra, P. K. Parhi, and S. Mishra. Bioleaching approach for extraction of metal values from secondary solid wastes: A critical review. *Hydrometallurgy*, 189:105122, November 2019.

[82] T. Gehrke, J. Telegdi, D. Thierry, and W. Sand. Importance of Extracellular Polymeric Substances from Thiobacillus ferrooxidans for Bioleaching. *Applied and Environmental Microbiology*, 64(7):2743–2747, July 1998.

[83] S. Feng, K. Li, Z. Huang, Y. Tong, and H. Yang. Specific mechanism of Acidithiobacillus caldus extracellular polymeric substances in the bioleaching of copper-bearing sulfide ore. *Plos One*, 14(4):e0213945, April 2019.

[84] L. Fang, Q. Huang, X. Wei, W. Liang, X. Rong, W. Chen, and P. Cai. Microcalorimetric and potentiometric titration studies on the adsorption of copper by extracellular polymeric substances (EPS), minerals and their composites. *Bioresource Technology*, 101(15):5774–5779, August 2010.

[85] W. Sand and T. Gehrke. Extracellular polymeric substances mediate bioleaching/biocorrosion via interfacial processes involving iron(III) ions and acidophilic bacteria. *Research in Microbiology*, 157(1):49–56, January 2006.

[86] R.-L. Yu, J.-X. Tan, Y. Peng, S. U. N. Jing, X.-J. Ouyang, and Y.-J. Dai. EPS-contact-leaching mechanism of chalcopyrite concentrates by A. ferrooxidans. *Transactions of Nonferrous Metals Society of China*, 18(6):1427–1432, 2008.

[87] Z. Huang, S. Feng, Y. Tong, and H. Yang. Enhanced “contact mechanism” for

interaction of extracellular polymeric substances with low-grade copper-bearing sulfide ore in bioleaching by moderately thermophilic Acidithiobacillus caldus. *Journal of Environmental Management*, 242:11–21, July 2019.

[88] J. Zhu, Q. Li, W. Jiao, H. Jiang, W. Sand, J. Xia, X. Liu, W. Qin, G. Qiu, Y. Hu, and L. Chai. Adhesion forces between cells of Acidithiobacillus ferrooxidans, Acidithiobacillus thiooxidans or Leptospirillum ferrooxidans and chalcopyrite. *Colloids and Surfaces B: Biointerfaces*, 94:95–100, June 2012.

[89] D. E. Rawlings. Heavy Metal Mining Using Microbes. *Annual Review of Microbiology*, 56(1):65–91, October 2002.

[90] A. Schippers, P. Jozsa, and W. Sand. Sulfur chemistry in bacterial leaching of pyrite. *Applied and Environmental Microbiology*, 62(9):3424–3431, September 1996.

[91] A. Schippers and W. Sand. Bacterial Leaching of Metal Sulfides Proceeds by Two Indirect Mechanisms via Thiosulfate or via Polysulfides and Sulfur. *Applied and Environmental Microbiology*, 65(1):319–321, January 1999.

[92] F. Crundwell. The influence of the electronic structure of solids on the anodic dissolution and leaching of semiconducting sulphide minerals. *Hydrometallurgy*, 21(2):155–190, December 1988.

[93] H. Srichandan, R. K. Mohapatra, P. K. Parhi, and S. Mishra. Bioleaching approach for extraction of metal values from secondary solid wastes: A critical review. *Hydrometallurgy*, 189:105122, November 2019.

[94] H. Tao and L. Dongwei. Presentation on mechanisms and applications of chalcopyrite and pyrite bioleaching in biohydrometallurgy – a presentation. *Biotechnology Reports*, 4:107–119, December 2014.

[95] P. D'Hugues, F. Battaglia-Brunet, M. Clarens, and D. Morin. Microbial diversity of various metal-sulfides bioleaching cultures grown under different operating conditions using 16S-rDNA analysis. 2003.

[96] J. P. Gramp, F. S. Jones, J. M. Bigham, and O. H. Tuovinen. Monovalent cation concentrations determine the types of Fe(III) hydroxysulfate precipitates formed in bioleach solutions. *Hydrometallurgy*, 94(1):29–33, November 2008.

[97] A. H. Kaksonen, C. Morris, S. Rea, J. Li, J. Wylie, K. M. Usher, M. P. Ginige, K. Y. Cheng, F. Hilario, and C. A. du Plessis. Biohydrometallurgical iron oxidation and precipitation: Part I — Effect of pH on process performance. *Hydrometallurgy*, 147-148:255–263, August 2014.

[98] A. H. Kaksonen, C. Morris, S. Rea, J. Li, K. M. Usher, R. G. McDonald, F. Hilario, T. Hosken, M. Jackson, and C. A. du Plessis. Biohydrometallurgical iron oxidation and precipitation: Part II — Jarosite precipitate characterisation and acid recovery by conversion to hematite. *Hydrometallurgy*, 147-148:264–272, August 2014.

[99] H. Wang, J. M. Bigham, and O. H. Tuovinen. Formation of schwertmannite

and its transformation to jarosite in the presence of acidophilic iron-oxidizing microorganisms. *Materials Science and Engineering: C*, 26(4):588–592, May 2006.

[100] H. Watling. Microbiological Advances in Biohydrometallurgy. *Minerals*, 6(2):49, June 2016.

[101] F. Battaglia-Brunet, M. Clarens, P. d'Hugues, J. Godon, S. Foucher, and D. Morin. Monitoring of a pyrite-oxidising bacterial population using DNA single-strand conformation polymorphism and microscopic techniques. *Applied Microbiology and Biotechnology*, 60(1):206–211, October 2002.

[102] N. Okibe, M. Gericke, K. B. Hallberg, and D. B. Johnson. Enumeration and Characterization of Acidophilic Microorganisms Isolated from a Pilot Plant Stirred-Tank Bioleaching Operation. *Applied and Environmental Microbiology*, 69(4):1936–1943, April 2003.

[103] D. Mikkelsen, U. Kappler, A. G. McEwan, and L. I. Sly. Archaeal diversity in two thermophilic chalcopyrite bioleaching reactors. *Environmental Microbiology*, 8(11):2050–2056, 2006.

[104] J. P. Amend and E. L. Shock. Energetics of overall metabolic reactions of thermophilic and hyperthermophilic Archaea and Bacteria. *FEMS Microbiology Reviews*, 25(2):175–243, April 2001.

[105] A. Schippers. Microorganisms Involved in Bioleaching and Nucleic Acid-Based Molecular Methods for Their Identification and Quantification. In E. R. Donati and W. Sand, editors, *Microbial Processing of Metal Sulfides*, pages 3–33. Springer Netherlands, Dordrecht, 2007.

[106] D. W. Shiers, D. M. Collinson, and H. R. Watling. The impact of heap self-heating on microbial activity during the bioleaching of low-grade copper sulfide ores. In *Solid State Phenomena*, volume 262, pages 233–236. Trans Tech Publ, 2017.

[107] W. Liu and G. Granata. Temperature control in copper heap bioleaching. *Hydrometallurgy*, 176:26–32, March 2018.

[108] J. A. Brierley. Response of microbial systems to thermal stress in biooxidation-heap pretreatment of refractory gold ores. *Hydrometallurgy*, 71(1):13–19, October 2003.

[109] T. C. Logan, T. Seal, and J. A. Brierley. Whole-Ore Heap Biooxidation of Sulfidic Gold-Bearing Ores. In D. E. Rawlings and D. B. Johnson, editors, *Biomining*, pages 113–138. Springer, Berlin, Heidelberg, 2007.

[110] P. Soto, M. Acosta, P. Tapia, Y. Contador, A. Velásquez, C. Espoz, C. Pinilla, P. A. Galleguillos, and C. Demergasso. From mesophilic to moderate thermophilic populations in an industrial heap bioleaching process. In *Advanced Materials Research*, volume 825, pages 376–379. Trans Tech Publ, 2013.

[111] J. C. Cox, D. G. Nicholls, and W. J. Ingledew. Transmembrane electrical potential

and transmembrane pH gradient in the acidophile Thiobacillus ferro-oxidans. *Biochemical Journal*, 178(1):195–200, January 1979.

[112] D. E. Rawlings. Characteristics and adaptability of iron- and sulfur-oxidizing microorganisms used for the recovery of metals from minerals and their concentrates. *Microbial Cell Factories*, 4(1):13, May 2005.

[113] J. J. Plumb, R. Muddle, and P. D. Franzmann. Effect of pH on rates of iron and sulfur oxidation by bioleaching organisms. *Minerals Engineering*, 21(1):76–82, January 2008.

[114] P. Nurmi, B. Özkaya, A. Kaksonen, O. Tuovinen, and J. Puhakka. Inhibition kinetics of iron oxidation by Leptospirillum ferriphilum in the presence of ferric, nickel and zinc ions. *Hydrometallurgy*, 97(3-4):137–145, July 2009.

[115] D. Sobolev and M. F. T. Begonia. Effects of Heavy Metal Contamination upon Soil Microbes: Lead-induced Changes in General and Denitrifying Microbial Communities as Evidenced by Molecular Markers. *International Journal of Environmental Research and Public Health*, 5(5):450–456, December 2008.

[116] E. L. J. Watkin, S. E. Keeling, F. A. Perrot, D. W. Shiers, M.-L. Palmer, and H. R. Watling. Metals tolerance in moderately thermophilic isolates from a spent copper sulfide heap, closely related to Acidithiobacillus caldus, Acidimicrobium ferrooxidans and Sulfobacillus thermosulfidooxidans. *Journal of Industrial Microbiology & Biotechnology*, 36(3):461, December 2008.

[117] W. Wu, X. Liu, X. Zhang, M. Zhu, and W. Tan. Bioleaching of copper from waste printed circuit boards by bacteria-free cultural supernatant of iron–sulfur-oxidizing bacteria. *Bioresources and Bioprocessing*, 5(1):10, February 2018.

[118] M. E. Clark, J. D. Batty, C. B. van Buuren, D. W. Dew, and M. A. Eamon. Biotechnology in minerals processing: Technological breakthroughs creating value. *Hydrometallurgy*, 83(1):3–9, September 2006.

[119] A. H. Kaksonen, X. Deng, T. Bohu, L. Zea, H. N. Khaleque, Y. Gumulya, N. J. Boxall, C. Morris, and K. Y. Cheng. Prospective directions for biohydrometallurgy. *Hydrometallurgy*, 195:105376, August 2020.

[120] S. C. Bouffard and D. G. Dixon. Investigative study into the hydrodynamics of heap leaching processes. *Metallurgical and Materials Transactions B*, 32(5):763–776, October 2001.

[121] J. Petersen. Modelling of bioleach processes: Connection between science and engineering. *Hydrometallurgy*, 104(3):404–409, October 2010.

[122] A. Mahmoud, P. Cézac, A. F. A. Hoadley, F. Contamine, and P. D'Hugues. A review of sulfide minerals microbially assisted leaching in stirred tank reactors. *International Biodeterioration & Biodegradation*, 119:118–146, April 2017.

[123] J. Petersen and D. G. Dixon. Modeling and Optimization of Heap Bioleach Processes. In D. E. Rawlings and D. B. Johnson, editors, *Biomining*, pages 153–176. Springer, Berlin, Heidelberg, 2007.

[124] P. J. van Staden, A. Naseri, and J. Petersen. HeapSim modelling of high temperature heap bioleaching data. In *ALTA 2017 Conference and Exhibition, Pan Pacific Hotel, Perth, Western Australia*, pages 210–246, 2017.

[125] A. Ahmadi, M. Ranjbar, M. Schaffie, and J. Petersen. Kinetic modeling of bioleaching of copper sulfide concentrates in conventional and electrochemically controlled systems. *Hydrometallurgy*, 127-128(Supplement C):16–23, October 2012.

[126] P. R. Holmes and F. K. Crundwell. The kinetics of the oxidation of pyrite by ferric ions and dissolved oxygen: An electrochemical study. *Geochimica et Cosmochimica Acta*, 64(2):263–274, January 2000.

[127] S. C. Bouffard, B. F. Rivera-Vasquez, and D. G. Dixon. Leaching kinetics and stoichiometry of pyrite oxidation from a pyrite–marcasite concentrate in acid ferric sulfate media. *Hydrometallurgy*, 84(3):225–238, November 2006.

[128] C. L. Wiersma and J. D. Rimstidt. Rates of reaction of pyrite and marcasite with ferric iron at pH 2. *Geochimica et Cosmochimica Acta*, 48(1):85–92, 1984.

[129] M. A. McKibben and H. L. Barnes. Oxidation of pyrite in low temperature acidic solutions: Rate laws and surface textures. *Geochimica et Cosmochimica Acta*, 50(7):1509–1520, July 1986.

[130] F. C. Boogerd, C. van den Beemd, T. Stoelwinder, P. Bos, and J. G. Kuenen. Relative contributions of biological and chemical reactions to the overall rate of pyrite oxidation at temperatures between 30°C and 70°C. *Biotechnology and Bioengineering*, 38(2):109–115, 1991.

[131] J. Rimstidt and W. D. Newcomb. Measurement and analysis of rate data: The rate of reaction of ferric iron with pyrite. *Geochimica et Cosmochimica Acta*, 57(9):1919–1934, May 1993.

[132] W. E. King Jr and D. D. Perlmutter. Pyrite oxidation in aqueous ferric chloride. *AIChE Journal*, 23(5):679–685, 1977.

[133] C. Q. Zheng, C. C. Allen, and R. G. Bautista. Kinetic study of the oxidation of pyrite in aqueous ferric sulfate. *Industrial & Engineering Chemistry Process Design and Development*, 25(1):308–317, January 1986.

[134] K. Kawakami, J. Sato, K. Kusunoki, K. Kusakabe, and S. Morooka. Kinetic study of oxidation of pyrite slurry by ferric chloride. *Industrial & engineering chemistry research*, 27(4):571–576, 1988.

[135] M. A. Williamson and J. Rimstidt. The kinetics and electrochemical rate-determining step of aqueous pyrite oxidation. *Geochimica et Cosmochimica Acta*, 58(24):5443–5454, December 1994.

[136] B. B. Nayak, R. K. Paramguru, and H. S. Ray. Studies on initial dissolution kinetics from polarization data. III. Pyrite in ferric sulphate. *Trans. Indian Inst. Met.*, 48(1):35–41, 1995.

[137] M. Boon and J. Heijnen. Chemical oxidation kinetics of pyrite in bioleaching

processes. *Hydrometallurgy*, 48(1):27–41, March 1998.

[138] M. Boon, H. Brasser, G. Hansford, and J. Heijnen. Comparison of the oxidation kinetics of different pyrites in the presence of Thiobacillus ferrooxidans or Leptospirillum ferrooxidans. *Hydrometallurgy*, 53(1):57–72, July 1999.

[139] M. J. Nicol. The role of electrochemistry in hydrometallurgy. In *Nicol, M.J. <http://researchrepository.murdoch.edu.au/view/author/Nicol, Mike.Html> (1993) The Role of Electrochemistry in Hydrometallurgy. In: 4th International Symposium on Hydrometallurgy, 1 - 5 August 1993, Salt Lake City, UTAH*, Salt Lake City, UTAH, 1993.

[140] S. Bouffard. *Understanding the Heap Biooxidation of Sulfidic Refractory Gold Ores*. PhD thesis, University of British Columbia, 2003.

[141] J. Petersen and D. G. Dixon. Competitive bioleaching of pyrite and chalcopyrite. *Hydrometallurgy*, 83(1):40–49, September 2006.

[142] D. G. Dixon and J. L. Hendrix. A mathematical model for heap leaching of one or more solid reactants from porous ore pellets. *Metallurgical Transactions B*, 24(6):1087–1102, December 1993.

[143] S. C. Bouffard and D. G. Dixon. Modeling pyrite bioleaching in isothermal test columns with the HeapSim model. *Hydrometallurgy*, 95(3):215–226, February 2009.

[144] C. González-Figueredo, R. A. Flores-Estrella, and O. A. Rojas-Rejón. Fermentation: Metabolism, Kinetic Models, and Bioprocessing. *Current Topics in Biochemical Engineering*, November 2018.

[145] D. G. MacDonald and R. H. Clark. The oxidation of aqueous ferrous sulphate by thiobacillus ferrooxidans. *The Canadian Journal of Chemical Engineering*, 48(6):669–676, 1970.

[146] B. Özkaya, E. Sahinkaya, P. Nurmi, A. H. Kaksonen, and J. A. Puhakka. Kinetics of iron oxidation by Leptospirillum ferriphilum dominated culture at pH below one. *Biotechnology and Bioengineering*, 97(5):1121–1127, 2007.

[147] M. Boon, T. A. Meeder, C. Thöne, C. Ras, and J. J. Heijnen. The ferrous iron oxidation kinetics of Thiobacillus ferrooxidans in continuous cultures. *Applied Microbiology and Biotechnology*, 51(6):820–826, June 1999.

[148] T. V. Ojumu, J. Petersen, G. E. Searby, and G. S. Hansford. A review of rate equations proposed for microbial ferrous-iron oxidation with a view to application to heap bioleaching. *Hydrometallurgy*, 83(1):21–28, September 2006.

[149] C. A. Jones and D. P. Kelly. Growth of Thiobacillus ferrooxidans on ferrous iron in chemostat culture: Influence of product and substrate inhibition. *Journal of Chemical Technology and Biotechnology. Biotechnology*, 33(4):241–261, 1983.

[150] J. F. Braddock, H. V. Luong, and E. J. Brown. Growth Kinetics of Thiobacillus ferrooxidans Isolated from Arsenic Mine Drainage. *Applied and Environmental Microbiology*, 48(1):48–55, July 1984.

[151] L. N. Nikolov and D. G. Karamanev. Kinetics of the Ferrous Iron Oxidation by Resuspended Cells of Thiobacillus ferrooxidans. *Biotechnology Progress*, 8(3):252–255, 1992.

[152] F. K. Crundwell. The kinetics of the chemiosmotic proton circuit of the iron-oxidizing bacterium Thiobacillus ferrooxidans. *Bioelectrochemistry and bioenergetics*, 43(1):115–122, 1997.

[153] M. S. Liu, R. M. R. Branion, and D. W. Duncan. The effects of ferrous iron, dissolved oxygen, and inert solids concentrations on the growth of thiobacillus ferrooxidans. *The Canadian Journal of Chemical Engineering*, 66(3):445–451, 1988.

[154] R. Huberts. *Modelling of Ferrous Sulphate Oxidation by Iron Oxidizing Bacteria: A Chemiosmotic and Electrochemical Approach.* PhD thesis, University of the Witwatersrand, 1994.

[155] M. Boon, J. J. Heijnen, and G. S. Hansford. Recent developments in modelling bio-oxidation kinetics: Part I: Measurement methods. In *Minerals Bioprocessing II: Proceedings of the Engineering Foundation Conference "Minerals Processing II", Held in Snowbird, Utah from July 10-15, 1995*, pages 41–61. Minerals, Metals and Materials Society, December 1995.

[156] G. S. Hansford. Recent Developments in Modeling the Kinetics of Bioleaching. In D. E. Rawlings, editor, *Biomining: Theory, Microbes and Industrial Processes*, Biotechnology Intelligence Unit, pages 153–175. Springer, Berlin, Heidelberg, 1997.

[157] M. Nemati and C. Webb. Inhibition effect of ferric iron on the kinetics of ferrous iron. *Biotechnology Letters*, 20(9):873–877, September 1998.

[158] H. M. Lizama and I. Suzuki. Synergistic Competitive Inhibition of Ferrous Iron Oxidation by Thiobacillus ferrooxidans by Increasing Concentrations of Ferric Iron and Cells. *Applied and Environmental Microbiology*, 55(10):2588–2591, October 1989.

[159] T. V. Ojumu and J. Petersen. The kinetics of ferrous ion oxidation by Leptospirillum ferriphilum in continuous culture: The effect of pH. *Hydrometallurgy*, 106(1):5–11, February 2011.

[160] P. R. Norris. Acidophilic bacteria and their activity in mineral sulfide oxidation. *Microbial mineral recovery*, pages 3–27, 1990.

[161] P. D. Franzmann, C. M. Haddad, R. B. Hawkes, W. J. Robertson, and J. J. Plumb. Effects of temperature on the rates of iron and sulfur oxidation by selected bioleaching Bacteria and Archaea: Application of the Ratkowsky equation. *Minerals Engineering*, 18(13):1304–1314, November 2005.

[162] A. Sánchez-Chacón and G. Lapidus. Model for heap leaching of gold ores by cyanidation. *Hydrometallurgy*, 44(1-2):1–20, January 1997.

[163] A.-G. Guezennec, C. Joulian, J. Jacob, A. Archane, D. Ibarra, R. de Buyer,

F. Bodénan, and P. d'Hugues. Influence of dissolved oxygen on the bioleaching efficiency under oxygen enriched atmosphere. *Minerals Engineering*, 106:64–70, May 2017.

[164] S. Harrison, A. Kotsiopoulos, R. Stevenson, and J. Cilliers. Mixing indices allow scale-up of stirred tank slurry reactor conditions for equivalent homogeneity. *Chemical Engineering Research and Design*, 153:865–874, January 2020.

[165] C. Zheng, J. Guo, C. Wang, Y. Chen, H. Zheng, Z. Yan, and Q. Chen. Experimental study and simulation of a three-phase flow stirred bioreactor. *Chinese Journal of Chemical Engineering*, June 2018.

[166] C. Zheng, Y. Huang, J. Guo, R. Cai, H. Zheng, C. Lin, and Q. Chen. Investigation of cleaner sulfide mineral oxidation technology: Simulation and evaluation of stirred bioreactors for gold-bioleaching process. *Journal of Cleaner Production*, 192:364–375, August 2018.

[167] A. Nienow. Suspension of solid particles in turbine agitated baffled vessels. *Chemical Engineering Science*, 23(12):1453–1459, December 1968.

[168] S. T. Harrison, R. Stevenson, and J. J. Cilliers. Assessing solids concentration homogeneity in Rushton-agitated slurry reactors using electrical resistance tomography (ERT). *Chemical Engineering Science*, 71:392–399, March 2012.

[169] M. M. Buffo, L. J. Corrêa, M. N. Esperança, A. J. G. Cruz, C. S. Farinas, and A. C. Badino. Influence of dual-impeller type and configuration on oxygen transfer, power consumption, and shear rate in a stirred tank bioreactor. *Biochemical Engineering Journal*, 114:130–139, October 2016.

[170] A. W. Nienow, M. F. Edwards, and N. Harnby. *Mixing in the Process Industries*. Butterworth-Heinemann, 1997.

[171] G. Ascanio. Mixing time in stirred vessels: A review of experimental techniques. *Chinese Journal of Chemical Engineering*, 23(7):1065–1076, July 2015.

[172] A. Nienow. On impeller circulation and mixing effectiveness in the turbulent flow regime. *Chemical Engineering Science*, 52(15):2557–2565, August 1997.

[173] P. Vrábel, R. G. van der Lans, K. C. Luyben, L. Boon, and A. W. Nienow. Mixing in large-scale vessels stirred with multiple radial or radial and axial uppumping impellers: Modelling and measurements. *Chemical Engineering Science*, 55(23):5881–5896, December 2000.

[174] A. Paglianti, C. Carletti, A. Busciglio, and G. Montante. Solid distribution and mixing time in stirred tanks: The case of floating particles. *The Canadian Journal of Chemical Engineering*, 95(9):1789–1799, 2017.

[175] W. Bujalski, K. Takenaka, S. Paoleni, M. Jahoda, A. Paglianti, K. Takahashi, A. W. Nienow, and A. W. Etchells. Suspension and Liquid Homogenization in High Solids Concentration Stirred Chemical Reactors. *Chemical Engineering Research and Design*, 77(3):241–247, May 1999.

[176] R. Jafari, P. A. Tanguy, and J. Chaouki. Experimental investigation on solid

dispersion, power consumption and scale-up in moderate to dense solid–liquid suspensions. *Chemical Engineering Research and Design*, 90(2):201–212, February 2012.

[177] F. Bouquet and D. Morin. BROGIM®: A new three-phase mixing system testwork and scale-up. *Hydrometallurgy*, 83(1):97–105, September 2006.

[178] A. W. Nienow. Stirring and Stirred-Tank Reactors. *Chemie Ingenieur Technik*, 86(12):2063–2074, 2014.

[179] J. H. Rushton. Power Characteristics of Mixing Impellers Part 1. *Chem. Eng. Prog.*, 46:395–404, 1950.

[180] D. Chapple, S. M. Kresta, A. Wall, and A. Afacan. The Effect of Impeller and Tank Geometry on Power Number for a Pitched Blade Turbine. *Chemical Engineering Research and Design*, 80(4):364–372, May 2002.

[181] M. Bouaifi and M. Roustan. Power consumption, mixing time and homogenisation energy in dual-impeller agitated gas–liquid reactors. *Chemical Engineering and Processing: Process Intensification*, 40(2):87–95, February 2001.

[182] J. Zhang, Z. Gao, Y. Cai, H. Cao, Z. Cai, and Y. Bao. Power consumption and mass transfer in a gas-liquid-solid stirred tank reactor with various triple-impeller combinations. *Chemical Engineering Science*, 170:464–475, October 2017.

[183] M. Roustan. Agitation. Mélange - Caractéristiques des mobiles d'agitation. *Techniques de l'ingénieur*, March 2005.

[184] H. Zhu, A. W. Nienow, W. Bujalski, and M. J. H. Simmons. Mixing studies in a model aerated bioreactor equipped with an up- or a down-pumping 'Elephant Ear' agitator: Power, hold-up and aerated flow field measurements. *Chemical Engineering Research and Design*, 87(3):307–317, March 2009.

[185] C. Loubière, A. Delafosse, E. Guedon, D. Toye, I. Chevalot, and E. Olmos. Optimization of the Impeller Design for Mesenchymal Stem Cell Culture on Microcarriers in Bioreactors. *Chemical Engineering & Technology*, 42(8):1702–1708, 2019.

[186] T. Kumaresan and J. B. Joshi. Effect of impeller design on the flow pattern and mixing in stirred tanks. *Chemical Engineering Journal*, 115(3):173–193, January 2006.

[187] G. Montante, A. Paglianti, and F. Magelli. Analysis of dilute solid–liquid suspensions in turbulent stirred tanks. *Chemical Engineering Research and Design*, 90(10):1448–1456, October 2012.

[188] A. Tamburini, A. Cipollina, G. Micale, A. Brucato, and M. Ciofalo. Influence of drag and turbulence modelling on CFD predictions of solid liquid suspensions in stirred vessels. *Chemical Engineering Research and Design*, 92(6):1045–1063, June 2014.

[189] H. A. Nasr-El-Din, R. S. Mac Taggart, and J. H. Masliyah. Local solids concentration measurement in a slurry mixing tank. *Chemical Engineering Science*,

51(8):1209–1220, 1996.

[190] A. Ochieng and A. E. Lewis. CFD simulation of solids off-bottom suspension and cloud height. *Hydrometallurgy*, 82(1-2):1–12, July 2006.

[191] R. Stevenson, S. T. L. Harrison, M. D. Mantle, A. J. Sederman, T. L. Moraczewski, and M. L. Johns. Analysis of partial suspension in stirred mixing cells using both MRI and ERT. *Chemical Engineering Science*, page 9, 2010.

[192] T. N. Zwietering. Suspending of solid particles in liquid by agitators. *Chemical Engineering Science*, 8(3):244–253, June 1958.

[193] A. Brucato, A. Cipollina, G. Micale, F. Scargiali, and A. Tamburini. Particle suspension in top-covered unbaffled tanks. *Chemical Engineering Science*, 65(10):3001–3008, May 2010.

[194] A. Tamburini, A. Cipollina, G. Micale, A. Brucato, and M. Ciofalo. CFD simulations of dense solid–liquid suspensions in baffled stirred tanks: Prediction of suspension curves. *Chemical Engineering Journal*, 178:324–341, December 2011.

[195] A. Tamburini, A. Brucato, A. Cipollina, G. Micale, and M. Ciofalo. CFD Predictions of Sufficient Suspension Conditions in Solid-Liquid Agitated Tanks. *International Journal of Nonlinear Sciences and Numerical Simulation*, 13(6), January 2012.

[196] A. T.-C. Mak. *Solid-Liquid Mixing in Mechanically Agitated Vessels*. Doctoral, University of London, 1992.

[197] A. R. Khopkar, G. R. Kasat, A. B. Pandit, and V. V. Ranade. Computational Fluid Dynamics Simulation of the Solid Suspension in a Stirred Slurry Reactor. *Industrial & Engineering Chemistry Research*, 45(12):4416–4428, June 2006.

[198] B. N. Murthy, R. S. Ghadge, and J. B. Joshi. CFD simulations of gas–liquid–solid stirred reactor: Prediction of critical impeller speed for solid suspension. *Chemical Engineering Science*, 62(24):7184–7195, December 2007.

[199] S. Hosseini, D. Patel, F. Ein-Mozaffari, and M. Mehrvar. Study of Solid-Liquid Mixing in Agitated Tanks through Computational Fluid Dynamics Modeling. *Industrial & Engineering Chemistry Research*, 49(9):4426–4435, May 2010.

[200] D. S. Savić, V. B. Veljković, M. L. Lazić, M. M. Vrvić, and J. I. Vučetić. Effects of the oxygen transfer rate on ferrous iron oxidation by Thiobacillus ferrooxidans. *Enzyme and Microbial Technology*, 23(7):427–431, November 1998.

[201] A. Mazuelos, R. Romero, I. Palencia, F. Carranza, and F. J. Borjas. Oxygen transfer in ferric iron biological production in a packed-bed reactor. *Hydrometallurgy*, 65(1):15–22, July 2002.

[202] M. Gleisner, R. B. Herbert, and P. C. Frogner Kockum. Pyrite oxidation by Acidithiobacillus ferrooxidans at various concentrations of dissolved oxygen. *Chemical Geology*, 225(1):16–29, January 2006.

[203] A.-G. Guezennec, C. Joulian, J. Jacob, A. Archane, D. Ibarra, R. de Buyer, F. Bodénan, and P. d'Hugues. Influence of dissolved oxygen on the bioleaching

efficiency under oxygen enriched atmosphere. *Minerals Engineering*, 106:64–70, May 2017.

[204] J. P. Cárdenas, F. Moya, P. Covarrubias, A. Shmaryahu, G. Levicán, D. S. Holmes, and R. Quatrini. Comparative genomics of the oxidative stress response in bioleaching microorganisms. *Hydrometallurgy*, 127-128(Supplement C):162–167, October 2012.

[205] G. C. Jones, K. C. Corin, R. P. van Hille, and S. T. L. Harrison. The generation of toxic reactive oxygen species (ROS) from mechanically activated sulphide concentrates and its effect on thermophilic bioleaching. *Minerals Engineering*, 24(11):1198–1208, September 2011.

[206] J. Y. Witne and C. V. Phillips. Bioleaching of Ok Tedi copper concentrate in oxygen- and carbon dioxide-enriched air. *Minerals Engineering*, 14(1):25–48, January 2001.

[207] P. d'Hugues, C. Joulian, P. Spolaore, C. Michel, F. Garrido, and D. Morin. Continuous bioleaching of a pyrite concentrate in stirred reactors: Population dynamics and exopolysaccharide production vs. bioleaching performance. *Hydrometallurgy*, 94(1):34–41, November 2008.

[208] H. Wang, X. Zhang, M. Zhu, and W. Tan. Effects of dissolved oxygen and carbon dioxide under oxygen-rich conditions on the biooxidation process of refractory gold concentrate and the microbial community. *Minerals Engineering*, 80(Supplement C):37–44, September 2015.

[209] A.-G. Guezennec, C. Joulian, C. Delort, F. Bodénan, S. Hedrich, and P. D'hugues. CO2 mass transfer in bioleaching reactors: CO2 enrichment applied to a complex copper concentrate. *Hydrometallurgy*, 180:277–286, September 2018.

[210] P. d'Hugues, P. Cezac, T. Cabral, F. Battaglia, X. M. Truong-Meyer, and D. Morin. Bioleaching of a cobaltiferous pyrite: A continuous laboratory-scale study at high solids concentration. *Minerals Engineering*, 10(5):507–527, 1997.

[211] A. A. Kulkarni. Mass Transfer in Bubble Column Reactors: Effect of Bubble Size Distribution. *Industrial & Engineering Chemistry Research*, 46(7):2205–2211, March 2007.

[212] W. G. Whitman. The two-film theory of gas absorption. *Chem. Metall. Eng.*, 29:146–148, 1923.

[213] W. K. Lewis and W. G. Whitman. Principles of gas absorption. *Industrial & Engineering Chemistry*, 16(12):1215–1220, 1924.

[214] R. Higbie. The rate of absorption of a pure gas into a still liquid during short periods of exposure. *Trans. AIChE*, 31:365–389, 1935.

[215] M. Davoody, A. A. B. Abdul Raman, and R. Parthasarathy. Maximizing gas–liquid interfacial area in a three-phase stirred vessel operating at high solids concentrations. *Chemical Engineering and Processing: Process Intensification*, 104:133–147, June 2016.

[216] C. Zheng, Y. Huang, J. Guo, R. Cai, H. Zheng, C. Lin, and Q. Chen. Investigation of cleaner sulfide mineral oxidation technology: Simulation and evaluation of stirred bioreactors for gold-bioleaching process. *Journal of Cleaner Production*, 192:364–375, August 2018.

[217] H. L. Clever. Setchenov salt-effect parameter. *Journal of Chemical & Engineering Data*, 28(3):340–343, July 1983.

[218] A. Schumpe. The estimation of gas solubilities in salt solutions. *Chemical engineering science*, 48(1):153–158, 1993.

[219] M. Taghavi, R. Zadghaffari, J. Moghaddas, and Y. Moghaddas. Experimental and CFD investigation of power consumption in a dual Rushton turbine stirred tank. *Chemical Engineering Research and Design*, 89(3):280–290, March 2011.

[220] A. W. Nienow. Hydrodynamics of Stirred Bioreactors. *Applied Mechanics Reviews*, 51(1):3–32, January 1998.

[221] A. W. Nienow. Scale-Up, Stirred Tank Reactors. In *Encyclopedia of Industrial Biotechnology*, pages 1–38. American Cancer Society, 2010.

[222] Y. Rodríguez, A. Ballester, M. L. Blázquez, F. González, and J. A. Muñoz. Study of Bacterial Attachment During the Bioleaching of Pyrite, Chalcopyrite, and Sphalerite. *Geomicrobiology Journal*, 20(2):131–141, March 2003.

[223] L. Xia, X. Liu, J. Zeng, C. Yin, J. Gao, J. Liu, and G. Qiu. Mechanism of enhanced bioleaching efficiency of Acidithiobacillus ferrooxidans after adaptation with chalcopyrite. *Hydrometallurgy*, 92(3):95–101, June 2008.

[224] P. d'Hugues, S. Foucher, P. Gallé-Cavalloni, and D. Morin. Continuous bioleaching of chalcopyrite using a novel extremely thermophilic mixed culture. *International Journal of Mineral Processing*, 66(1):107–119, September 2002.

[225] A. Sissing and S. T. L. Harrison. Thermophilic mineral bioleaching performance: A compromise between maximizing mineral loading and maximizing microbial growth and activity. *Journal of the Southern African Institute of Mining and Metallurgy*, page 4, 2003.

[226] P. d'Hugues, C. Joulian, P. Spolaore, C. Michel, F. Garrido, and D. Morin. Continuous bioleaching of a pyrite concentrate in stirred reactors: Population dynamics and exopolysaccharide production vs. bioleaching performance. *Hydrometallurgy*, 94(1-4):34–41, November 2008.

[227] S. Raja. The effect of particulate-induced hydrodynamic stress on the bioleaching of chalcopyrite by a Sulfolobus sp. 2005.

[228] M. Nemati and S. T. L. Harrison. Effect of solid loading on thermophilic bioleaching of sulfide minerals. *Journal of Chemical Technology & Biotechnology*, 75(7):526–532, 2000.

[229] H.-J. Henzler. Particle Stress in Bioreactors. In K. Schügerl, G. Kretzmer, H. J. Henzler, P. M. Kieran, G. Kretzmer, P. E. MacLoughlin, D. M. Malone, W. Schumann, P. A. Shamlou, and S. S. Yim, editors, *Influence of Stress on Cell Growth*

and Product Formation, Advances in Biochemical Engineering/Biotechnology, pages 35–82. Springer, Berlin, Heidelberg, 2000.

[230] D. G. Thomas. Turbulent disruption of flocs in small particle size suspensions. *AIChE Journal*, 10(4):517–523, 1964.

[231] A. N. Kolmogorov, V. Levin, J. C. R. Hunt, O. M. Phillips, and D. Williams. The local structure of turbulence in incompressible viscous fluid for very large Reynolds numbers. *Proceedings of the Royal Society of London. Series A: Mathematical and Physical Sciences*, 434(1890):9–13, July 1991.

[232] A. N. Kolmogorov, V. Levin, J. C. R. Hunt, O. M. Phillips, and D. Williams. Dissipation of energy in the locally isotropic turbulence. *Proceedings of the Royal Society of London. Series A: Mathematical and Physical Sciences*, 434(1890):15–17, July 1991.

[233] A. W. Nienow. Reactor Engineering in Large Scale Animal Cell Culture. *Cytotechnology*, 50(1):9, June 2006.

[234] R. S. Cherry and E. T. Papoutsakis. Physical mechanisms of cell damage in microcarrier cell culture bioreactors. *Biotechnology and Bioengineering*, 32(8):1001–1014, 1988.

[235] M. S. Croughan, J.-F. Hamel, and D. I. C. Wang. Hydrodynamic effects on animal cells grown in microcarrier cultures. *Biotechnology and Bioengineering*, 67(6):841–852, 2000.

[236] A. W. Nienow. Scale-Up, Stirred Tank Reactors. In *Encyclopedia of Industrial Biotechnology*, pages 1–38. American Cancer Society, 2010.

[237] G. Montante, D. Pinelli, and F. Magelli. Scale-up criteria for the solids distribution in slurry reactors stirred with multiple impellers. *Chemical Engineering Science*, 58(23):5363–5372, December 2003.

[238] M. Zlokarnik. *Scale-up in Chemical Engineering*. John Wiley & Sons, August 2006.

[239] S. T. L. Harrison, A. Kotsiopoulos, R. Stevenson, and J. J. Cilliers. Mixing indices allow scale-up of stirred tank slurry reactor conditions for equivalent homogeneity. *Chemical Engineering Research and Design*, 153:865–874, January 2020.

[240] D. Wadnerkar, R. P. Utikar, M. O. Tade, and V. K. Pareek. CFD simulation of solid–liquid stirred tanks. *Advanced Powder Technology*, 23(4):445–453, July 2012.

[241] H. E. A. Van den Akker. The Details of Turbulent Mixing Process and their Simulation. In G. B. Marin, editor, *Advances in Chemical Engineering*, volume 31 of *Computational Fluid Dynamics*, pages 151–229. Academic Press, January 2006.

[242] D. McBride, J. Gebhardt, N. Croft, and M. Cross. Heap Leaching: Modelling and forecasting using CFD technology. *Minerals*, 8(1):9, 2018.

[243] S. M. Mousavi, A. Jafari, S. Chegini, and I. Turunen. CFD simulation of mass transfer and flow behaviour around a single particle in bioleaching process. *Pro-*

cess Biochemistry, 44(7):696–703, 2009.

[244] B. Metodiev, K. Lilova, D. Karamanev, and L. Lilov. Computational fluid dynamics (CFD) simulation of velocity and concentration profiles in the vicinity of immobilized Acidithiobacillus ferrooxidans cells. *Biochemical Engineering Journal*, 29(3):182–190, April 2006.

[245] T. Song, K. Jiang, J. Zhou, Z. Shen, and Y. Feng. CFD impeller speed evaluation of an industrial scale two-phase flow stirred tank. page 5, 2015.

[246] M. S. Shadloo, D. Le Touzé, and G. Oger. Smoothed particle hydrodynamics method for fluid flows, towards industrial applications-Motivations, current state, and challenges. June 2016.

[247] H. Van den Akker. Momentum Equations in Dispersed Two-Phase Flows. volume 3, pages 371–400. January 1986.

[248] J. Morchain, J.-C. Gabelle, and A. Cockx. A coupled population balance model and CFD approach for the simulation of mixing issues in lab-scale and industrial bioreactors. *AIChE Journal*, 60(1):27–40, 2014.

[249] D. Ramkrishna. *Population Balances: Theory and Applications to Particulate Systems in Engineering*. Academic Press, San Diego, CA, 2000.

[250] R. S. S. Raja Ehsan Shah, B. Sajjadi, A. A. Abdul Raman, and S. Ibrahim. Solid-liquid mixing analysis in stirred vessels. *Reviews in Chemical Engineering*, 31(2), January 2015.

[251] C. Haringa, H. J. Noorman, and R. F. Mudde. Lagrangian modeling of hydrodynamic–kinetic interactions in (bio)chemical reactors: Practical implementation and setup guidelines. *Chemical Engineering Science*, 157:159–168, January 2017.

[252] J. J. Heijnen. Impact of Thermodynamic Principles in Systems Biology. In C. Wittmann and R. Krull, editors, *Biosystems Engineering II: Linking Cellular Networks and Bioprocesses*, Advances in Biochemical Engineering / Biotechnology, pages 139–162. Springer, Berlin, Heidelberg, 2010.

[253] C. Haringa, W. Tang, A. T. Deshmukh, J. Xia, M. Reuss, J. J. Heijnen, R. F. Mudde, and H. J. Noorman. Euler-Lagrange computational fluid dynamics for (bio)reactor scale down: An analysis of organism lifelines. *Engineering in Life Sciences*, 16(7):652–663, 2016.

[254] G. Wang, C. Haringa, W. Tang, H. Noorman, J. Chu, Y. Zhuang, and S. Zhang. Coupled metabolic-hydrodynamic modeling enabling rational scale-up of industrial bioprocesses. *Biotechnology and Bioengineering*, 117(3):844–867, 2020.

[255] A. Delafosse, M.-L. Collignon, S. Calvo, F. Delvigne, M. Crine, P. Thonart, and D. Toye. CFD-based compartment model for description of mixing in bioreactors. *Chemical Engineering Science*, 106:76–85, March 2014.

[256] M. Reuss. Improvements for scalability of Lagrangian-Eulerian approaches for tracking lifelines of single cells in large bioreactors, March 2021.

[257] P. Vrábel, R. G. J. M. van der Lans, F. N. van der Schot, K. C. A. M. Luyben,

B. Xu, and S.-O. Enfors. CMA: Integration of fluid dynamics and microbial kinetics in modelling of large-scale fermentations. *Chemical Engineering Journal*, 84(3):463–474, December 2001.

[258] F. Bezzo and S. Macchietto. A general methodology for hybrid multizonal/CFD models: Part II. Automatic zoning. *Computers & Chemical Engineering*, 28(4):513–525, April 2004.

[259] E. K. Nauha, Z. Kálal, J. M. Ali, and V. Alopaeus. Compartmental modeling of large stirred tank bioreactors with high gas volume fractions. *Chemical Engineering Journal*, 334:2319–2334, February 2018.

[260] Y. Le Moullec, C. Gentric, O. Potier, and J. P. Leclerc. Comparison of systemic, compartmental and CFD modelling approaches: Application to the simulation of a biological reactor of wastewater treatment. *Chemical Engineering Science*, 65(1):343–350, January 2010.

Chapter 2

Characterization of bioleaching in STR through biotic and abiotic experimentations

Contents

2.1 Introduction

The aim of this chapter was to describe a laboratory-scale bioleaching STR through an extended experimental study. Literature studies indeed mainly focus on a limited number of parameters, such as kinetic or hydrodynamic parameters, which provides a partial description of the tank [1]. Due to this, it is difficult to model the various phenomena occurring during a bioleaching batch based on literature data alone. Furthermore, no studies offer a complete data set of a bioleaching STR. To fill this gap, it was proposed in this chapter to carry out a complete set of hydrodynamic and kinetic measurements on a defined common bioleaching system. This chapter is thus divided into two sections: bioleaching experiments dedicated to kinetics determination and abiotic experiments dedicated to hydrodynamics studies.

Bioleaching kinetics is represented by chemical mineral dissolution coupled with biological oxidations of elemental sulfur and ferrous iron. These phenomena are complementary and mutually dependent as the absence of one could limit or negate the other. Section 2.3 aims to describe these processes through the evolution of the main components along the time of the experiments. Furthermore, the microbial communities involved in the bioleaching mechanisms were characterized for the experimental conditions used and the respective distribution on the solid and in the liquid was determined for each microbe.

Abiotic phenomena should also be considered as the geometric design of the tank and the composition of the medium could affect the bioleaching efficiency. As seen in the previous chapter, hydromechanical stress may impact the process performance and it was often recommended to use the just-suspended speed to limit this stress [2]. Similarly, oxygen transfer rate is critical as dissolved oxygen is a limiting component for microorganism growth. The oxygen mass transfer coefficient has thus to be determined to evaluate the capacity of the system to dissolve oxygen. In section 2.4, the just-suspended agitation rate and oxygen mass transfer coefficient were determined and compared with data and models from the literature. Furthermore, this work proposed a new model for the representation of the just-suspended agitation rate under gassed conditions.

2.2 Material and methods

2.2.1 Sulfidic material source and characteristics

The sulfidic material used for this work consisted of flotation tailings particles from a European copper mine (Aïtik, Sweden). On site, the valuable chalcopyrite is concentrated by flotation after grinding of the ore. From the flotation step, two types of tailings are produced: low sulfide tailings and high sulfide tailings. The latter is mainly composed of pyrite and silicates and was selected to carry out this study. It does not hold any economic value but its bioleaching amenability was already proven and its mineralogical characteristics makes it a suitable material to establish kinetics model. The final particle size distribution was determined by a "Gilas-Alcatel" granulometer HR 850 and found to have a P80 of 59 µm on average. The complete granulometry of the sample is shown on Fig. 2.1.

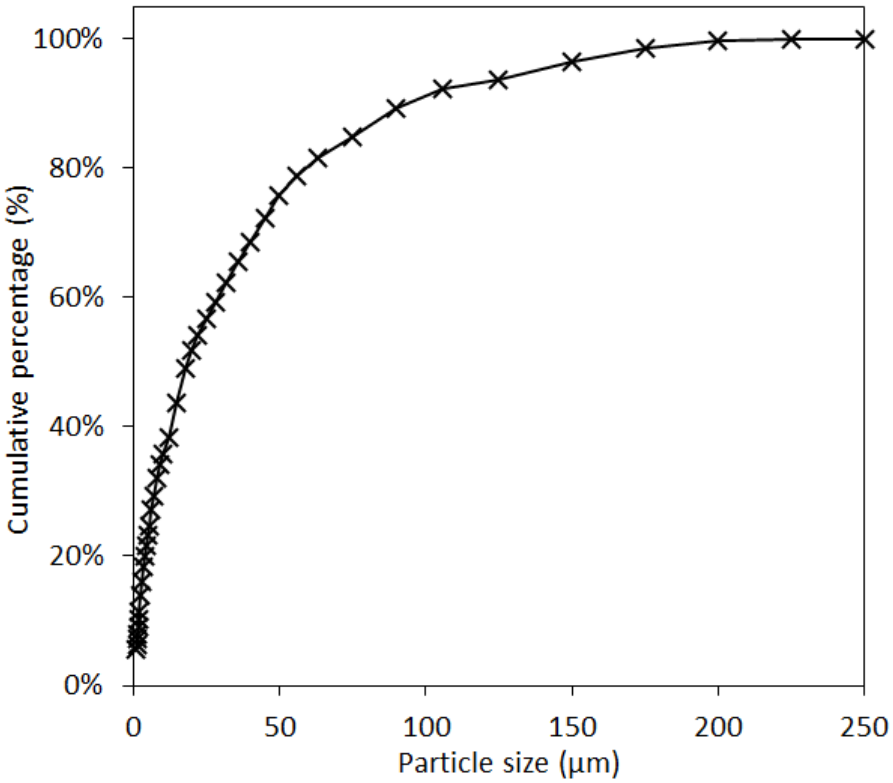

Figure 2.1: Size distribution of the flotation tailings sample used for the experiments.

Analytical determination of the chemical composition of the tailings particle was performed and the results are shown on Table 2.1. S_0 and SO^4_{2-} concentrations were determined by gravimetry and total S by combustion. Co and Cu concentrations were obtained through triacid leaching (HNO_3 – $HClO_4$ – HF) followed by inductively coupled plasma mass spectrometry (ICP-MS) using a Thermo Scientific XSERIES 2. Lastly, concentrations of CaO, FeO, K_2O, MgO, P_2O_5 and SiO_2 were found using X-Ray Fluorescence (XRF) using a Malvern Panalytical Zetium.

Table 2.1: Composition of the sulfidic material used for the experiments.

Component	Concentration	Unit
SO_4^{2-}	2.66	% w/w
S_0	0.34	% w/w
S	32.4	% w/w
Co	586	$mg\,kg^{-1}$
Cu	951	$mg\,kg^{-1}$
FeO	37.8	% w/w
CaO	1.47	% w/w
SiO_2	23.6	% w/w
K_2O	1.47	% w/w
MgO	0.58	% w/w
P_2O_5	0.11	% w/w

The tailings material was mainly comprised of pyrite minerals, while the remaining part corresponded to the gangue, composed of silicate minerals. Pyrite concentration was estimated from the total iron and sulfur concentrations where both components were considered to be only part of pyrite minerals. This concentration was found to be 63.1% w/w using total iron and 60.6% w/w using total sulfur. The lower value, namely from total sulfur, was kept as the limiting component that could be part of pyrite.

2.2.2 Microorganisms and culture conditions

The BRGM-KCC microbial consortium was used to inoculate the bioreactors. It included *Leptospirillum*, *Acidithiobacillus* and *Sulfobacillus* species which are the main and predominant bacteria that can be found in industrial bioleaching STR, due to their efficiency in the process [3, 4]. The culture originated from BRGM stock culture which is continually kept in a shaking incubator at 40 °C and 100 rpm. It was subcultured several times from 150 ml Erlenmeyer flask up to 2-litre stirred tank reactor according to the adaptation protocol used by Hedrich et al. (2016), which aimed at progressively adapting the microorganisms to the mineral used (which is different from the stock culture) and to higher solid concentrations [5]. The different steps are showed on Fig. 2.2. The first set was done in 150 ml Erlenmeyer flasks where the initial stock culture was subcultured three times, in duplicate, at a solid concentration of 3% w/w and an inoculum of 10% v/v, taken from the previous culture. The same experimental conditions were used for the cultures: 40 °C, 100 rpm on a shaking incubator and a culture time between 5 to 7 days depending on the kinetics, as the culture was stopped at the end of the exponential growth phase and subcultured. The second series of cultures was performed in a 2-liter batch STR at 42 °C to approach the optimal temperature conditions of the consortium. The first test, named MDX1, was performed at 4.8% w/w solid concentration using the last cultures in shake flasks as inoculum. It was followed by 2 successive subcultures performed at a solid concentration of 9.2% w/w (MDX2

and MDX3). The last culture, MDX3, was the base of all experiments as few to no evolution of the kinetics and yields were observed, showing that the culture had reached its maximum efficiency and could be used for a kinetic study. MDX3 was successively subcultured 5 times in duplicate, from MDX4 to MDX8, using similar experimental conditions described in the following subsection.

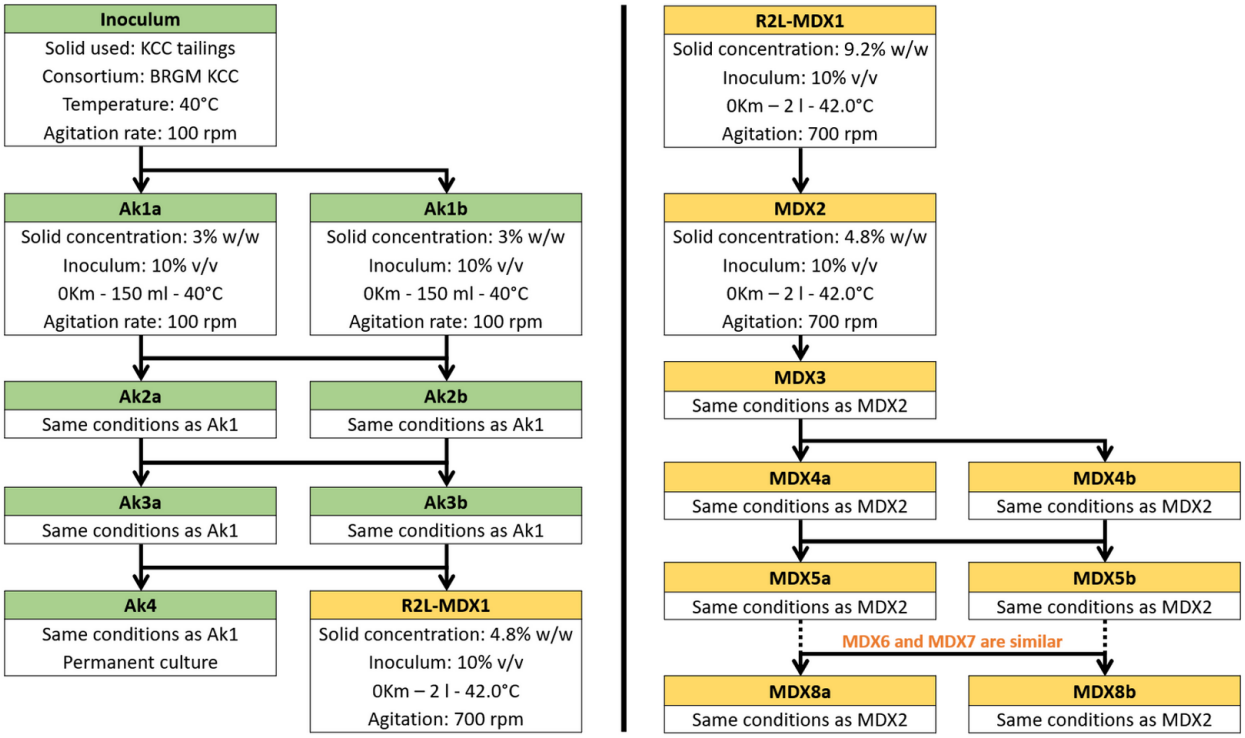

Figure 2.2: Summary of the bioleaching experiments in Erlenmeyer flasks (left) and stirred tank reactors (right).

The nutrient medium used was 0Km medium, which is adapted for bacterial growth on cobaltiferous pyrites. It is a modification of the standard 9K medium as it contains no iron and the basal salts composition was slightly modified. It contained $(NH_4)_2SO_4$, 3.70 $g\,l^{-1}$, H_3PO_4 85% w/w, 0.80 $g\,l^{-1}$, $MgSO_4 \cdot 7\,H_2O$, 0.52 $g\,l^{-1}$ and KOH, 0.48 $g\,l^{-1}$.

2.2.3 Experimental setup and procedures

All experiments were done using the standard BRGM laboratory-scale bioreactor, a glass tank (Fig. 2.3) with a working volume of 2 l, a diameter $T = 0.12$ m, liquid height $H = 0.187$ m and a flat bottom. The tank was equipped with four conical baffles of width equal to $T/10$, placed symmetrically. Reactors temperature was maintained at a constant value of 42 °C using a refrigerated/heated circulation of water and thermocouples placed in the tank. Water losses from the tank were prevented using a water cooled condenser placed at the top of the tank. Considering the height on tank diameter ratio ($H/T = 1.56$), the choice of a multi-stage design is recommended to provide sufficient liquid mixing near the surface. For this, a dual impeller config-

uration was chosen using a bottom 6-bladed Rushton turbine (RT6B ; diameter D = 0.05 m) providing a radial flow which allows an efficient gas and solid dispersion. The top Lightnin A310 impeller operated in up-pumping mode (A310 ; diameter = 0.06 m) which combined with the radial flow of the bottom RT6B and assisted stirring of the tank. The RT6B was placed with an off-bottom clearance $C = D$ above the gas sparger and a spacing equal to 0.06 m was chosen between the RT6B and the A310 impeller.

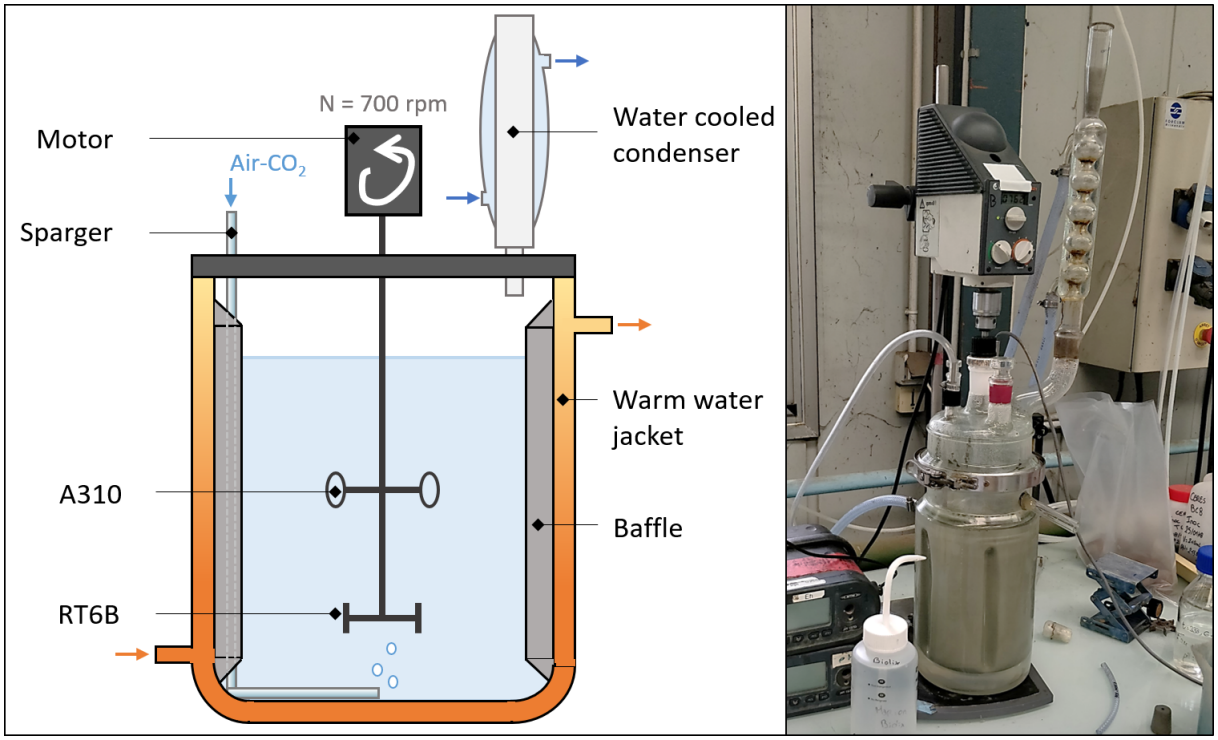

Figure 2.3: Two-stage stirred tank reactor used for the bioleaching experiments with: (left) schematic representation and (right) photography of the tank.

10 tests were performed consisting of 5 successive duplicates sharing the same experimental conditions. The initial solution was comprised of 1.8 l culture medium and 200 g of a quartered sample of the previously described sulfidic material (9.2% weight of solid per weight of pulp). Inoculations were performed at 10% v/v approximately by adding 0.2 l taken from the previous culture to 1.8 l of 0Km medium, as described previously. The agitation rate was set to 700 rpm, allowing full turbulent conditions within the medium ($Re = 5 \times 10^4$). CO_2 enriched air (1% CO_2 v/v) was provided at a rate of 0.5 $\mathrm{l\,min^{-1}}$ using a cylindrical non-porous sparger (diameter = 0.005 m), in order to provide CO_2 for the biomass growth and O_2 for the oxidation of ferrous iron and sulfur species [6]. The pH was adjusted daily to ensure a value between 1.2 and 1.4 by using either a 1 $\mathrm{mol\,l^{-1}}$ H_2SO_4 solution or a 1 $\mathrm{mol\,l^{-1}}$ NaOH solution. The water level was also maintained daily by adding distilled water to the tank.

2.2.4 Analysis techniques

The purpose of these experiments was to obtain a complete set of data to feed different models of a bioleaching STR. This was ensured by doing this set of analysis:

- *Physicochemical parameters:* pH, electrochemical potential and temperature,
- *Dissolved metals:* iron, cobalt and copper,
- *Solid fractions:* metal content, sulfur and carbon speciation,
- *Gas analysis:* in and out O_2 / CO_2 gas flows, and dissolved O_2,
- *Biological parameters:* cell counting and strain identification.

Daily monitoring

The daily monitoring consisted of basic measurements to ensure a robust operation of the tank, namely pH, electrochemical potential and temperature. The electrochemical potential was measured using a mixed electrode consisting of a platinum electrode and a Ag/AgCl/KCl ($3\,\mathrm{mol\,l^{-1}}$) reference electrode, which was then normalized to the standard hydrogen electrode (SHE) using the temperature value. Using the electrochemical potential, the Fe^{2+}/Fe^{3+} ratio was calculated from the empirical correlation of Yue et al. (2014) , as shown in Eq. 2.1 [7]. This method is based on the electrochemical potential, ferrous and ferric iron in the solution.

$$E = -10^{-3} \cdot \theta^2 + 0.91 \cdot \theta + 2.303 \cdot 10^3 \cdot \frac{R\theta}{nF} \cdot \log \frac{\left[Fe^{3+}\right]}{\left[Fe^{2+}\right]} + 492 \tag{2.1}$$

With E (V) the normalized electrochemical potential, θ the temperature (here in K), n (= 2) the number of electrons involved in the Nernst equation of the Fe^{2+}/Fe^{3+} couple, and F (= 96485 $\mathrm{C\,mol^{-1}}$) the Faraday's constant.

The concentrations of O_2 and CO_2 in the gas phase were determined at the gas inlet and outlet using a multi-gas analyzer ADC MGA 3000 (Analytical Development Company Ltd). Also, dissolved oxygen concentration $[O_2]$ ($\mathrm{mg\,l^{-1}}$) was measured using a polarographic probe. Using these data and mass balance on oxygen and nitrogen, the oxygen uptake rate (OUR) ($\mathrm{mg\,l^{-1}}$) and oxygen transfer rate (OTR) ($\mathrm{mg\,l^{-1}}$) were calculated:

$$\mathrm{OTR} = \mathrm{OUR} + \frac{\mathrm{d}\left[O_2\right]}{\mathrm{d}t} = \frac{Q_{\mathrm{in},O_2} - Q_{\mathrm{out},O_2}}{V} \tag{2.2}$$

With Q_{O_2} ($\mathrm{mg\,h^{-1}}$) the oxygen gas flow rate, where the subscripts "in" and "out" respectively represent the inlet and outlet, and V (l) the liquid phase volume.

The variation of dissolved oxygen concentration ($\mathrm{d}\left[O_2\right]/\mathrm{d}t$) in Eq. 2.2 was considered negligible in front of the OUR at all time. This is true at steady-state because the gas flow content in the inlet and outlet was stabilized, meaning that the dissolved oxygen concentration remained constant, hence $\mathrm{d}\left[O_2\right]/\mathrm{d}t = 0$. However, $\mathrm{d}\left[O_2\right]/\mathrm{d}t \neq 0$ for the remaining of the experiment, but due to the high oxygen demand of the bioleaching oxidations, the OUR was several order of magnitude higher than the variation of dissolved oxygen ($\mathrm{d}\left[O_2\right]/\mathrm{d}t$) in the tank. With these assumptions, we can consider OTR = OUR at any time. Furthermore, the inlet and outlet gas flow rate can be determined using the gas partial pressure, obtained from the gas analyzer, as shown by the following equations:

$$Q_{\mathrm{in},O_2} = Q_{\mathrm{in}} \cdot P_{O_2,\mathrm{in}} \tag{2.3}$$

$$Q_{\mathrm{out},O_2} = Q_{\mathrm{out}} \cdot P_{O_2,\mathrm{out}} \tag{2.4}$$

With Q the gas flow rate, and P_{O_2} (Pa) the O_2 partial pressure.

Additionally, Q_{out} may be simplified considering that nitrogen concentration does not change between the inlet and outlet, leading to $Q_{\mathrm{in},N_2} = Q_{\mathrm{out},N_2}$. Eq. 2.2 can then be rewritten into the following equation:

$$\mathrm{OTR} = \mathrm{OUR} = \frac{Q_{\mathrm{in}}}{V} \cdot \left(P_{O_2,\mathrm{in}} - P_{O_2,\mathrm{out}} \cdot \frac{P_{N_2,\mathrm{in}}}{P_{N_2,\mathrm{out}}} \right) \tag{2.5}$$

Using similar considerations, the carbon uptake rate (CUR) can also be calculated by the following expression:

$$\mathrm{CUR} = \frac{Q_{\mathrm{in}}}{V} \cdot \left(P_{CO_2,\mathrm{in}} - P_{CO_2,\mathrm{out}} \cdot \frac{P_{N_2,\mathrm{in}}}{P_{N_2,\mathrm{out}}} \right) \tag{2.6}$$

With P_{CO_2} (Pa) the CO_2 partial pressure.

Metal content was measured via atomic absorption spectrometry using a VARIAN SpectrAA 220FS spectrometer. For the daily measurement, only the main metals of the medium were considered, namely iron, cobalt and copper. The sample consisted of 5 ml of medium filtered at 0.45 µm and stabilized using 1% w/w nitric acid. The concentration of metal was then obtained by atomization of the sample under adapted hollow cathode lamps (Fe, Co and Cu absorption wavelengths).

Lastly, planktonic cells density was obtained using a Thoma cell counting chamber. For this, a 2 ml unfiltered sample was taken from the medium. The sample was then diluted (1:20 to 1:200 depending on the leaching stage) and dropped on a Thoma cell before counting. The procedure was reproduced thrice, and the mean value of the measurements was used.

Microbial community characterization

The microbial diversity was characterized by DNA sequencing of the consortium used in the experiments. Moreover, the evolution and distribution of the microbial strains on the solid and in the liquid were monitored by characterizing the biomass in the liquid phase, on the solid phase and in the whole pulp. For this, two homogeneous pulp samples of 2 ml each were taken daily. In one of the samples, a decantation was performed by letting it stand for 15 minutes before collecting the supernatant. The two resulting samples (referred to as liquid and solid samples) were then filled to 2 ml using distilled water. The three samples obtained (solid, liquid and pulp) were washed in Tris buffer (100 mM, pH = 8) to neutralize the acidity. The washing was done by centrifuging the samples at 14000 g for 10 minutes then re-suspended in Tris buffer. This protocol was repeated 3 times until a pH around 7 was reached. DNA were extracted from the samples using the MP Biomedicals FastDNA SPIN Kit for Soil and the associated protocol. These extractions were validated by PCR (Polymerase Chain Reaction) amplification using the universal reverse primer w34 (5'-TTACCGCGGCTGCTGGCAC-3') labelled with FAM and the cubacterial forward primer w49 (5'-ACGGTCCAGACTCCTACGGG-3'). Amplification was done in a C-1000 BioRad thermocycler and then analyzed by gel electrophoresis on agarose followed by fluorescent revealing using ethidium bromide. Specific PCR were carried out to detect the presence of the main BRGM-KCC consortium bacteria: *Leptospirillum ferriphilum* (primers Lpf392F and Lpf556R), *Acidithiobacillus caldus* (primers AcaldusP1 and NRR2), *Sulfobacillus benefaciens* (primers Sb96F and Sb355R) and *Sulfobacillus thermosulfidooxidans* (primers StFwd and StRev). Moreover, a cloning and sequencing were performed to specify the bacterial strain, this was done using the TOPO TA Cloning Kits for Sequencing and the associated protocol. DNA sequences were analyzed and their phylogeny was observed by comparing the sequences to the BRGM sequence database. For validation purposes, SSCP (Single Strand Conformation Polymorphism) were performed on the clones. This was done by diluting 5 to 200-fold the PCR products of the clones, mixing 1 µl of the product with 0.4 µl of GeneScan 600 LIZ dye size standard and 18.6 µl of Applied Biosystems Hi-Di formamide, and heat-denaturing the product for 5 minutes at 95 °C. Lastly, the product was analyzed by the Applied Biosystems ABI Prism 310 Genetic Analyzer and the provided software.

The quantification of the different strains was performed by quantitative real-time polymerase chain reaction (qPCR) using the assays developed by Hedrich et al. (2016) due to their performances for targeting the KCC consortium species [5]. For this, the SYBR Green PCR master mix from Applied Biosystems was used with the previously mentioned specific primers. The reaction was performed in a C-1000 BioRad thermocycler for amplification of the 16S rRNA of each species. The results relating the abundance of each species was given in gene copy number per ml (for liquid and pulp) or per mg (for solid).

Solid analysis and mass balances

Mass balance was verified through complete analysis of major elements of the solid and liquid at the end of each test. For this, the full final pulp was filtered through Whatman filter paper (2.7 µm) and the remaining cake was washed using 20 ml of acidified water (pH 1.6), prepared using nitric acid. The resulting liquid was weighted and the solid was dried and weighted before being used for analysis.

Dissolved metals (Fe, Co, Cu, Mg and K) were analyzed by a Thermo Scientific XSERIES 2 ICP-MS (Inductively coupled plasma mass spectrometry) using the NF EN ISO 17294-2 standard on filtered (0.45 µm) and stabilized samples (1% w/w nitric acid). The medium nutrients were also measured: NH_4^+ and PO_4^{3-} were determined by colorimetry assays (NF ISO 15923-1 standard), and SO_4^{2-} by ICP (NF EN ISO 11885). Total organic carbon was obtained by heat-activated persulfate oxidation.

Additionally, daily samples from two of the batch experiments were analyzed to obtain the kinetics of sulfate, total sulfur, inorganic and organic carbon using the aforementioned methods.

2.2.5 Methods for abiotic characterization of the bioreactor

Additionally to the bioleaching experiments, two abiotic parameters were measured, the just-suspended speed and the oxygen mass transfer coefficient.

Measurement of the just-suspended agitation rate N_{js}

The just-suspended agitation rate N_{js} was measured according to Zwietering definition and procedure that defines N_{js} as the minimal agitation rate ensuring the suspension of all solid particles [8]. For this, a mirror was placed below the vessel to allow a visual determination of the particle settling. For each experimental condition, the just-suspended speed was determined with two measurements. Firstly, all particles were settled, followed by a slow increase of the agitation rate until N_{js} was reached, represented by the cyclical movement of the particles at the bottom of the vessel. Then,

all particles were suspended followed by a slow decrease of the agitation rate until N_{js} was reached. The just-suspended agitation rate was then obtained using the mean of the two measurements. It was observed that both measurements had, at most, a 10 rpm difference, which was negligible.

These experiments were performed using the same solid used for the bioleaching experiments. The particle size distribution is shown on Fig. 2.1. In preparation for these tests, this solid was divided into size classes using sieves of varying frames. This led to 5 size classes: $\leq$ 20 µm ; 20-40 µm ; 40-100 µm ; 100-200µm ; $\geq$ 200 µm.

Approximately 120 conditions were studied using the following parameters:

- **Particle size categories:**, obtained from the sieving of the sulfidic material used for the bioleaching experiments: $\leq$ 20 µm ; 20-40 µm ; 40-100 µm ; 100-200µm ; $\geq$ 200 µm,
- **Solid concentration:** 4.8% (w/w) ; 9.2% (w/w) ; 13.1% (w/w) ; 16.8% (w/w),
- **Impeller configuration:** double RT6B (referred to as DR) ; RT6B + A310 (referred to as RH),
- **Aeration rate:** $0\,\mathrm{l\,h^{-1}}$; $30\,\mathrm{l\,h^{-1}}$; $60\,\mathrm{l\,h^{-1}}$.

The results were then used to determine the dimensionless parameters S of the Zwietering correlation (Eq. 2.7).

$$N_{\mathrm{js}} = S \cdot \nu_{\mathrm{l}}^{0.1} \cdot \left[\frac{g\,(\rho_{\mathrm{s}} - \rho_{\mathrm{l}})}{\rho_{\mathrm{l}}}\right]^{0.45} \cdot W_{\mathrm{s}}^{0.13} \cdot d_{\mathrm{p}}^{0.2} \cdot D^{-0.85} \tag{2.7}$$

with ν_{l} ($\mathrm{m^2\,s^{-1}}$) the liquid kinematic viscosity, W_{s} ($-$) the solid-liquid mass ratio, d_{p} (m) the particle diameter, D (m) the bottom impeller diameter and S ($-$) a function of different geometrical ratios and position of the tank and impeller. The solid-liquid mass ratio W_{s} was used for the calculations in weight of solid per weight of liquid. However, for clarity purposes of the chapter, the values were presented in weight of solid per weight of pulp. The particle diameter d_{p} was taken as the mean particle diameter of any particle size category, based on the granulometry of the initial sample. Although the selected averaging method will influence the final value of the correlation, this choice was decided by convention for these experiments and will have a negligible effect on the final values. The exponents on the different variables are parameters that have been determined experimentally by Zwietering.

The Zwietering model does not account for the presence of gas, which led to the establishment of a gaseous just-suspended speed, N_{jsg}. For this, two models were used where gas parameters such as the aeration rate were added to the ungassed N_{js}. The first model, named $N_{\mathrm{jsg,add}}$, was used and validated by previous literature studies and was represented by a linear increase of $N_{\mathrm{jsg,add}}$ with the gas flow rate, as shown by Eq. 2.8 [9–11].

$$N_{\mathrm{jsg,add}} = N_{\mathrm{js}} + a_{\mathrm{add}} \cdot Q_{\mathrm{g,vvm}} \tag{2.8}$$

where a_{add} (min^{-1}) is a constant and $Q_{\mathrm{g,vvm}}$ (vvm) the air flow rate.

However, this model is not dimensionless due to the presence of a time-dependent constant. Thus, this may impact its robustness during a scale-up strategy or when sensible modifications of bioreactor design are made. For this, the present work developed a second model, provided by $N_{\mathrm{jsg,na}}$, which depends on the aeration number N_A, as shown by Eq. 2.9.

$$\frac{N_{\mathrm{jsg,na}}}{N_{\mathrm{js}}} = 1 + A \cdot N_A^{\alpha} \tag{2.9}$$

Where A $(-)$ and α $(-)$ are dimensionless parameters. The aeration number $N_A = Q_{\mathrm{g}} / (N \cdot d^3)$ represents the ratio between the gas flow rate and the liquid flow rate generated by the impeller. In the turbulent regime, the flow number $N_Q = Q_{\mathrm{p}} / (N \cdot d^3)$ is indeed constant. Thus, $N_A = N_Q \cdot Q_{\mathrm{g}} / Q_p$. The aeration number has been proved to clearly correlate the power loss of impellers due to aeration (especially impeller flooding effects) ; this loss may negatively impact particle suspension.

Characterization of the oxygen mass transfer coefficient $k_{\mathrm{l}}a$

The overall oxygen mass transfer coefficient $k_{\mathrm{l}}a$ was determined through the static gassing-out method. The dissolved oxygen concentration was obtained by a polarographic probe linked to an acquisition unit. All measurements were done in a 0Km medium of the same composition as the one used for the bioleaching experiments. The experiment was initialized by flushing nitrogen in the tank until the oxygen concentration reached a value near zero. After setting the desired experimental conditions, gassing of air was performed and dissolved oxygen concentration was measured every second until saturation. The $k_{\mathrm{l}}a$ (h^{-1}) was determined by the following equation:

$$\frac{d\left[\mathrm{O_2}\right]}{dt} = k_{\mathrm{l}}a \cdot \left(\left[\mathrm{O_2}\right]^* - \left[\mathrm{O_2}\right]\right) \tag{2.10}$$

With $[\mathrm{O_2}]$ ($\mathrm{mg\,l}^{-1}$) the dissolved oxygen concentration and $[\mathrm{O_2}]^*$ ($\mathrm{mg\,l}^{-1}$) the saturated dissolved oxygen concentration.

The previous equation was integrated, as shown by Eq. 2.11, and the k_la was calculated as the slope of the function $-ln\left([O_2]^* - [O_2]\right) = f(t)$.

$$-ln\left([O_2]^* - [O_2]\right) = k_la \cdot t \tag{2.11}$$

The experiments were done in triplicate and two different probes were used to ensure the validity of the results. In total, 72 conditions were studied:

- **Solid concentration:** 0% (w/w) ; 4.8% (w/w) ; 9.2% (w/w) using the sulfidic material described previously,
- **Impeller configuration:** double RT6B (refered as DR) ; RT6B + A310 (refered as RH),
- **Agitation rate:** 300 rpm ; 500 rpm ; 700 rpm,
- **Gas flow rate:** $30\,l\,h^{-1}$; $60\,l\,h^{-1}$; $90\,l\,h^{-1}$; $111.3\,l\,h^{-1}$.

2.3 Bioleaching experiments results

2.3.1 Bioleaching kinetics

The bioleaching kinetics were expected to be similar for the 10 batch experiments and, as such, were represented by their mean and standard deviation. The material used contained predominantly cobaltiferous pyrite. As part of the main component, cobalt was used as a marker of pyrite dissolution and the dissolution was estimated from the dissolved cobalt concentration.

Fig. 2.4 shows the pyrite dissolution over time, it includes the instantaneous pyrite dissolution rate and the change in dissolved Co concentration. The instantaneous pyrite dissolution rate corresponds to the rate of pyrite dissolution between two measurements, calculated from the amount of dissolved cobalt divided by the total available cobalt in the sulphidic material. Kinetics was represented by a two-phase process: (i) settling phase with a low, increasing rate of pyrite dissolution, lasting for approximately 4 days and (ii) plateau with constant pyrite dissolution which ended with the depletion of pyrite.

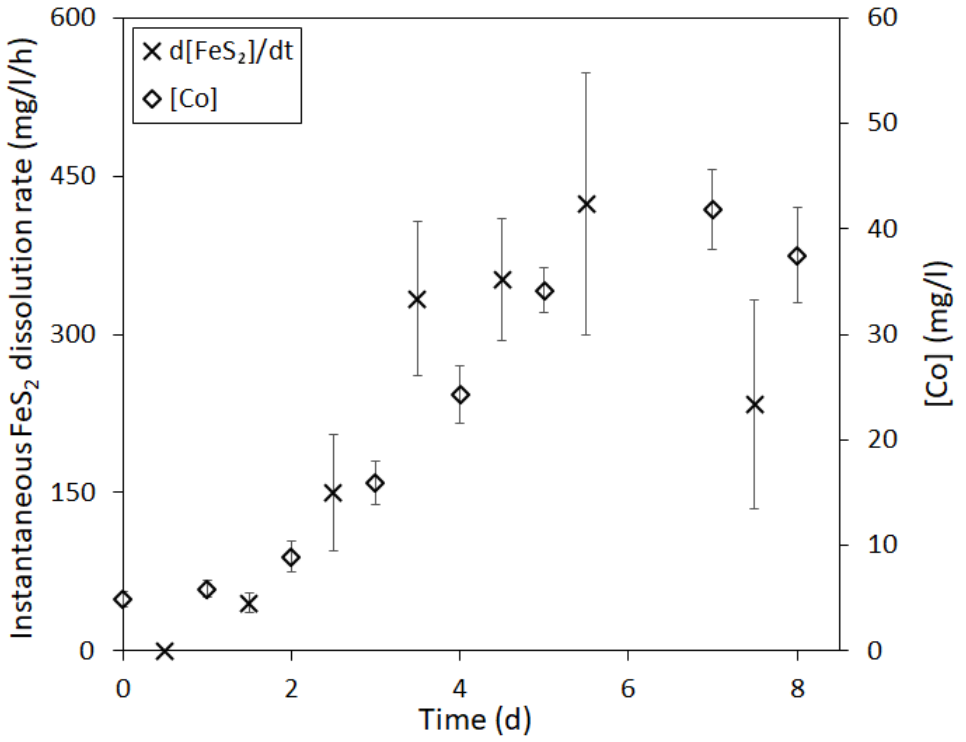

Figure 2.4: Instantaneous pyrite dissolution rate and cobalt concentration over time.

In parallel with the dissolution of pyrite, the evolution of the bacterial population was observed through the increase in biomass concentration (Fig. 2.5) and bacterial activity. Bacterial activity is characterized differently depending on the strain type considered. On one hand, iron-oxidizing bacteria activity is represented by the evolution of the $\left[Fe^{3+}\right] / \left[Fe^{2+}\right]$ ratio (Fig. 2.5) and by the increase of electrochemical potential, as shown on Fig. 2.6. On the other hand, sulfur-oxidizing bacteria activity is translated into a pH decrease, as shown by Fig. 2.6. For the first day, the bacterial activity was low because of the low biomass concentration. Moreover, ferric iron consumption by the chemical oxidation of pyrite was faster than its regeneration by iron-oxidizing bacteria, as represented by the low $\left[Fe^{3+}\right] / \left[Fe^{2+}\right]$ ratio. This was quickly followed by an exponential growth of the microorganisms lasting for 3 to 4 days and represented by a high bacterial activity. The rise of electrochemical potential, from 750 mV to nearly 900 mV, translated the iron-oxidizing bacteria activity because of the increasing ferric iron regeneration. This was also marked by a rapid increase of the $\left[Fe^{3+}\right] / \left[Fe^{2+}\right]$ ratio, up to 2200. Also, the oxidation of reduced sulfur species into H_2SO_4 by the sulfur-oxidizing bacteria was represented by a quick diminution of the pH, down to 1.1. Both bacterial activities were connected to the growing dissolution rate of the sulphidic material, which released both Fe^{2+} and S^0 into the medium. Moreover, this dissolution was, in return, emphasized by the bacterial activity which provided the regeneration of the substrate, Fe^{3+}, and low pH conditions which minimized the precipitation phenomena. After the exponential growth phase, a plateau of the bacterial population was observed, likely due to the diminution of available substrates such as Fe^{2+} and S^0.

At this point, around the fifth day, the maximum instantaneous pyrite dissolution rate was calculated at 434±75 $mg\,l^{-1}\,h^{-1}$. Thus, the maximal formation rate of Fe^{2+} and S^0 was also attained at this moment.

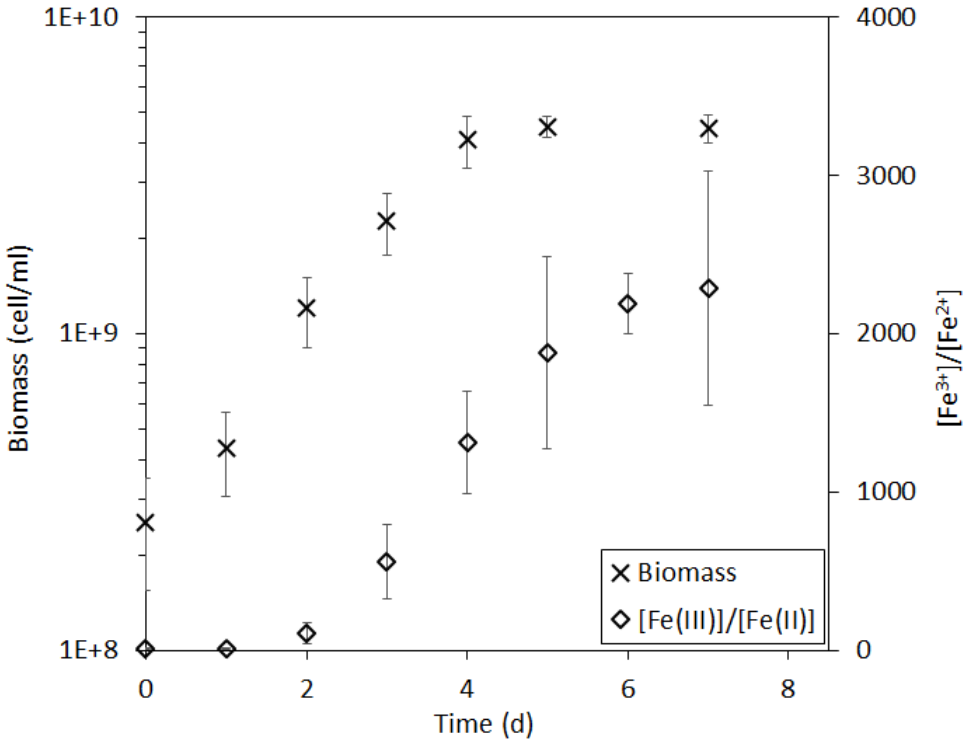

Figure 2.5: Biomass concentration and ferric to ferrous iron ratio over time.

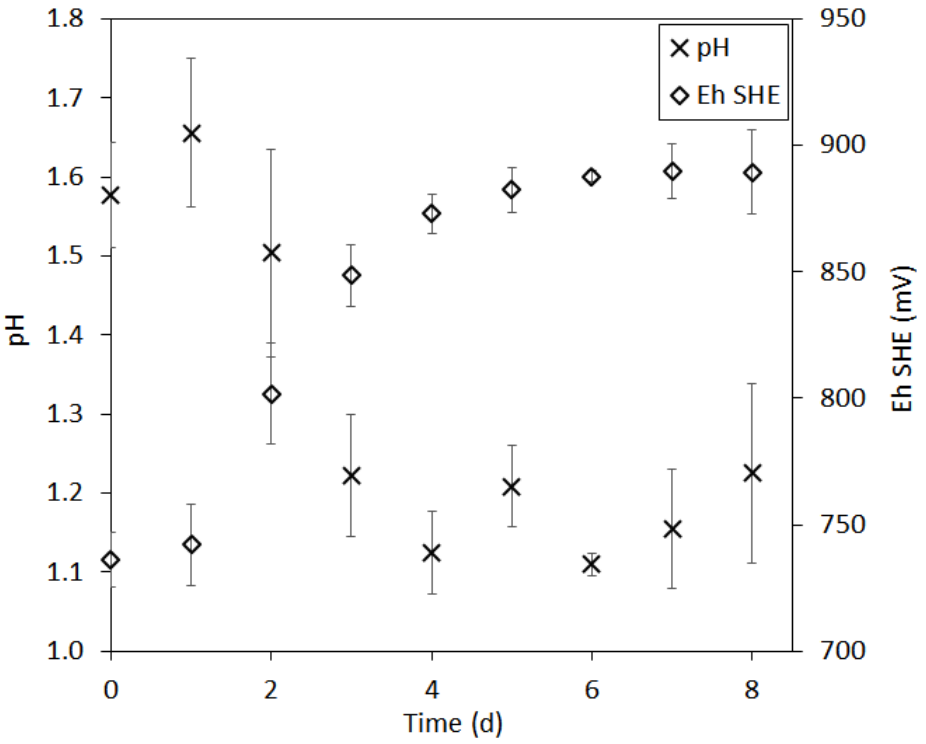

Figure 2.6: pH and electrochemical potential change over time.

As cobalt is embedded in the sulfidic material, the liberation of cobalt is related to the dissolution of pyrite. The extent of pyrite dissolution at the end of each batch can be extrapolated from the quantity of dissolved cobalt, which was closed to 74% of total cobalt after 8 days. The complete dissolution was avoided to maintain the state of exponential growth of the biomass for the following culture. However, one of the experiment, which was maintained for 13 days, showed a dissolution closed to 99% of total pyrite material. As a main component of pyrite, iron concentration was also looked for and demonstrated a similar evolution as cobalt concentration, as shown by Fig. 2.7. However, while a liberation of 74% of total cobalt was observed, only 54% of the iron, previously contained in the sulphidic material, was detected within the media. This difference can be attributed to the precipitation of jarosite, which is expected at the pH and temperature used for this experiment [12].

Copper dissolution occurred at the very beginning of the tests but remained low compared to cobalt dissolution, as shown by Fig. 2.7, probably because of the recalcitrance of chalcopyrite to leaching in atmospheric conditions [13].

A study of the sulfur species present in the medium was also carried out by measuring total sulfur and sulfates in the liquid phase. The results are shown in Fig. 2.8. As expected, the total sulfur showed a similar trend to that of the iron. However, it was expected that most of the sulfur in the medium would be present as sulfate as the most oxidized species. The results showed that, after the second day, a growing part of the sulfur species was not obtained in the form of sulfate, with a difference between total sulfur and sulphate up to 45% at the end of the experiment. Further analysis of the different forms of sulfur would have been necessary to identify the missing elements. This study was also used to validated the previous assumption that the difference in dissolved iron observed could be attributed to the precipitation of jarosite. For this, the evolution of cobalt concentration was compared to the total sulfur present in the medium. The results showed that at the end of the experiment, 68% of the total sulfur contained in the pyrite was found in the medium, which concurred with the dissolved cobalt concentration.

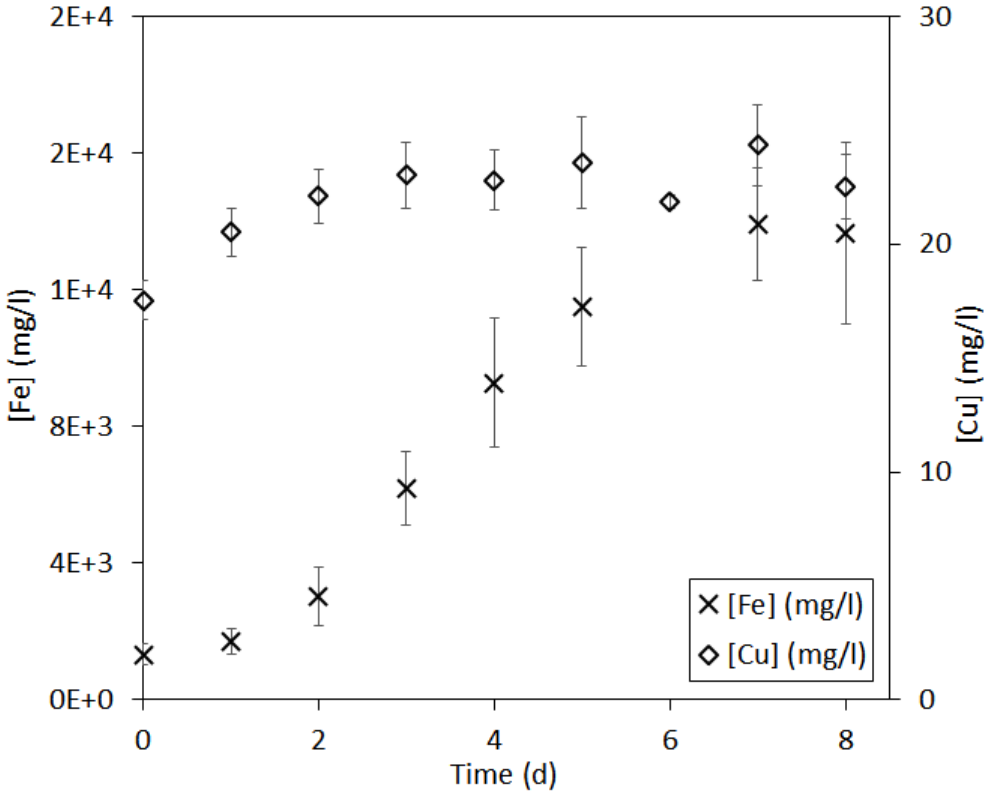

Figure 2.7: Dissolved iron and copper concentration over time.

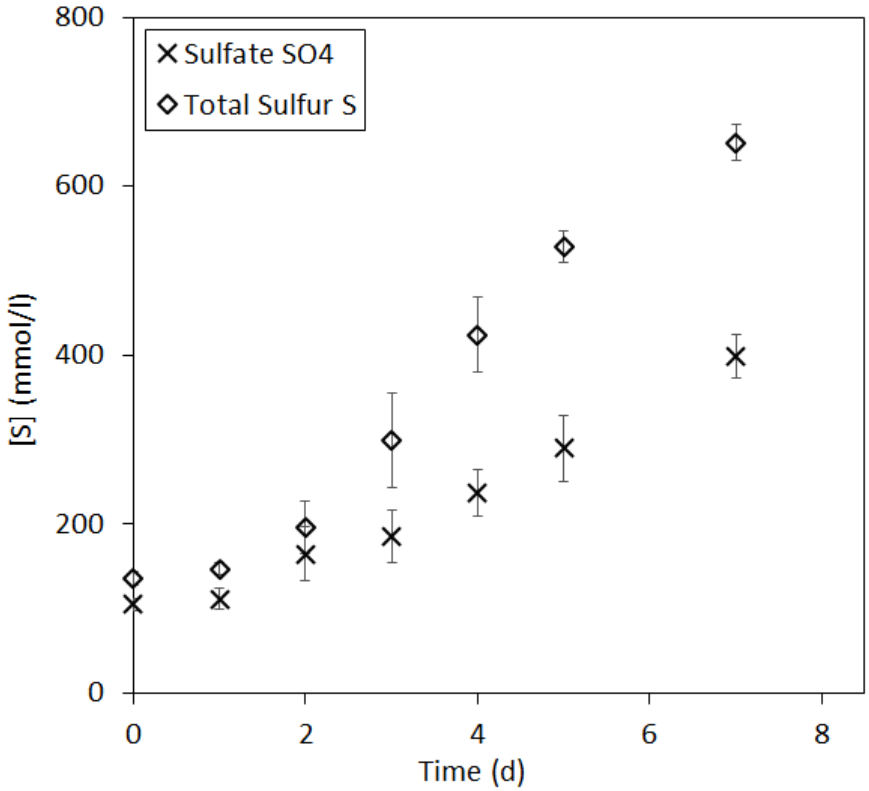

Figure 2.8: Variation of sulfate and total sulfur over time.

Gas analysis were also performed along the experiments and used to determine their uptake rate. The OUR was determined and reported on Fig. 2.9. OUR evolution was characterized by a two-phase process, similar to the sulfidic material instantaneous dissolution rate : (i) low and increasing uptake rate phase, lasting for 4 to 5 days and (ii) decreasing uptake rate phase until the end of the experiment. The trend of the first phase is similar to the sulfidic material dissolution rate due to the oxygen demand for the various oxidation reactions. As shown on a previous study by Guezennec et al. (2017) using the stoechiometry of the dissolution equation (Eq. 2.12), it is estimated that 1 kg of oxygen is consumed for the bioleaching of 1 kg of pyrite [14]. This concurred with our data as the OUR grew with the pyrite dissolution rate, up to 396±116 $mg\,l^{-1}\,h^{-1}$ of oxygen consumed for 434±75 $mg\,l^{-1}\,h^{-1}$ of pyrite on day 5. After this growing phase, the value slowly decreases due to the exhaustion of accessible pyrite, which is also marked by a decrease of microbial growth and activity.

$$2\,FeS_2 + 4\,H^+ + 7\,O_2 + 2\,H_2O \longrightarrow 2\,Fe^{2+} + 4\,H_2SO_4 \tag{2.12}$$

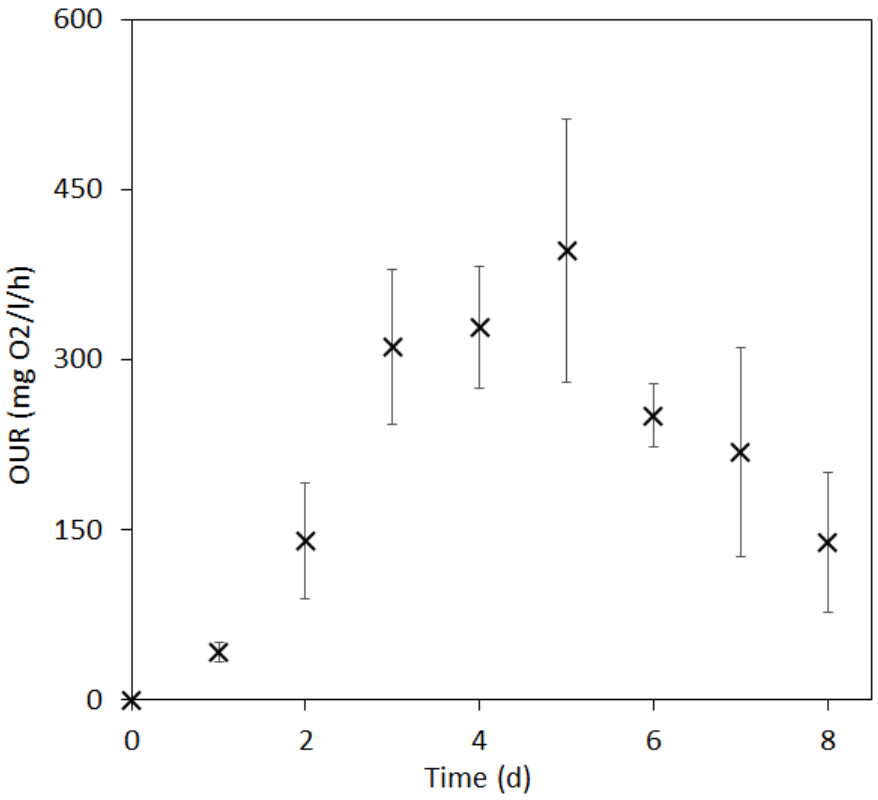

Figure 2.9: Evolution of the OUR during the culture.

2.3.2 Microbial community evolution

The daily characterization of the microorganisms consisted in counting the cells present in the supernatant, which is only an approximate method; it did not allow neither to quantify the biomass attached on the solid particles nor to differentiate the bacterial genera. For this, molecular biology methods were used to identify the bacterial strains, to determine their biomass concentration through DNA quantification and to observe their distribution in the medium, i.e attached to the solid particles or suspended in the liquid.

Specific PCR and SSCP were used to validate the presence of the expected BRGM-KCC bacterial strains, namely *L. ferriphilum*, *At. caldus*, *Sb. thermosulfidooxidans*. These results were approved by sequence comparison between the isolated clone and a database. Firstly, it is interesting to note that *Sb. benefaciens*, commonly found in the BRGM-KCC consortium, was absent of the liquid. This result is not uncommon as it was shown that, depending on the experimental conditions, the bacterial composition may be highly variable [5, 15]. This is due to the respective affinity to temperature, pH or dissolved components of each microbe, leading to competitive advantages in a given condition. This variability has no particular impact on bioleaching efficiency.

The spatial distribution of the different strains was assessed through qPCR of the previous samples. The biomass concentration and the strain specific abundances were measured using the quantity of gene copies of the bacterial 16S rRNA, expressed per ml (for the liquid and pulp) or per mg (for the solid). Observation of the bacterial distribution, as shown by Fig. 2.10, indicates that more than 99% of biomass was within the liquid. However, these results may be discussed considering the drawbacks of the separation method. Firstly, separating by decantation may not be the best suitable method for solid-liquid separation as a portion of the liquid will still be within the solid sample. And secondly, the DNA extraction on the solid may be inefficient due to the porous nature of the sulfidic particles during and at the end of the experiment, which would lead to only a small portion of microorganism DNA to be extracted. It could be advised to use a more suitable method for solid-liquid separation or to carry out the DNA extraction on triplicates in order to validate the value obtained. The later was not feasible on this experiment due to the multiple samples which were already taken from the tank.

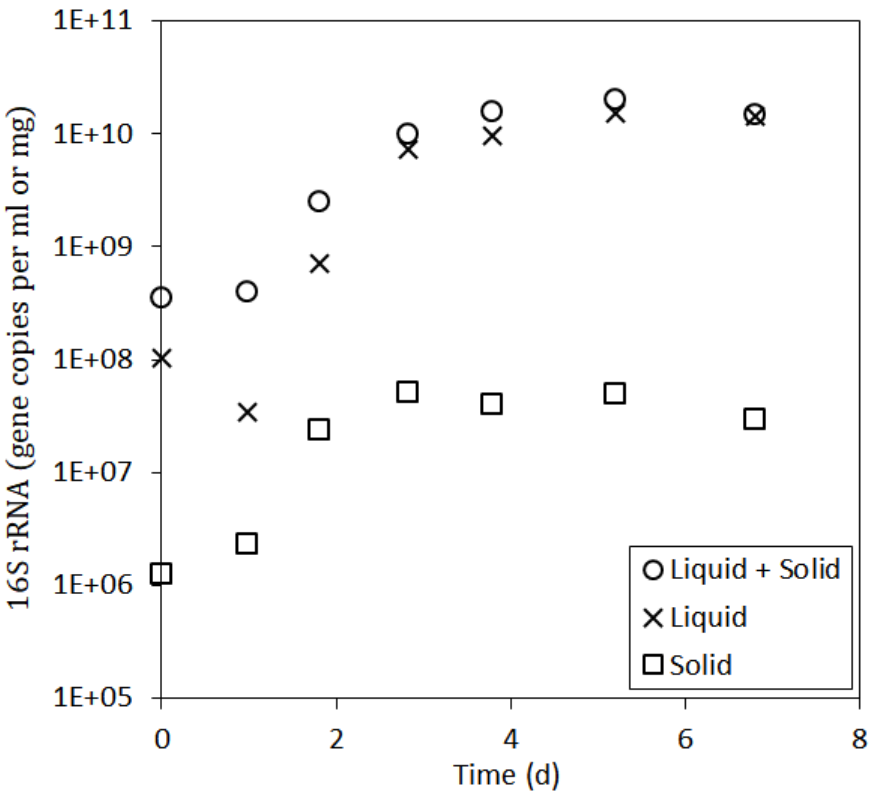

Figure 2.10: Distribution of the biomass in the reactor by assessing the number of 16S rRNA gene copies in the pulp, liquid and solid. The data are shown for one representative batch.

The strain specific abundances were also determined in the pulp, solid and liquid, as shown in Fig. 2.11. The results showed that the liquid contained a higher ratio of suspended *L. ferriphilum* while attached *At. caldus* and *Sb. thermosulfidooxidans* are more prevalent than *L. ferriphilum* on the solid. This agrees with previous experiments of Zhou et al. (2007), which showed that *At. caldus* improved bioleaching efficiency by removing the sulfur layer that form on the surface of the mineral [16]. Nonetheless, it is important to qualify this result by remembering that in quantitative terms, most of the bacteria were suspended in the liquid. Looking at the ratios evolution along time, *At. caldus* and *Sb. thermosulfidooxidans* displayed a better growth than *L. ferriphilum* on the first two days, with *L. ferriphilum* representing as low as 15% of the 16S rRNA gene copies in comparison to the 50% of the inoculum. Due to its relative abundance, *At. caldus* acted as the main sulfur-oxidizing bacteria. As *Sb. thermosulfidooxidans* is both a sulfur-oxidizing and iron-oxidizing bacteria, it assists the process of sulfur removal while allowing ferrous iron to be oxidize back to ferric iron. After the first few days, the growth trend of the consortium is quickly reversed as *L. ferriphilum* became the main iron-oxidizer, consisting of 45% of biomass. This also leads to a relative diminution of *Sb. thermosulfidooxidans* down to 3% of biomass as *L. ferriphilum* is more efficient at oxidizing ferrous iron. Moreover, Nurmi et al. (2009) has shown that *L. ferriphilum* displays a polymetallic resistance, which explains its abundance at later

stage of the batch [17]. Lastly, *At. caldus* was the dominant sulfur-oxidizer, as shown by its ratio of 55% of total biomass. Previous studies had also shown the high efficiency of co-cultures of *At. caldus* and *L. ferriphilum* for mineral dissolution [16, 18, 19].

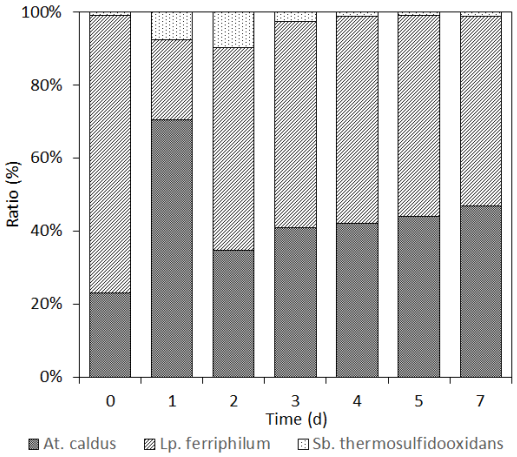

(a) Liquid ratio

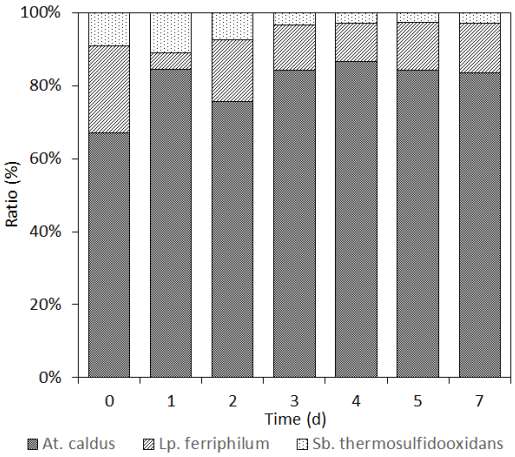

(b) Solid ratio

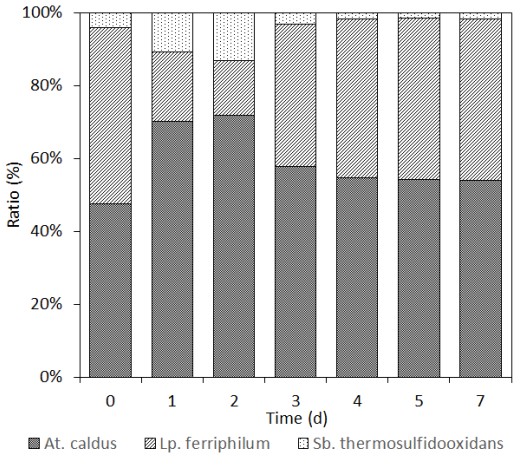

(c) Pulp ratio

Figure 2.11: Strain specific abundances of the biomass in the reactor.

A comparison between qPCR and cell count results was also performed, as shown on Fig. 2.12. Since the Thoma cell counting method can only differentiate suspended cells in the liquid phase, comparison was made with qPCR results obtained from the liquid. The results showed that both counting methods results were in agreement and can be linearly correlated with a coefficient equal to 0.97. This comparison may be summed up with the number of gene copies equal to 1.48 times the number of cells counted.

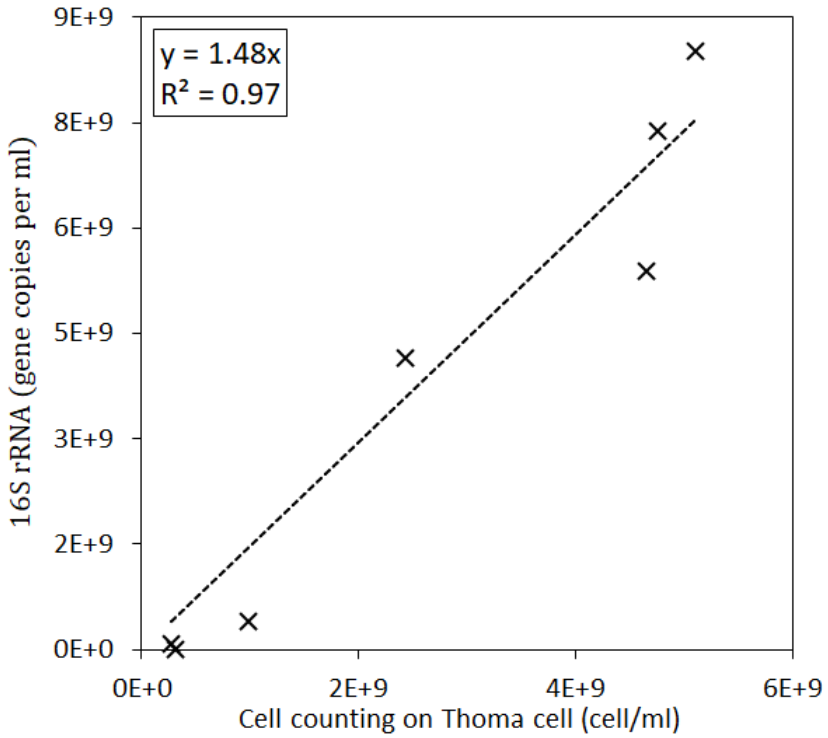

Figure 2.12: Comparison between qPCR and cell count results. Data from the liquid were used as the qPCR results.

2.4 Abiotic experiments

2.4.1 Measurement and modeling of the just-suspended speed

The just-suspended agitation rate was measured for the various conditions of particle size, solid concentration, impeller configuration and aeration rate. The results were compared to the Zwietering correlation and the gassed just-suspended agitation rate models. Lastly, the effects of the studied parameters on the just-suspended agitation rate were observed.

Comparison of the experimental results with the Zwietering correlation

The just-suspended agitation rates were modeled using Eq. 2.7 and the exponents proposed by Zwietering for different variables. For this, the same ungassed conditions as used experimentally were employed. The unknown for the model was the parameter S, which was determined by minimizing the mean squared error between experimental and modeled just-suspended speed to adjust its value. As S is dependent on geometrical ratio such as D/T, C/T or the impeller type, it was determined separately for the double RT6B (DR) and for the RT6B + A310 (RH) configurations. As observed on Fig. 2.13, the results showed that the experimental values of N_{js} could be modeled with a mean relative error of 3.9%. The values of the constant S were obtained for both configurations and it was found that $S_{\text{DR}} = 8.60$ and $S_{\text{RH}} = 9.06$, which is close

to the value of 7 found by Zwietering for similar $C/T = 0.42$ [8].

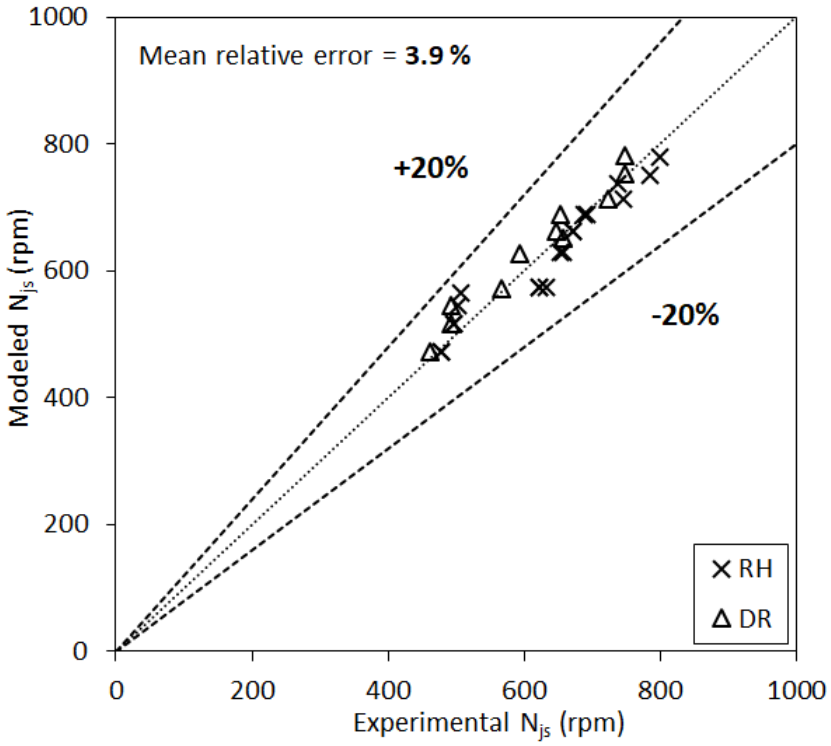

Figure 2.13: Comparison of the experimental and modeled just-suspended speed N_{js} for various impeller configuration and $Q_{\mathrm{g}} = 0$ vvm.

The previous just-suspended agitation rate model was extended to account for the presence of gas. This was done using the results from the ungassed conditions to calculate $N_{\mathrm{jsg,add}}$ and $N_{\mathrm{jsg,na}}$, as shown by Eq. 2.8−2.9. The results, reported on Fig. 2.14, showed that $N_{\mathrm{jsg,add}}$ offered a good fit on the experimental values, with a mean approximation error of 4.0%. This was done using $a_{\mathrm{add}} = 315.9$ min^{-1} as a constant, which was found of the same order of magnitude that of similar studies [11], leading to a global equation:

$$N_{\mathrm{jsg,add}} = N_{\mathrm{js}} + 315.9 \cdot Q_{\mathrm{g}} \tag{2.13}$$

The second model was used to determine the relation between $N_{\mathrm{jsg,na}}/N_{\mathrm{js}}$ and the aeration number N_A using Eq. 2.9. The results showed a good fit of the relation ($R^2 = 0.95$) using the parameters $A = 26.9$ and $\alpha = 1$. The coefficient of α equal to 1 suggested that $N_{\mathrm{jsg,na}}/N_{\mathrm{js}}$ and N_A are linearly related, hence the relation $N_{\mathrm{jsg,na}}/N_{\mathrm{js}} = 1+26.9 \cdot N_A$ for $0 < N_A < 0.012$. Both correlations used additive terms to represent the impact of the aeration rate on the just-suspended agitation rate and could be used to extrapolate N_{jsg} in the range of parameters employed in this study. It is also important here to note that the previous model is valid for the range of aeration numbers studied. Design of the sparging system may also significantly impact the effects of the aeration on the suspension process. From a physical point of view, the mechanical power needed to

ensure particle suspension should be the same whatever the gas flowrate applied. Gas flow rate may have two opposite impacts on this power dissipation:

- First, gas expansion within the liquid phase (let suppose it adiabatic) is converted into mechanical power. This brings additional power that should lead to a decrease of the agitation rate at the just-suspended state. This additional power P_{add} is given by the following equation:

$$\frac{P_{\text{add}}}{V_{\text{l}}} = \rho_{\text{l}} u_{\text{g}} g = \frac{\rho_{\text{l}} Q_{\text{g}} g}{\pi T^2} \tag{2.14}$$

With u_{g} ($\text{m}\,\text{s}^{-1}$) the superficial gas velocity. The order of magnitude of this additional power is approximately :

$$\frac{P_{\text{add}}}{V_{\text{l}}} \simeq 1000 \times \frac{100 \times \frac{10^{-3}}{3600}}{\pi \times 0.12^2} \times 10 = 6\ W/m^3 \tag{2.15}$$

Which is sensibly lower than the mechanical power brought by the impeller. These positive effects of gas flow rate on particle suspension could be thus neglected.

- The second effect of gas flow rate arises from progressive impeller flooding due to weak dispersion of bubbles by the bottom impeller. Despite incomplete impeller flooding obtained during the experiments, power loss due to aeration was expected. Calderbank (1958) showed that, for a Rushton turbine impeller, the power loss was related to the aeration number [20]:

$$\frac{P_{\text{g}}}{P_0} = 1 - 12.6 \cdot N_A \tag{2.16}$$

For $N_A < 0.035$.

This relation is expected to be strongly dependent of bioreactor and sparger designs due to their impact on gas dispersion. However, no measurements of power loss were done in our study and thus, only suggestion regarding the impact of agitation rate may be made. It is suggested that the increase of agitation rate to ensure particle suspension is related to a weaker bubbles dispersion by the impeller and a progressive loss of mechanical power.

In order to decipher the various phenomena taking place in the bioreactor, the specific impact of Q_{g} on N_{jsg} was established, as shown on Fig. 2.15 for each range of particle diameters. Using multiple linear regressions, the relation between N_{jsg} and Q_{g} was determined and found to be linked by the relation $N_{\text{jsg}} \propto 2.64 \cdot Q_{\text{g}}$. These results also show that this impact seems significantly independent of particle diameter, in the range of particle diameters studied.

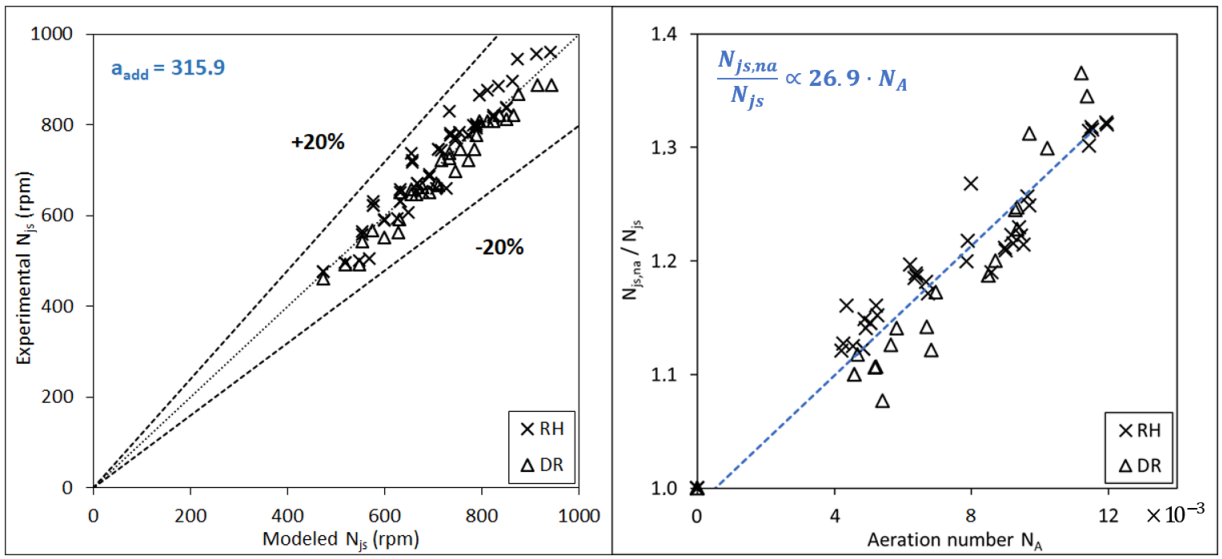

Figure 2.14: Comparison of the models for the just-suspended speed N_{js} under gassed conditions for various impeller configuration using (left) $N_{\mathrm{jsg,add}}$ and (right) $N_{\mathrm{jsg,na}}$.

Consequences on bioreactor and process control are thus clearly important and should be considered prior optimization. Oxygenation control is indeed generally based on either modification of agitation rate or gas flow rate. These results show that the increase of the gas flowrate only may rapidly have deleterious effects on particle suspension as $N_{\mathrm{js,g}} \propto Q_{\mathrm{g}}$. Regarding dimensionless model of suspension, it should be advised either to apply an oxygenation control that maintains the aeration number constant throughout the process (which is equivalent to $N \propto Q_{\mathrm{g}}$) or to verify that, when the oxygen demand is maximal, the agitation rate is still sufficient to ensure a good dispersion of the particles.

Effect of the different variables affecting the just-suspended agitation rate

The impact of particle size and solid concentration on the just-suspended agitation rate was also investigated. The respective influence of these parameters was compared with the trends observed by Zwietering.

The effect of particle size on N_{js} was observed for three particles size categories, ranging from 20 to 200 µm and under different conditions of aeration rates and solid concentrations, as shown by Fig. 2.16. The Zwietering correlation suggested a strong impact of the particle size due to its influence on terminal settling velocities. This effect was confirmed in this study as the global exponent on the particle size was found to be 0.25 ± 0.02 ($R^2 > 0.95$), leading to $N_{\mathrm{js}} \propto d_{\mathrm{p}}^{0.25}$. This value, higher than the 0.2 determined by Zwietering, is not uncommon as similar impact were reported by other studies, which was found to be relative to the difference of geometry [11]. It should be also noted that the dependence of N_{js} on the particle diameter is not impacted either by the solid concentration or by the gas flow rate. From an economical point of view,

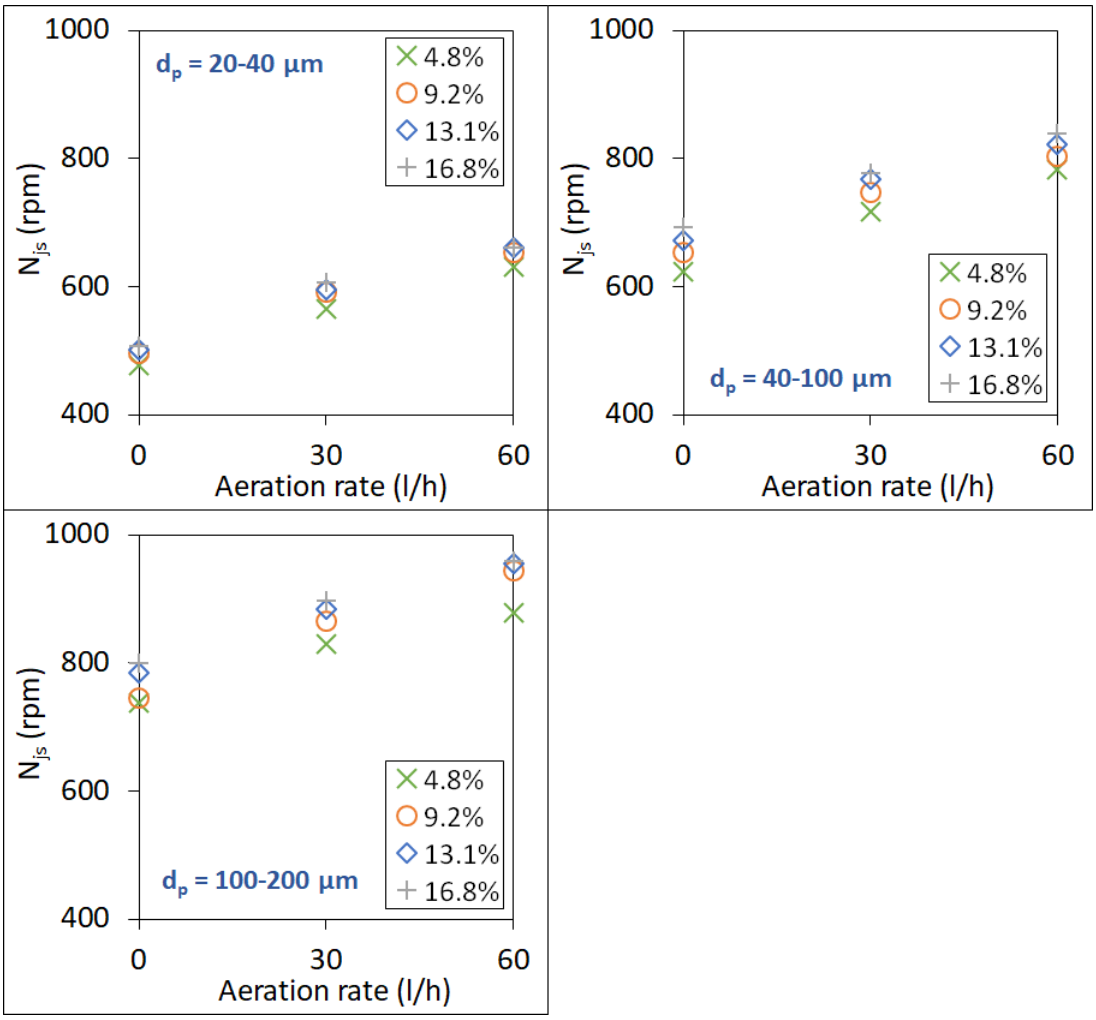

Figure 2.15: Effect of the aeration rate on the just-suspended agitation rate for different solid concentrations and particle diameters. Solid concentrations are given in weight of solid per weight of pulp.

the dependence of N_{js} on d_{p} shows that, the corresponding mechanical power necessary to ensure particle suspension would be related to $P \propto N^3 \propto d_{\mathrm{p}}^{0.75}$.

Lastly, the impact of solid concentration was also considered for values ranging from 4.8 to 16.8% w/w solid. The results, shown on Fig. 2.17, demonstrated a weak effect of solid concentration on N_{js}. The calculated overall coefficient on solid concentration was found to be 0.06 ± 0.01 ($R^2 > 0.95$), which is lower than the 0.13 found by Zwietering. This difference could be attributed to the low clearance used for the bottom RT6B impeller, which assisted particle suspension.

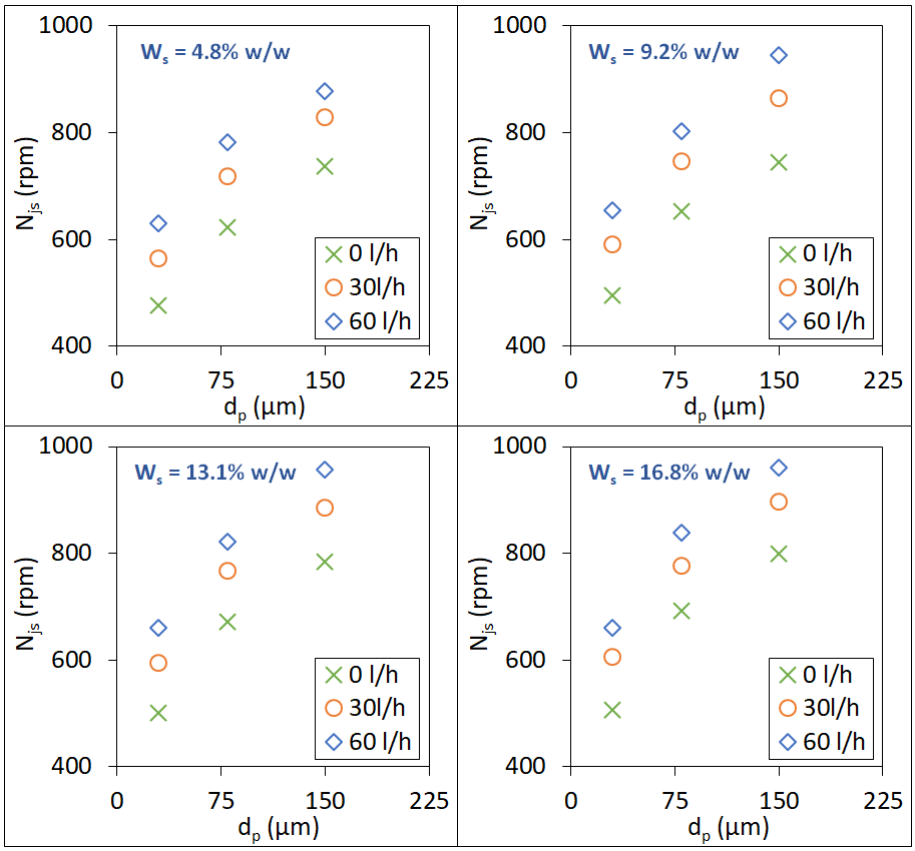

Figure 2.16: Effect of the particle diameter on the just-suspended agitation rate.

2.4.2 Determination of oxygen mass transfer coefficient

The oxygen mass transfer coefficient was measured in the 2-liter tank for various conditions of impeller configuration, agitation rate, gas flow rate and solid concentration. The results are represented on Fig. 2.18. The results for 300 rpm were unsatisfying due to bubble accumulation on the probe that could not be prevented at this agitation rate, as the probe used for measuring dissolved oxygen was not beveled and was responsible for bubble retention at its surface. Therefore, these data were not shown.

For all conditions tested, as expected, the oxygen mass transfer coefficient increased with the aeration rate, with a single exception for the DR at 500 rpm and 4.8% solid where it decreased, which could be attributed to experimental error margin. Similarly to the aeration rate, the agitation rate impacted positively the k_La values, with a k_La up to 3 to 5 times higher at 700 rpm compared to 500 rpm. Lastly, the solid concentration also affected positively the k_La. The k_La was, on average, increased by 16% when solid was added in the vessel, except for the RH configuration at 500 rpm where rises up to up to 120% were observed. However, few differences were observed between 4.8 and 9.2% (w/w) of solid. At first glance, it could be expected a decrease of the k_La with increasing solid fraction, as reported in most of studies of literature. However, it was also shown that for low volume fractions of solid in suspension in water, an increase of

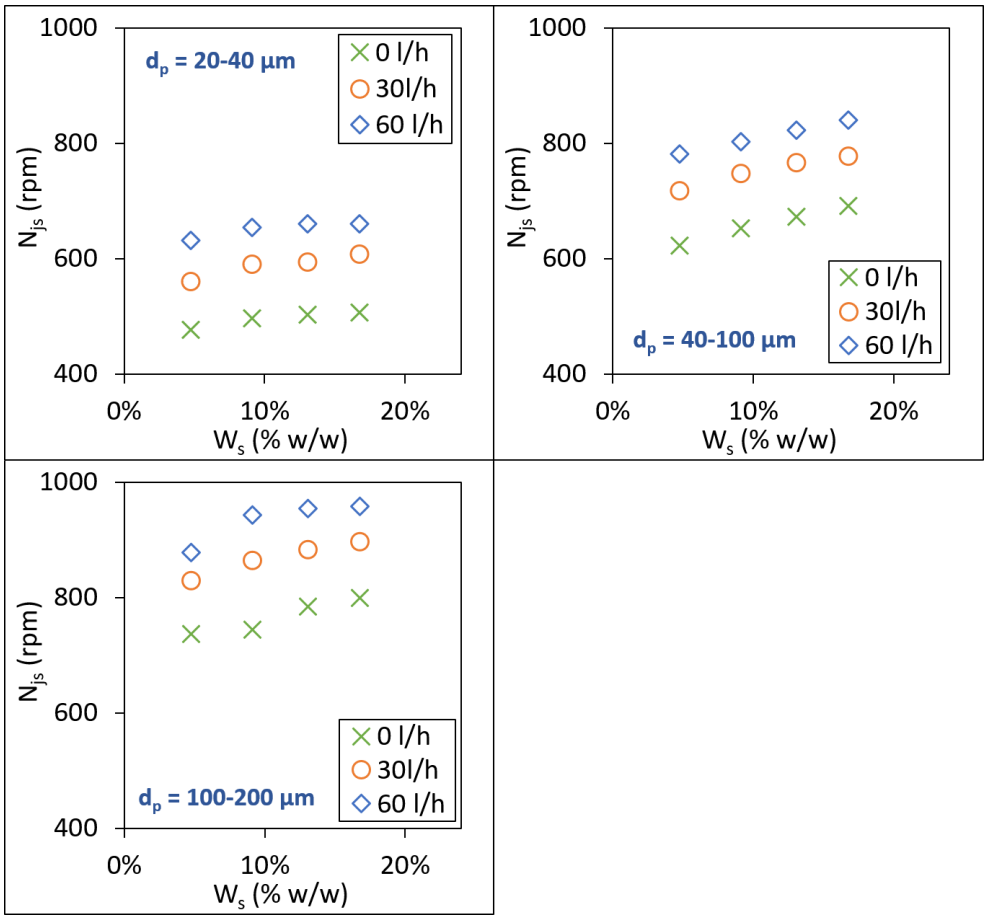

Figure 2.17: Effect of the solid concentration on the just-suspended agitation rate for various aeration rates and particle diameters.

the k_La could also be observed [21]. These complementary results and the one obtained in the present study confirm the conflicting effects of solid phase on mass transfer. For low volume fractions, the presence of a solid phase with a diameter close to the liquid film thickness encountered at the gas-liquid interface may disrupt bubble coalescence in coalescing media such as the one used here. In this case, a decrease of the interfacial area may be suggested. On the other hand, higher solid fractions may contaminate the gas-liquid interface and limit the diffusion of oxygen through it or even reduce the available "clear" interface for the highest concentrations. Consequently, establishing general rules for gas-liquid mass transfer in slurry reactors remains hardly realizable regarding the effects of bioreactor design, particle diameters, or physicochemical properties of the liquid phase. A case-by-case study is thus certainly still necessary during bioleaching process sizing.

By comparing the two impeller settings, it is shown that the DR configuration offered better gas dispersion capabilities than the RH configuration due to its higher k_La values for all used conditions. However, the difference of k_La was relative to the agitation rate, with up to 50% differences at 500 rpm but little to no differences at 700 rpm.

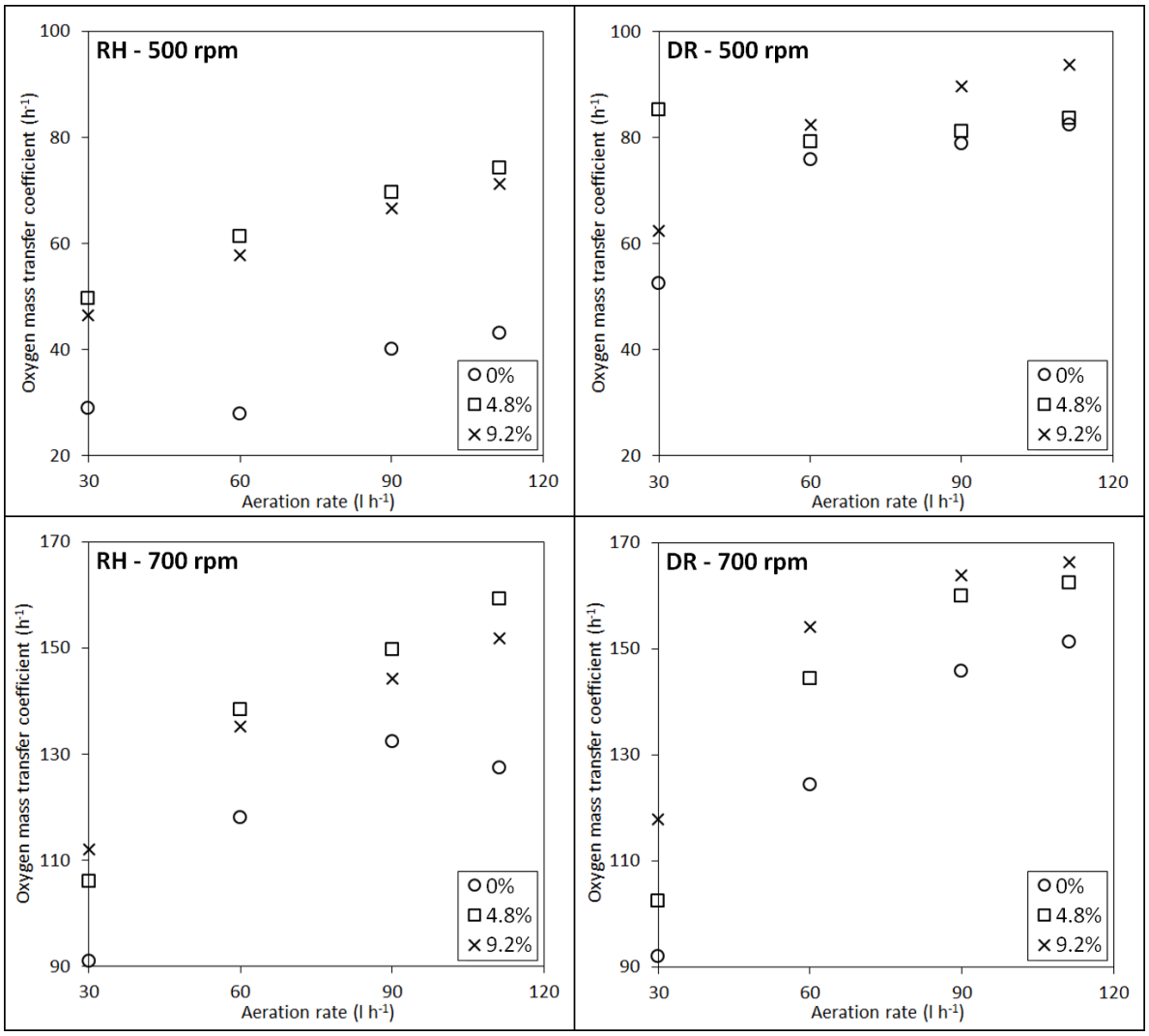

Figure 2.18: Oxygen mass transfer coefficient in function of aeration rate for various configuration, agitation rates and solid concentrations. (top left) RH configuration at 500 rpm ; (top right) DR configuration at 500 rpm ; (bottom left) RH configuration at 700 rpm ; (bottom right) DR configuration at 700 rpm. Solid concentrations are given in weight of solid per weight of pulp.

The results of each set of conditions of configuration, agitation rate and solid concentration were fitted using a power law ($k_{\mathrm{L}}a = a \cdot Q_{\mathrm{g}}^{b}$). The models, shown on Table 2.2, offered good matches ($R^2 > 0.90$) with the same exception for the DR at 500 rpm and 4.8% w/w. The power constant b was found to be equivalent for all results at 0.31±0.04. The constant a had a higher variability and is dependent of the impeller but remains in the same order of magnitude than values than can be found in literature (see for instance [22]).

Table 2.2: Coefficient for the power law fitting of the $k_L a$ values for various conditions of configuration, agitation rate and solid concentration.

		500 rpm			**700 rpm**		
		0% w/w	**4.8% w/w**	**9.2% w/w**	**0% w/w**	**4.8% w/w**	**9.2% w/w**
RH	**a**	8.96	17.44	15.18	36.11	37.84	51.93
	b	0.32	0.31	0.33	0.28	0.31	0.23
	R^2	0.70	1.00	1.00	0.92	0.98	0.99
DR	**a**	17.13	89.56	22.08	24.75	30.82	48.60
	b	0.34	-0.02	0.31	0.39	0.36	0.27
	R^2	0.91	0.13	0.97	0.99	0.95	0.93

2.5 Chapter conclusions

In this chapter, a complete description of a laboratory-scale bioleaching stirred tank reactor was obtained through biotic and abiotic experiments.

At first, 10 batch bioleaching STR were carried out with common experimental parameters, in order to generate data on solid, liquid, gas and biomass and for modelling purpose. Progression of the experiments was determined over the time using dissolved metal content and gas analysis. Furthermore, biological kinetics were observed using biomass counting and molecular biology. DNA sequence analysis was used to recognize the different strains present in the medium during the experiment. The results validated the presence of expected BRGM-KCC bacterial strains, namely *L. ferriphilum*, *At. caldus* and *Sb. thermosulfidooxidans*. It was also found that *L. ferriphilum* acted as the main iron-oxidizer and *At. caldus* as the main sulfur-oxidizer. Moreover, DNA quantification allowed to observe the distribution of these strains in the medium, which helped determining their attachment to the solid particles or suspension in the liquid. It was shown that over 99% of biomass were suspended in the liquid. Furthermore, the strain specific abundances of the biomass was observed for each phase (liquid, solid or pulp). Lastly, a relationship between cell count and the gene copy number was established.

As a matter of fact, most biokinetic models are constrained by experimental constants such as the gas-liquid mass transfer coefficient or bacterial growth parameters. The previously obtained data will be used in the chapter 4 as a baseline for the estimation of these constants. Moreover, the experimental data will also be used as a mean to validate the different models established, before their transposition to industrial scale.

Abiotic experiments were also performed to characterize the tank ability to homogenize solid, liquid and gas. Two different parameters were determined: just-suspended speed and gas-liquid mass transfer. Both parameters were obtained for a wide range of conditions, including solid fraction, solid concentration, impeller configuration and gas flow rate. Moreover, supplementary studies were done on the just-suspended speed to model it using the Zwietering correlation and it was also shown that adjustments of the correlation could lead to a correct approximation of the gassed just-suspended speed. Based on this assumption, a new dimensionless model was established to link the just-suspended agitation rate under gassed conditions to the aeration number. Similarly, the gas-liquid mass transfer was modeled using a power law with a common power superscript for all results. Our results confirm the complex interactions that take place within gas-liquid-solid stirred tank bioleaching reactors. From this point of view, global experimental measurements, despite their utility for proposing basal

scale-up and process optimization rules, can not be sufficient to decipher the physical phenomena coupling that take place in the bioreactor. One consequence is thus the need to perform more advanced hydrodynamic characterizations, which is proposed in the next chapter through CFD simulations.

Bibliography

[1] J. Petersen. Modelling of bioleach processes: Connection between science and engineering. *Hydrometallurgy*, 104(3):404–409, October 2010.

[2] S. T. Harrison, R. Stevenson, and J. J. Cilliers. Assessing solids concentration homogeneity in Rushton-agitated slurry reactors using electrical resistance tomography (ERT). *Chemical Engineering Science*, 71:392–399, March 2012.

[3] F. Battaglia-Brunet, M. Clarens, P. d'Hugues, J. Godon, S. Foucher, and D. Morin. Monitoring of a pyrite-oxidising bacterial population using DNA single-strand conformation polymorphism and microscopic techniques. *Applied Microbiology and Biotechnology*, 60(1):206–211, October 2002.

[4] A. Mahmoud, P. Cézac, A. F. A. Hoadley, F. Contamine, and P. D'Hugues. A review of sulfide minerals microbially assisted leaching in stirred tank reactors. *International Biodeterioration & Biodegradation*, 119:118–146, April 2017.

[5] S. Hedrich, A.-G. Guézennec, M. Charron, A. Schippers, and C. Joulian. Quantitative Monitoring of Microbial Species during Bioleaching of a Copper Concentrate. *Frontiers in Microbiology*, 7, 2016.

[6] A.-G. Guezennec, C. Joulian, C. Delort, F. Bodénan, S. Hedrich, and P. D'hugues. CO2 mass transfer in bioleaching reactors: CO2 enrichment applied to a complex copper concentrate. *Hydrometallurgy*, 180:277–286, September 2018.

[7] G. Yue, L. Zhao, O. G. Olvera, and E. Asselin. Speciation of the H2SO4–Fe2(SO4)3–FeSO4–H2O system and development of an expression to predict the redox potential of the Fe3+/Fe2+ couple up to 150°C. *Hydrometallurgy*, 147-148:196–209, August 2014.

[8] T. N. Zwietering. Suspending of solid particles in liquid by agitators. *Chemical Engineering Science*, 8(3):244–253, June 1958.

[9] C. W. Wong, J. P. Wang, and S. T. Huang. Investigations of fluid dynamics in mechanically stirred aerated slurry reactors. *The Canadian Journal of Chemical Engineering*, 65(3):412–419, 1987.

[10] N. N. Dutta and V. G. Pangarkar. Critical impeller speed for solid suspension in multi-impeller three phase agitated contactors. *The Canadian Journal of Chemical Engineering*, 73(3):273–283, 1995.

[11] A. P. van der Westhuizen and D. A. Deglon. Solids suspension in a pilot-scale mechanical flotation cell: A critical impeller speed correlation. *Minerals Engineering*, 21(8):621–629, July 2008.

[12] J. E. Dutrizac and J. L. Jambor. Jarosites and Their Application in Hydrometallurgy. *Reviews in Mineralogy and Geochemistry*, 40(1):405–452, January 2000.

[13] S. Feng, H. Yang, and W. Wang. Improved chalcopyrite bioleaching by Acidithiobacillus sp. via direct step-wise regulation of microbial community structure. *Bioresource Technology*, 192:75–82, September 2015.

[14] A.-G. Guezennec, C. Joulian, J. Jacob, A. Archane, D. Ibarra, R. de Buyer, F. Bodénan, and P. d'Hugues. Influence of dissolved oxygen on the bioleaching efficiency under oxygen enriched atmosphere. *Minerals Engineering*, 106:64–70, May 2017.

[15] A.-G. Guezennec, C. Joulian, J. Jacob, A. Archane, D. Ibarra, R. de Buyer, F. Bodénan, and P. d'Hugues. Influence of dissolved oxygen on the bioleaching efficiency under oxygen enriched atmosphere. *Minerals Engineering*, 106:64–70, May 2017.

[16] Q. G. Zhou, F. Bo, Z. Hong Bo, L. Xi, G. Jian, L. Fei Fei, and C. Xin Hua. Isolation of a strain of Acidithiobacillus caldus and its role in bioleaching of chalcopyrite. *World Journal of Microbiology and Biotechnology*, 23(9):1217–1225, September 2007.

[17] P. Nurmi, B. Özkaya, A. Kaksonen, O. Tuovinen, and J. Puhakka. Inhibition kinetics of iron oxidation by Leptospirillum ferriphilum in the presence of ferric, nickel and zinc ions. *Hydrometallurgy*, 97(3-4):137–145, July 2009.

[18] S. Foucher, F. Battaglia-Brunet, P. d'Hugues, M. Clarens, J. J. Godon, and D. Morin. Evolution of the bacterial population during the batch bioleaching of a cobaltiferous pyrite in a suspended-solids bubble column and comparison with a mechanically agitated reactor. *Hydrometallurgy*, 71(1):5–12, October 2003.

[19] N. Okibe, M. Gericke, K. B. Hallberg, and D. B. Johnson. Enumeration and Characterization of Acidophilic Microorganisms Isolated from a Pilot Plant Stirred-Tank Bioleaching Operation. *Applied and Environmental Microbiology*, 69(4):1936–1943, April 2003.

[20] P. H. Calderbank. Physical rate processes in industrial fermentations part i: The interfacial area in gas-liquid contacting with mechanical agitation. *Transactions of the Institution of Chemical Engineers*, 36:443–463, 1958.

[21] O. Ozkan, A. Calimli, R. Berber, and H. Oguz. Effect of inert solid particles at low concentrations on gas–liquid mass transfer in mechanically agitated reactors. *Chemical Engineering Science*, 55(14):2737–2740, 2000.

[22] K. Van't Riet. Review of measuring methods and results in nonviscous gas-liquid mass transfer in stirred vessels. *Industrial & Engineering Chemistry Process Design and Development*, 18(3):357–364, 1979.

Chapter 3

Modelling of particles suspension and hydromechanical stress in multi-scale bioleaching STR

Contents

3.1 Introduction

Bioleaching in stirred tank reactor is a powerful application of hydrometallurgy to extract metals on a short time with high efficiency. However, this process shows high OPEX, mainly due to the substantial energy consumption, which limit its use to high value-added resources. For this, operative conditions and tank characteristics must be carefully chosen to maximize cost efficiency. As seen in the state of the art, this surely includes adaptation of multiphase hydrodynamics generated in the tank, with the help of reliable models, especially Computational Fluid Dynamics (CFD).

The main goal of this chapter was to determine the impact of various process parameters on particle suspension, known as one of the critical parameters for optimization of the reacting conditions. For this, descriptive laboratory and pilot scale CFD models were applied to two BRGM tanks hydrodynamics. As a first step of the complete description of this hydrodynamics, liquid-solid numerical simulations were carried out and the impact of the impeller geometry, agitation rate and solid concentration were asserted on power dissipation and mixing efficiency.

Studies demonstrated that cells attachment was linked to bioleaching efficiency [1]. For this, the previously developed models were also used to quantify the hydromechanical stress perceived by the particles and its spatial distribution for various solid concentrations. For this purpose, approximately 50 numerical simulations were realized at the 2 l laboratory-scale (published paper in *Hydrometallurgy*, see section 3.2) and the results robustness was evaluated at the 800 l pilot-scale (section 3.3). From the results obtained, it was proposed new insights for reactor design and scaling of bioleaching stirred tank reactor and more specifically on the limitation of the shear stress encountered by the attached bacterial communities.

3.2 Impact of impeller design and solid concentration on particle suspension and hydromechanical stress

As seen previously, particle suspension is a critical parameter for both chemical and biological reactions efficiency. It is closely linked to the tank and impellers geometries as responsible for hydrodynamics of the medium. These parameters must be carefully chosen in order to maximize solid homogeneity while limiting hydromechanical stress on the biomass. This first study will describe the results for a laboratory scale STR in the form of a scientific paper in *Hydrometallurgy*.

CFD numerical simulation of particle suspension and stress in various designs of multi-stage bioleaching reactors

Jonathan CHERON[a], Céline LOUBIERE[b], Stéphane DELAUNAY[a], Anne-Gwénaëlle GUEZENNEC[b], Eric OLMOS[a,*]

[a] Laboratoire Réactions et Génie des Procédés, Université de Lorraine, CNRS, LRGP, 54000 Nancy, France
[b] Bureau de Recherches Géologiques et Minières, BRGM, 45100 Orléans, France

[*] Corresponding author: eric.olmos@univ-lorraine.fr (E. Olmos).

Abstract: The performance of bioleaching stirred tank reactors (STR) is related to the homogeneity of biomass, substrates and dissolved gases. This work was focused on the characterization of the impeller design on bioreactor hydrodynamics and, more specifically on power, mixing efficiency and particle stress. Few studies addressed the issue of the impact of the impeller design on these, especially for multi-stage bioreactors which are the most commonly used at the industrial scale. To fill this lack, a two-stage solid-liquid computational fluid dynamics (CFD) model was simulated on more than 50 conditions to assess power consumption, dissipated power, suspension quality and particle stress. A dual impeller configuration was chosen using Rushton turbines, R600, Hydrofoil, Elephant Ear and HTPG impellers. Grinded pyrite-rich materials (average particles size: 80 µm) were considered as the solid phase at 3 different solid concentrations (10, 18 and 26 % w/w). Considering the impeller power number (N_P), the configuration with an axial impeller consumed less energy than a radial impeller in concordance with literature data. The results show that the impeller design had few to no effect on mixing efficiency considering a given power dissipation per unit volume. Independently on the impeller used, unique relationships were found between particle stress and mixing efficiency. This study gives new insights for reactor design and scaling of bioleaching stirred tank reactor and more specifically on the reduction of shear stress for the attached bacterial communities.

3.2.1 Introduction

In the last decades, bioleaching has been successfully implemented at the industrial scale and used, either in the form of dump or heap treatments, or by using large-scale stirred tank reactors (STR) [2, 3]. Dump or heap treatments were widely used for low-grade copper-based sulphides because of the low cost of implementation and maintenance of these processes. On the other hand, bioleaching STR have proven to be more efficient to extract metals from low-grade or refractory ores but are limited to precious metals because of their significant cost of implementation [4]. Nonetheless, bioleaching is evolving towards the exploitation of 'unconventional' resources caused by the declining trend in mean ore grades [5, 6]. These resources are represented with unusual features such as very low-grades, complex mineralogy, or high sulphur content. If heap bioleaching has been the main process option for their treatment until now, it is not always suitable. The main reasons that precludes heap application are the composition of the materials to be treated (presence of carbonate causing heap clogging, or high concentrations of sulphides that lead to uncontrolled and excessive temperature increase in the heap) and the lack of sufficient space, especially in densely populated areas like in Europe. In such cases, bioleaching STR might be a technical alternative but is mostly too expensive except in very few cases when the metal value is high enough (e.g. such as in Uganda for the cobalt recovery in flotation tailings [7] or in Finland for the valorization of nickel from talc mining residues [8, 9]). The expansion of STR bioleaching requires thus further technical optimization to reach an economic viability.

As in any chemical engineering process, the management of bioleaching bioreactors is aimed at optimizing the reacting conditions to accelerate the oxidation processes of the sulphides and to maximize the solubilization or liberation efficiency of valuable metals. This optimization of the reacting conditions is closely related to the homogeneity of biomass, substrates and dissolved gases throughout the reactor. This is especially important considering that the interactions between the microorganisms and sulphides (microbial attachment and biofilm formation) are considered key parameters to improve bioleaching [3]. To this end, improving mixing efficiency would result in a better mass transfer of the components in the system [10, 11]. Furthermore, significant power consumption of the process comes from mechanical mixing, which is directly related to the solid content (through sufficient agitation rate ensuring suspension and gas-liquid mass transfer efficiency) and its physical properties [12, 13]. Bioleaching in STR involves substantial power consumption, which results in large operating costs and limits, until now, the use of this technology to the treatment of high added-value resources (mainly refractory gold ores). Besides these commodities, the expansion of bioleaching to 'unconventional' primary resources with lower value, such as low-grade ores or base

metal ores and tailings, requires adapting the STR process to the characteristics of these resources in order to limit investment and operating costs while maintaining high extraction efficiency [7, 14] as these resources present a wide range of shape, size and physical properties.

Solid-liquid stirred tanks were widely studied in the literature to define standard designs in order to optimize their efficiency through a better solid distribution [15, 16]. The power consumption per unit of volume P/V is generally considered as one of the best criterion for the scale-up of these vessels [17, 18] as it could be related to mass transfer capacities or mixing times [19, 20]. Dimensional analysis indicates that its value is provided by dimensionless models relating the power number N_P to the Reynolds number Re, the impeller power number N_P being represented by the following equation:

$$N_P = \frac{P}{\rho_l N^3 D^5} = f\left(Re = \frac{\rho_l N D^2}{\mu}\right) \tag{3.1}$$

with P the power required for the impeller rotation, ρ_l the fluid density, N the agitation rate, μ the liquid viscosity and D the impeller diameter. It is a well-known result that, in baffled vessels, the power number is independent of the Reynolds number in the turbulent regime ($\mathrm{Re} > 10^4$) and reaches a constant value that only depends on bioreactor design [17]. It is also important to emphasize that the required power P (which is related to the electric power consumption) should be preferentially minimized to limit the OPEX of the bioleaching process.

Nevertheless, this parameter is not sufficient to describe the suspension quality, defined by the spatial distribution of the particles within the flow. To describe the suspension quality, the just-suspended agitation rate N_{js}, defined as the minimal agitation rate ensuring the suspension of all solid particles, has often been used as a good compromise between optimal mass transfer and minimal power consumption [21–24]. However, this criterion fails to describe the solid suspension quality [25]. Mak (1992) used the standard deviation of the local solid concentration as a way to characterize the solid distribution but the experimental set-up complexity makes difficult the use of this method to screen a high number of bioreactor designs [26]. Furthermore, the solid distribution within the liquid phase should be related to the local values of turbulent dissipation rates [27] which strongly depend on both the vessel and the impeller design [28]. However, while an increase of power dissipation is expected to sensibly improve the mixing efficiency of the bioreactor from a physical point of view, the hydromechanical stress generated by the agitation may also weaken the microbial adhesion or even lower the process performances. This is particularly detrimental for bioleaching processes due to the major importance of microbial attachment and biofilm formation [29, 30]. This was observed with *Acidithiobacillus ferrooxidans* cultures in shaking flasks [31].

Similar observations were made in STR during thermophilic cultures of *Sulfolobus* sp. [32, 33]. Moreover, it was shown by Wang et al. (2014) that, for moderately thermophiles cultures, the proportion of attached cells is higher than of planktonic cells [34]. Also, altering the capacity of the cell to attach on the mineral surface leads to a decrease of bioleaching efficiency [35]. Considering the effect of solid loading, it was demonstrated by Witne and Phillips (2001) that the increase of solid concentration in continuous STR induced an increase of the leaching rate until a point where it had a negative effect, which could be caused by the attrition of cells [1]. Similar results were observed by Raja (2005) in shaking bottles where a decrease in specific oxygen consumption rate and cell viability was observed at increasing quartzite concentrations [36]. In the same way, Nemati and Harrison (2000) observed that if a partial suspension of the pulp was obtained for a concentration of 18 % w/v (corresponding to 16 % w/w with the hypothesis of $\rho_s = 2610\,\mathrm{kg\,m^{-3}}$), the rate of iron solubilization was reduced [37]. However, achieving complete particle suspension led to an apparent cell damage, as shown by a reduced cell count. More generally, it must be underlined that solid concentration has not the same influence on mesophilic and moderately thermophilic bacteria (such as *Leptosirillum* and *Acidithiobacillus* sp.), and extremely thermophilic archaea (such as *Acidianus*, *Metallosphaera*, and *Sulfolobus* sp.). As reviewed by Brierley and Brierley (2013), STR bioleaching with archaea, which have no rigid cell wall, necessitates a somewhat lower solid concentration than 12.5 % in reactor opposed to the common 20 % in plants processing sulphidic-gold concentrates with mesophilic and moderately thermophilic bacteria, due to their difference of shear sensitivity [3].

To understand the previous results, it is important to consider that, in bioleaching reactors, hydromechanical stresses may impact the process performance following three phenomena: (i) direct shear of the liquid phase on the microorganisms in suspension (Fig. 3.1a), (ii) shear stress on particles that potentially hold adhered microorganisms or biofilms (Fig. 3.1b), and (iii) particle-particle frictions and collisions (Fig. 3.1c). The occurrence of direct shear is still debated. It is generally assumed, but not completely demonstrated, that hydrodynamics has no impact on planktonic microorganisms if, locally, the Kolmogorov length scale $l_K = (\nu^3/\varepsilon)^{0.25}$ is higher than the microorganism diameter [38]. In this equation, ε ($\mathrm{W\,kg^{-1}}$) is the power dissipation per unit of mass (or turbulent dissipation rate) and ν is the kinematic viscosity ($\mathrm{m^2\,s^{-1}}$). Considering microorganisms of the micrometer scale, the maximal power dissipation necessary to induce direct cell damage would be $\varepsilon \sim 10^6$ $\mathrm{W\,kg^{-1}}$, which is unlikely to be reached in standard stirred tank bioreactors. In comparison, the value of power dissipation that would induce hydrodynamic stress on particle with a diameter in the range 10-100 µm would be $\varepsilon \sim$ 0.01-100 $\mathrm{W\,kg^{-1}}$, which is more likely to be observed with usual mixing conditions. Lastly, particle-particle frictions frequency and intensity depend on the local volume fraction of particles and the relative velocity between particles, and

consequently on the design of the bioreactor, the agitation rate and the mean particle concentration.

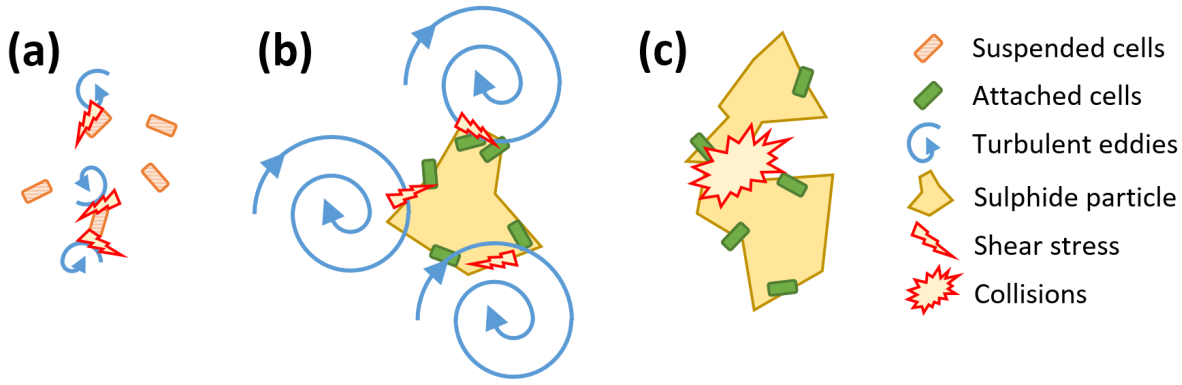

Figure 3.1: Description of the hydromechanical stress applied on microorganisms due to: (a) direct shear of the liquid; (b) shear stress on particles; (c) particle-particle frictions and collisions.

From a physical point of view, a quantitative description of the bioreactor hydrodynamics relies on a better knowledge of the coupling between bioreactor design, operating conditions, solid distribution within the bioreactor and particle stress. Computational Fluid Dynamics (CFD) can be used as an efficient approach to locally represent or calculate the hydrodynamics parameters of these processes. Among others, the local solid concentration, the liquid mean and fluctuating velocities and the impeller torque are representative parameters [39, 40]. In a gas-mixed leaching tank, Song et al. (2015) used a gas-liquid Euler-Euler approach to enhance the design of the reactor in terms of bubble diameter or draft tube diameter [41]. In the study of Gradov et al. (2017), the rheology of the slurry was modelled using a power law while a gas-liquid Euler-Euler approach was used to determine the volumetric distribution of the gas-liquid mass transfer coefficient within the bioreactor [42]. Three-phase flow was simulated in a vessel equipped with an HEDT impeller by Zheng et al. (2018a) [40]; the authors showed that a gas-liquid-solid Euler-Euler-Euler combined with a k-ε turbulence model was able to predict the mechanical power dissipation with an error lower than 15 %. Recently, Loubière et al. (2019) developed strategies to determine optimal bioreactor configurations for the culture of mesenchymal stem cells in stirred tank vessels, on spherical microcarriers by using a coupled CFD-genetic algorithm approach [43]. The optimization criterion was a minimization of power dissipation encountered by the particles, at the particle just-suspended state.

Despite the referenced studies, the identification of the impact of impeller geometry choice on bioleaching reactor hydrodynamics remains incomplete, especially in multi-stage bioreactors, which are the most commonly used at the industrial scale. Moreover, no studies put into evidence the coupling between power dissipation, solid homogeneity and occurrence of particle stress. The present work was focused on the

comparison of the effects of the impellers design on the hydrodynamics of a two-stage solid-liquid bioleaching reactor. For this, more than 50 CFD simulations based on a liquid-solid granular Euler-Euler model were carried-out with six radial and axial impeller designs. The performance of each impeller was quantified through the power number N_P and compared with literature data. Furthermore, the standard deviation of the solid concentration distribution was calculated to determine the respective efficiency of the impellers on solid scattering. The spatial distribution of hydromechanical stress on particles was determined for each bioreactor configuration and for three solid concentrations of 10, 18 and 26 % w/w.

3.2.2 Material and Methods

Model description

In this work, a steady-state Eulerian-Eulerian multiphase approach was used to simulate the solid-liquid flow, where the continuous and dispersed phases are considered as interpenetrating continua. Both phases are identified by their own volume fraction and are related as:

$$\alpha_\mathrm{s} + \alpha_\mathrm{l} = 1 \tag{3.2}$$

where α_s and α_l are the volume fractions of the solid and liquid phases respectively. The continuity equation for each phase can be written as:

$$\nabla \cdot (\alpha_\mathrm{l} \rho_\mathrm{l} \mathbf{u}_\mathrm{l}) = -\nabla (\gamma_\mathrm{s} \nabla \alpha_\mathrm{s}) \tag{3.3}$$

$$\nabla \cdot (\alpha_\mathrm{s} \rho_\mathrm{s} \mathbf{u}_\mathrm{s}) = \mathbf{F}_\mathrm{TD} = -\nabla (\gamma_\mathrm{s} \nabla \alpha_\mathrm{s}) \tag{3.4}$$

where ρ and $\mathbf{u}$ are the density and velocity of each phase, and $\mathbf{F}_\mathrm{TD}$ is related to the turbulent dispersion force. This turbulent dispersion force takes into account the dispersion due to turbulent velocity fluctuations and was modelled using the diffusion-in-VOF model. The diffusion coefficient γ_s is related to the turbulent viscosity $\mu_\mathrm{t,l}$ by $\gamma_\mathrm{s} = \mu_\mathrm{t,l}/0.75$. The momentum conservation equation for each phase is:

$$\nabla \cdot (\alpha_\mathrm{l} \rho_\mathrm{l} \mathbf{u}_\mathrm{l} \mathbf{u}_\mathrm{l}) = -\alpha_\mathrm{l} \nabla p + \alpha_\mathrm{l} \rho_\mathrm{l} \mathbf{g} + \nabla \cdot \overline{\overline{\boldsymbol{\tau}}}_\mathrm{l} + \mathbf{F}_\mathrm{D,ls} \tag{3.5}$$

$$\nabla \cdot (\alpha_\mathrm{s} \rho_\mathrm{s} \mathbf{u}_\mathrm{s} \mathbf{u}_\mathrm{s}) = -\alpha_\mathrm{s} \nabla p - \nabla p_\mathrm{s} + \alpha_\mathrm{s} \rho_\mathrm{s} \mathbf{g} + \nabla \cdot \overline{\overline{\boldsymbol{\tau}}}_\mathrm{s} - \mathbf{F}_\mathrm{D,ls} \tag{3.6}$$

where p is the pressure field shared by the two phases, p_s is the solid pressure, $\mathbf{g}$ the gravitational acceleration, $\overline{\overline{\boldsymbol{\tau}}}$ the phase stress strain tensor and $\mathbf{F}_\mathrm{D,ls}$ the interphase momentum transfer.

Interphase forces that are generally expected in a multiphase liquid-solid flow include: turbulent dispersion, drag, virtual mass, Basset and lift forces. Previous studies have shown that solid-liquid flows in STR are correctly represented using only turbulent dispersion and drag forces with a low effect of other forces on simulation results [44–46]. The turbulent dispersion force $\mathbf{F}_{\mathrm{TD}}$ should be modelled when the size of turbulent eddies is larger than the particle size [39, 47] which is a priori expected in standard bioreactors. Furthermore, the virtual mass, Basset and lift forces may be neglected as they have a much lower magnitude than the drag forces [16, 48, 49].

The drag force $\mathbf{F}_{\mathrm{D,ls}}$ between liquid and solid phases was calculated by the following equation:

$$\mathbf{F}_{\mathrm{D,ls}} = K_{\mathrm{ls}} \left(\mathbf{u}_{\mathrm{s}} - \mathbf{u}_{\mathrm{l}} \right) \tag{3.7}$$

with K_{ls} the interphase exchange coefficient between liquid and solid phases respectively, determined by:

$$K_{\mathrm{ls}} = C_{\mathrm{D,ls}} \frac{3}{4} \rho_{\mathrm{l}} \frac{\alpha_{\mathrm{s}} \alpha_{\mathrm{l}}}{d_{\mathrm{p}}} \left| \mathbf{u}_{\mathrm{s}} - \mathbf{u}_{\mathrm{l}} \right| \tag{3.8}$$

The drag coefficient $C_{\mathrm{D,ls}}$ is given by the Schiller and Naumann model [50]:

$$C_{\mathrm{D,ls}} = \begin{cases} 24 \left(1 + 0.15 Re_{\mathrm{p}}^{0.687} \right) / Re_{\mathrm{p}} & Re_{\mathrm{p}} < 1000 \\ 0.44 & Re_{\mathrm{p}} \geq 1000 \end{cases} \tag{3.9}$$

with Re_{p} the particle Reynolds number:

$$Re_{\mathrm{p}} = d_{\mathrm{p}} \left(\mathbf{u}_{\mathrm{s}} - \mathbf{u}_{\mathrm{l}} \right) / \nu_{\mathrm{l}} \tag{3.10}$$

The dispersed k-ε model was chosen as it is recommended for multiphase flows considering a continuous and a dispersed phases with a density ratio between phases equal or higher to 2.5 (s.n. [51]). This is often validated in bioleaching as most substrates are sulphidic materials of density higher than 2.5. In our case, water was chosen as the liquid phase ($\rho_{\mathrm{l}} = 1000\,\mathrm{kg\,m^{-3}}$, $\mu_{\mathrm{l}} = 0.001\,\mathrm{Pa\,s}$) and particles with the characteristics of grinded pyrite-rich materials ($\rho_{\mathrm{s}} = 2610\,\mathrm{kg\,m^{-3}}$, $d_{\mathrm{p}} = 80$ µm, pyrite fraction = 51 %) were considered for the solid phase. In this approach, turbulence is fully-modelled for the continuous phase and the turbulence of the dispersed phase is possibly taken into account through additional interaction terms. The k-ε model provides the transport equations of the turbulent kinetic energy k and its dissipation rate ε:

$$\nabla \cdot \left(\alpha_{\mathrm{l}} \rho_{\mathrm{l}} \mathbf{u}_{\mathrm{l}} k_{\mathrm{l}} \right) = \nabla \cdot \left(\alpha_{\mathrm{l}} \left(\mu_{\mathrm{l}} + \frac{\mu_{\mathrm{t,l}}}{\delta_k} \right) \nabla k_{\mathrm{l}} \right) + \alpha_{\mathrm{l}} G_{k,\mathrm{l}} - \alpha_{\mathrm{l}} \rho_{\mathrm{l}} \varepsilon_{\mathrm{l}} \tag{3.11}$$

$$\nabla \cdot (\alpha_\mathrm{l} \rho_\mathrm{l} \mathbf{u}_\mathrm{l} \varepsilon_\mathrm{l}) = \nabla \cdot \left(\alpha_\mathrm{l} \left(\mu_\mathrm{l} + \frac{\mu_{\mathrm{t,l}}}{\delta_\varepsilon} \right) \nabla \varepsilon_\mathrm{l} \right) + \alpha_\mathrm{l} \frac{\varepsilon_\mathrm{l}}{k_\mathrm{l}} \left(C_{\varepsilon 1} G_{k,\mathrm{l}} - C_{\varepsilon 2} \rho_\mathrm{l} \varepsilon_\mathrm{l} \right) \tag{3.12}$$

$\mu_{\mathrm{t,l}}$ is the turbulent viscosity of the continuous liquid phase:

$$\mu_{\mathrm{t,l}} = \rho_\mathrm{l} C_\mu \frac{k_\mathrm{l}^2}{\varepsilon_\mathrm{l}} \tag{3.13}$$

$G_{k,\mathrm{l}}$ is the term of production of turbulent kinetic energy and the constants are defined as follow: $C_\mu = 0.09$, $C_{\varepsilon 1} = 1.44$, $C_{\varepsilon 2} = 1.92$, $\delta_k = 1$ and $\delta_\varepsilon = 1$.

Lastly, no additional interaction terms were taken into account for turbulence as preliminary simulations showed no impact of these terms on simulation results (data not shown).

The particle-particle interactions were modelled by the kinetic theory of granular flows, which is an extension of the model for molecular motion in a dense gas phase. It aims at determining the solid pressure p_s which represents the normal forces due to particle interactions. From the kinetic theory, Jenkins and Savage (1983) proposed that this solid pressure is the sum of a kinetic energy term and of one term that includes the particle-particle collisions [52]:

$$p_\mathrm{s} = \alpha_\mathrm{s} \rho_\mathrm{s} \theta_\mathrm{s} + 2 \rho_\mathrm{s} \left(1 + e_\mathrm{ss} \right) \alpha_\mathrm{s}^2 r_0 \theta_\mathrm{s} \tag{3.14}$$

The coefficient of restitution of particle collision e_ss is set to 0.9. The granular temperature θ_s is a measure of the kinetic energy due to the fluctuating velocities u'_s of the particles:

$$\theta_\mathrm{s} = \frac{1}{3} {u'_\mathrm{s}}^2 \tag{3.15}$$

Neglecting the convective and diffusive transports, the transport of the granular temperature within the bioreactor is provided by Ding and Gidaspow (1990) [53]:

$$\left(-p_\mathrm{s} \bar{\bar{\mathbf{I}}} + \bar{\bar{\boldsymbol{\tau}}}_\mathrm{s} \right) : \nabla \mathbf{u}_\mathrm{s} - \gamma_{\theta_\mathrm{s}} + \phi_\mathrm{ls} \tag{3.16}$$

First-term of the left-hand side represents the generation of fluctuating energy due to the solid pressure and viscous force; the second term is the dissipation of the fluctuating energy and the last term is the exchange of fluctuating energy between liquid and solid phases respectively. The transfer of fluctuating energy is given by:

$$\phi_\mathrm{ls} = -3 K_\mathrm{ls} \theta_\mathrm{s} \tag{3.17}$$

The collisional dissipation of energy γ_{θ_s} is provided by:

$$\gamma_{\theta_s} = \frac{12\left(1-e_{ss}^2\right) r_0}{d_p \pi^{0.5}} \rho_s \alpha_s^2 \theta_s^{3/2} \tag{3.18}$$

The radial distribution function r_0 is a correction factor that modifies the probability of collisions between particles when the solid granular phase becomes dense:

$$r_0 = \frac{a + d_p}{a} \tag{3.19}$$

with a the distance between the particles. In our case, this distribution is determined by:

$$r_0 = \left[1 - \left(\frac{\alpha_s}{\alpha_{s,max}}\right)^{1/3}\right]^{-1} \tag{3.20}$$

with $\alpha_{s,max} = 82$ % w/w (corresponding to 63 % v/v), the particle packing limit.

The solid shear stress tensor $\overline{\overline{\boldsymbol{\tau}}}_s$ arises from particle momentum exchange due to translations and collisions and depends on the solid viscosity:

$$\overline{\overline{\boldsymbol{\tau}}}_s = \mu_s \nabla \mathbf{u}_s = \left(\mu_{s,col} + \mu_{s,kin}\right) \nabla \mathbf{u}_s \tag{3.21}$$

The collisional contribution to the shear viscosity is given by:

$$\mu_{s,col} = \frac{4}{5} \alpha_s \rho_s d_p r_0 \left(1 + e_{ss}\right) \left(\frac{\theta_s}{\pi}\right)^{1/2} \tag{3.22}$$

And the kinetic viscosity by:

$$\mu_{s,kin} = \frac{10 \rho_s d_p \sqrt{\theta_s \pi}}{96 \alpha_s \left(1 + e_{ss}\right) r_0} \left[1 + \frac{4}{5} r_0 \alpha_s \left(1 + e_{ss}\right)\right]^2 \tag{3.23}$$

Simulation setup

The geometry setup for the simulation of the lab-scale bioreactor is shown on Fig. 3.2; this bioreactor is routinely used for bioleaching experiments. The tank was a cylindrical vessel of diameter $T = 0.12$ m and liquid height $H = 0.187$ m. The tank was equipped with four conical baffles of width equal to $T/10$, placed symmetrically.

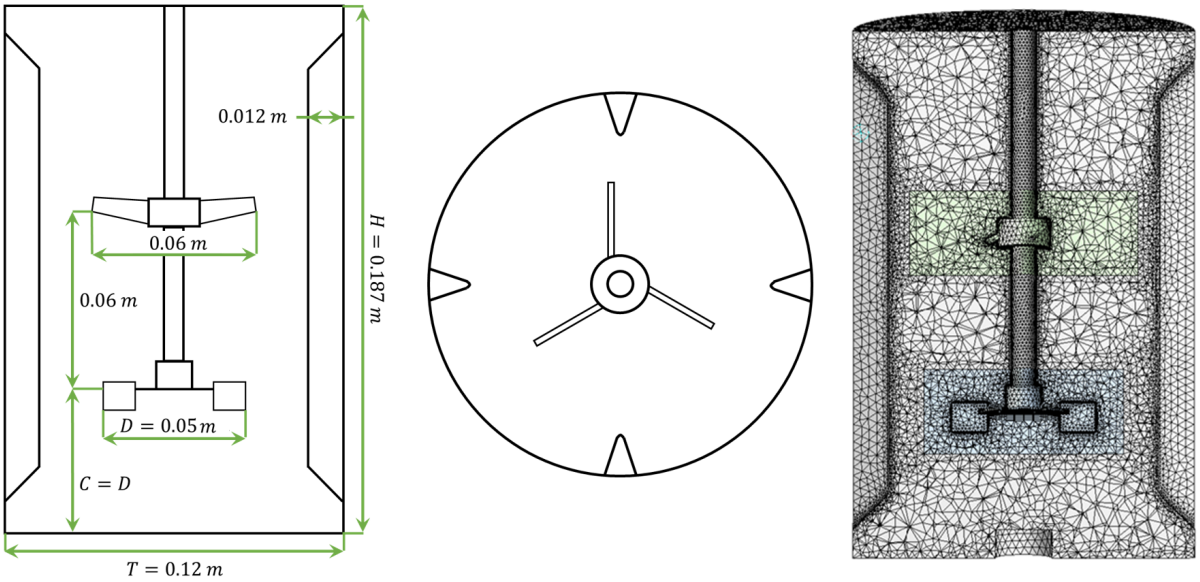

Figure 3.2: Planar view (left), cross-section (middle) and mesh (right) of the two-stage stirred tank reactor.

A dual impeller configuration was chosen using various bottom impeller designs but a fixed design for the top impeller (Fig. 3.3). Considering the height on tank diameter ratio, the choice of a multi-stage design is recommended to provide sufficient liquid mixing near the surface. As the focus was put on particles suspension and stress, and to limit the number of configurations simulated, only the bottom impeller design was modified. The bottom impellers had a fixed diameter $D = 0.05$ m with an off-bottom clearance $C = D$. The top impeller, a three-blade hydrofoil (A310), was positioned at a spacing $S = 0.06$ m above the bottom impeller and had a diameter equal to 0.06 m.

Each impeller configuration was simulated at 6 different agitation rates ($N = 200$, 300, 400, 500, 600 and 700 rpm), ensuring fully turbulent conditions for each case ($10^4 < \mathrm{Re} < 5 \times 10^4$). Moreover, the impact of the solid concentration on solid-liquid suspension was also determined by fixing three different solid concentrations: 10, 18 and 26 % w/w. A non-uniform mesh structure was created to divide the geometry setup using the Fluent Meshing tool and was composed of 400,000 tetrahedral elements. Refinements were done along the wall and in the impellers regions. Mesh independence was preliminary verified by comparing velocity vectors fields and volume-averaged power dissipation.

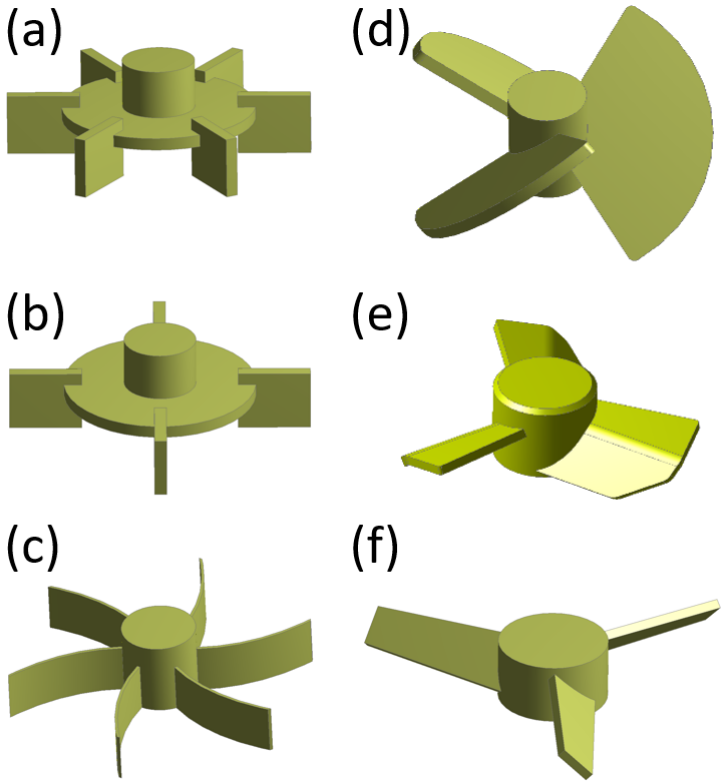

Figure 3.3: Impellers used in simulations. (a) 6-bladed Rushton turbine (RT6B); (b) 4-bladed Rushton turbine (RT4B); (c) R600 spiral backswept impeller (R600); (d) Elephant-Ear impeller operating in down-pumping mode (EEd); (e) HTPG impeller operating in down-pumping mode (HTPGd); (f) Lightnin A310 impeller operating in up-pumping mode (A310).

Power consumption

To obtain the power number N_{p} defined in eq.3.1, the power consumption P was calculated by the following equation:

$$P = 2\pi N C_w \tag{3.24}$$

with N the agitation rate and C_w the impeller torque, which was determined by the numerical simulations. Mechanical energy balance within the bioreactor imposes that the power consumption P should be of the same order of magnitude as the dissipated power P_{diss} determined by the turbulence model:

$$P_{\mathrm{diss}} = \rho_{\mathrm{l}} \langle \varepsilon \rangle V_{\mathrm{l}} \tag{3.25}$$

Solid dispersion

Solid dispersion is a key process parameter in solid-liquid bioreactors as it strongly impacts the mass transfer to the particles but also the microenvironment of substrates around the particles. One way to determine the suspension quality is to use the Zwietering correlation which models the just-suspended agitation rate of the particles N_{js} in

the bioreactor (based on the Zwietering criterion that considers the particles as they do not remain settled more than 2 seconds near the vessel bottom at the just-suspended state). It is generally assumed that the bioreactor and impeller geometries have an impact on N_{js} but also on the operating conditions of the process:

$$N_{\mathrm{js}} \propto \nu_{\mathrm{l}}^{0.1} \left[\frac{g\left(\rho_{\mathrm{s}} - \rho_{\mathrm{l}}\right)}{\rho_{\mathrm{l}}}\right]^{0.45} \cdot W_{\mathrm{s}}^{0.13} d_{\mathrm{p}}^{0.2} D^{-0.85} \tag{3.26}$$

Thus, for a given bioreactor configuration and operating conditions, the scaling law $N_{\mathrm{js}} \propto W_{\mathrm{s}}^{0.13}$ should be obtained. Despite the interest of determining this criterion, it is insufficient if the distribution of particle concentrations or stresses are also looked for. One way to improve the description of the particles suspension behaviour is to determine the suspension quality H_{s} which can be calculated as the volume-averaged difference between the local and the mean concentration of solid particles [26, 45, 54, 55]. This parameter is determined using the local fraction of each elements of the mesh:

$$H_{\mathrm{s}} = 1 - \sqrt{\frac{1}{V_{\mathrm{tot}}} \cdot \iiint_{V_{\mathrm{tot}}} \left(\alpha_{\mathrm{s}} - \langle \alpha_{\mathrm{s}} \rangle\right)^2 \, dV} \tag{3.27}$$

where α_{s} denotes the local volume fraction of the solid phase and $\langle \alpha_{\mathrm{s}} \rangle$ represents the volume-averaged value of particle concentration in the vessel. This value of H_{s} had to be adjusted to take into account the packing limit of the particles given by the maximal local solid concentration of 82 % w/w:

$$H_{\mathrm{s,adj}} = \frac{H_{\mathrm{s}} - H_{\mathrm{s,min}}}{H_{\mathrm{s,max}} - H_{\mathrm{s,min}}} \tag{3.28}$$

where $0.75 < H_{\mathrm{s,min}} < 0.85$ and $H_{\mathrm{s,max}} = 1$ are respectively the minimal and maximal values of H_{s} for $\alpha_{\mathrm{s}} = \alpha_{\mathrm{s,max}} = 0.82$ and $\alpha_{\mathrm{s}} = \alpha_{\mathrm{s,min}} = \langle \alpha_{\mathrm{s}} \rangle$. The value of $H_{\mathrm{s,min}}$ is dependent on the volume-averaged concentration of particles considered in the calculations.

Solution method

The commercial software ANSYS Fluent 2019R3 was used for the numerical simulation of the multiphase flow. The conservation equations presented in Eq.3.2-3.23 were applied in all meshes and were solved using the steady-state Eulerian method. The impellers rotation was modelled using the multiple reference frame approach. The rotating domain was positioned at $r_{\mathrm{bottom}} = 0.035$ m, $0.036 \text{ m} \leq z_{\mathrm{bottom}} \leq 0.066$ m and $r_{\mathrm{top}} = 0.040$ m, $0.096 \text{ m} \leq z_{\mathrm{top}} \leq 0.126$ m, respectively for the bottom and the top impellers. The pressure-velocity based solver using the SIMPLE algorithm was used to solve the set of conservation equations. Discretization of the mass, momentum and volume fraction equations was carried-out using the second-order upwind scheme while pressure was spatially discretized using the PRESTO! scheme (s.n. [51]). Convergence

of the simulations was admitted when transport equations residuals were less than 10^{-3} and when the local solid volume fraction reached a steady state at three locations of the vessel ($r = 0.025$ m and $z = 0.025$, 0.090 and 0.160 m).

3.2.3 Results and discussion

Liquid flow patterns

Firstly, to validate the accuracy of the CFD model, the flow patterns were qualitatively compared with data from the literature. The dimensionless liquid velocity profiles shown in Fig. 3.4 present the flow patterns induced by the dual-impellers bioreactor. The top A310 showed the predicted pattern of a mixed flow, presenting a one-loop flow pattern as it operates in up-pumping mode, which was also shown by Vrábel et al. (2000) on a multiple impellers configuration [56]. The proximity of the liquid surface promoted the formation of two supplementary liquid loops. For the bottom impeller, various flow patterns were observed depending on the impeller used: the radial impellers (RT4B, RT6B and R600) generated a two-loop pattern with a radial ejection of the liquid towards the reactor wall while the down-flow axial impellers (HTPGd and EEd) showed a single-loop flow pattern. These results agreed with the experimental results of previous studies as similar flow patterns were shown for radial impellers by Zhang et al. (2017) and for down-flow axial impellers by Bouaifi and Roustan (2001) [19, 20]. As expected, the choice of the tip speed $u_{\text{tip}} = \pi ND$. as a representative design parameter is highly questionable, as shown by the variability of the flow pattern from one configuration to another [38].

Power consumption

The power numbers of each impeller were calculated using eq. 3.1 for each agitation rates and solid concentrations and the mean value obtained and standard deviation were compared with data from literature, as shown in Table 3.1.

Table 3.1: Mean value and standard deviation of the calculated impeller power numbers for each impeller configuration used and comparison with data from literature (referenced N_{p}).

Impeller	**Calculated N_{p}**	**Referenced N_{p}**	**Literature reference**
RT4B	3.1 ± 0.1	4.0	[57]
RT6B	4.0 ± 0.1	4.0 - 6.0	[18]
R600	3.6 ± 0.3	4.2	[57]
HTPGd	0.73 ± 0.07	0.67	[57]
EEd	1.9 ± 0.1	1.7 - 2.1	[43, 58]
A310	0.76 ± 0.05	0.3 - 0.5	[27]

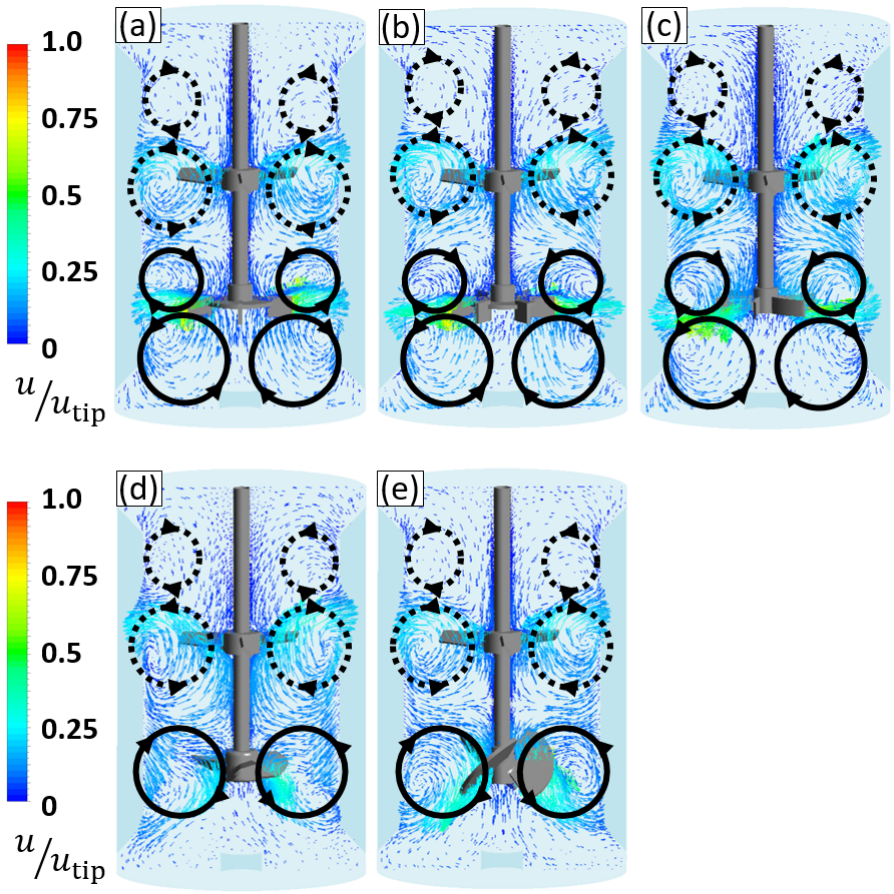

Figure 3.4: Normalized liquid velocity vectors profiles at 500 rpm for: (a) the RT4B-A310 configuration; (b) the RT6B-A310 configuration; (c) the R600-A310 configuration; (d) the HTPGd-A310 configuration; (e) the EEd-A310 configuration. The tip speed was given by $u_{\text{tip}} = \pi N D$.

The results showed that for fully turbulent conditions, the variation of agitation rates induced few variations of the power numbers compared to the expected values, as classically expected in turbulent regime [17, 59]. Moreover, the predicted values of N_{p}, calculated for each impeller in the two-stage configurations, are similar to those reported for single-impeller configurations meaning that the total power consumption is approximately equal to the additive power consumption of both impellers. This can be explained by the fact that, with enough spacing between the impellers ($S/D > 1$), the respective dissipated power of the impellers in a two-stage reactor is similar to those obtained in a single-stage reactor [60, 61]. Lastly, the power consumption of the upper A310 impeller was independent of the bottom impeller design (data not shown), which confirmed that both impellers were not interacting with each other. The CFD simulations also showed that the power dissipation calculated by the turbulence model was, on average over all configurations, equal to 58 % of the power consumption determined by the torque of the impeller. This result is in accordance with most CFD simulations carried-out with the $k - \varepsilon$ turbulence model [62].

As shown by Loubière et al. (2019) for various designs of impellers, the particle just-suspended state is clearly related to the total power consumption per unit of volume P_{tot}/V, which considers the power demand of both impellers [43]. Thus, the values of this parameter were evaluated for the different impeller configurations in order to determine the best configuration in term of particle suspension, at a given agitation rate (Fig. 3.5). The results showed that, independently of the agitation rate, the configurations with a bottom axial impeller (HTPGd and EEd) consumed less energy than the configurations with a bottom radial impeller (RT4B, RT6B and R600). This agreed with the relative power numbers given in Table 3.1 and with the experimental results reported by Bouaifi and Roustan (2001) and Wang et al. (2010) [19, 63].

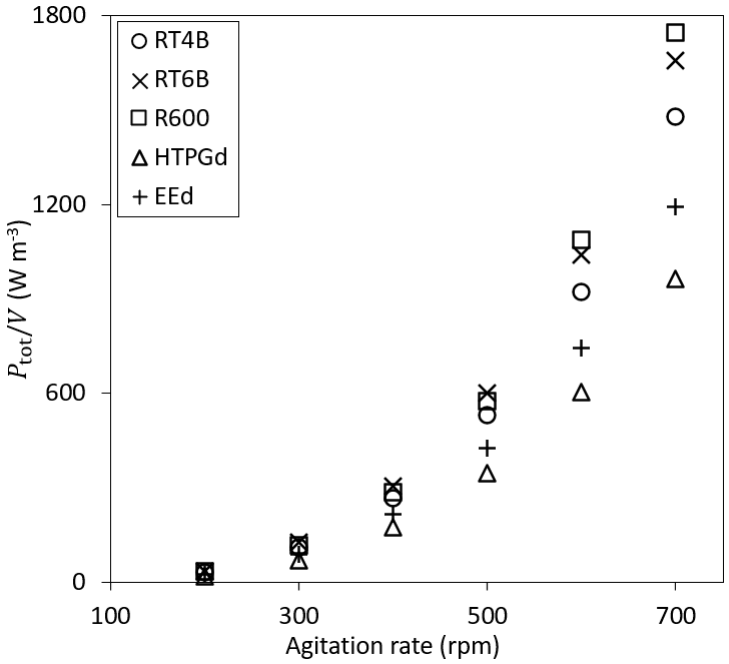

Figure 3.5: Variation of the total power consumption per unit volume P_{tot}/V with the agitation rate, for each impeller configuration. Particle concentration was 10 % w/w.

Particle mixing degree

To determine the particle mixing degree, the values of $H_{\text{s,adj}}$ were calculated for each configuration and operating condition of the bioreactor (Fig. 3.6). The values obtained showed a logarithmic increase with the agitation rate, with values ranging from 35 to 95 %. All configurations showed the same shape of particle mixing profile but with non-negligible relative differences, especially at low agitation rates. These differences were up to 40 % at 200 rpm between HTPGd and RT6B impellers but less than 10 % at 500 rpm and below. Independently of the agitation rate, both the RT6B and the EEd were the best to scatter particles throughout the tank at a given agitation rate. On the other hand, the HTPGd was the less efficient impeller in term of solid homogenization, with the lowest $H_{\text{s,adj}}$ for all the simulated agitation rates. This was

emphasized by the discrepancies observed on the particle distribution, as shown by Fig. 3.7 (a-b) for 400 rpm. While for the RT6B impeller, the just-suspended state was clearly observed, the suspension of particles was still partial in the case of the HTPGd impeller, as indicated by the occurrence of settled particles ($\alpha_{s,max} = 0.82$ w/w) near the vessel bottom. Moreover, the radial impellers clearly showed a higher efficiency at bringing the particles upward (Fig. 3.7a), making the particle bed evolves to a cone shape at high agitation rate while the axial impellers promoted a pseudo-planar shape of particle bed.

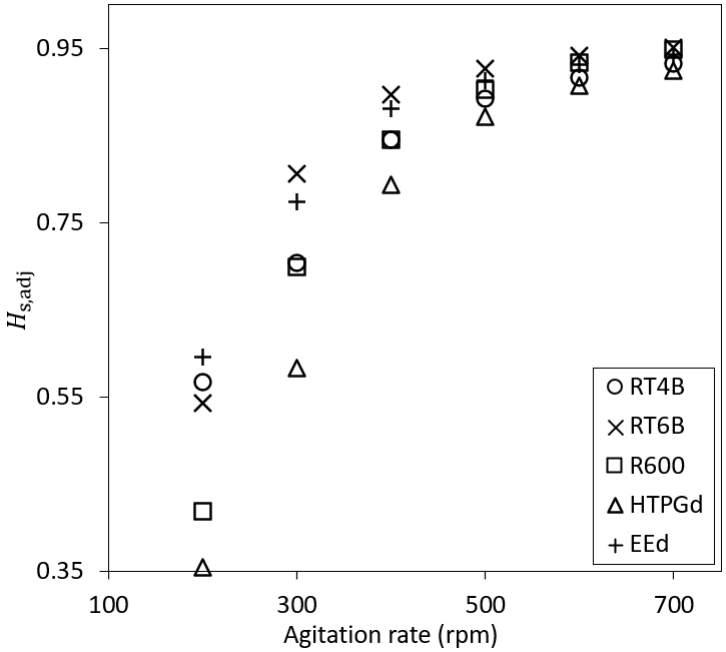

Figure 3.6: Suspension quality $H_{s,adj}$ for each impeller configuration. Particle concentration was 10 % w/w.

Aiming at determining a robust design criterion, the suspension quality $H_{s,adj}$ variation with the total power dissipation per unit volume was also determined (Fig. 3.8a). This variation could be divided into two zones. For power dissipation per unit of volume less than 600 W m^{-3} approximately, the parameter $H_{s,adj}$ rapidly increased till a value of $H_{s,adj} \simeq 0.90$; regarding the particles distribution obtained for this range of power dissipation, only partial suspension was determined. For P_{tot}/V higher than 600 W m^{-3}, the value of $H_{s,adj}$ slowly increased till 0.95 approximately, indicating a progressive particle homogenization beyond the just-suspended state. Thus, a substantial increase of mechanical energy consumption is required to achieve a minor enhancement of the particle homogenization. Moreover, it was also shown that total homogeneity ($H_{s,adj} = 1.0$) is not achievable as all the data tend to stagnate below $H_{s,adj} = 0.95$. This could be explained by the fact that, even for high power dissipation per unit of volume, a small region near the free surface remained free or poorly concentrated in particles, as demonstrated by Delafosse et al. (2018) [64]. Lastly, it is interesting to

note that, for a given power dissipation per unit of volume, the variations of $H_{s,adj}$ were approximately independent of the bioreactor designs, meaning that power dissipation per unit of volume could be used not only as scaling parameter for particles just-suspended state determination but also to predict the quality of particles homogenization. Previous experiments by Magelli et al. (1991) have shown similar results in a single-stage vessel and pointed that it could be a basis for design optimization [65]. Based on these results, it could be advised to promote the use an impeller which can achieve a high power dissipation per unit volume, even at the lowest agitation rate. This could indeed allow to get particle suspension at lower values of agitation rate and tip speed, which should limit the mechanical problems expected at high tip speeds.

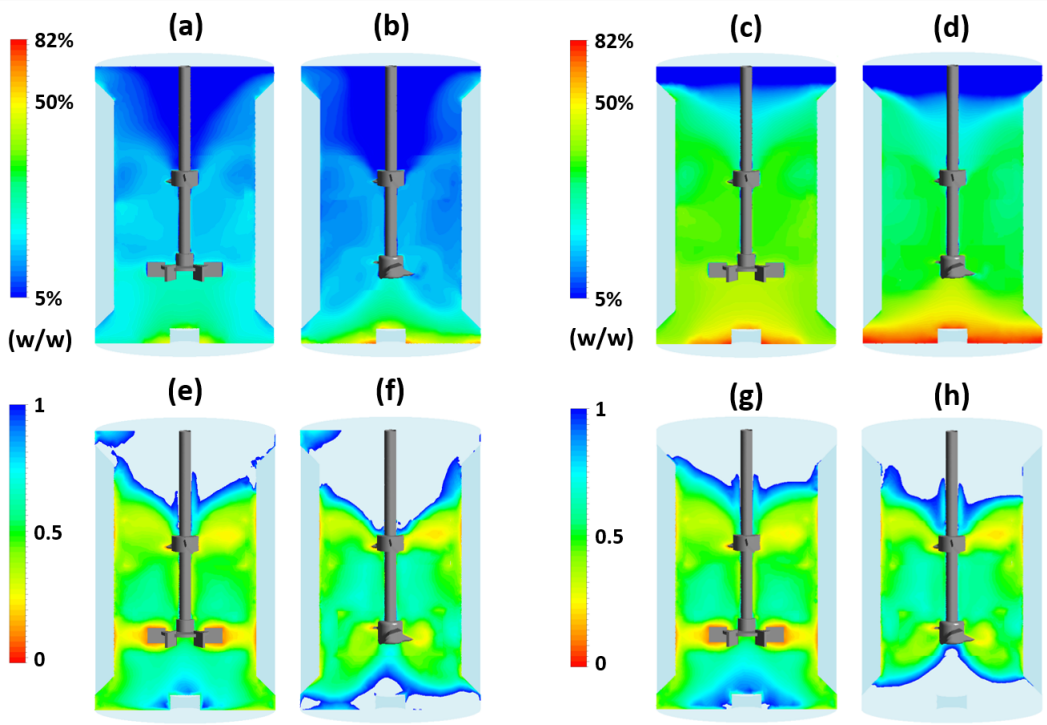

Figure 3.7: Simulated particles distribution at N = 400 rpm for: (a) RT6B-A310 configuration with 10 % w/w solid; (b) HTPGd-A310 configuration with 10 % w/w solid; (c) RT6B-A310 configuration with 26 % w/w solid; (d) HTPGd-A310 configuration with 26 % w/w solid. Comparison of the particle size with the Kolmogorov length scale (l_K/d_p) for: (e) RT6B-A310 configuration with 10 % w/w solid; (f) HTPGd-A310 configuration with 10 % w/w solid; (g) RT6B-A310 configuration with 26 % w/w solid; (h) HTPGd-A310 configuration with 26 % w/w solid.

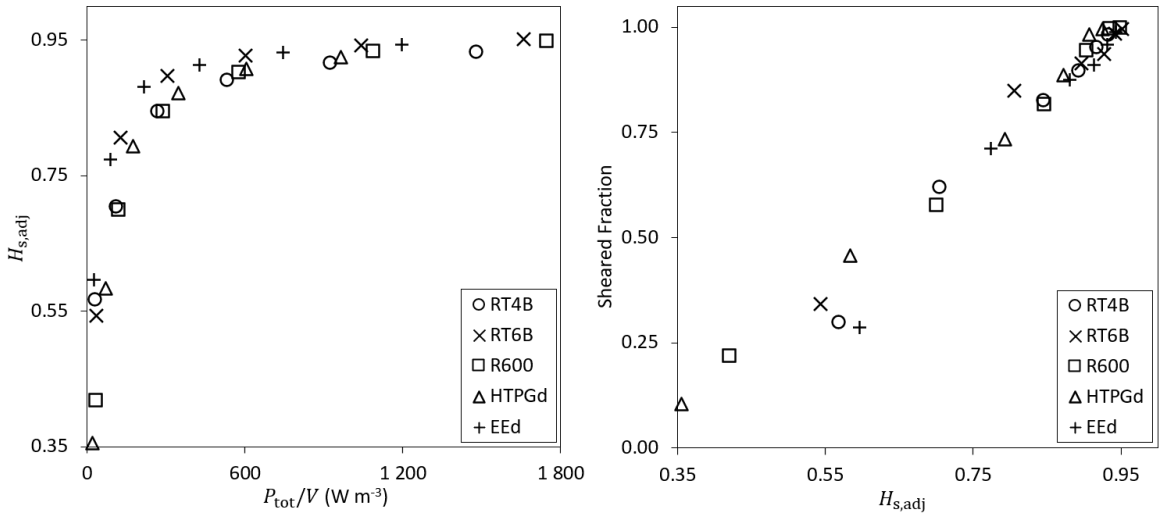

Figure 3.8: Solid distribution $H_{s,adj}$ as a function of power dissipation per unit volume P_{tot}/V (left) ; Suspension quality $H_{s,adj}$ as a function of the sheared fraction (right). Particle concentration was 10 % w/w.

Particle stress

As discussed in the introductory part, it is generally assumed that only the turbulent eddies of the same order of length or lower than the particle size are potentially detrimental to the particles and thus the microbial adhesion and biofilm formation. Henzler (2000) stated that turbulent eddies of the same size of the particles are the most likely to damage the particles [66]. In this case, namely some turbulent eddies are lower than the particle diameter, particles are transported in the inertial subrange of turbulence and are subjected to turbulent stresses. To quantify the relationships between particle stress and hydrodynamics, Thomas (1964) provided the expression of particle stress as related to the local mean square fluctuating liquid velocities $\overline{u_l'}$ [67].

$$\sigma_p = \rho_l \overline{u_l'^2} = 0.7\rho_l \left(\varepsilon d_p\right)^{2/3} \propto \varepsilon^{2/3} \tag{3.29}$$

In isotropic and homogeneous turbulence, the local mean square fluctuating liquid velocities depends on the local turbulent dissipation rate ε and on particle diameter d_p. If $d_p < l_K$, the particles are transported in the viscous subrange of the turbulence and are mainly subjected to viscous stresses given by:

$$\sigma_p = \mu G = \mu \sqrt{\frac{\varepsilon}{\nu_l}} \propto \varepsilon^{1/2} \tag{3.30}$$

with G (s^{-1}) the local velocity gradient.

From the preceding results, it appears clear that the determination of hydromechanical stresses acting on particles when suspended in the mixing tank should be determined locally and considering the relative ratio of the particle size on the Kolmogorov length scale. Thus, it was proposed here to assert the hydromechanical stress by calculating the sheared fraction SF (eq. 3.31), representing the percentage of particles volume under sheared conditions, namely in areas showing Kolmogorov scales lower than the particle diameter ($l_{\mathrm{K}} < d_{\mathrm{p}}$).

$$SF = \frac{1}{V_{\mathrm{s}}} \cdot \iiint_{V_{\mathrm{s}}(l_K < d_{\mathrm{p}})} dV_{\mathrm{s}} = \frac{1}{V_{\mathrm{s}}} \cdot \iiint_{V_{\mathrm{s}}(l_K < d_{\mathrm{p}})} \alpha_{\mathrm{s}}\, dV \tag{3.31}$$

The variation of the sheared fraction SF with the suspension quality $H_{\mathrm{s,adj}}$ was reported in Fig. 3.8. As one could expect, the stress on particles was growing higher as the suspension quality increased. You et al. (2020) obtained similar results using bioleaching continuous STR and reported that it was clearly linked to the mechanical forces acting on microbial productivity through the damaging mechanisms explained in this work [68]. The variation of SF also showed that all the impeller designs presented the same linear evolution of SF, meaning that all the configurations would generate a similar particle stress for a given suspension quality. This could be partially explained by the previous results that put into evidence the relation between particle homogenization and total power demand. It is also interesting to note that, reaching a quasi-consistent homogenization of the particles implied that almost all the particles would encounter potentially damaging turbulent eddies that could promote biofilm detachment. When particles were not homogeneously distributed in the bioreactor, it is also important to consider the spatial distribution of the Kolmogorov length scales l_{K}, as it differed from one impeller to another, as shown in Fig. 3.7e and Fig. 3.7f. In conclusion, despite each bioreactor configuration generated different turbulent dissipation fields, the physical link between flow velocity, turbulent dissipation and particle concentrations led to unique relationships between sheared fraction of particles and suspension quality, whatever the impeller used. This also potentially questions the existence of 'shearing' or 'non-shearing' impellers when the degree of homogenization is considered as comparison parameter.

Impact of particle concentrations on bioreactor hydrodynamics

Considering that an increase of solid concentrations could potentially simultaneously promote an increase in bioprocess productivity and detrimental physical phenomena, the impact of solid concentration (from 10 to 18 and 26 % w/w) on bioreactor hydrodynamics was determined. For these simulations, only the designs RT6B-A310 and HTPGd-A310 were considered. First, regarding the just-suspended state of the particles, the basic Zwietering's model predicts that the just-suspended agitation rate would be related to $N_{\mathrm{js}} \propto X^{0.13}$. The influence of X on N_{js} was confirmed by the CFD simula-

tions of the particles distributions generated by the RT6B and HTPGd configurations using solid concentrations of 10 and 26 % w/w as shown in Fig. 3.7 (a-d). Whereas no particle accumulation was observed for a particle loading of 10 % w/w at an agitation rate of 400 rpm for the RT6B impeller, settled particles were predicted by the simulations at the same agitation rate for a solid concentration of 26 % w/w, indicating that the agitation rate switched below N_{js} (Fig. 3.7a and Fig. 3.7c). For the HTPGd impeller, the small accumulation observed for a solid concentration of 10 % was clearly magnified for a solid concentration of 26 % (Fig. 3.7b and Fig. 3.7d). Considering the Zwietering's model, for a constant power number expected in the turbulent regime, the total power demand at the just-suspended state would be $P_{\mathrm{js}} \propto N_{\mathrm{js}}^3 \propto X^{0.4}$. On the basis of this global scaling law, the power demand for a mean solid concentration of 26 % would be $P_{\mathrm{js}}^{26\%} \simeq 1.55 \cdot P_{\mathrm{js}}^{10\%}$.

The effect of the solid concentration on particle homogenization is shown in Fig. 3.9 for RT6B-A310 and HTPGd-A310 configurations. For both of them, the CFD simulation results confirmed that the increase in solid concentration led to a rise of power demand per unit volume to reach a given suspension quality. Moreover, it was also put into evidence that the asymptotic value of $H_{\mathrm{s,adj}}$, obtained for the highest P_{tot}/V considered in this study, was progressively reduced as long as the solid concentration increased. For comparison, the power needed to achieve $H_{\mathrm{s,adj}} = 0.90$ with the RT6B was $(P_{\mathrm{tot}}/V)_{26\%} \simeq 2 \cdot (P_{\mathrm{tot}}/V)_{18\%} \simeq 6 \cdot (P_{\mathrm{tot}}/V)_{10\%}$. A similar trend was observed for the HTPGd with a smaller increase of power demand as the solid concentration rose, for $H_{\mathrm{s,adj}} = 0.87$, $(P_{\mathrm{tot}}/V)_{26\%} \simeq 1.7 \cdot (P_{\mathrm{tot}}/V)_{18\%} \simeq 3 \cdot (P_{\mathrm{tot}}/V)_{10\%}$. Considering the sheared fraction SF, it was shown that, for a given $H_{\mathrm{s,adj}}$, a higher fraction of particles was transported in the inertial subrange at higher solid concentrations. However, for both configurations and the three solid concentrations, the parameter SF reached a value close to 1 for the highest degrees of homogenization $H_{\mathrm{s,adj}}$ (Fig. 3.10). This could explained by the fact that, for the particles that were suspended, the local variations in solid concentration in the areas where $d_{\mathrm{p}} > l_{\mathrm{K}}$ were similar between 10 and 26 % w/w (Fig. 3.7 (e-h)). This was not true near the reactor bottom where settling was predicted for particle concentration of 26 % w/w and which explained the less efficient particle homogenization.

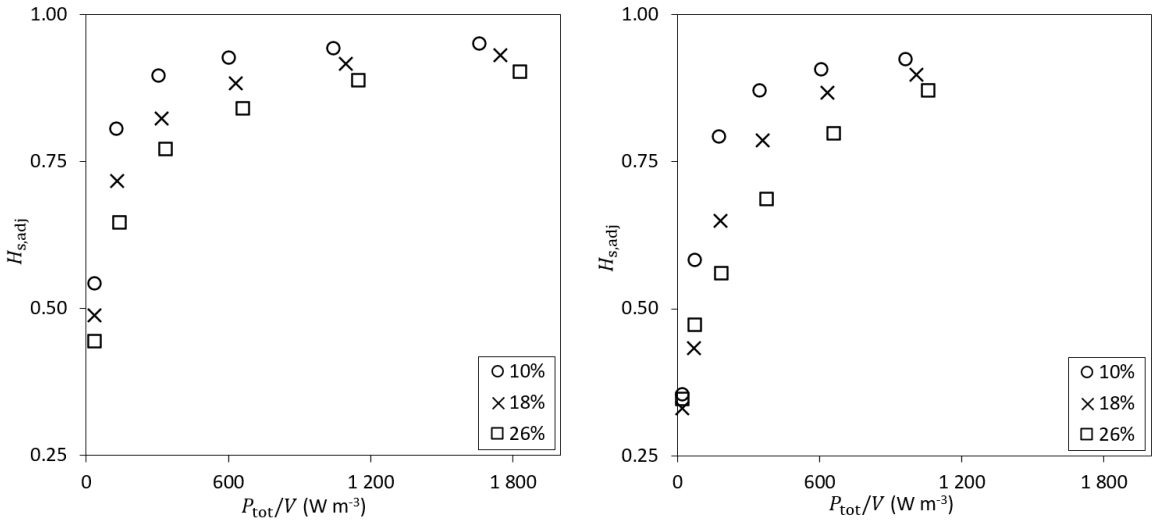

Figure 3.9: Solid distribution $H_{s,adj}$ as a function of power consumption per unit volume P_{tot}/V at different solid concentration for: (left) the RT6B-A310 configuration; (right) the HTPGd-A310 configuration.

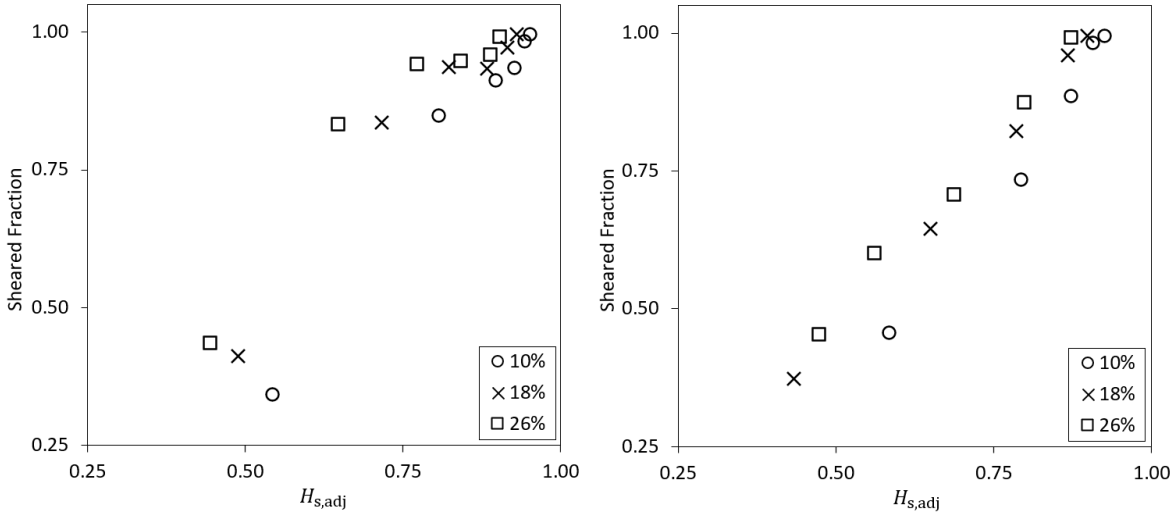

Figure 3.10: Suspension quality $H_{s,adj}$ as a function of the sheared fraction at different solid concentration for: (left) the RT6B-A310 configuration; (right) the HTPGd-A310 configuration.

3.2.4 Conclusion

The effect of the impeller design on the solid suspension was determined using 5 dual-impeller configurations and 3 solid concentrations. For this, the power consumption per unit of volume, the mixing efficiency and the particle stress were characterized by 50 CFD numerical simulations and theoretical models of particle stress.

The results indicated that the power demand per unit volume could be used to predict the suspension quality as the variations of $H_{s,adj}$ were independent of the bioreactor design for a given P_{tot}/V. However, due to higher power numbers, the impellers RT6B and EEd could achieve particle suspension at lower agitation rates. Further-

more, it was shown that increasing the solid loading let to a significant rise of the power consumption per unit volume to attain a given suspension quality. Lastly, the impact of each configuration on particle stress was assessed and the results showed that particle stress was independent of the reactor design at a given suspension quality. Consequently, it is difficult to advise a specific configuration and experimental conditions regarding particle stress when using the suspension quality as an optimisation criterion.

The choice of impeller design in a bioleaching STR is critical to ensure the best solid dispersion within the tank while maintaining a low power consumption and limiting the impact of shear stress on particles. For higher scales (pilot and industrial scales), the energy cost due to mixing represents a large part of OPEX expenses and impeller optimization should be closely considered. Nonetheless, further studies are still necessary to take into account the biological aspect of bioleaching and the impact of the design and the agitation on biomass.

3.2.5 Acknowledgments

The authors acknowledge the Institut Carnot ICEEL and the Institut Carnot BRGM for their financial support.

3.3 Study of particles dispersion and hydromechanical stress in a pilot-scale tank

In this section, it was determined whether the main conclusions that were previously drawn, namely that particle stress remains globally independent of the reactor design at a given suspension quality, could be confirmed at a larger bioreactor scale. For this purpose, the impact of the power demand per unit of volume P_{tot}/V, the suspension quality $H_{\text{s,adj}}$ and the sheared fraction SH were also modelled at the 800-liter scale using the same set of previous equations.

3.3.1 Geometry and meshing of the pilot-scale tank

Simulation setup

As scaling of the cylindrical 2-liter bioreactor, the BRGM pilot-scale tank was used as reference. The tank, shown on Fig. 3.11, had a working volume of 800 l, with a diameter $T = 0.950$ m, a liquid height $H = 1.159$ m and was equipped with 4 rectangular baffles of width equal to a tenth of the diameter and placed symmetrically.

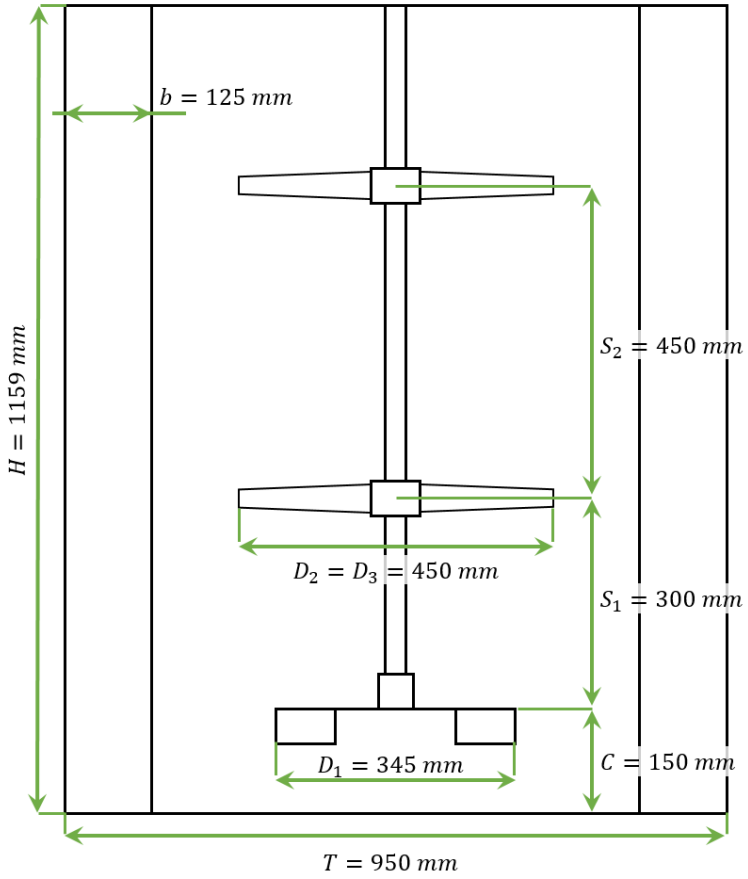

Figure 3.11: Representation of the three-stage stirred tank reactor. Bioreactor volume is 800l.

Despite a low aspect ratio $H/T = 1.22$, the tank was initially equipped with a three-stage impeller configuration, to ensure both solid homogenization and gas dispersion ; these impellers were represented on Fig. 3.12. For this, a bottom 6-bladed radial turbine (6B-DRT) was used with a low clearance $C = 0.150$ m that is expected to facilitate solid dispersion even at low agitation rates. The middle and top impellers were respectively represented by a Robin turbine HPM10 13° (HPM10A) and a Robin turbine HPM10 18° (HPM10B) ; the degree corresponds to the torsion angle of the blades. These impellers were placed at a respective distance of 0.300 and 0.450 m to theoretically ensure macroscopic liquid circulations within the tank.

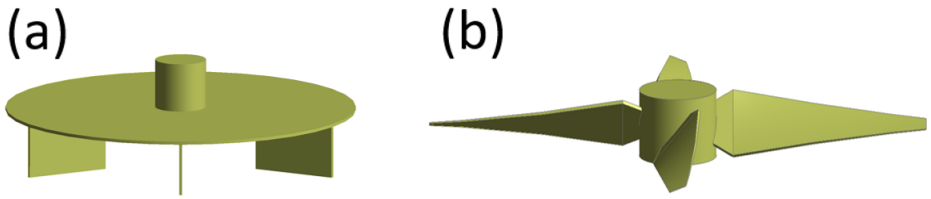

Figure 3.12: Impellers used in simulations. (a) 6-bladed radial turbine (6B-DRT); (b) Robin Turbine HPM 10 (HPM10).

The simulations were carried out at 6 different agitation rates ($N = 30$, 60, 90, 120, 150 and 250 rpm), ensuring fully turbulent conditions for each case ($5 \times 10^4 < \mathrm{Re} < 5 \times 10^5$). Similarly to the laboratory-scale bioreactor, various solid concentration conditions were studied, namely 6, 14 and 21% w/w. To ensure comparison between both simulation setup, the same liquid and solid properties were used. However, the available experimental data on this bioreactor, which were used for comparison to validate the model, employed a solid with a density nearing $4000\,\mathrm{kg\,m^{-3}}$, which could be responsible for differences in mechanical power consumption and solid homogenization.

Model description and solution method

Additionally to the previously mentioned geometrical characteristics, a rotating domain was added for each impellers. They were positioned at $r_{\mathrm{bottom}} = 0.230$ m, $0.050\ \mathrm{m} \leq z_{\mathrm{bottom}} \leq 0.200$ m, $r_{\mathrm{middle}} = r_{\mathrm{top}} = 0.300$ m, $0.375\ \mathrm{m} \leq z_{\mathrm{middle}} \leq 0.525$ m, $0.825\ \mathrm{m} \leq z_{\mathrm{top}} \leq 0.975$ m, respectively for the bottom, middle and top impellers. This domain was later used as a reference frame for rotation but had no influence on the geometry of the tank. The modelled setup was then divided into a non-uniform mesh structure, composed of 8.7 million of tetrahedral elements. Multiple mesh refinements were added along the wall and into the impellers rotating domains. Lastly, improvements of the mesh quality were done using internal Fluent tools which allowed a minimum orthogonal quality of 0.5.

The SIMPLE pressure-velocity based solver was used to solve the set of conservation equations. Discretization of the mass, momentum and volume fraction equations was carried-out using the second-order upwind scheme while pressure was spatially discretized using the PRESTO! scheme (s.n. [51]). Convergence of the simulations was admitted when transport equations residuals were less than 10^{-3} and when the local solid volume fraction reached a steady state at three locations of the vessel ($r = 0.300$ m and $z = 0.075$, 0.675 and 1.050 m). The conservation equations and solving methods used were the same as for the laboratory-scale tank, with a convergence criterion admitted when the local solid volume fraction reached a steady-state at three locations of the vessel ($r = 0.300$ m and $z = 0.075$, 0.675 and 1.050 m).

3.3.2 Simulation results

Liquid flow patterns

In the first place, the model was validated using BRGM experimental data of the pilot-scale STR (data not shown). For this, the liquid flow patterns induced by the three-stage impellers, which are described in Fig. 3.13, were observed and compared to the manufacturer and experimental data. The bottom 6B-DRT generated a single-loop flow pattern supplying a pseudo-vortex in its center. This configuration could be expected due the low clearance of the impeller, which was chosen to promote solid dispersion. Due to the high velocities obtained around the bottom impeller, high hydromechanical stresses were also expected and may have deleterious effects on the solid phase (breaking down or scattering of solid particles). Concerning the HPM10 recirculating impellers, they globally showed the expected vertical one-loop flow pattern of axial impellers and, as suggested by weak slope of their blades. In the present system, they were used in up-pumping mode, which permits to globally obtain a satisfactory liquid velocity distribution. Moreover, the spacing between both HPM10 allowed a synergistic effect by coupling their respective flow patterns. However, it should also be noted that some central zones showed significantly lower liquid velocities, between bottom and intermediate impeller but also near the free surface. They could be explained by the relative mixed flow generated by the HPM10 which limited the liquid flux "connections" between top impeller and free surface from one side and intermediate HPM10 and bottom impeller on the other hand.

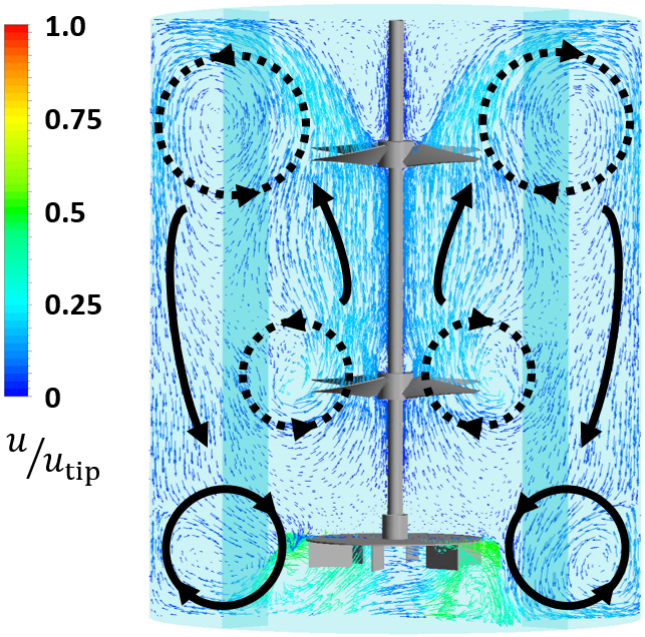

Figure 3.13: Normalized liquid velocity vectors profiles at 150 rpm for the pilot-scale STR. The tip speed was given by $u_{tip} = \pi ND$.

Power consumption

The power consumption per unit volume (P/V) was calculated using eq. 3.24 and compared with the experimental measurements for 90, 120 and 150 rpm, as shown by Fig. 3.14. For the three agitation rates that were simultaneously studied experimentally and numerically, the modeled P/V were on average 35% lower than the experimental data. As explained previously, the experimentation used a denser solid than the one studied numerically ; due to the increase of the gas-solid mixture density a higher P/V could be expected at a given agitation rate as $P \propto \rho N^3 D^5$. Moreover, a part of the power difference can be attributed to the mechanical friction of the shaft guidance system that was probably also given by the torque measurement, which artificially increased the P/V. These differences may indeed reach 10 to 30% depending on the agitations conditions applied and on the material used [69]. The power number was also calculated for each impeller using eq. 3.1. The 6B-DRT showed a calculated power number of 1.44 $\pm$ 0.09 compared to the 1.80 $\pm$ 0.02 obtained experimentally. Similarly, both HPM10 presented a power number of 0.22 $\pm$ 0.02 while the experimental power number was 0.30. These differences are the direct consequence of uncertainties of the torque measurements. Moreover, few to no differences of power numbers were observed for the different agitation rates, which is expected in turbulent regime [17, 59].

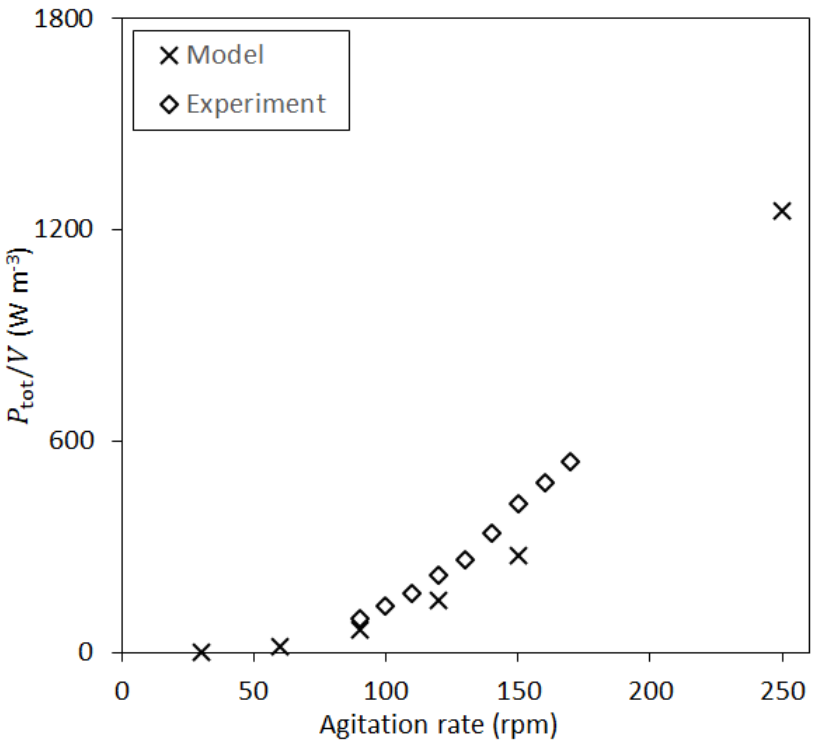

Figure 3.14: Variation of the total power consumption per unit volume P_{tot}/V with the agitation rate and comparison with experimental data. Particle concentration was 10 % w/w.

3.3.3 Impact of solid concentration on particle distribution

The particle mixing degree $H_{\mathrm{s,adj}}$ was determined, using eq. 3.28, for each solid concentrations conditions, as shown on Fig. 3.15. The results showed a logarithmic increased of $H_{\mathrm{s,adj}}$ ranging from 38 to 99%, which was consistent with the results obtained for the 2-liter tank. Regarding the solid concentration, its increase had a negative effect on $H_{\mathrm{s,adj}}$, with values of $H_{\mathrm{s,adj}}^{6\%} = 0.53$, $H_{\mathrm{s,adj}}^{14\%} = 0.42$ and $H_{\mathrm{s,adj}}^{21\%} = 0.38$ for $P_{\mathrm{tot}}/V = 2\,\mathrm{W\,m^{-3}}$. The effect of particle concentration on $H_{\mathrm{s,adj}}$ decreased at higher P_{tot}/V with nearly no differences observed above $P_{\mathrm{tot}}/V = 600\,\mathrm{W\,m^{-3}}$. Comparison of these results with the laboratory-scale reactor showed a higher particle mixing degree for a given power dissipation, which could be first explained by the smaller clearance of the bottom impeller in the pilot-scale reactor ($(C/T)_{2\mathrm{l}} = 0.42$ compared to $(C/T)_{800\mathrm{l}} = 0.12$) that promoted higher velocities and power dissipation in the bottom region of the tank. This observation is in agreement with studies that previously reviewed the impact of impeller clearance on particle suspension [70]. Secondly, whereas the two bioreactor scales showed a comparable aspect ratio H/T, the pilot-scale bioreactor was equipped with three impellers (vs 2 for the 2 l scale) that limited the lower particle concentration near the free surface observed for the 2-liter tank and increased particle homogeneity. Considering the results of both tanks, it could be interesting to adapt the maximum value of $H_{\mathrm{s,adj}}$ in order to take into account the impeller clear-

ance. This would have need complementary experiments that were not carried-out in the present study. Nonetheless, it remains interesting to note that the results revealed that the maximal $H_{s,adj}$ was reached for equivalent P_{tot}/V for both configuration (approximately $500\,W\,m^{-3}$). This thus confirmed that this parameter could be used for design optimization and scaling as far as particle dispersion is concerned. Regarding the significant differences of designs between both scales, this may also suggest that the determination of an "optimized" impeller design (namely the one that is able to ensure particle suspension and homogeneity at the lowest power demand) should not be considered without integrating vessel design, impeller clearance and number of agitation stages. This suggestion was implicitly also made by previous studies on particle just-suspended state [43] or mixing degree [71].

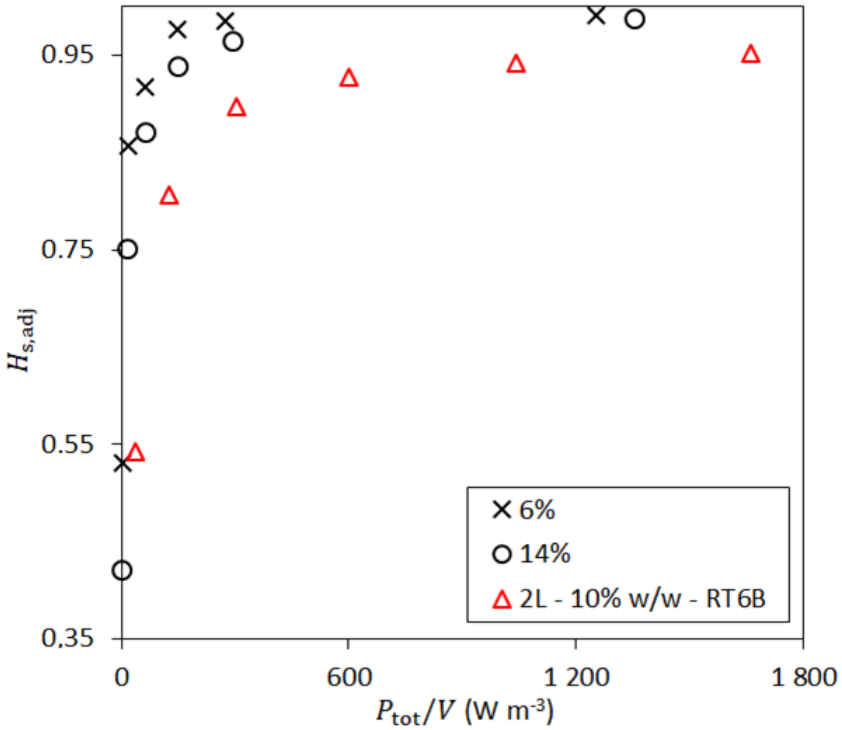

Figure 3.15: Suspension quality $H_{s,adj}$ as a function of power dissipation per unit volume P_{tot}/V for various solid concentrations. The 2-liter tank data are taken for 10% w/w solid concentration and a RT6B configuration.

The simulated particle distribution was also depicted for various agitation rates, as shown in Fig. 3.16(a-b). At low agitation rates, the 6B-DRT impeller was unable to provide a sufficient solid dispersion, resulting in a low fraction of the solid going to the upper part of the tank and a relative accumulation of particles. This suggested some drawbacks of such impeller geometry, especially of the turbine disk that limits the up-pumping above the disk, as already shown by the velocity vectors field. Compared to the 60 rpm condition, at 120 rpm, the 6B-DRT supplied enough power to disperse the particles through the middle and top impellers flow patterns, allowing a near-perfect particle mixing degree with $H_{s,adj} = 0.98$.

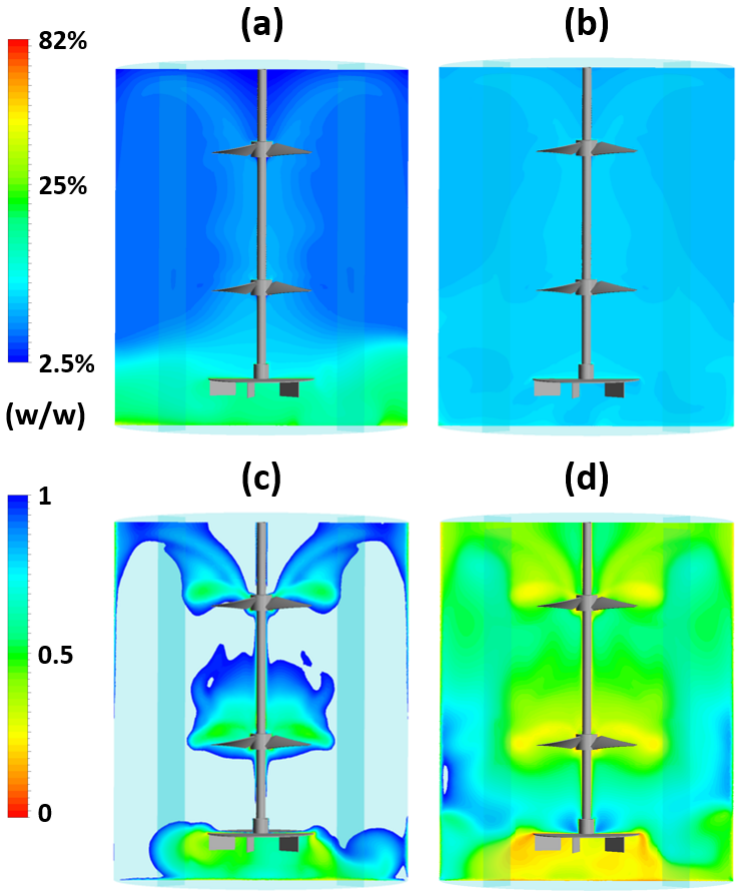

Figure 3.16: Simulated particles distribution of the pilot scale STR with 6% w/w solid for: (a) 60 rpm; (b) 120 rpm. Comparison of the particle size with the Kolmogorov length scale (l_K/d_p) with 6% w/w solid for: (c) 60 rpm; (d) 120 rpm.

3.3.4 Impact of solid concentration on hydromechanical stress

The hydromechanical stresses were quantified by the percentage of particle volumes that were theoretically sheared, as proposed previously in eq. 3.31. The impact of $H_{s,adj}$ on the sheared fraction SF was reported on Fig. 3.17. Similarly to the laboratory-scale tank, the sheared fraction increased with the suspension quality, as they are both related to power dissipation. However, the results showed some discrepancies with the simulation results at the laboratory-scale. Despite, for $H_{s,adj}$ below 75%, the linear evolution observed for the laboratory-scale tank was also proven for the pilot-scale tank, the slope for the pilot-scale tank was steeper, with up to 30% difference of $H_{s,adj}$ for $SF = 33\%$ but a similar maximum value close to 100%. This result could be due to the clearance of the bottom impeller that promotes solid dispersion at lower power dissipation per unit volume. On the other hand, for $H_{s,adj}$ above 75%, the variation of SF with mixing degree was less pronounced which could be explained by the occurence of a partial solid suspension. As the sheared fraction was related to the local ratio of the Kolmogorov length scale l_K, it is interesting to observe the distribution of particles of size higher than l_K, as shown on Fig. 3.16(c-d) (in this figure, only the shearing zones

were colored). At lower agitation rates, near the just-suspended speed, the particles under stressed conditions were only located in high turbulent dissipation rate zones, in the direct vicinity of the impellers such as below the RT-6B or above the HPM10 impellers. However, at higher agitation rates, the sheared fraction rapidly increased exponentially for only a small gain of solid dispersion, with $SF = 93\%$ for $H_{\mathrm{s,adj}} = 0.98$.

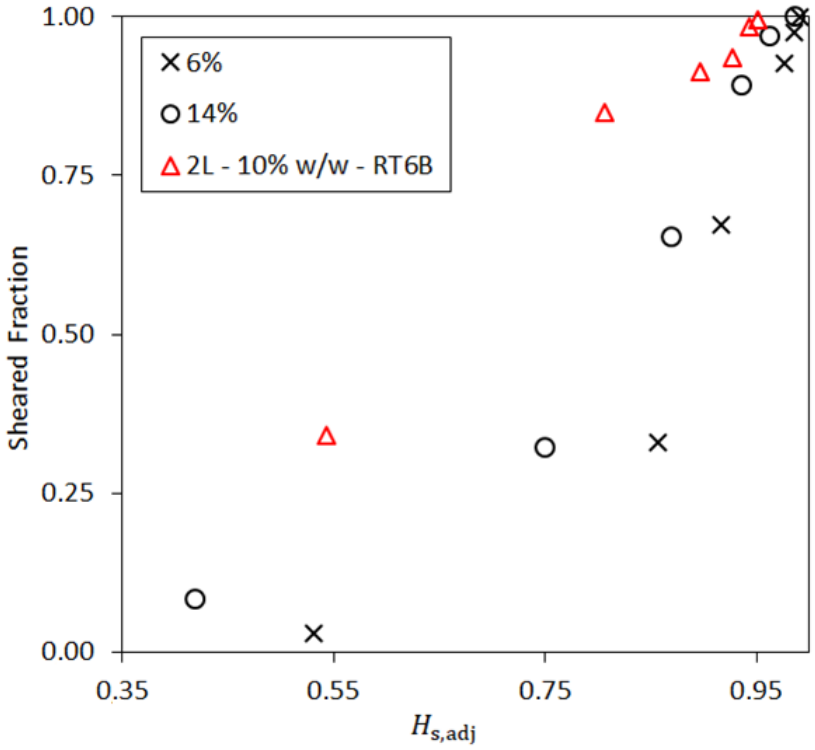

Figure 3.17: Suspension quality $H_{\mathrm{s,adj}}$ as a function of the sheared fraction SF for various solid concentrations. The 2-liter tank data are taken for 10% w/w solid concentration and a RT6B configuration.

The impact of solid concentration on the sheared fraction SF was also considered, as shown by Fig. 3.17. For higher solid concentration, a larger portion of particles was under stressed conditions at equivalent $H_{\mathrm{s,adj}}$. From a global point of view and considering that a relative homogeneity of the particle is looked for (i.e. $H_{\mathrm{s,adj}} > 95\%$), the impact of bioreactor scale on SF was somehow rather low, which is consistent with the results obtained on power dissipation impact of particle dispersion. Thus, similarly to the 2-liter scale, and in the range of operating conditions studied here, it was not possible to efficiently suspend the particles without transporting them in the inertial subrange of turbulence ($l_{\mathrm{K}} < d_{\mathrm{p}}$). In this case, the particle stress was proportional to $(d_{\mathrm{p}} \cdot \varepsilon)^{2/3}$, meaning that for given particle diameter and turbulent dissipation rate distributions, the particle stress distribution was also maintained. Thus, a finer grinding of the particles should sensibly reduce the hydromechanical stress that encounters the particle in the vessel and also promotes higher $l_{\mathrm{K}}/d_{\mathrm{p}}$ ratios and possibly a transport of the particle in the viscous subrange of the turbulence. In viscous subrange, the particle

stress indeed becomes mainly non-dependent of particle diameter. These results should be put into perspective with those of chapter 2 that showed that the power demand to put the particles in suspension was $P_{js} \propto d_{\mathrm{p}}^{0.25}$. Despite refining, particles clearly present additional CAPEX and OPEX [72], these results globally suggest that the particle size distribution should be also considered through the prism of the liquid-solid bioreactor hydrodynamics.

3.4 Chapter conclusions

This chapter was dedicated to the study of the impact of impeller design and solid concentration on particle suspension and particle stress in a laboratory- and a pilot-scale bioreactor. For this purpose, liquid-solid CFD numerical simulations and theoretical models of particle stress were carried-out and validation of the simulations was established with the already available data.

The study of the laboratory scale STR was more specifically aimed at determining the dependency of particle homogeneity and sheared fraction on bioreactor operating conditions (impeller design, particle concentration). It was found that, independently of the reactor design, the suspension quality $H_{\mathrm{s,adj}}$ was strongly linked to the power consumption per unit of volume P_{tot}/V. Similar results were found for the particles stress with a weak impact of the reactor design observed. During the transition from partial to complete suspension, the sheared fraction of particles rapidly increased from 0 to a value close to 100%. Lastly, considering the solid concentration, it was shown that an increase in solid concentration was linked to a significant rise of power consumption per unit of volume to reach the same suspension homogeneity.

Following the previous results, the impact of bioreactor scale-up was studied at the pilot-scale. The results on the impact of the solid concentration on the solid distribution and particle stress concurred with the laboratory-scale bioreactor despite significant differences in bioreactor design. However, small differences were observed on the maximum suspension quality $H_{\mathrm{s,adj}}$, which were probably related to different values of bottom impeller clearance. Additionally, looking at the relationship between the sheared fraction SF and suspension quality $H_{\mathrm{s,adj}}$ more significant differences were obtained between each scale for intermediate mixing degree that most likely arose from particle partial suspension and bioreactor design modifications.

The results obtained in this chapter proposed original data in the literature for particle stress estimation in bioleaching mixing tank, especially regarding the impact of particle diameter on the mechanical micro-environment encountered by the particles during their transport in the vessel. However, regarding the complexity of the description of turbulent dissipation rate distribution, which is inherent to stirred tank vessels, it would be risky to draw any conclusions on bioleaching performance of the tank. The purpose of this study was here to characterize the critical key parameters that seem to govern the liquid-solid hydrodynamics of the bioleaching reactor ; this study should be, in the future, coupled with bioleaching experiments in fully-characterized mechanical environment to determine the critical mechanical operating condition.

Bibliography

[1] J. Y. Witne and C. V. Phillips. Bioleaching of Ok Tedi copper concentrate in oxygen- and carbon dioxide-enriched air. *Minerals Engineering*, 14(1):25–48, January 2001.

[2] M. E. Clark, J. D. Batty, C. B. van Buuren, D. W. Dew, and M. A. Eamon. Biotechnology in minerals processing: Technological breakthroughs creating value. *Hydrometallurgy*, 83(1):3–9, September 2006.

[3] C. L. Brierley and J. A. Brierley. Progress in bioleaching: Part B: Applications of microbial processes by the minerals industries. *Applied Microbiology and Biotechnology*, 97(17):7543–7552, September 2013.

[4] D. E. Rawlings and D. B. Johnson. The microbiology of biomining: Development and optimization of mineral-oxidizing microbial consortia. *Microbiology*, 153(2):315–324, February 2007.

[5] G. M. Mudd, Z. Weng, and S. M. Jowitt. A Detailed Assessment of Global Cu Resource Trends and Endowments. *Economic Geology*, 108(5):1163–1183, August 2013.

[6] M. Frenzel, J. Kullik, M. A. Reuter, and J. Gutzmer. Raw material 'criticality'—sense or nonsense? *Journal of Physics D: Applied Physics*, 50(12):123002, March 2017.

[7] D. H. R. Morin and P. d'Hugues. Bioleaching of a Cobalt-Containing Pyrite in Stirred Reactors: A Case Study from Laboratory Scale to Industrial Application. In D. E. Rawlings and D. B. Johnson, editors, *Biomining*, pages 35–55. Springer, Berlin, Heidelberg, 2007.

[8] K. D. Wakeman, P. Honkavirta, and J. A. Puhakka. Bioleaching of flotation by-products of talc production permits the separation of nickel and cobalt from iron and arsenic. *Process Biochemistry*, 46(8):1589–1598, August 2011.

[9] J. Neale, J. Seppälä, A. Laukka, P. Aswegen, S. Barnett, and M. Gericke. The MONDO Minerals Nickel Sulfide Bioleach Project: From Test Work to Early Plant Operation. *Solid State Phenomena*, 262:28–32, August 2017.

[10] J. Petersen. Modelling of bioleach processes: Connection between science and engineering. *Hydrometallurgy*, 104(3):404–409, October 2010.

[11] M. M. Buffo, L. J. Corrêa, M. N. Esperança, A. J. G. Cruz, C. S. Farinas, and A. C. Badino. Influence of dual-impeller type and configuration on oxygen transfer, power consumption, and shear rate in a stirred tank bioreactor. *Biochemical Engineering Journal*, 114:130–139, October 2016.

[12] W. Bujalski, K. Takenaka, S. Paoleni, M. Jahoda, A. Paglianti, K. Takahashi, A. W. Nienow, and A. W. Etchells. Suspension and Liquid Homogenization in High Solids Concentration Stirred Chemical Reactors. *Chemical Engineering Research and Design*, 77(3):241–247, May 1999.

[13] R. Jafari, P. A. Tanguy, and J. Chaouki. Experimental investigation on solid dispersion, power consumption and scale-up in moderate to dense solid–liquid suspensions. *Chemical Engineering Research and Design*, 90(2):201–212, February 2012.

[14] F. Bouquet and D. Morin. BROGIM®: A new three-phase mixing system test-work and scale-up. *Hydrometallurgy*, 83(1):97–105, September 2006.

[15] G. Montante, A. Paglianti, and F. Magelli. Analysis of dilute solid–liquid suspensions in turbulent stirred tanks. *Chemical Engineering Research and Design*, 90(10):1448–1456, October 2012.

[16] A. Tamburini, A. Cipollina, G. Micale, A. Brucato, and M. Ciofalo. Influence of drag and turbulence modelling on CFD predictions of solid liquid suspensions in stirred vessels. *Chemical Engineering Research and Design*, 92(6):1045–1063, June 2014.

[17] J. H. Rushton. Power Characteristics of Mixing Impellers Part 1. *Chem. Eng. Prog.*, 46:395–404, 1950.

[18] D. Chapple, S. M. Kresta, A. Wall, and A. Afacan. The Effect of Impeller and Tank Geometry on Power Number for a Pitched Blade Turbine. *Chemical Engineering Research and Design*, 80(4):364–372, May 2002.

[19] M. Bouaifi and M. Roustan. Power consumption, mixing time and homogenisation energy in dual-impeller agitated gas–liquid reactors. *Chemical Engineering and Processing: Process Intensification*, 40(2):87–95, February 2001.

[20] J. Zhang, Z. Gao, Y. Cai, H. Cao, Z. Cai, and Y. Bao. Power consumption and mass transfer in a gas-liquid-solid stirred tank reactor with various triple-impeller combinations. *Chemical Engineering Science*, 170:464–475, October 2017.

[21] T. N. Zwietering. Suspending of solid particles in liquid by agitators. *Chemical Engineering Science*, 8(3):244–253, June 1958.

[22] A. Brucato, A. Cipollina, G. Micale, F. Scargiali, and A. Tamburini. Particle suspension in top-covered unbaffled tanks. *Chemical Engineering Science*, 65(10):3001–3008, May 2010.

[23] A. Tamburini, A. Cipollina, G. Micale, A. Brucato, and M. Ciofalo. CFD simulations of dense solid–liquid suspensions in baffled stirred tanks: Prediction of suspension curves. *Chemical Engineering Journal*, 178:324–341, December 2011.

[24] A. Tamburini, A. Brucato, A. Cipollina, G. Micale, and M. Ciofalo. CFD Predictions of Sufficient Suspension Conditions in Solid-Liquid Agitated Tanks. *International Journal of Nonlinear Sciences and Numerical Simulation*, 13(6), January 2012.

[25] S. T. L. Harrison, R. Stevenson, and J. J. Cilliers. Assessing solids concentration homogeneity in Rushton-agitated slurry reactors using electrical resistance tomography (ERT). *Chemical Engineering Science*, 71:392–399, March 2012.

[26] A. T.-C. Mak. *Solid-Liquid Mixing in Mechanically Agitated Vessels*. Doctoral,

University of London, 1992.

[27] T. Kumaresan and J. B. Joshi. Effect of impeller design on the flow pattern and mixing in stirred tanks. *Chemical Engineering Journal*, 115(3):173–193, January 2006.

[28] I. Houcine, E. Plasari, and R. David. Effects of the Stirred Tank's Design on Power Consumption and Mixing Time in Liquid Phase. *Chemical Engineering & Technology*, 23(7):605–613, July 2000.

[29] Y. Rodríguez, A. Ballester, M. L. Blázquez, F. González, and J. A. Muñoz. Study of Bacterial Attachment During the Bioleaching of Pyrite, Chalcopyrite, and Sphalerite. *Geomicrobiology Journal*, 20(2):131–141, March 2003.

[30] A.-G. Guezennec, C. Joulian, J. Jacob, A. Archane, D. Ibarra, R. de Buyer, F. Bodénan, and P. d'Hugues. Influence of dissolved oxygen on the bioleaching efficiency under oxygen enriched atmosphere. *Minerals Engineering*, 106:64–70, May 2017.

[31] L. Xia, X. Liu, J. Zeng, C. Yin, J. Gao, J. Liu, and G. Qiu. Mechanism of enhanced bioleaching efficiency of Acidithiobacillus ferrooxidans after adaptation with chalcopyrite. *Hydrometallurgy*, 92(3):95–101, June 2008.

[32] P. d'Hugues, S. Foucher, P. Gallé-Cavalloni, and D. Morin. Continuous bioleaching of chalcopyrite using a novel extremely thermophilic mixed culture. *International Journal of Mineral Processing*, 66(1):107–119, September 2002.

[33] A. Sissing and S. T. L. Harrison. Thermophilic mineral bioleaching performance: A compromise between maximizing mineral loading and maximizing microbial growth and activity. *Journal of the Southern African Institute of Mining and Metallurgy*, page 4, 2003.

[34] C. Wang, D. Harbottle, Q. Liu, and Z. Xu. Current state of fine mineral tailings treatment: A critical review on theory and practice. *Minerals Engineering*, 58:113–131, April 2014.

[35] P. d'Hugues, C. Joulian, P. Spolaore, C. Michel, F. Garrido, and D. Morin. Continuous bioleaching of a pyrite concentrate in stirred reactors: Population dynamics and exopolysaccharide production vs. bioleaching performance. *Hydrometallurgy*, 94(1):34–41, November 2008.

[36] S. Raja. The effect of particulate-induced hydrodynamic stress on the bioleaching of chalcopyrite by a Sulfolobus sp. 2005.

[37] M. Nemati and S. T. L. Harrison. Effect of solid loading on thermophilic bioleaching of sulfide minerals. *Journal of Chemical Technology & Biotechnology*, 75(7):526–532, 2000.

[38] A. W. Nienow. Reactor Engineering in Large Scale Animal Cell Culture. *Cytotechnology*, 50(1):9, June 2006.

[39] D. Wadnerkar, R. P. Utikar, M. O. Tade, and V. K. Pareek. CFD simulation of solid–liquid stirred tanks. *Advanced Powder Technology*, 23(4):445–453, July 2012.

[40] C. Zheng, Y. Huang, J. Guo, R. Cai, H. Zheng, C. Lin, and Q. Chen. Investigation of cleaner sulfide mineral oxidation technology: Simulation and evaluation of stirred bioreactors for gold-bioleaching process. *Journal of Cleaner Production*, 192:364–375, August 2018.

[41] T. Song, K. Jiang, J. Zhou, Z. Shen, and Y. Feng. CFD impeller speed evaluation of an industrial scale two-phase flow stirred tank. page 5, 2015.

[42] D. V. Gradov, G. González, M. Vauhkonen, A. Laari, and T. Koiranen. Experimental and Numerical Study of Multiphase Mixing Hydrodynamics in Batch Stirred Tank Applied to Ammoniacal Thiosulphate Leaching of Gold. *Journal of Chemical Engineering & Process Technology*, 08(03), 2017.

[43] C. Loubière, A. Delafosse, E. Guedon, D. Toye, I. Chevalot, and E. Olmos. Optimization of the Impeller Design for Mesenchymal Stem Cell Culture on Microcarriers in Bioreactors. *Chemical Engineering & Technology*, 42(8):1702–1708, 2019.

[44] M. Ljungqvist and A. Rasmuson. Numerical Simulation of the Two-Phase Flow in an Axially Stirred Vessel. *Chemical Engineering Research and Design*, 79(5):533–546, July 2001.

[45] A. R. Khopkar, G. R. Kasat, A. B. Pandit, and V. V. Ranade. Computational Fluid Dynamics Simulation of the Solid Suspension in a Stirred Slurry Reactor. *Industrial & Engineering Chemistry Research*, 45(12):4416–4428, June 2006.

[46] N. Qi, H. Zhang, K. Zhang, G. Xu, and Y. Yang. CFD simulation of particle suspension in a stirred tank. *Particuology*, 11(3):317–326, June 2013.

[47] G. R. Kasat, A. B. Pandit, and V. V. Ranade. CFD Simulation of Gas-Liquid Flows in a Reactor Stirred by Dual Rushton Turbines. *International Journal of Chemical Reactor Engineering*, 6(1), 2008.

[48] G. B. Tatterson. *Fluid Mixing and Gas Dispersion in Agitated Tanks*. McGraw-Hill, 1991.

[49] R. S. S. Raja Ehsan Shah, B. Sajjadi, A. A. Abdul Raman, and S. Ibrahim. Solid-liquid mixing analysis in stirred vessels. *Reviews in Chemical Engineering*, 31(2), January 2015.

[50] L. Schiller. A Drag Coefficient Correlation. *Zeit. Ver. Deutsch. Ing.*, 77:318–320, 1933.

[51] J. Abrahamson. Fluent Theory Guide. page 962, 2019.

[52] J. T. Jenkins and S. B. Savage. A theory for the rapid flow of identical, smooth, nearly elastic, spherical particles. *Journal of Fluid Mechanics*, 130:187–202, May 1983.

[53] J. Ding and D. Gidaspow. A bubbling fluidization model using kinetic theory of granular flow. *AIChE Journal*, 36(4):523–538, 1990.

[54] B. N. Murthy, R. S. Ghadge, and J. B. Joshi. CFD simulations of gas–liquid–solid stirred reactor: Prediction of critical impeller speed for solid suspension. *Chemical Engineering Science*, 62(24):7184–7195, December 2007.

[55] S. Hosseini, D. Patel, F. Ein-Mozaffari, and M. Mehrvar. Study of Solid-Liquid Mixing in Agitated Tanks through Computational Fluid Dynamics Modeling. *Industrial & Engineering Chemistry Research*, 49(9):4426–4435, May 2010.

[56] P. Vrábel, R. G. van der Lans, K. C. Luyben, L. Boon, and A. W. Nienow. Mixing in large-scale vessels stirred with multiple radial or radial and axial up-pumping impellers: Modelling and measurements. *Chemical Engineering Science*, 55(23):5881–5896, December 2000.

[57] M. Roustan. Agitation. Mélange - Caractéristiques des mobiles d'agitation. *Techniques de l'ingénieur*, March 2005.

[58] H. Zhu, A. W. Nienow, W. Bujalski, and M. J. H. Simmons. Mixing studies in a model aerated bioreactor equipped with an up- or a down-pumping 'Elephant Ear' agitator: Power, hold-up and aerated flow field measurements. *Chemical Engineering Research and Design*, 87(3):307–317, March 2009.

[59] H. Furukawa, Y. Kato, Y. Inoue, T. Kato, Y. Tada, and S. Hashimoto. Correlation of Power Consumption for Several Kinds of Mixing Impellers. *International Journal of Chemical Engineering*, 2012:1–6, 2012.

[60] V. Hudcova, V. Machon, and A. W. Nienow. Gas–liquid dispersion with dual Rushton impellers. *Biotechnology and Bioengineering*, 34(5):617–628, 1989.

[61] S. T. You, A. A. A. Raman, R. S. S. R. E. Shah, and M. I. Mohamad Nor. Multiple-impeller stirred vessel studies. *Reviews in Chemical Engineering*, 30(3), January 2014.

[62] A. Ochieng and M. S. Onyango. Homogenization energy in a stirred tank. *Chemical Engineering and Processing: Process Intensification*, 47(9):1853–1860, September 2008.

[63] T. Wang, G. Yu, Y. Yong, C. Yang, and Z.-S. Mao. Hydrodynamic Characteristics of Dual-Impeller Configurations in a Multiple-Phase Stirred Tank. *Industrial & Engineering Chemistry Research*, 49(3):1001–1009, February 2010.

[64] A. Delafosse, C. Loubière, S. Calvo, D. Toye, and E. Olmos. Solid-liquid suspension of microcarriers in stirred tank bioreactor – Experimental and numerical analysis. *Chemical Engineering Science*, 180:52–63, April 2018.

[65] F. Magelli, D. Fajner, M. Nocentini, G. Pasquali, V. Marisko, and P. Ditl. Solids concentration distribution in slurry reactors stirred with multiple axial impellers. *Chemical Engineering and Processing: Process Intensification*, 29(1):27–32, January 1991.

[66] H.-J. Henzler. Particle Stress in Bioreactors. In K. Schügerl, G. Kretzmer, H. J. Henzler, P. M. Kieran, G. Kretzmer, P. E. MacLoughlin, D. M. Malone, W. Schumann, P. A. Shamlou, and S. S. Yim, editors, *Influence of Stress on Cell Growth and Product Formation*, Advances in Biochemical Engineering/Biotechnology, pages 35–82. Springer, Berlin, Heidelberg, 2000.

[67] D. G. Thomas. Turbulent disruption of flocs in small particle size suspensions.

AIChE Journal, 10(4):517–523, 1964.

[68] J. You, S. K. Solongo, A. Gomez-Flores, S. Choi, H. Zhao, M. Urík, S. Ilyas, and H. Kim. Intensified bioleaching of chalcopyrite concentrate using adapted mesophilic culture in continuous stirred tank reactors. *Bioresource Technology*, 307:123181, July 2020.

[69] G. Ascanio, B. Castro, and E. Galindo. Measurement of Power Consumption in Stirred Vessels—A Review. *Chemical Engineering Research and Design*, 82(9):1282–1290, September 2004.

[70] P. M. Armenante, E. U. Nagamine, and J. Susanto. Determination of correlations to predict the minimum agitation speed for complete solid suspension in agitated vessels. *The Canadian Journal of Chemical Engineering*, 76(3):413–419, 1998.

[71] C. Macqueron. *Solid-Liquid Mixing in Stirred Vessels: Numerical Simulation, Experimental Validation and Suspension Quality Prediction Using Multivariate Regression and Machine Learning*. August 2018.

[72] J. de Bakker. Energy Use of Fine Grinding in Mineral Processing. *Metallurgical and Materials Transactions E*, 1(1):8–19, March 2014.

Chapter 4

Development of a hydro-kinetic compartment model of a bioleaching STR

Contents

4.1 Introduction

The efficiency of metal extraction through bioleaching in stirred tank reactor is connected to two sets of parameters: (i) the choice of metal sulphide (composition and particle size), microbial environment and medium composition, and (ii) the parameters influencing the hydrodynamics, namely the tank and impeller geometries, the medium temperature, the solid concentration and gas parameters (mass flow rate and bubble size). The first set is often predetermined as most of metal sulphides used in bioleaching come from tailings and efficient microbial consortia and media have already been obtained through experimental trials. Considering the second set, temperature is dependent on the chosen microbial consortia and adapted for optimal operation. The previous chapter considered the impact of geometrical parameters and solid concentration and proposed scaling rules relating these parameters to solid distribution and hydromechanical stress. Regardless of the chosen conditions, the agitation rate should be set up on or above the just-suspended speed, which will provide sufficient solid homogeneity within the medium. To complete this representation, it is also necessary to model the impact of the gas phase on hydrodynamics knowing that, as mentioned in the literature review and the second chapter, gas dispersion and mass transfer needs will require higher agitation rates than solid suspension. Furthermore, as oxygen consumption is rather a fast reaction and, due to low solubilities of oxygen in water, gas heterogeneities are expected within the tank, especially at industrial scales for which mixing times may become larger than characteristic consumption times. Therefore, not only the gas phase hydrodynamics but also the dynamics of oxygen solubilization and transport in the liquid phase must be carefully considered.

In this chapter, the development of bioleaching STR model was achieved through the implementation of the gas-liquid hydrodynamics modelling and the coupling with kinetics models, as summarized by Fig. 4.1. For this, the impact of gas phase on the hydrodynamics of a bioleaching reactor was studied through gas-liquid CFD simulations of stirred reactors at two scales (2- and 800-liter). This model was validated by the determination of the mass transfer coefficient $k_{\mathrm{L}}a$ based on hydrodynamic parameters and comparison with experimental data. On a second study, bioleaching kinetics were implemented to the model to represent a sulphide mineral dissolution and biological oxidations. Validation of the model was obtained by comparing modelled and experimental data obtained previously. The previous models were simplified through a compartmental approach that modelled oxygen dissolution and transport. This approach supposed a division of the tank into a relatively small number of compartments, supposed perfectly mixed, based on liquid and gas velocity fields data. Main hydrodynamic variables were averaged in each of these and mass balance was applied between each compartment for both gas and liquid phases. The compartment model could be

then simulated using MATLAB and validated using a modelled gassing-out method in order to determine the $k_{\mathrm{L}}a$. This approach allowed to avoid CFD simulation issues that may appear due to small-scale heterogeneities (such as important gas fraction gradients) and to facilitate the transposition of the model to industrial scale ($V > 100\,\mathrm{m}^3$). Thus, in a last section of the chapter, a scaling study was carried out to predict the distribution of oxygen in the bioreactor from pilot- to industrial-scale (volume of 0.8, 8, 80, 800 and 2000 m^3 were studied).

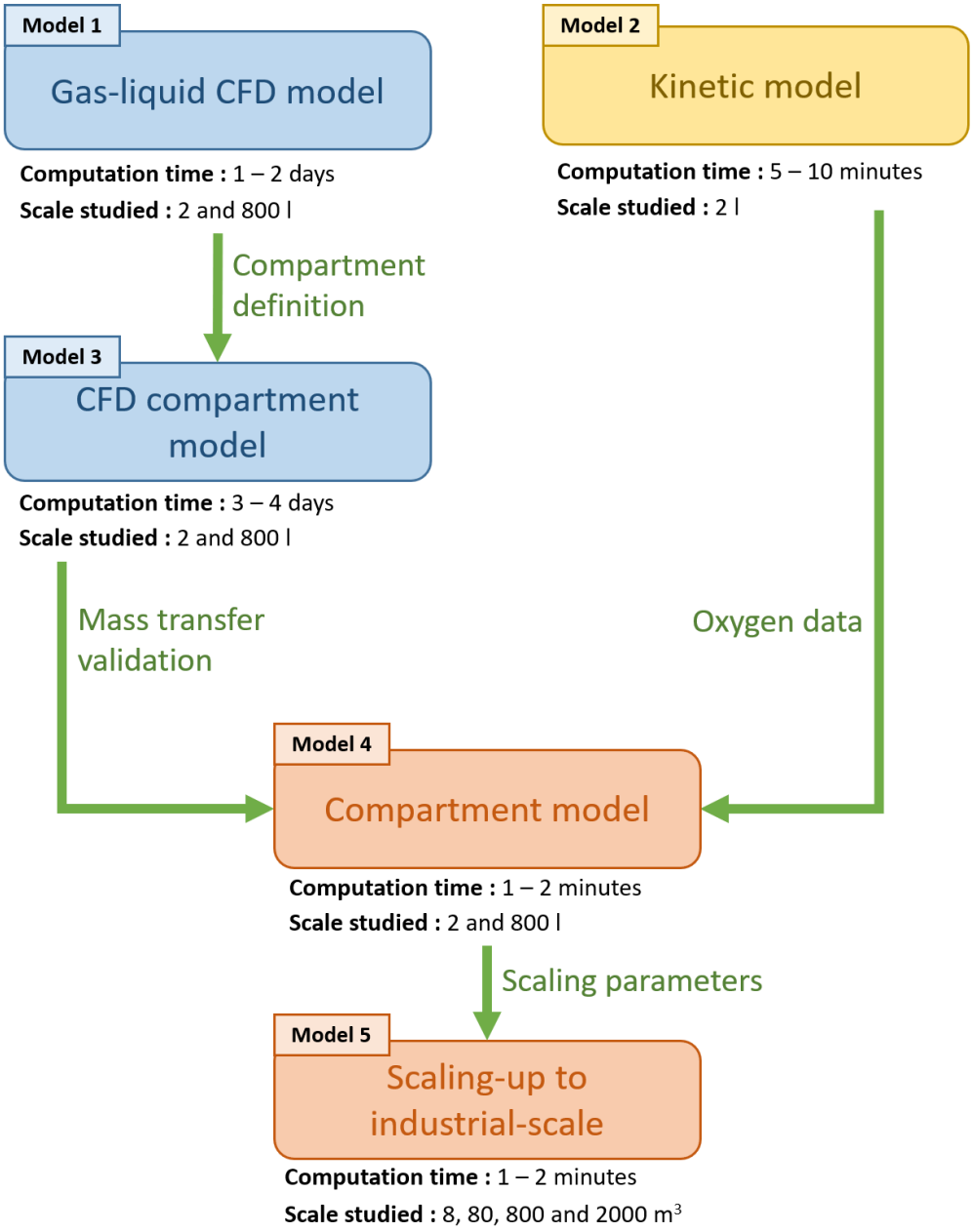

Figure 4.1: Methodology for developing a hydrokinetic model. Computation times are based on the 2-liter tank. Frame colors represent the equations solved: (blue) hydrodynamics ; (yellow) kinetics ; (orange) hydrodynamics and kinetics.

4.2 CFD modelling of gas-liquid hydrodynamics at 2- and 800-liter scale

Gas-liquid hydrodynamics highly differs from solid-liquid hydrodynamics due to significant differences of density and size. Furthermore, mass transfer phenomena must be taken into account as oxygen have to cross multiple barriers before being usable for chemical dissolution or biological oxidations.

The following section presents a gas-liquid CFD model of a commonly used bioleaching STR in BRGM. The mass transfer coefficient $k_{\mathrm{L}}a$ was determined based on the tank hydrodynamics and compared with experimental results.

4.2.1 Material and Methods

CFD model description

A steady-state Eulerian-Eulerian multiphase approach was used to simulate the gas-liquid flow, with the continuous and dispersed phases considered as interpenetrating continua. Both phases are identified by their respective volume fraction and are related as:

$$\alpha_{\mathrm{g}} + \alpha_{\mathrm{l}} = 1 \tag{4.1}$$

where α_{g} and α_{l} are the volume fractions of the gas and liquid phases respectively. The continuity equation for each incompressible phase can be written as:

$$\nabla \cdot (\alpha_{\mathrm{l}} \mathbf{u}_{\mathrm{l}}) = 0 \tag{4.2}$$

$$\nabla \cdot (\alpha_{\mathrm{g}} \mathbf{u}_{\mathrm{g}}) = 0 \tag{4.3}$$

where ρ ($\mathrm{kg\,m^{-3}}$) and $\mathbf{u}$ ($\mathrm{m\,s^{-1}}$) are the density and velocity of each phase.

The momentum conservation equation for each phase is:

$$\nabla \cdot (\alpha_{\mathrm{l}} \rho_{\mathrm{l}} \mathbf{u}_{\mathrm{l}} \mathbf{u}_{\mathrm{l}}) = -\alpha_{\mathrm{l}} \nabla p + \alpha_{\mathrm{l}} \rho_{\mathrm{l}} \mathbf{g} + \nabla \cdot \overline{\overline{\boldsymbol{\tau}}}_{\mathrm{l}} + \mathbf{F}_{\mathrm{D,lg}} \tag{4.4}$$

$$\nabla \cdot (\alpha_{\mathrm{g}} \rho_{\mathrm{g}} \mathbf{u}_{\mathrm{g}} \mathbf{u}_{\mathrm{g}}) = -\alpha_{\mathrm{g}} \nabla p + \alpha_{\mathrm{g}} \rho_{\mathrm{g}} \mathbf{g} + \nabla \cdot \overline{\overline{\boldsymbol{\tau}}}_{\mathrm{g}} - \mathbf{F}_{\mathrm{D,lg}} \tag{4.5}$$

where p (Pa) is the pressure field shared by the two phases, $\mathbf{g}$ ($\mathrm{m\,s^{-2}}$) the gravitational acceleration, $\overline{\overline{\boldsymbol{\tau}}}$ ($\mathrm{kg\,m^{-1}\,s^{-2}}$) the phase stress strain tensor and $\mathbf{F}_{\mathrm{D,lg}}$ ($\mathrm{kg\,m^{-1}\,s^{-2}}$) the interphase momentum transfer.

Interphase forces in multiphase gas-liquid flows were considered by multiple studies to observe their impact on hydrodynamics. Joshi (2001) observed in bubble column reactors that wall lubrication and Basset's forces could be neglected in relation to the lift and virtual mass forces [1]. Scargiali et al. (2007) compared the impact of the turbulent dispersion, the lift and virtual mass forces on gas hold-up in stirred tank reactors and found no impact of these forces and, therefore, could be disregarded [2]. However, it is important to precisely model drag forces as it is the most significant interphase force in gas-liquid flows.

The drag force $\mathbf{F}_{\mathrm{D,lg}}$ between liquid and gas phases was calculated by the following equation:

$$\mathbf{F}_{\mathrm{D,lg}} = K_{\mathrm{lg}} \left(\mathbf{u}_{\mathrm{g}} - \mathbf{u}_{\mathrm{l}} \right) \tag{4.6}$$

with K_{lg} the interphase exchange coefficient between liquid and gas phases respectively, determined by:

$$K_{\mathrm{lg}} = C_{\mathrm{D,lg}} \frac{3}{4} \rho_{\mathrm{l}} \frac{\alpha_{\mathrm{g}} \alpha_{\mathrm{l}}}{d_{\mathrm{b}}} \left| \mathbf{u}_{\mathrm{g}} - \mathbf{u}_{\mathrm{l}} \right| \tag{4.7}$$

The drag coefficient $C_{\mathrm{D,lg}}$ is given by the Schiller and Naumann model which is valid for rigid sphere [3], as shown by Eq. 4.8. As bubbles in bioleaching media may be considered fully contaminated, the slip velocity at the gas-liquid interface is null and therefore the bubbles may be considered as following the aforementioned drag force [4].

$$C_{\mathrm{D,lg}} = \begin{cases} 24 \left(1 + 0.15 Re_{\mathrm{b}}^{0.687} \right) / Re_{\mathrm{b}} & Re_{\mathrm{b}} < 1000 \\ 0.44 & Re_{\mathrm{b}} \geq 1000 \end{cases} \tag{4.8}$$

with Re_{b} the relative Reynolds number:

$$Re_{\mathrm{b}} = d_{\mathrm{b}} \left(\mathbf{u}_{\mathrm{g}} - \mathbf{u}_{\mathrm{l}} \right) / \nu_{\mathrm{l}} \tag{4.9}$$

Furthermore, a drag modification term, K'_{lg}, was considered to adapt the drag model for a polydispersed bubble flow. Brucato et al. (1998) proposed a correlation that modify the interphase exchange coefficient K_{lg} based on local turbulence:

$$K'_{\mathrm{lg}} = K_{\mathrm{lg}} \cdot \left[1 + K \left(\frac{d_{\mathrm{b}}}{l_{\mathrm{K}}} \right)^3 \right] \tag{4.10}$$

Where $K = 6.5 \times 10^{-6}$ is a constant adapted for a gas dispersed phase, d_{b} (m) the bubble diameter and l_{K} (m) the Kolmogorov length scale.

For the studied conditions, turbulence was modelled due to the high Reynolds numbers ($\mathrm{Re} > 10^4$). The dispersed k-ε model was chosen as it is recommended for multiphase flows considering a continuous and a dispersed phases with a density ratio between phases equal or higher to 2.5, which is validated for a gas dispersed phase (s.n. Ansys (2019) [5]). In this approach, turbulence is fully modelled for the continuous phase and the turbulence of the dispersed phase is possibly taken into account through additional interaction terms but preliminary simulations showed no impact of these terms on simulation results (data not shown).The k-ε model provides the transport equations of the turbulent kinetic energy k and its dissipation rate ε:

$$\nabla \cdot (\alpha_\mathrm{l} \rho_\mathrm{l} \mathbf{u}_\mathrm{l} k_\mathrm{l}) = \nabla \cdot \left(\alpha_\mathrm{l} \left(\mu_\mathrm{l} + \frac{\mu_{\mathrm{t,l}}}{\delta_k} \right) \nabla k_\mathrm{l} \right) + \alpha_\mathrm{l} G_{k,\mathrm{l}} - \alpha_\mathrm{l} \rho_\mathrm{l} \varepsilon_\mathrm{l} \tag{4.11}$$

$$\nabla \cdot (\alpha_\mathrm{l} \rho_\mathrm{l} \mathbf{u}_\mathrm{l} \varepsilon_\mathrm{l}) = \nabla \cdot \left(\alpha_\mathrm{l} \left(\mu_\mathrm{l} + \frac{\mu_{\mathrm{t,l}}}{\delta_\varepsilon} \right) \nabla \varepsilon_\mathrm{l} \right) + \alpha_\mathrm{l} \frac{\varepsilon_\mathrm{l}}{k_\mathrm{l}} \left(C_{\varepsilon 1} G_{k,\mathrm{l}} - C_{\varepsilon 2} \rho_\mathrm{l} \varepsilon_\mathrm{l} \right) \tag{4.12}$$

$\mu_{\mathrm{t,l}}$ (Pa s) is the turbulent viscosity of the continuous liquid phase:

$$\mu_{\mathrm{t,l}} = \rho_\mathrm{l} C_\mu \frac{k_\mathrm{l}^2}{\varepsilon_\mathrm{l}} \tag{4.13}$$

$G_{k,\mathrm{l}}$ ($\mathrm{kg\,m^{-1}\,s^{-2}}$) is the term of production of turbulent kinetic energy and the constants are defined as follow: $C_\mu = 0.09$, $C_{\varepsilon 1} = 1.44$, $C_{\varepsilon 2} = 1.92$, $\delta_k = 1$ and $\delta_\varepsilon = 1$.

Modelling of the volumetric gas-liquid mass transfer coefficient $k_\mathrm{L}a$

As presented in the literature review, the local mass transfer coefficient $k_\mathrm{L}a$ may be estimated by various models which depend on the description of the interface between gas and liquid [6]. $k_\mathrm{L}a$ is calculated as the product of the liquid side mass transfer coefficient k_L and the interfacial area a, represented by the mean Sauter diameter of the bubbles ($a = 6 \cdot \alpha_\mathrm{g} / d_\mathrm{b}$).

This work compared three models for the liquid side mass transfer coefficient k_L. The penetration theory of Higbie, which assumes mass transfer as long as there is a contact between gas and liquid, can be calculated using the following equation [7]:

$$k_\mathrm{L}^{\mathrm{pen}} = \frac{2}{\sqrt{\pi}} \cdot \sqrt{D_\mathrm{l}} \cdot \left(\frac{\varepsilon}{\nu_\mathrm{l}} \right)^{1/4} \tag{4.14}$$

Where D_l ($\mathrm{m^2\,s^{-1}}$) is the liquid diffusion coefficient, ε ($\mathrm{m^2\,s^{-1}}$) the turbulent energy dissipation rate and ν_l ($\mathrm{m^2\,s^{-3}}$) the liquid kinematic viscosity.

A modification of the penetration theory was suggested by Danckwerts who accounted for the surface renewal rate due to the contact of the bubbles with the turbulent eddies, which led to the following equation [8]:

$$k_{\mathrm{L}}^{\mathrm{eddy}} = 0.4 \cdot \sqrt{D_{\mathrm{l}}} \cdot \left(\frac{\varepsilon}{\nu_{\mathrm{l}}}\right)^{1/4} \tag{4.15}$$

Lastly, Calderbank (1959) suggested a mobile interface of the bubble [9]. This interface is related to the slip velocity u_{slip} ($\mathrm{m\,s^{-1}}$) which is the gas-liquid velocity difference, resulting in the renewal of the liquid at the surface of a bubble. The model of Calderbank is given by this equation:

$$k_{\mathrm{L}}^{\mathrm{slip}} = \frac{2}{\sqrt{\pi}} \cdot \sqrt{D_{\mathrm{l}}} \cdot \sqrt{\frac{u_{\mathrm{slip}}}{d_{\mathrm{b}}}} \tag{4.16}$$

From these different relations, the $k_{\mathrm{L}}a$ can thus be calculated locally. As it will be detailed later, the simulation of the gas dissolution and the transport of gaseous and dissolved oxygen in the two phases may theoretically be obtained using complementary simulations. However unsolvable numerical divergences were systematically obtained, probably to erroneous local mass balance arising from the simultaneous use of MRF approach and species transport equations. These concerns will be specified in the compartmental model.

Simulation setup of the laboratory-scale bioreactor

The geometry setup for the simulation of the 2-liter laboratory-scale bioreactor is shown on Fig. 4.2; this bioreactor is routinely used for bioleaching experiments in BRGM. The tank was a cylindrical vessel of diameter $T = 0.12$ m and liquid height $H = 0.187$ m. The tank was equipped with four conical baffles of width equal to $T/10$, placed symmetrically.

A dual impeller configuration was chosen using a bottom 6-bladed Rushton turbine with a fixed diameter $D = 0.05$ m and an off-bottom clearance $C = D$. The top impeller, a three-blade hydrofoil (A310), was positioned at a spacing $S = 0.06$ m above the bottom impeller and had a diameter equal to 0.06 m. Previous experimental work showed the efficiency of bottom Rushton impeller for gas dispersion [10, 11]. The impellers rotation was modelled using the multiple reference frame (MRF) approach. The rotating domain was positioned at $r_{\mathrm{bottom}} = 0.035$ m, $0.036\ \mathrm{m} \leq z_{\mathrm{bottom}} \leq 0.066$ m and $r_{\mathrm{top}} = 0.040$ m, $0.096\ \mathrm{m} \leq z_{\mathrm{top}} \leq 0.126$ m, respectively for the bottom and the top impellers. Fully turbulent conditions were ensured by carrying out the simulations at $N = 700$ rpm ($\mathrm{Re} = 4.5 \times 10^4$).

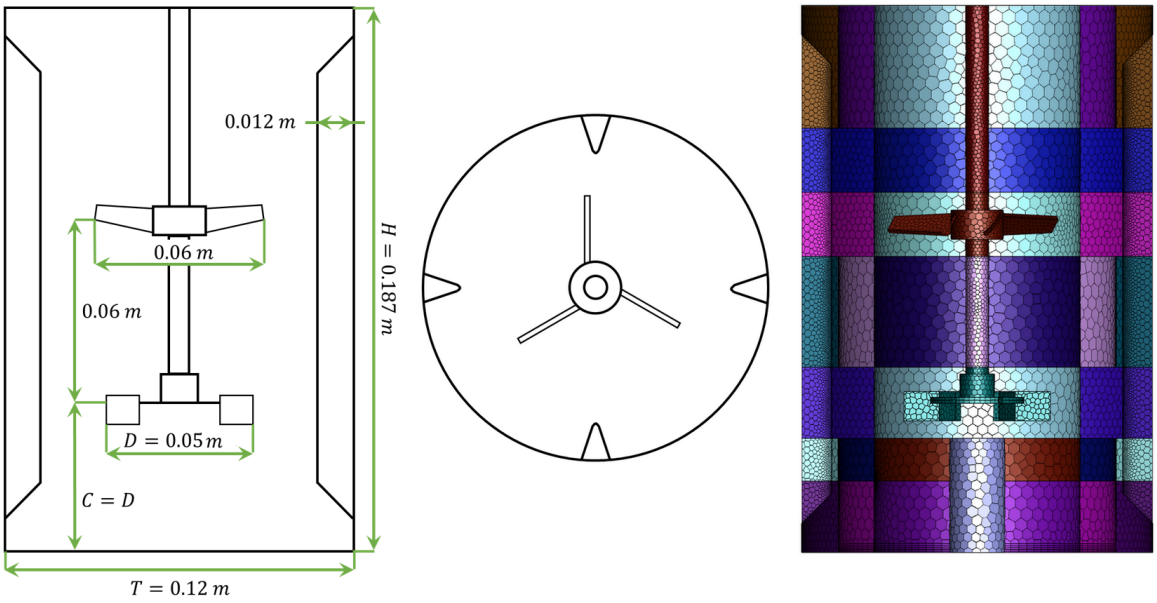

Figure 4.2: Planar view (left), cross-section (middle) and mesh (right) of the 2-liter two-stage stirred tank reactor. On the right: the colors represent the divisions of the compartment model, which used the same mesh as the non-divided simulation.

The gas inlet was described by a 0.025 m circle, placed at the bottom of the tank. Air was sparged at a flow rate of 0.25 vvm and consisted of bubbles of fixed diameter ($d_\mathrm{b} = 5 \times 10^{-3}$ m). The outlet, placed at the top surface of the tank, was represented by a degassing condition which specified a mass sink focused on the dispersed gas phase [5]. The gas-liquid free surface was supposed planar with a no-shear condition for the liquid and outlet for the gas. The gas flow regime was estimated for the system to ensure that no flooding will occur. This regime is classified using the aeration number N_A $(= Q_\mathrm{g}/(N \cdot D^3))$ and the Froude number F_r $(= N^2 \cdot D/g)$ [12]. It is considered that no flooding occurs below $N_A = 0.035$ or for $N_A/F_r < 0.3$ [13]. No flooding nor gas cavities were thus expected for this configuration as the aeration number N_A $(= Q_\mathrm{g}/(N \cdot D^3))$ was equal to 0.006.

A non-uniform mesh structure, shown on Fig. 4.2, was created to divide the geometry using the Fluent Meshing tool and was composed of 400,000 tetrahedral elements. Refinements were done along the wall and in the impellers regions. Mesh independence was preliminary verified by comparing velocity vectors fields and volume-averaged power dissipation.

Simulation setup of the pilot-scale bioreactor

The pilot-scale tank, shown on Fig. 4.3, had a working volume of 800 l, with a diameter of 0.950 m, a liquid height of 1.159 m and was equipped with 4 rectangular baffles whose width is equal to a tenth of the vessel diameter, placed symmetrically. This setup is the digital reproduction of an experimental setup located at the BRGM.

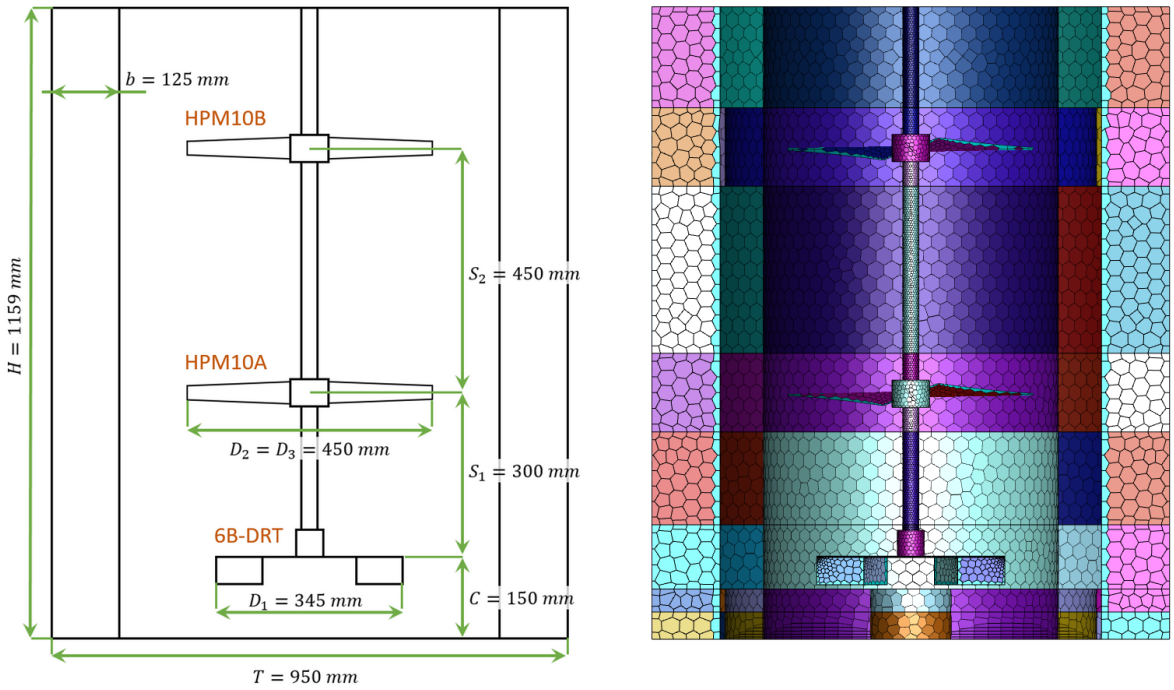

Figure 4.3: Drawing of the three-stage stirred tank reactor (left) and its mesh (right). The colors represent the divisions of the compartmental model, which used the same mesh.

Due to its aspect ratio ($H/T = 1.22$), the tank used a three-stage impeller configuration, needed for both solid homogenization and gas dispersion, with the impellers represented on Fig. 4.4. For this, at the bottom, a 6-bladed radial turbine (6B-DRT) was used with a clearance of 0.150 m. The middle and top impellers were respectively represented by a Robin turbine HPM10 13° (HPM10A) and a Robin turbine HPM10 18° (HPM10B), the degree corresponding to the torsion angle of the blades. These impellers, placed at a respective lower spacing of 0.300 and 0.450 m, facilitated global homogeneity within the tank.

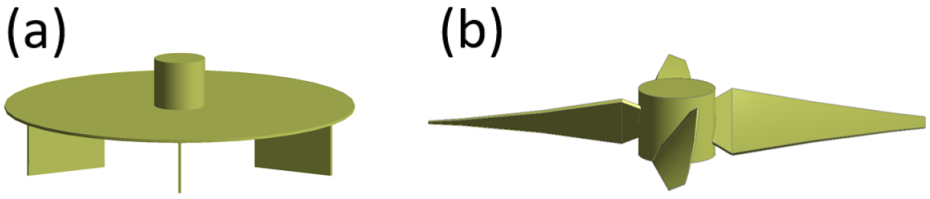

Figure 4.4: Impellers used in simulations. (a) 6-bladed radial turbine (6B-DRT); (b) Robin Turbine HPM 10 (HPM10).

Additionally to the previously mentioned geometrical characteristics, as the impellers rotation was modelled using the multiple reference frame approach, a rotating domain was added for each impellers. They were positioned at $r_{\text{bottom}} = 0.230$ m, 0.050 m $\leq z_{\text{bottom}} \leq 0.200$ m, $r_{\text{middle}} = r_{\text{top}} = 0.300$ m, 0.375 m $\leq z_{\text{middle}} \leq 0.525$ m, 0.825 m $\leq z_{\text{top}} \leq 0.975$ m, respectively for the bottom, middle and top impellers. This domain was later used as a reference frame for impeller rotation. The simulations were carried out at an agitation rate $N = 150$ rpm, ensuring fully turbulent conditions ($\text{Re} = 5{\times}10^5$).

Similarly to the laboratory-scale tank, the sparger was represented using a circular inlet of diameter equal to 1.5×10^{-1} m, placed at the bottom of the tank. A volumetric flow rate of 0.3 vvm was employed with a fixed bubble size of 5×10^{-3} m. Previous studies used a similar fixed value to represent the gas flow [14, 15]. A population balance on bubble size could have been used but was here not performed due to the difficulty of implementation as well as the high computing cost of such method. The outlet was described by a degassing condition at the top surface. The gas flow regime was obtained by calculating the aeration number N_A and the Froude number F_r. While N_A was found to be equal to 0.039, $N_A/F_r = 0.18$, indicating a loading regime but no flooding [12, 16].

The modelled setup was then divided into a non-uniform mesh structure, composed of 400,000 tetrahedral elements, as shown on Fig. 4.3. In order to avoid any numerical anomalies, multiple refinements were added along the wall and into the impellers rotating domains. Mesh independence was verified by comparing velocity vectors fields and volume-averaged power dissipation.

Solution method

The commercial software ANSYS Fluent 2019R3 was used for the numerical simulation of the multiphase flow. The conservation equations were solved on all meshes using the steady-state Eulerian method. The pressure-velocity based solver using the SIMPLE algorithm was used to solve the set of conservation equations. Discretization of the mass, momentum and volume fraction equations was carried-out using the second-order upwind scheme while pressure was spatially discretized using the PRESTO! scheme (s.n. Ansys (2018) [5]). Convergence of the simulations was admitted when transport equations residuals were less than 10^{-3}.

4.2.2 Validation of the gas-liquid CFD model

Power consumption

Model validity was ensured by determining whether the mechanical energy balance within the bioreactor was respected. For this, the power consumption P ($= 2\pi N C_w$) and the dissipated power P_{diss} ($= \rho_{\text{l}} \langle \varepsilon \rangle V$) were calculated and compared, as shown by Table 4.1. At the 2-liter scale, the results showed a significant difference between P and P_{diss} with $P_{\text{diss}}/P = 1.72$. The impact on $k_{\text{L}}a$ values will be proportional to $1.72^{1/4} = 1.14$ (see equation 4.14−4.15), which remains *a priori* acceptable. For the 800-liter, a good match was found between P and P_{diss} with only 8% of difference.

Table 4.1: Comparison of the power consumption and dissipated power for the impellers.

	P (W)	P_{diss} (W)	P_{diss}/P
2-liter tank	2.6	4.5	1.72
800-liter tank	271.4	250.6	0.92

The impeller power numbers N_P ($= P/(\rho_{\text{l}} N^3 d^5)$), mainly of the bottom impeller, were also looked for and compared with literature data. For the 2-liter tank, the RT6B showed $N_P = 3.52$, which is slightly lower than the literature values (usually between 4 and 6) [17]. The power number for the 6B-DRT of the 800-liter was equal to 2.62, which is slightly higher than the experimentally obtained value of 1.80. Once again, despite these differences, the consequences on the determination of the local oxygen transfer remain acceptable.

Gas hold-up

The gas hold-up was determined by volume-averaging the local gas volume fraction and comparison with the literature data. It was found that $\langle \alpha_{\text{g}} \rangle = 3.0\%$ for the 2-liter tank and 5.3% for the 800-liter tank. These value are in accordance with multiple sources from the literature that estimated a gas hold-up between 3 and 5% for similar conditions [2, 4, 18].

4.2.3 Determination of the mass transfer coefficient

The gas-liquid flows were simulated and the volume-averaged mass transfer coefficient $k_{\text{L}}a$ was obtained either using the penetration theory, or the Danckwerts or the Calderbank approach (Table 4.2). These results were compared with the experimental measurements, namely the results shown Chapter 2 for the laboratory-scale tank and BRGM data for the pilot-scale tank. Additionally, the local $k_{\text{L}}a$ was determined for the laboratory-scale tank at the position of the dissolved oxygen probe ($r_{\text{probe}} = 0.036$ m and $z_{\text{probe}} = 0.058$ m) using a static method.

Table 4.2: Mass transfer coefficients for the laboratory- and pilot-scale tanks.

k_La (s^{-1})		**CFD**		**Experimental**
	Higbie	**Danckwerts**	**Calderbank**	**-**
2-liter tank	0.066	0.024	0.006	0.025
800-liter tank	0.077	0.027	0.018	0.030

The results showed that all models were of the same order of magnitude as the experimental results. The penetration theory of Higbie indicated higher k_La values than the experimental results (164% for the 2-liter and 157% for the 800-liter). These results were in agreement with finding of Devi et al. (2017) who also reported an overfitting using the penetration theory for various configurations using a stirred tank reactor [6]. The model of Calderbank showed a better fit than the penetration theory, especially considering the pilot-scale tank, but predicted lower values than the experimental results (76% for the 2-liter and 40% for the 800-liter). Lastly, the model of Danckwerts displayed the best predictions for both configurations, with less than 4% error for the 2-liter tank and 10% for the 800-liter tank. Thus, comparing the three models, the Danckwerts model is the best fit but the model of Calderbank may still be acceptable in the case of the pilot-scale tank.

As previously pointed out, the global k_La only gives a part of the information needed to fully understand the impact of the tank and impeller geometries on gas-liquid mass transfer. For this, local considerations are needed to observe the disparity of k_La within the tank and, following this, the local distribution of k_La was looked at, as shown on Fig. 4.5. First of all, the comparison of the three models showed similar disparities, which is expected for the penetration theory and the Danckwerts models as the local liquid side mass transfer is related to $k_L \propto \varepsilon^{1/4}$. As of the model of Calderbank, it was shown by Calderbank (1959) that $d_b \propto \varepsilon^{1/2}$ and, furthermore, Midoux et al. (1980) observed that $k_L \propto d_b^{1/2}$ [9, 19]. This leads to a similar equivalence for the liquid side mass transfer of $k_L \propto d_b^{1/2} \propto \varepsilon^{1/4}$, which explained the similarities for the three models in terms of local mass transfer distribution. This distribution was also represented by an histogram using the Danckwerts model, as shown by Fig. 4.6. This showed an unimodal distribution of the local k_La with the largest bin being for $k_La \in [0.03; 0.04]$.

Looking at the local k_La distribution, the tank clearly showed 3 distinct zones of transfer. The first zone is represented by low values of k_La ($k_La \leq 2 \times 10^{-2}\,s^{-1}$ using the Danckwerts' model), located on a ring around the sparger and on top of the A310 impeller. This is explained knowing that $k_L \propto \varepsilon^{1/4}$ and, moreover, $a \propto \alpha_g\, d_b^{-1} \propto \alpha_g\, \varepsilon^{-1/2}$, which leads to $k_La \propto \alpha_g\, \varepsilon^{-1/4}$. The low k_La values around the sparger are indeed due to low gas concentrations α_g, as shown on Fig. 4.7a. Similar considerations are observed on the outer edge of the tank top and the inner sections are represented

by low values of ε, which results from the limited capacity of the A310 impeller at transmitting mechanical power in this area. In the second zone, the values of $k_{\mathrm{L}}a$ were close to the mean values ($2 \times 10^{-2}\,\mathrm{s}^{-1} \leq k_{\mathrm{L}}a \leq 1 \times 10^{-2}\,\mathrm{s}^{-1}$). This section was placed on the central part of the tank, where the impellers had the most impact on the mixing of the phases. Lastly, the third zone, represented by $k_{\mathrm{L}}a \geq 1 \times 10^{-2}\,\mathrm{s}^{-1}$, consisted mostly of sections with high gas fraction (on top of the sparger) or high ε (in direct vicinity to the impellers' blades).

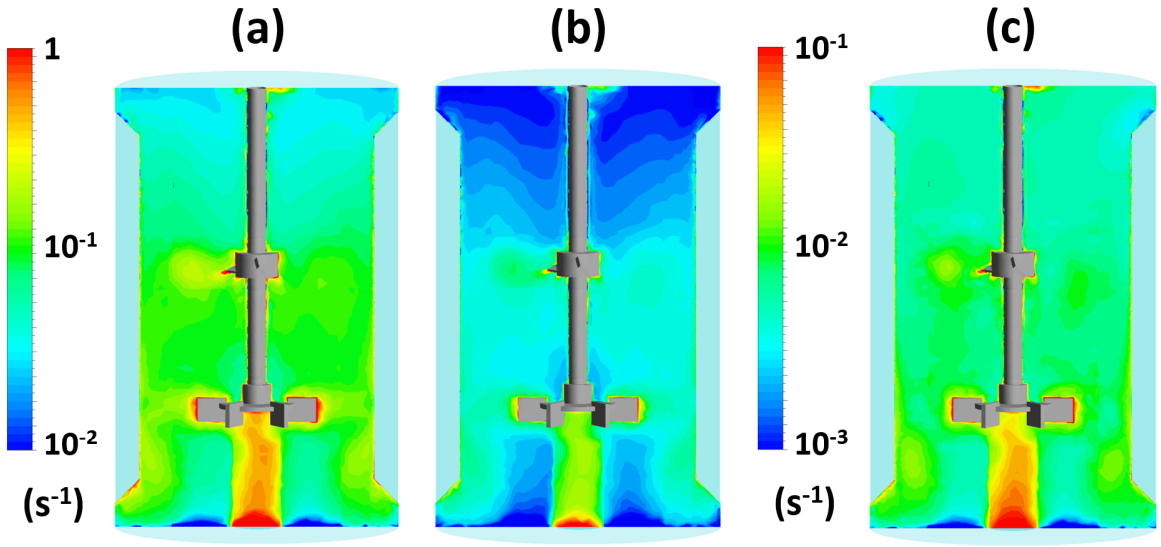

Figure 4.5: Simulated local mass transfer coefficient for the laboratory-scale tank for: (a) the penetration theory; (b) the Danckwerts model; (c) the Calderbank model.

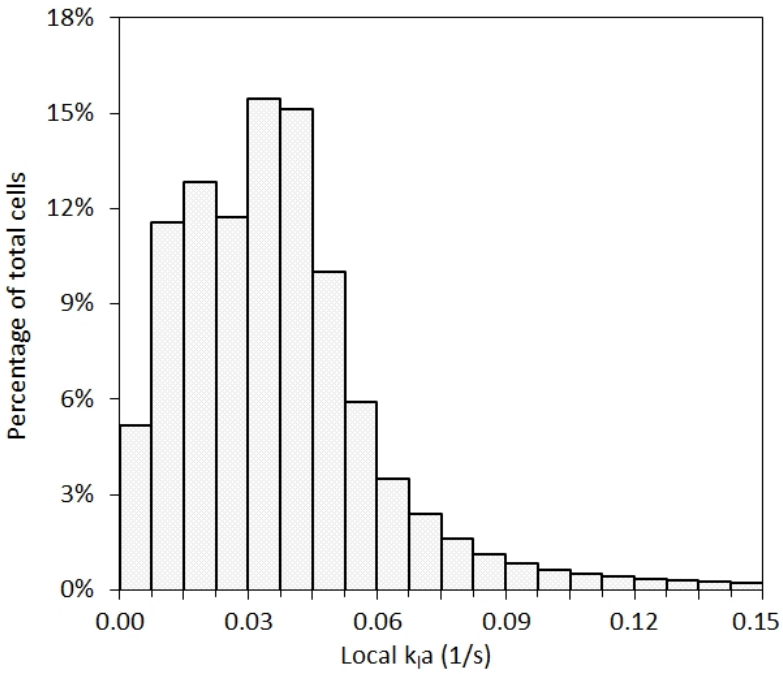

Figure 4.6: Histogram of $k_{\mathrm{L}}a$ distribution in the laboratory-scale tank using the Danckwerts model. The mesh consisted of 400000 cells.

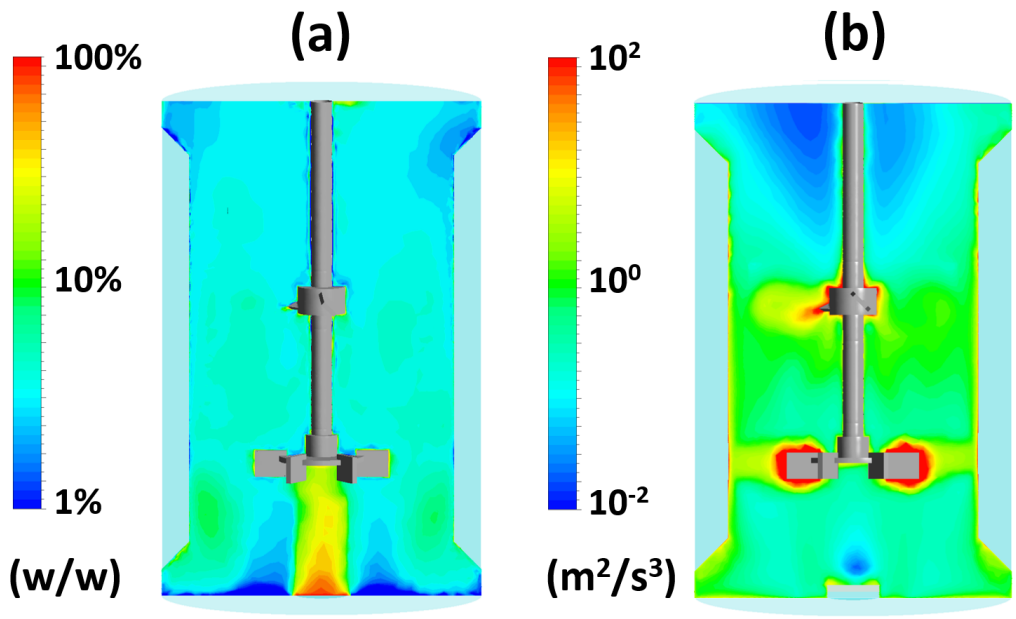

Figure 4.7: Simulated (a) gas holdup and (b) turbulence eddy dissipation rate ε for the laboratory-scale tank.

In addition to this study, the local value of $k_{\mathrm{L}}a$ was observed at the position of the dissolved oxygen probe used experimentally. A local value of $0.032\,\mathrm{s}^{-1}$ was reported compared to the experimental value of $0.025\,\mathrm{s}^{-1}$, which is higher than the global modelled value. This difference can be explained by the methods to obtain the $k_{\mathrm{L}}a$ experimentally. The oxygen probe not only measured the oxygen transfer in the reactor but also its transport due to the variation of oxygen concentration during the gassing-out experiment. This led to the measure of a mean value in the tank instead of the local instantaneous value reported by the CFD simulation and the Danckwerts model.

Considering the results of the pilot-scale tank, shown on Fig. 4.8a, the distribution of $k_{\mathrm{L}}a$ was more homogeneous, mostly due to the more uniform placement of the impellers throughout the tank. However, despite the presence of the disk on the 6B-DRT which forced the bubbles to disperse in the tank, the majority of the gas remained on the central part and only a small fraction was observed on the outer part, as shown by Fig. 4.8c. In addition, this configuration was responsible for a partial flooding of the impeller, which was expected for an aeration number $N_A = 0.039$ [12]. This led to a decrease of the energy consumption and thus a limitation of the dissipated energy, which may also result in a negative effect on the solid dispersion in the case of a bioleaching reactor.

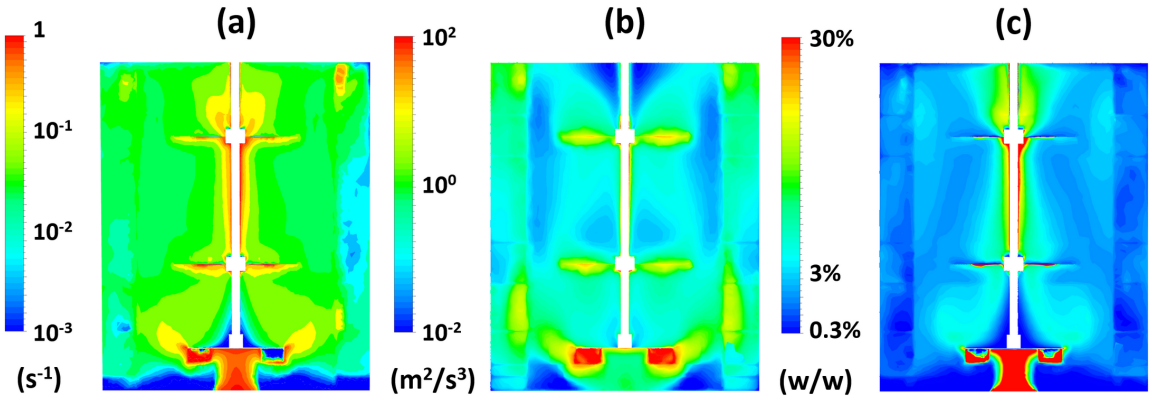

Figure 4.8: Simulated (a) $k_{\mathrm{L}}a$ distribution using the Danckwerts' model, (b) turbulence eddy dissipation rate ε and (c) gas holdup for the pilot-scale tank.

4.3 Kinetic modelling of main bioleaching reactions at the laboratory-scale

In this section, in parallel with the development of the CFD based compartmental gas-liquid model, the development of a kinetic model of bioleaching was carried out. This modelling step was established at the 2-liter scale and aimed at providing robust oxygen mass transfer and consumption rates to the compartmental model (presented in Subsection 4.3.1 and 4.3.2). At this scale, bioreactor homogeneity can be supposed ; thus, the kinetic model was simulated with an hypothesis of perfectly mixed gas and liquid phases.

4.3.1 Kinetic model description

The kinetic model consisted in biological and chemical reactions that were presented and discussed in Chapter 1. For validation purpose of the model, the experimental results obtained in Chapter 2 were used.

Sulphide mineral oxidation

The rate equation representing the mineral dissolution was described by the model of Bouffard et al. (2003) [20]. The model, presented in Eq. 4.17, related the rate of mineral dissolution r_{s} ($\mathrm{mol\,kg^{-1}\,h^{-1}}$) through a thermal function $K(T)$ ($\mathrm{h^{-1}}$), a chemical function $f(C)$ ($-$) and a topological parameter $g(d_{\mathrm{p},0}, X_{c,\mathrm{s}})$ ($-$).

$$r_{\mathrm{s}} = G_{\mathrm{s}} \cdot \frac{\mathrm{d}X_{c,\mathrm{s}}}{\mathrm{d}t} = G_{\mathrm{s}} \cdot K(T) \cdot f(C) \cdot g(d_{\mathrm{p},0}, X_{c,\mathrm{s}}) \tag{4.17}$$

With G_{s} ($\mathrm{mol\,kg^{-1}}$) the initial sulfide mineral grade and $X_{c,\mathrm{s}}$ ($-$) the mineral conversion.

- **Thermal function**

The thermal function $K(T)$ may be described using the Arrhenius equation representing the temperature-dependency on the chemical dissolution:

$$K(T) = K_{\text{ref}} \cdot \exp\left[-\frac{E_a}{R}\left(\frac{1}{T} - \frac{1}{T_{\text{ref}}}\right)\right] \tag{4.18}$$

where K_{ref} (h^{-1}) and T_{ref} (K) represent the reference temperature and kinetic constant value respectively, E_a (J mol^{-1}) is the activation energy and R (=8.314 $\text{J mol}^{-1}\,\text{K}^{-1}$) is the ideal gas constant.

- **Chemical function**

As the experimental data used to validate the model considered pyrite as sulphide mineral, the chemical function was chosen accordingly. For this, the chemical function $f(C)$ was modelled by a type III leaching, as presented by Nicol (1993) [21]:

$$f(C) = \left(\frac{[Fe^{3+}]}{[Fe^{2+}]}\right)^{0.5} \tag{4.19}$$

where $[Fe^{2+}]$ and $[Fe^{3+}]$ (mol l^{-1}) are the respective concentration of ferrous and ferric iron.

- **Topological parameter**

Lastly, the topological parameter $g(d_{\text{p},0}, X_{c,\text{s}})$ represented the steady decline of available mineral surface during the leaching. For this, the shrinking core model was used, as presented by Eq. 4.20:

$$g(1 - X_{c,\text{s}}) = (1 - X_{c,\text{s}})^{\varphi} \tag{4.20}$$

where φ is a topological parameter depending on the particles characteristics.

The parameters used for the rate equation of the sulphide mineral dissolution considered the leaching of spherical particles of pyrite in the laboratory-scale stirred tank reactor described in Chapter 2. The various parameters were reported in Table 4.3.

Table 4.3: Chemical parameters used for the kinetics equations.

Parameter	**Value**	**Unit**
Mineral oxidation parameters		
G_s	4.83	$\mathrm{mol\,kg^{-1}}$
T	42	°C
$K(T)$	3.2×10^{-4}	$\mathrm{h^{-1}}$
φ	3/2	−
Initial conditions		
$[FeS_2]_{\mathrm{ini}}$	100	$\mathrm{g\,l^{-1}}$
$[Fe^{2+}]_{\mathrm{ini}}$	2.1×10^{-3}	$\mathrm{mol\,l^{-1}}$
$[Fe^{3+}]_{\mathrm{ini}}$	1.8×10^{-2}	$\mathrm{mol\,l^{-1}}$
$[O_2]_{\mathrm{ini}}$	2.8×10^{-4}	$\mathrm{mol\,l^{-1}}$

Microbial growth modelling

Microbial growth was modelled using a Monod equation adapted to include the impact of ferric iron inhibition and dissolved oxygen as a second limiting substrate [22, 23]. Two separate equations were used for the iron-oxidizing and the sulfur-oxidizing bacteria:

$$\mu_{\mathrm{FO}} = \mu_{\mathrm{max,Fe}} \cdot \frac{[\mathrm{Fe^{2+}}]}{K_{\mathrm{Fe}} \cdot [\mathrm{Fe^{3+}}] + [\mathrm{Fe^{2+}}]} \cdot \frac{[\mathrm{O_2}]}{K_{\mathrm{O_2}} + [\mathrm{O_2}]} \tag{4.21}$$

$$\mu_{\mathrm{SO}} = \mu_{\mathrm{max,S}} \cdot \frac{[\mathrm{S^0}]}{K_{\mathrm{S}} + [\mathrm{S^0}]} \cdot \frac{[\mathrm{O_2}]}{K_{\mathrm{O_2}} + [\mathrm{O_2}]} \tag{4.22}$$

Where μ ($\mathrm{h^{-1}}$) is the specific growth rate, K_{Fe}, K_{S} and $K_{\mathrm{O_2}}$ ($\mathrm{mol\,l^{-1}}$) are the half-velocity constants and the subscripts FO and SO represent the iron-oxidizing and sulfur-oxidizing bacteria, respectively.

Using the previous equations, the biomass growth rate can be modelled using X (cell $\mathrm{l^{-1}}$) as the biomass concentration:

$$r_{X,FO} = \mu_{FO} \cdot X_{FO} \tag{4.23}$$

$$r_{X,SO} = \mu_{SO} \cdot X_{SO} \tag{4.24}$$

Similarly, the rate of substrates consumption and product formation can be obtained using the yield of biomass on substrate Y (cell $\mathrm{mol^{-1}}$):

$$r_{Fe^{2+}} = r_{X_{\mathrm{FO}}} / Y_{XFe^{2+}} \tag{4.25}$$

$$r_{S^0} = r_{X_{\mathrm{SO}}} / Y_{XS^0} \tag{4.26}$$

Considering the experimental results obtained using the BRGM-KCC consortia, it is safe to consider a system with two dominant bacteria, an iron-oxidizing and a sulfur-oxidizing. The biological parameters modelling the behaviour of these microorganisms were reported in Table 4.4.

Table 4.4: Kinetic parameters for the bioleaching microorganisms used in the models.

Parameter	**Value**	**Unit**
Biological parameters		
μ_{FO}	0.20	h^{-1}
μ_{SO}	0.01	h^{-1}
K_{FO}	7×10^{-3}	$\mathrm{mol\,l}^{-1}$
K_{SO}	1×10^{-1}	$\mathrm{mol\,l}^{-1}$
$K_{\mathrm{O_2}}$	5×10^{-5}	$\mathrm{mol\,l}^{-1}$
$Y_{XFe^{2+}}$	8.7×10^{11}	cell mol^{-1}
Y_{XS^0}	2×10^{12}	cell mol^{-1}
Initial conditions		
X_{FO}	1×10^{9}	cell l^{-1}
X_{SO}	1×10^{9}	cell l^{-1}

Oxygen mass transfer

Oxygen mass transfer was implemented using the overall model for gas-liquid mass transfer, as shown by the following equation:

$$r_{O_2}^{\mathrm{g}\to\mathrm{l}} = k_{\mathrm{L}}a\left([\mathrm{O_2}]_{\mathrm{l}} - [\mathrm{O_2}]_{\mathrm{l}}^{*}\right) \tag{4.27}$$

Where the constants were chosen using the measured values obtained with the gassing-out experiments, as shown in Chapter 2. Using these, $k_{\mathrm{L}}a = 85\,\mathrm{h}^{-1}$ and $[\mathrm{O_2}]_{\mathrm{l}}^{*}$ $= 2.84 \cdot 10^{-4}\ \mathrm{mol\,l}^{-1}$ were taken.

4.3.2 Simulation of the kinetic model

This model was developed independently from any consideration of hydrodynamic heterogeneities ; hence, it was simulated in an homogeneous stirred tank reactor using the 2-liter tank data previously obtained experimentally.

The modelled biomass was obtained and compared with experimental data, as shown by Fig. 4.9. In the same way as the evolution of the biomass during the experiment, the model shows an evolution following a short latency phase on the first day, an exponential phase between the second and seven day and finally a stationary phase for the time remaining. Comparing the two results, a lower concentration of biomass was observed at all times. Nevertheless, this difference was reduced when approaching

the stationary phase.

The evolution of pyrite dissolution was also observed, as shown by the conversion rate in Fig. 4.10. Experimentally, this conversion rate is the amount of cobalt released over time relative to the total amount contained in the sulfide mineral. The comparison of this experimental conversion rate with the model data showed a very good fitting with a relative error of less than 10% before day 6. However, the modeled values deviated from the experimental values beyond day 6. It is shown that the experimental values seem to remain around 75% dissolution while the model predicted a dissolution that rose up to 100% near day 8. Similar observations were obtained using the Fe^{3+}/Fe^{2+} ratio over time, as shown on Fig. 4.11. The experimental ratio remained constant after day 6, mainly due to the absence of further mineral dissolution at this point, which was not observed for the model as the dissolution became exponential. This difference could be attributed to jarosite precipitation occurring during the experiments. From the moment the particles are becoming small enough, a layer of jarosite could indeed form on their surface, strongly limiting the maximum dissolution observed. In the case of the model, precipitation was not taken into account and even if it were, the model could not predict a reduction of the reactive surface due to a passivation layer.

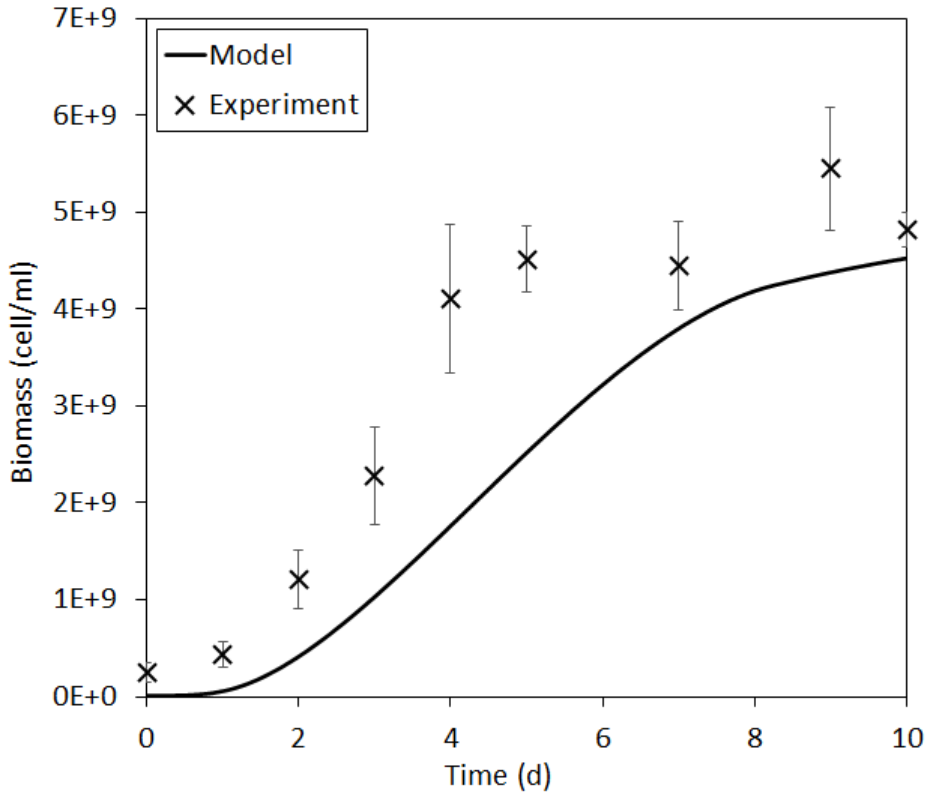

Figure 4.9: Comparison of the experimental and modelled biomass concentrations for the laboratory-scale tank.

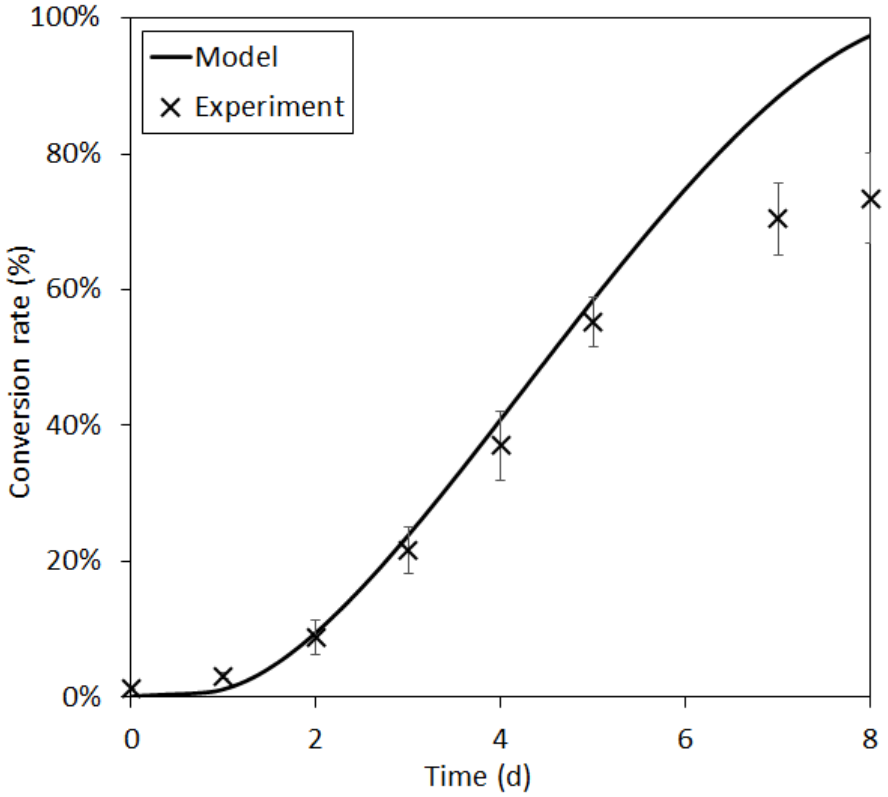

Figure 4.10: Comparison of the experimental and modelled pyrite conversion rate for the laboratory-scale tank.

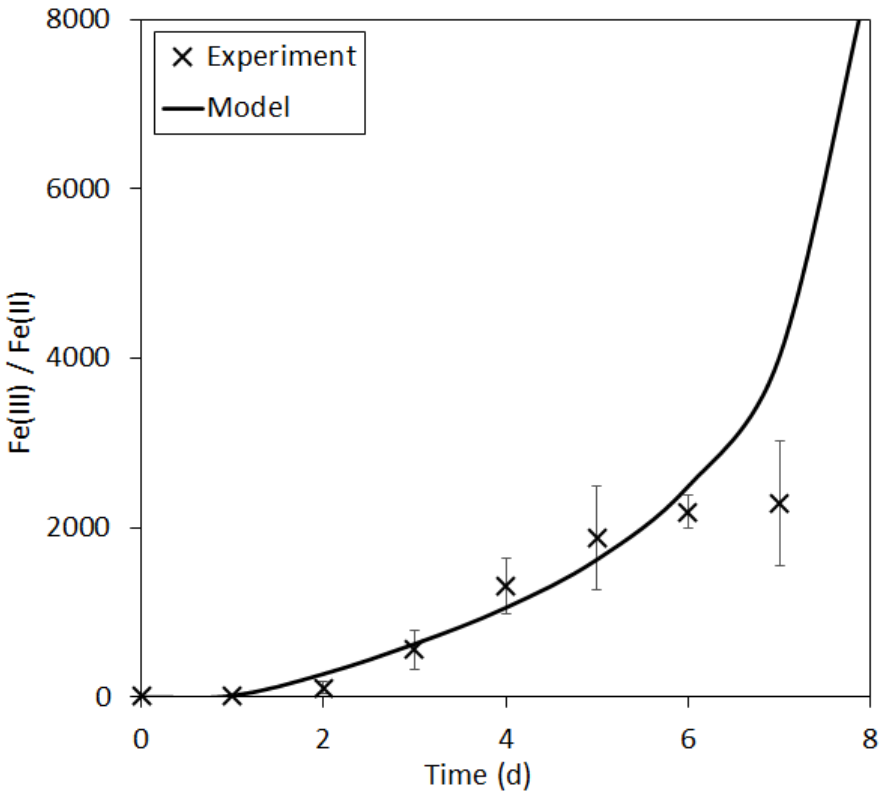

Figure 4.11: Evolution of the Fe^{3+}/Fe^{2+} ratio over time.

Lastly, the oxygen uptake rate was calculated as the variation of dissolved oxygen between two time steps, as observed on Fig. 4.12. Similarly to the dissolution rate, the comparison between the modelled and experimental data showed a good agreement. In both cases, the evolution of the OUR showed a bell-shaped curve with a slight latency phase on the first day, followed by a strong consumption over two following days. A lower maximum OUR was achieved, with $OUR_{mod} = 291\,\mathrm{mg\,l^{-1}\,h^{-1}}$ compared to the $396\,\mathrm{mg\,l^{-1}\,h^{-1}}$ obtained experimentally. Knowing that assumptions had to be made to obtain the OUR over time (see section 2.3), the experimentally observed maximum value was possibly overestimated.

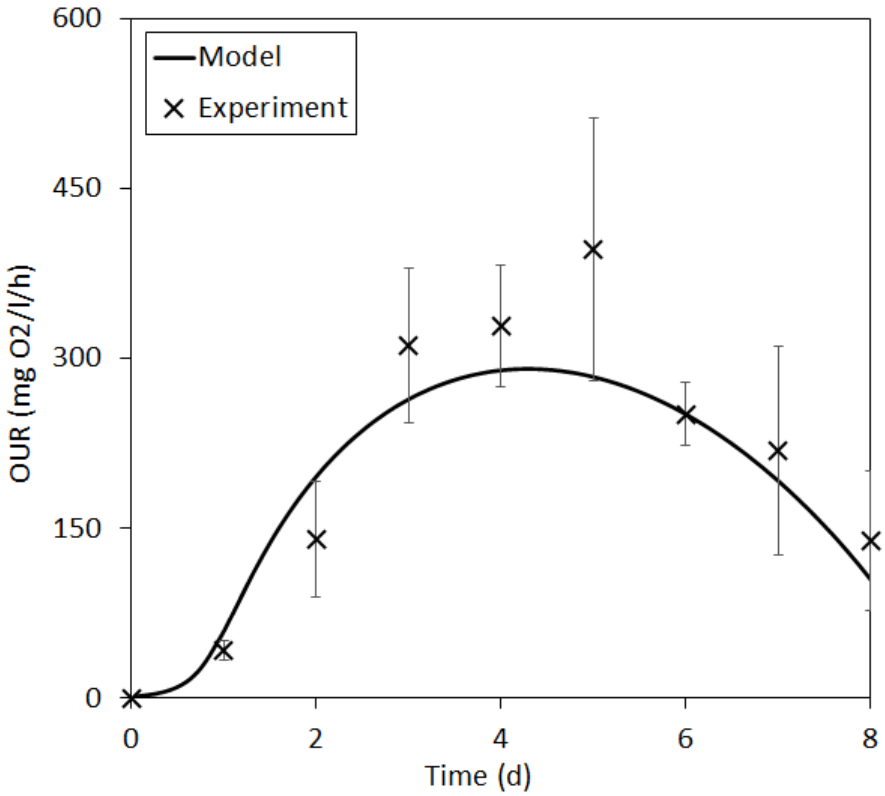

Figure 4.12: Comparison of the experimental and modelled OUR for the laboratory-scale tank.

The previous results thus showed that the kinetic model represented, with an acceptable error, what happened during the experiments and could be used to predict the evolution of the different components of the bioleaching reactor. Thus, in particular, data regarding the oxygen consumption and transfer were considered as valuable for implementation in the CFD-based compartmental approach.

4.4 Development of a gas-liquid CFD-based compartmental model

Now that full CFD gas-liquid simulations have been carried-out, a coupled kinetic / hydrodynamic approach was built in order to observe the impact of local heterogeneity in a bioleaching stirred tank reactor while limiting the computational cost of kinetic modelling. In the first place, this work attempted to achieve this approach via integration in the CFD model of the oxygen mass transfer mechanism coupled with a consumption term. This was done through the implementation of a user-defined function (UDF) describing a model of gas-liquid mass transfer using the local hydrodynamics conditions. However, the computational cost for the simulations increased dramatically, even for the laboratory-scale tank which showed an increase from 3 days to over 3 weeks after the addition of gas-liquid mass transfer. Furthermore, local numerical diffusion skewed the results by causing various erroneous sink terms to appear and significant discrepancies in the material balances. After analysis of the results, these errors were identified as resulting from the difference between the characteristic mass transfer time (of the order of a minute) and the mixing time (of the order of a few seconds) ; thus, the system progressed too fast, biasing the mass transfer through the STR. Considering these issues, a different approach was employed, using a CFD based compartmental model, developed in this section.

4.4.1 Description of the CFD-based compartmental model

The compartmental model was developed using the gas-liquid simulation showed in the previous section. For this, the methodology proposed by Gimbun et al. (2017) was essentially used and adapted [24]. This methodology consisted in dividing the tank into homogeneous compartments based on a chosen criterion. The compartments were defined on a radial section of the tank and then extended to the whole tank using surface revolution of each subsection. In this case, the division criterion was the velocity field data (liquid and gas) from the previously performed CFD simulation. The compartments were determined so that the mass transfer between each face of a given compartment would be predominantly in one direction only. To keep the same impeller-induced flows as in the CFD model, the previously established rotating zones were considered as compartments. The circulation loops induced by the different impeller motions were represented by two compartments for axial flow impellers and 4 compartments for radial flow impellers. As the sparger was mostly represented by a vertical gas flow, it was described by a single compartment below the bottom impeller. Lastly, the top surface was divided into multiple compartments (3 for the 2-liter tank and 2 for the 800-liter tank) to allow a recirculation in the tank. The laboratory-scale tank was thus divided into 17 compartments, accounting for the sparger gas discharge

and the flow patterns induced by the RT6B and the A310 impellers, as shown by Fig. 4.13.

The connection between the compartments was represented by the passage of a mass flow rate of liquid and gas across the compartment limits (Fig. 4.13). This mass flow rate Q was calculated by averaging the flow velocities across each surface depicting the interface between two compartments, as shown by Eq. 4.28. Although the division method led to a predominantly unidirectional mass flow, bidirectional flows through each compartment boundary were still considered. For this, inflow and outflow were represented for each interface and, moreover, the gas and liquid flows were independently considered for the gas and liquid, as showed in Table 4.6.

$$Q = \iint_S u \, dS \tag{4.28}$$

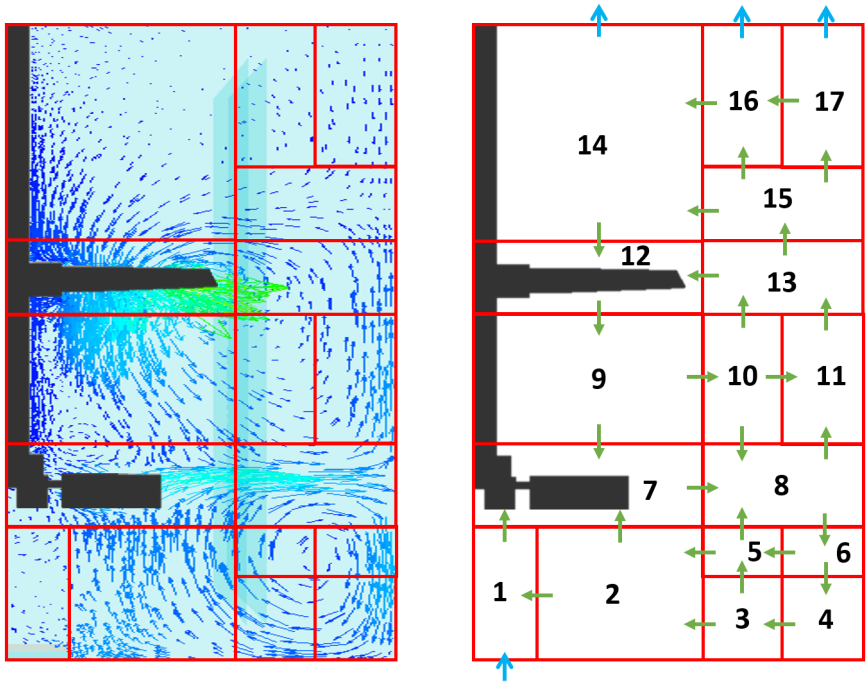

Figure 4.13: Description of the 2-liter compartmental model division with (left) the link between the liquid velocity profile and the compartments, and (right) the connections between the different compartments. The green arrows represent the predominant mass flow directions and the blue arrows represent the gas inlet and outlet. Scheme based on Gimbun et al. (2016) methodology [24].

Each individual compartments was considered homogeneous in terms of gas fraction α_g, turbulent dissipation ε, pressure and mass transfer coefficient $k_L a$. For this, the average value of these parameters were calculated by volume averaging across the calculation cells of the compartment. These averaged values were reported on Table 4.5. Here, the $k_L a$ was determined using the model of Danckwerts, as determined to be the best fit in the previous section [8].

Table 4.5: Averaged parameter for each compartment of the 2-liter tank.

Compartment	**Volume** ($\times 10^{-1}$ l)	$\langle \alpha_g \rangle$ (w/w)	$\langle \varepsilon \rangle$ ($m^2\,s^{-3}$)	$\langle P \rangle$ (Pa)	$\langle k_L a \rangle$* (s^{-1})
1	1.09	28.03%	0.50	101632	0.184
2	14.05	3.32%	0.30	101461	0.023
3	7.76	4.35%	0.32	101410	0.031
4	10.09	3.96%	0.57	101376	0.031
5	4.64	6.69%	0.24	101477	0.045
6	5.85	5.82%	0.85	101453	0.049
7	9.04	4.83%	34.33	101450	0.065
8	17.46	4.50%	1.75	101348	0.045
9	14.53	4.22%	0.79	101485	0.038
10	12.07	4.17%	0.75	101396	0.037
11	15.16	4.01%	0.89	101364	0.036
12	8.12	4.12%	14.40	101541	0.050
13	15.73	3.89%	0.53	101376	0.031
14	24.47	3.42%	0.10	101343	0.017
15	15.74	3.40%	0.14	101343	0.019
16	13.39	3.22%	0.05	101326	0.014
17	17.14	3.10%	0.07	101325	0.013

* based on the model of Danckwerts [8].

A similar approach was used for the 800-liter tank, which implied a greater number of compartments due to the additional recirculation loops induced by the third impeller, as shown by Fig. 4.14. Furthermore, the low clearance of the bottom impeller required the addition of extra compartments near the tank bottom. The mass flow rates were also represented bidirectionally at the interface of each compartment (Table 4.8) and the various parameters were averaged for each compartment (Table 4.7). Pressure is an important parameter to take into account when considering mass transfer as it will impact the saturation concentration of gases. The pilot-scale tank indeed displayed a pressure 9.4% higher than the atmospheric pressure at the bottom while the laboratory-scale was less than 0.1% higher. As the equilibrium concentration $c_g^* \propto P_{tot}$, the transfer rate will be increased. This effect is particularly significant for industrial-scale tanks and must be carefully considered for the process sizing.

Table 4.6: Mass in flows and out flows between each compartment of the 2-liter tank.

Flow direction	**Liquid**		**Gas**	
	In flow ($\times 10^{-5}$ m^3)	**Out flow** ($\times 10^{-5}$ m^3)	**In flow** ($\times 10^{-6}$ m^3)	**Out flow** ($\times 10^{-6}$ m^3)
1 to **2**	3.41	0.04	1.79	0.01
1 to **7**	0.00	3.38	0.00	9.45
2 to **3**	97.85	0.00	35.78	0.00
2 to **5**	9.00	2.68	4.73	1.30
2 to **7**	0.00	100.80	0.00	37.38
3 to **4**	137.98	0.00	64.90	0.00
3 to **5**	3.22	43.35	1.51	30.59
4 to **6**	138.04	0.07	65.12	0.19
5 to **6**	13.41	7.98	10.21	6.37
5 to **8**	0.99	40.22	0.54	30.01
6 to **8**	143.40	0.00	68.74	0.02
7 to **8**	0.00	179.53	0.00	76.13
7 to **9**	75.49	0.13	29.32	0.14
8 to **10**	29.83	0.65	10.03	0.49
8 to **11**	0.02	104.56	0.00	46.49
9 to **10**	0.12	66.64	0.12	25.97
9 to **12**	142.25	0.37	55.56	0.45
10 to **11**	21.53	26.43	9.86	9.90
10 to **13**	0.08	32.53	0.01	16.29
11 to **13**	0.00	109.43	0.00	46.54
12 to **13**	51.17	3.77	23.36	1.29
12 to **14**	94.49	0.02	33.07	0.01
13 to **15**	0.31	94.80	0.09	40.83
14 to **15**	72.45	0.00	28.25	0.00
14 to **16**	25.42	3.38	8.63	1.04
15 to **16**	1.48	16.27	0.11	7.98
15 to **17**	9.02	16.26	1.49	6.21
16 to **17**	16.93	9.69	5.34	3.15

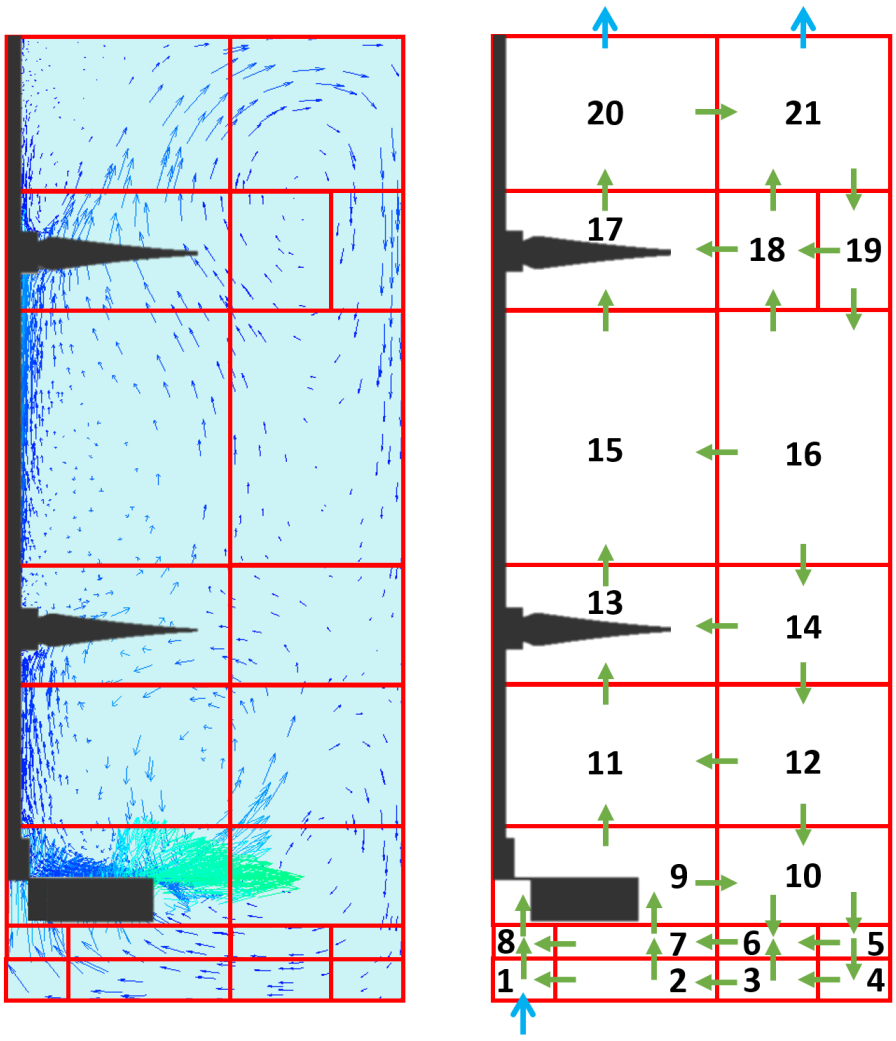

Figure 4.14: Description of the 800-liter compartment model division with (left) the link between the liquid velocity profile and the compartments, and (right) the connections between the different compartments. The green arrows represent the predominant mass flow directions and the blue arrows represent the gas inlet and outlet. Scheme based on Gimbun et al. (2016) methodology [24].

Table 4.7: Averaged parameter for each compartment of the 800-liter tank.

Compartment	**Volume** (l)	$\langle \alpha_g \rangle$ (w/w)	$\langle \varepsilon \rangle$ ($m^2\,s^{-3}$)	$\langle P \rangle$ (Pa)	$\langle k_L a \rangle$* (s^{-1})
1	0.85	35.79%	0.62	110911	0.274
2	10.63	0.26%	0.45	110935	0.002
3	6.73	0.37%	0.02	110997	0.001
4	17.19	0.63%	0.03	111025	0.003
5	14.44	2.47%	0.03	110570	0.009
6	5.65	1.79%	0.02	110543	0.006
7	8.93	1.57%	2.25	110394	0.016
8	0.73	20.38%	0.62	110341	0.153
9	26.81	8.10%	4.79	109510	0.090
10	56.43	3.99%	0.21	109786	0.020
11	39.00	7.44%	0.26	108086	0.045
12	81.28	4.84%	0.25	108482	0.028
13	32.87	6.06%	0.42	106788	0.039
14	68.85	4.43%	0.06	107050	0.018
15	70.20	5.65%	0.12	104784	0.028
16	146.31	5.12%	0.04	104921	0.019
17	32.87	6.12%	0.46	102721	0.040
18	19.36	6.14%	0.03	102775	0.022
19	49.49	6.24%	0.05	102786	0.025
20	42.43	7.67%	0.12	101299	0.037
21	88.46	5.48%	0.10	101325	0.024

* based on the model of Danckwerts [8].

Table 4.8: Mass in flows and out flows between each compartment of the 800-liter tank.

Flow direction	**Liquid**		**Gas**	
	In flow ($\times 10^{-3}$ m^3)	**Out flow** ($\times 10^{-3}$ m^3)	**In flow** ($\times 10^{-5}$ m^3)	**Out flow** ($\times 10^{-5}$ m^3)
1 to **2**	9.22	0.00	0.19	0.00
1 to **8**	0.00	9.22	0.00	39.72
2 to **3**	23.59	0.00	0.80	0.00
2 to **7**	4.61	19.00	1.15	1.72
3 to **4**	24.49	0.00	1.72	0.00
3 to **6**	0.48	1.40	0.00	0.85
4 to **5**	24.49	0.04	2.10	0.23
5 to **6**	0.00	18.75	0.00	5.02
5 to **10**	43.19	0.01	7.41	0.36
6 to **7**	0.00	18.30	0.00	3.00
6 to **10**	0.65	2.02	0.00	2.76
7 to **8**	0.21	3.13	0.30	0.12
7 to **9**	7.06	36.85	5.26	8.92
8 to **9**	0.00	12.15	0.00	39.47
9 to **10**	8.70	48.25	2.04	31.45
9 to **11**	20.05	22.91	10.65	25.89
10 to **12**	44.78	42.48	11.00	35.34
11 to **12**	15.28	21.01	11.41	15.06
11 to **13**	9.11	6.06	0.64	14.20
12 to **14**	14.20	18.07	1.07	26.40
13 to **14**	27.63	0.00	14.43	0.00
13 to **15**	1.18	25.97	0.00	26.23
14 to **16**	27.36	3.69	2.79	13.08
15 to **16**	39.02	0.02	21.04	0.01
15 to **17**	0.00	63.58	0.00	49.77
16 to **18**	0.03	16.90	0.00	17.07
16 to **19**	80.13	0.50	28.88	2.24
17 to **18**	22.32	0.39	13.35	0.29
17 to **20**	0.11	85.14	0.12	68.03
18 to **19**	19.21	0.05	13.38	0.05
18 to **21**	0.02	14.09	0.00	17.61
19 to **21**	98.97	0.17	41.06	1.55
20 to **21**	0.00	84.82	0.00	47.56

4.4.2 Oxygen mass balance and gas-liquid mass transfer

The compartment model was used in combination with equations modelling the gas-liquid mass transfer throughout the tank (see Section 4.3). For this, boundary conditions were set for the gas phase to model the gas inlet and outlet. Considering the 2-liter tank, the first compartment was described by a cylinder whose base had the same diameter as the sparger considered in the gas-liquid simulation. This inlet was fed using air ($\rho_{\mathrm{g}} = 1.225\,\mathrm{kg\,m^{-3}}$) with an oxygen molar fraction of 21% adjusted to the local pressure field. The gas outlet was depicted by the top surface of the compartments 14, 16 and 17.

Oxygen mass balance was established in each compartment and gave the evolution of oxygen concentration in the liquid and gas phases. Thus, this evolution took into account four phenomena in each compartment and for each phase: (i) incoming phase oxygen mass flow rate $r_{\mathrm{O_2}}^{\mathrm{j\to i}}$ from compartment j to compartment i, (ii) outgoing phase oxygen mass flow rate $r_{\mathrm{O_2}}^{\mathrm{i\to j}}$ from compartment i to compartment j, (iii) internal gas-liquid mass transfer rate $r_{\mathrm{O_2}}^{\mathrm{g\to l}}$ and (iv) internal consumption rate $r_{\mathrm{O_2}}^{\mathrm{cons}}$. The $r_{\mathrm{O_2}}^{\mathrm{j\to i}}$ ($\mathrm{g\,l^{-1}\,h^{-1}}$) was obtained using the incoming mass flow rates of the phase considered $Q^{\mathrm{j\to i}}$ ($\mathrm{l\,h^{-1}}$) and assuming that the oxygen concentration in these flows $[\mathrm{O_2}]$ ($\mathrm{g\,l^{-1}}$) was the same as the concentration of the compartment from which it came (compartments are supposed perfectly mixed). The following equations considered a compartment i fed by adjacent compartments denoted by the j subscript:

$$r_{\mathrm{O_2,l}}^{\mathrm{j\to i}} = \frac{1}{\alpha_{\mathrm{l,i}} V_{\mathrm{i}}} \sum_j \left(Q_{\mathrm{l}}^{\mathrm{j\to i}} \cdot [\mathrm{O_2}]_{\mathrm{l,j}} \right) \tag{4.29}$$

$$r_{\mathrm{O_2,g}}^{\mathrm{j\to i}} = \frac{1}{\alpha_{\mathrm{g,i}} V_{\mathrm{i}}} \sum_j \left(Q_{\mathrm{g}}^{\mathrm{i\to j}} \cdot [\mathrm{O_2}]_{\mathrm{g,j}} \right) \tag{4.30}$$

The outgoing mass flow rate $r_{\mathrm{O_2}}^{\mathrm{i\to j}}$ was retrieved using a similar expression and considering the concentration of the compartment considered:

$$r_{\mathrm{O_2,l}}^{\mathrm{i\to j}} = \frac{[\mathrm{O_2}]_{\mathrm{l,i}}}{\alpha_{\mathrm{l,i}} V_{\mathrm{i}}} \sum_j Q_{\mathrm{l}}^{\mathrm{i\to j}} \tag{4.31}$$

$$r_{\mathrm{O_2,g}}^{\mathrm{i\to j}} = \frac{[\mathrm{O_2}]_{\mathrm{g,i}}}{\alpha_{\mathrm{g,i}} V_{\mathrm{i}}} \sum_j Q_{\mathrm{g}}^{\mathrm{i\to j}} \tag{4.32}$$

The compartment gas-liquid mass transfer rate $r_{\mathrm{O_2}}^{\mathrm{g\to l}}$ was calculated based on the mass transfer coefficient $k_{\mathrm{L}}a$ obtained from the Danckwerts' model:

$$r_{\mathrm{O_2,l,i}}^{\mathrm{g\to l}} = k_{\mathrm{L}} a_{\mathrm{i}} \cdot \left([\mathrm{O_2}]_{\mathrm{l,i}}^{*} - [\mathrm{O_2}]_{\mathrm{l,i}} \right) = -r_{\mathrm{O_2,g,i}}^{\mathrm{g\to l}} \tag{4.33}$$

Where the equilibrium concentration $[O_2]_l^*$ is determined using the Henry's law:

$$[O_2]_{l,i}^* = H_{O_2} \cdot P_{O_2,i} \tag{4.34}$$

Using the previous expressions and considering a volumetric consumption of O_2 $r_{O_2,l}^{cons}$, the internal variation of oxygen concentration $d[O_2]/dt$ can be obtained:

$$\frac{d[O_2]_{l,i}}{dt} = r_{O_2,l}^{j\to i} - r_{O_2,l}^{i\to j} + r_{O_2,l,i}^{g\to l} - r_{O_2,l,i}^{cons} \tag{4.35}$$

$$\frac{d[O_2]_{g,i}}{dt} = r_{O_2,g}^{j\to i} - r_{O_2,g}^{i\to j} - r_{O_2,l,i}^{g\to l} \tag{4.36}$$

4.4.3 Validation of gas-liquid mass transfer modelling with the compartmental model

The compartmental model was firstly used for the laboratory-scale tank to simulate the gassing-out method carried out experimentally and observed the evolution of the dissolved oxygen concentration in each compartment. For this, the commercial software MATLAB R2017a was used in combination with the *ode23* solver in order to solve the set of ordinary differential equations in all compartments (Eq. 4.35 − 4.36). As the model needs the hydrodynamics to be solved, no modification of hydrodynamics may be done during compartmental approach use. Thus, the oxygen concentration in the bubbles for each compartment was initialized at $0\,g\,l^{-1}$ to model the absence of oxygen in the tank at the beginning of the experiment. Then, $P_{O_2,g}$ was set to 0.21 bar with a Henry's constant $H_{O_2} = 2.46 \times 10^9\,Pa\,l\,kg^{-1}$. The computation time to perform this simulation was much lower than the full-CFD model and lasted only a few seconds. The result of this experiment is shown on Fig. 4.15, with the compartment 8 selected as the model data as it is the experimental probe location.

The results showed that the model was in very good agreement with the experimental measurements, with a coefficient of determination $r^2 = 0.99$. The slight variation observed in the evolution and maximum value could be due to the modelling hypotheses used in the CFD simulation and compartment model. Despite the modelled data being shown for compartment 8, it was found that few to no differences where observed between the compartments, with a maximum standard variation of $0.05\,mg\,l^{-1}$ for the dissolved oxygen concentration. This was expected regarding the small volume of the bioreactor.

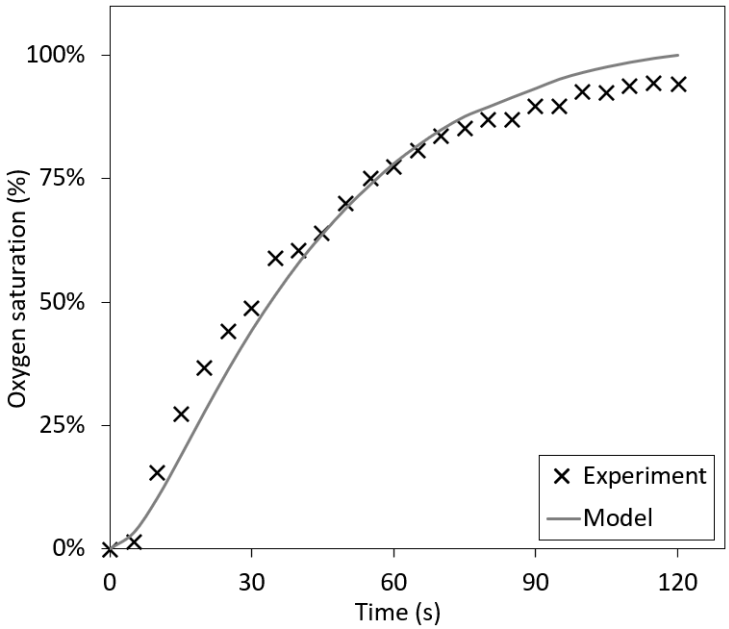

Figure 4.15: Evolution of oxygen saturation along time in a gassing-out experiment and comparison with the modelled values. For this simulation, $r^{\text{cons}}_{\text{O}_2,\text{l}} = 0$.

The distributions of $\langle k_\text{l}a \rangle$ in each compartment were also considered for each tank, as shown on Fig. 4.16. As expected, the highest $\langle k_\text{l}a \rangle$ values were at the level of the sparger and in areas of high turbulence such as in the vicinity of the impellers. The 2-liter tank showed areas of low $k_\text{l}a$ values near the surface of the tank, mainly due to the low energy dissipation in these areas. In the 800-liter tank, similar low $k_\text{l}a$ values areas are observed at the bottom of the tank near the outer edge. These areas are a result of the large aeration number of this system ($N_A = 0.039$), leading to a partial flooding of the impeller and the difficulty of the impeller in dispersing the gas throughout the bottom of the tank.

In the section 4.3, it was shown that the maximum oxygen uptake rate was around $396\,\text{mg}\,\text{l}^{-1}\,\text{h}^{-1}$. The compartment model was used to represent the evolution during the gassing-out method of various consumption rates on the dissolved oxygen concentration (Fig. 4.17). For low consumption rates ($r^{\text{cons}}_{\text{O}_2,\text{l}} \leq 180\,\text{mg}\,\text{l}^{-1}\,\text{h}^{-1}$), as observed in the first few days of a bioleaching experiment, the dissolved oxygen concentration was near the maximum value and no oxygen limitation could be detected in these conditions. At consumption rates similar to the maximum oxygen uptake rate phase observed in a bioleaching experiment, the oxygen saturation is dropping below the 50% threshold. Considering that these results are obtained for a global consumption rate, which is not representative of the experimental heterogeneities, it could mean that this threshold is the point where dissolved oxygen becomes the limiting substrate. Furthermore, it was observed for consumption rate past this value that the oxygen concentration dropped dramatically, down to $0\,\text{mg}\,\text{l}^{-1}$ for $r^{\text{cons}}_{\text{O}_2,\text{l}} \geq 1800\,\text{mg}\,\text{l}^{-1}\,\text{h}^{-1}$.

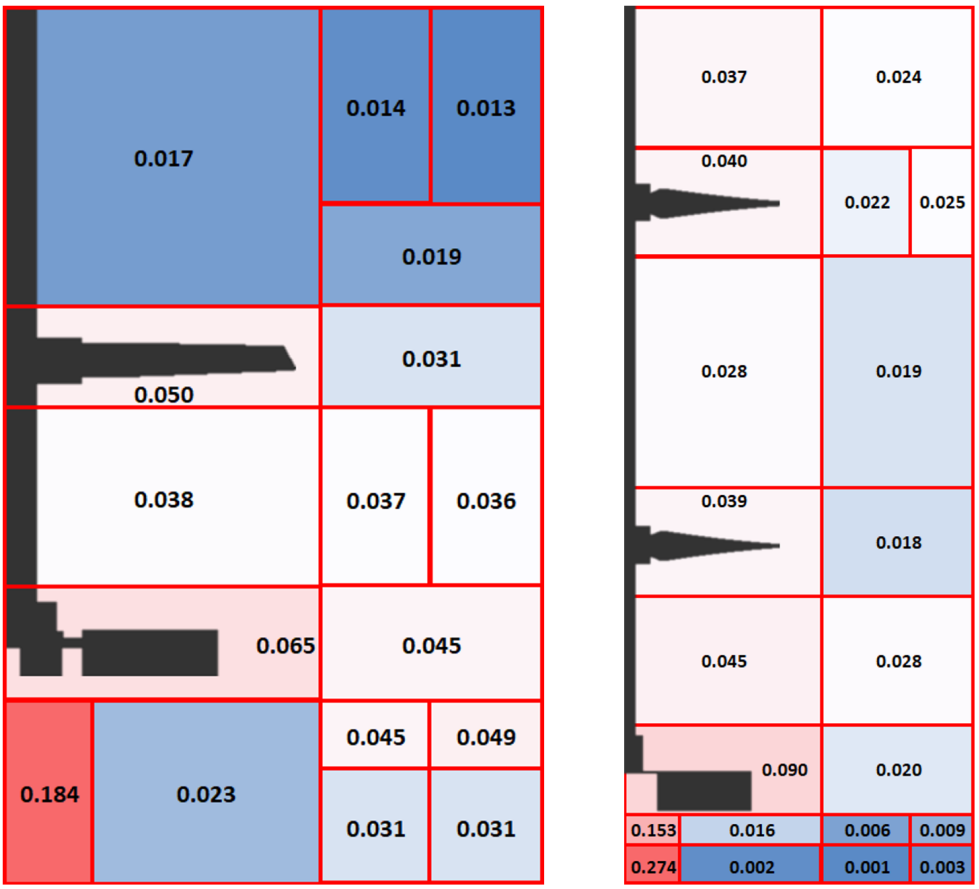

Figure 4.16: Representation of $\langle k_l a \rangle$ in each compartment for the laboratory- (left) and pilot-scale (right) tanks.

The pilot-scale tank was also considered but could not be compared to experimental bioleaching results due to lack of data. However, the impact of the scale of the tank was still observed. It was found that, compared to the 2-liter tank, the variation of dissolved oxygen concentration was higher and differences up to $0.5\,\mathrm{mg\,l^{-1}}$ were observed between the compartments during the gassing-out experiments without consumption term. The addition of a consumption term showed the same results that of the laboratory-scale tank, leading to a similar consumption rate $r^{\mathrm{cons}}_{\mathrm{O_2,l}} = 400\,\mathrm{mg\,l^{-1}\,h^{-1}}$ responsible for an oxygen saturation of 50%. These scale-up results will be developed in the following dedicated paragraph.

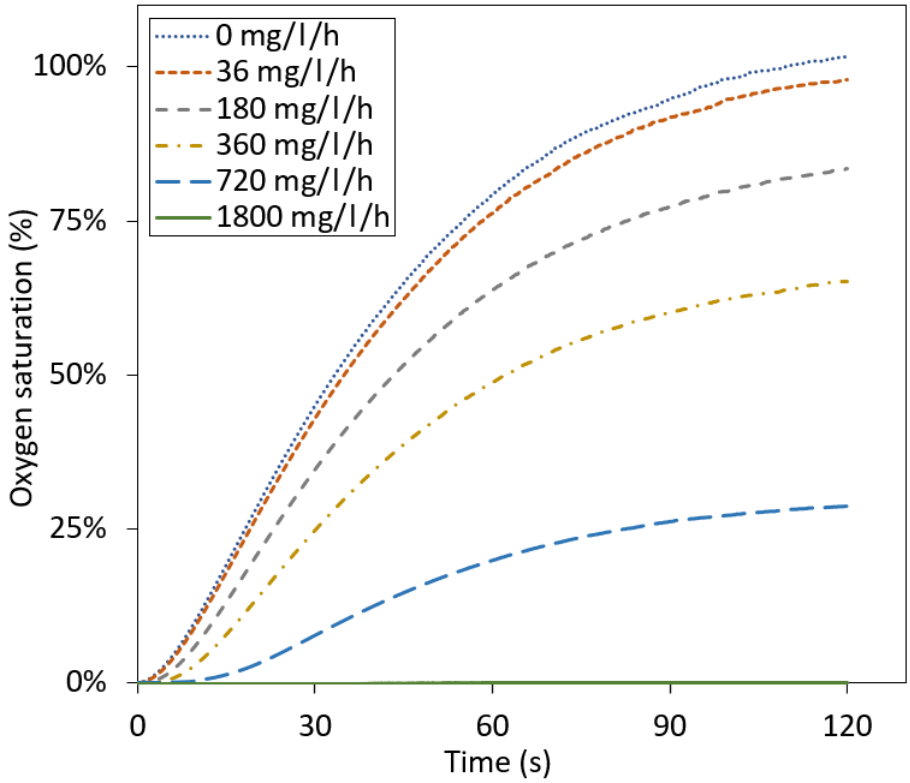

Figure 4.17: Impact of oxygen consumption on the evolution of the dissolved oxygen concentration. Values indicate the dissolved oxygen consumption rate $r^{\text{cons}}_{\text{O}_2,\text{l}}$.

4.5 Scaling-up the compartmental model and prediction of bioreactor oxygenation at the industrial scale

One key limitation of the compartmental approach generalization in the chemical and biochemical industries is the availability of an "industrial-scaled" compartment matrix that provides not only the circulation between each compartment but also the compartment-averaged values of main hydrodynamic variables (volume of compartment, gas-liquid mass transfer coefficient, solid and gas fractions, turbulent dissipation rate). This is jointly explained by the calculation times of CFD simulations for systems larger than 1 m^3 (namely when calculation cell number exceeds 10^7), the possible instability of the multiphase calculation and the lack of experimental validations at the industrial scale. However, the availability of the compartmental matrix at the pilot-scale allows a more sophisticated scale-up procedure in comparison with classic approach considering that the bioreactor is perfectly mixed. It was thus proposed here to scale-up the results for the compartmental matrix at 800 l to industrial scales of 800 and 2000 m^3, in complete geometric similarity. Some relatively strong hypothesis have been discussed but they probably remain sensibly weaker than the hypothesis of perfectly mixed bioreactor.

4.5.1 Scale-up strategy

Let us consider a 800 m^3 bioleaching bioreactor which is geometrically similar to the previously studied 800 l bioreactor. Let us define the geometric ratio K_L, which is the ratio between the lengths between two similar points in each bioreactor. More particularly:

$$K_L = \frac{T'}{T} = \frac{D'}{D} \tag{4.37}$$

With T' (m) and D' (m) the 800 m^3 tank and impeller diameters respectively.

Let us suppose till demonstrated that both bioreactors are decomposed using the same set of compartments, also in geometric similarities. The number of compartments c at both scale will be thus the same. For instance, the volume of each compartment V_i may be extrapolated using the following equation:

$$\forall i \in [1; c]\ V_i' = K_L^3 \times V_i \tag{4.38}$$

The classic scale-up strategy based on criteria of power dissipation per unit of volume P/V and volumetric gas-liquid mass transfer coefficient k_La was here chosen. This means that:

$$\left(\frac{P}{V}\right)' = \left(\frac{P}{V}\right) \tag{4.39}$$

Thus, a relationship between agitation rates at both scales can be established in turbulent regime:

$$\left(\frac{\rho_l N^3 D^5}{V}\right)' = \left(\frac{\rho_l N^3 D^5}{V}\right) \tag{4.40}$$

Furthermore, knowing that $V' \propto D'^3$ and $V \propto D^3$, it comes:

$$P/V \propto N^3 D^2 \Rightarrow N \propto D^{-2/3} \tag{4.41}$$

In turbulent regime, two bioreactors in geometric similarity also present dimensionless turbulent dissipation rate distributions similarities, which can be written:

$$\frac{\varepsilon(x,y,z)}{N^3 D^2} = A(x,y,z) \tag{4.42}$$

The variable A depends on the bioreactor design but not on its scale. For the two scales considered, this means that:

$$\frac{\varepsilon(x,y,z)}{N^3 D^2} = \left(\frac{\varepsilon(x,y,z)}{N^3 D^2}\right)' \tag{4.43}$$

Namely:

$$\varepsilon(x,y,z) = \varepsilon'(x',y',z') \tag{4.44}$$

and thus:

$$\forall i \in [1;c]\, \langle \varepsilon' \rangle_i = \frac{1}{V_i'} \int_{V_i} \varepsilon' dV_i' = \frac{1}{K_L^3 V_i} \int_{V_i} \varepsilon \cdot K_L^3 dV_i = \langle \varepsilon \rangle_i \tag{4.45}$$

Similar developments can be made for liquid velocities u_l with the bioreactor:

$$\frac{u_\mathrm{l}}{ND} = B\,(x,y,z) \tag{4.46}$$

With B a constant that does not depend on the bioreactor scale. This means that:

$$u_\mathrm{l} \propto ND \propto D^{-2/3} D \propto D^{1/3} \tag{4.47}$$

and that:

$$u_\mathrm{l}' = \left(\frac{D'}{D}\right)^{1/3} = K_L^{1/3} \times u_\mathrm{l} \tag{4.48}$$

This allows to set up the volumetric flow rate scale-up rule:

$$Q' \propto u_\mathrm{l}' \times D'^2 \propto D^{1/3} D^2 = D^{5/3} \tag{4.49}$$

and thus:

$$Q' = Q \times (K_L)^{5/3} \tag{4.50}$$

The previous relationship allows to predict the variation of liquid flow rate within the compartmental matrix when bioreactor scale is modified. To calculate the local oxygen saturation, il is also necessary to determine the mean pressure in each compartment. For a compartment i at a mean depth z from the surface, the mean pressure in the compartment is approximately equal to:

$$\langle P \rangle_i = P_{atm} + \rho_L g z \tag{4.51}$$

At the industrial scale, this mean pressure thus becomes:

$$\langle P' \rangle_i = P_{atm} + \rho_\mathrm{l} g z' = P_{atm} + \rho_\mathrm{l} g K_L z \tag{4.52}$$

It can be then demonstrated that:

$$\langle P' \rangle_i = k_L \langle P \rangle_i + (1 - K_L)\, P_{atm} \tag{4.53}$$

The determination of the change in inlet gas flowrate is based on the experimental results obtained in Chapter 2 and transposed to 800 l design as no complementary data are available at this scale. It was established that, at constant P/V, $k_{\mathrm{L}}a \propto Q_{\mathrm{g}}^{0.3}$. Thus, considering a constant $k_{\mathrm{L}}a$ strategy, and that the $k_{\mathrm{L}}a$ are classically related to the superficial gas velocity u_{g}, it comes:

$$u_{\mathrm{g}} \propto 1 \rightarrow Q_{\mathrm{g}} D^2 \propto 1 \rightarrow Q_{\mathrm{g}} \propto D^{-2} \tag{4.54}$$

and:

$$Q'_{\mathrm{g}} = K_L^2 Q_{\mathrm{g}} \tag{4.55}$$

The strongest hypothesis concerns the behaviour of the gas phase within the bioreactor and the similarity of the gas distribution within the vessel. Let us suppose that the spatial distribution is unchanged from one scale to another:

$$\alpha_{\mathrm{g}}(x, y, z) = C(x, y, z) \tag{4.56}$$

with C that is independent of bioreactor scale. Considering both spatial invariance of gas fraction and turbulent dissipation rate, it may be supposed that the spatial distribution of the $k_{\mathrm{L}}a$ values remained also unchanged, consequently:

$$\forall i \in [1; c], \langle k_{\mathrm{L}}a' \rangle_i = \langle k_{\mathrm{L}}a \rangle_i \tag{4.57}$$

4.5.2 Results of bioreactor scale-up

Bioreactor scale-up without oxygen control

The 800 l bioreactor was scaled-up using the previous strategy and the oxygen dissolution / consumption model was applied in the compartments. To simplify the kinetic modelling, the maximal oxygen consumption rate of $360\,\mathrm{mg\,l^{-1}\,h^{-1}}$ was supposed (hypothesis of independence of the reactions towards the local concentrations of substrates / microorganisms). The concentrations of the dissolved and gaseous oxygen in each compartment was determined once the equilibrium between the oxygen uptake and transfer was achieved. Five bioreactor scales were considered: 0.8, 8, 80, 800 and $2000\,\mathrm{m^3}$. A complementary simulation at a scale of $2000\,\mathrm{m^3}$ and a 5 times higher oxygen consumption rate of $1800\,\mathrm{mg\,l^{-1}\,h^{-1}}$ was also carried out. It is expected that, as the oxygen consumption is supposed constant within the bioreactor, the increase of mixing time with bioreactor scale will progressively promote oxygen gradients. Also, for this first situation, the operating conditions applied were directly transposed to larger scales ; this situation thus does not consider any oxygen control in the system.

The variation of mean and standard deviation of dissolved oxygen concentrations over bioreactor compartments are given in Fig. 4.18.

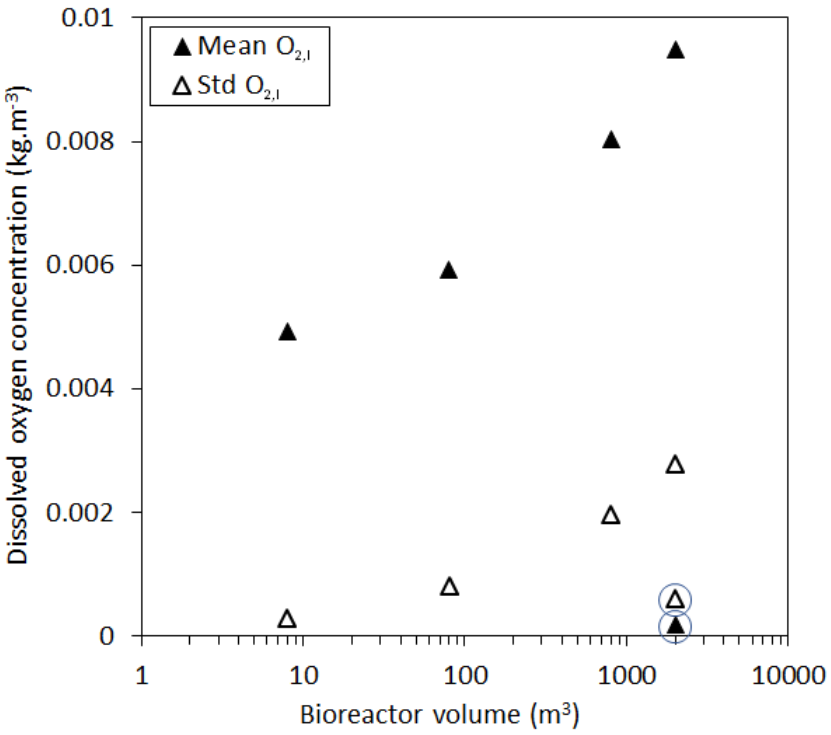

Figure 4.18: Variation of mean and standard deviation of oxygen concentrations in the bioreactor. Circled data correspond to $V = 2000\,\mathrm{m}^3$ and $r_{O2} = 1800\,\mathrm{mg\,l^{-1}\,h^{-1}}$.

Without any oxygen concentration control, the compartmental model results indicated that the mean dissolved oxygen concentrations globally increased in the bioreactor when reactor scale was increased. This can be explained by the increase of liquid height that promoted a higher oxygen saturation in the liquid phase. However, in the mean time, the standard deviation of dissolved oxygen concentrations evolved from 2 % in the 800 l bioreactor to 29 % at a scale of $2000\,\mathrm{m}^3$. When oxygen consumption was increased to $1800\,\mathrm{mg\,l^{-1}\,h^{-1}}$, the mean oxygen concentration was close to 0 indicating a complete oxygen limitation in the liquid phase. As the quantity of oxygen in the gaseous phase was thus far from being limiting. This limitation clearly came from from insufficient gas-liquid mass transfer and global homogenization of the tank.

To put into evidence the occurrence of gradients of oxygen concentrations in the liquid phase, it was arbitrary chosen to determine the ratio between dissolved oxygen concentration in compartment i and in compartment 10, which was supposed to be implemented with an oxygen probe. Results of the simulations are presented in Fig. 4.19 (the condition $V = 2000\,\mathrm{m}^3$ with highest oxygen consumption rate was not shown due to zero local concentrations).

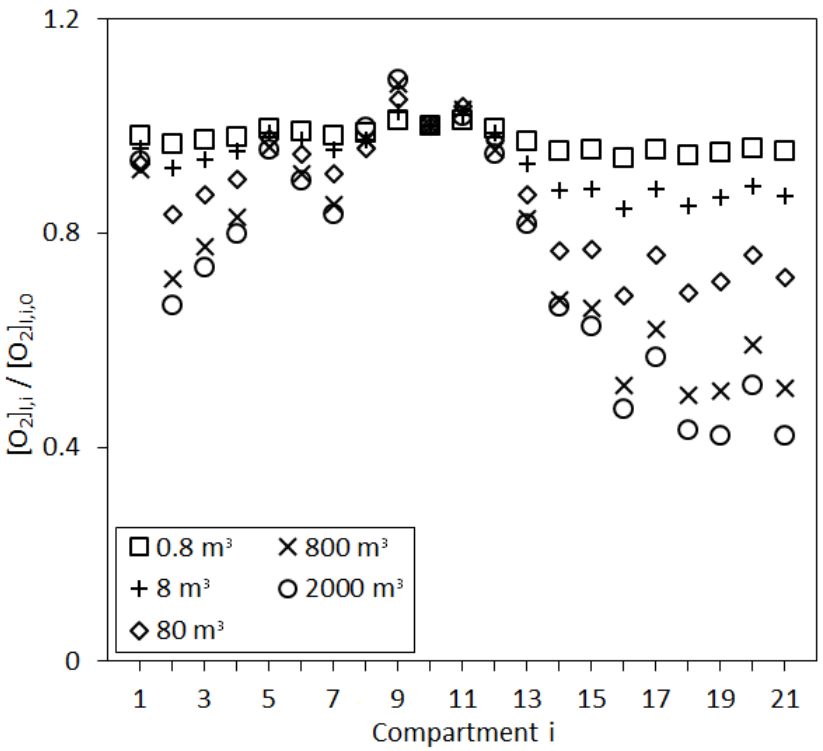

Figure 4.19: Ratio of dissolved oxygen concentration between compartment i and compartment 10. Impact of bioreactor scale and oxygen consumption rate.

It could be first noticed that the probe, placed in compartment 10, was systematically in one of the most favourable compartment regarding oxygen concentration (with compartments 9 and 11). This can be essentially explained by the important mass flow coming in this compartment through the ejection flux of the bottom impeller. The consequence of this result is that, for the system modelled here, the oxygen concentration was most of the time overestimated by the oxygen probe placed in compartment 10. Except in compartment 1 that showed high values of oxygen concentrations (zone of gas injection), the bottom compartments were progressively oxygen-deprived due to lack of bubbles recirculation in these zones. At the 800 and 2000 m^3, the decrease reached 30% in comparison with compartment 10. In the same way, the top compartments of the bioreactor were also less oxygenated due to the decrease of total pressure and oxygen saturation. The oxygenation concentrations in these zones were 50% lower than in compartment 10. These differences had probably weak impacts on bioreactor operation as far as oxygen concentrations remain sufficiently high to prevent oxygen limitations.

Bioreactor scale-up with oxygen control

Another strategy would consist in controlling the dissolved oxygen concentration in the bioreactor at all operation scales. For this purpose, it was supposed that the dissolved oxygen concentration was controlled at the probe (compartment 10) to the value obtained at the scale of 800 l without control ($O_{2,l,10} \simeq 5\,\mathrm{mg\,l^{-1}}$). To carry out this

control, agitation rates and gas flow rates are generally modified to adjust the k_La values of the bioreactor. Nevertheless, in the present study, this choice would have involve important modifications of the compartmental matrix and thus complementary CFD simulations with undefined operating conditions. To evaluate the impact of oxygen control, it was thus decided to tune the volume fraction of oxygen in the gas injected at the bioreactor bottom.

Thus, the oxygen fraction in the inlet gas was slightly decreased to 0.16 at the $800\,m^3$ scale to get approximately the targeted value of $5\,mg\,l^{-1}$ in the compartment next to the impeller. Distribution of mean dissolved oxygen concentrations in each compartment was reported in Fig. 4.20. Spatial distributions of dissolved oxygen concentrations observed at $800\,m^3$ with and without oxygen control were also reported in Fig. 4.21.

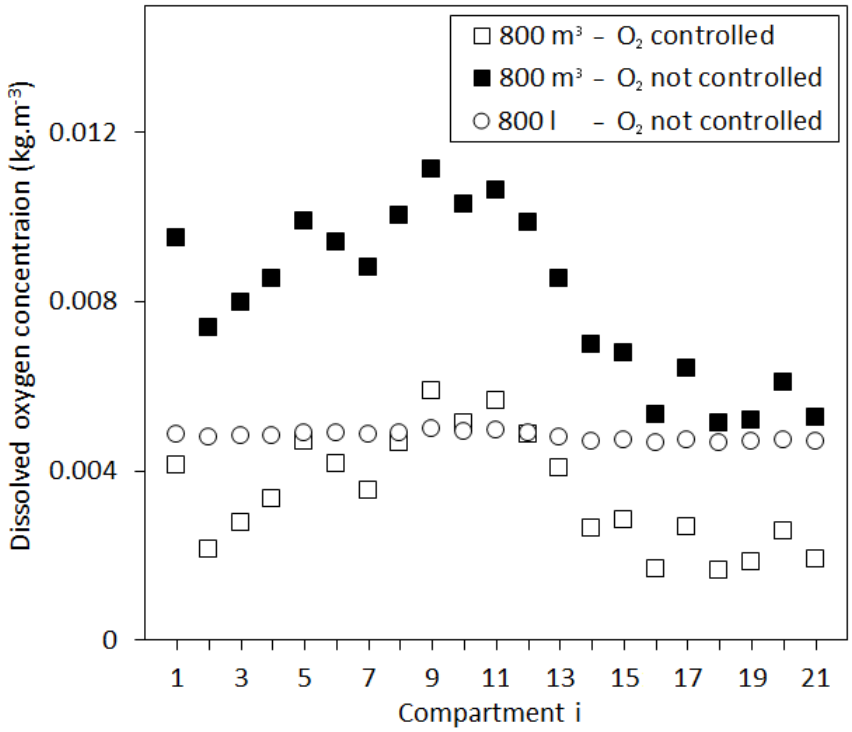

Figure 4.20: Distribution of dissolved oxygen concentrations at two bioreactor scales with and without oxygen control at the probe point.

It can be seen that, at the 800-liter scale, the homogeneity of the bioreactor permitted to maintain the set-point of dissolved oxygen to the targeted value everywhere in the vessel, even with a non- O_2 controlled process. However, at the $800\,m^3$ scale, important differences of O_2 distributions could be observed between non- and controlled systems. Using the scale-up strategy, in case of non-controlled oxygenation, all oxygenation concentrations have thus exceeded the set-point, except in the top-zones where

lower pressure are encountered. Importantly, in the case of the O_2-controlled process, the overestimation of the value at the probe location (compartment 10) in comparison with other compartments involved significantly lower concentrations, especially for the zones near the bioreactor surface ($< 2\,\mathrm{mg\,l^{-1}}$). These results thus suggested that, at the industrial scale, (i) compartmental modelling should be carried out prior to process design to define the best locations for O_2 measurements and (ii) the oxygen set-point should be reconsidered to ensure that each zone of the vessel is sufficiently aerated.

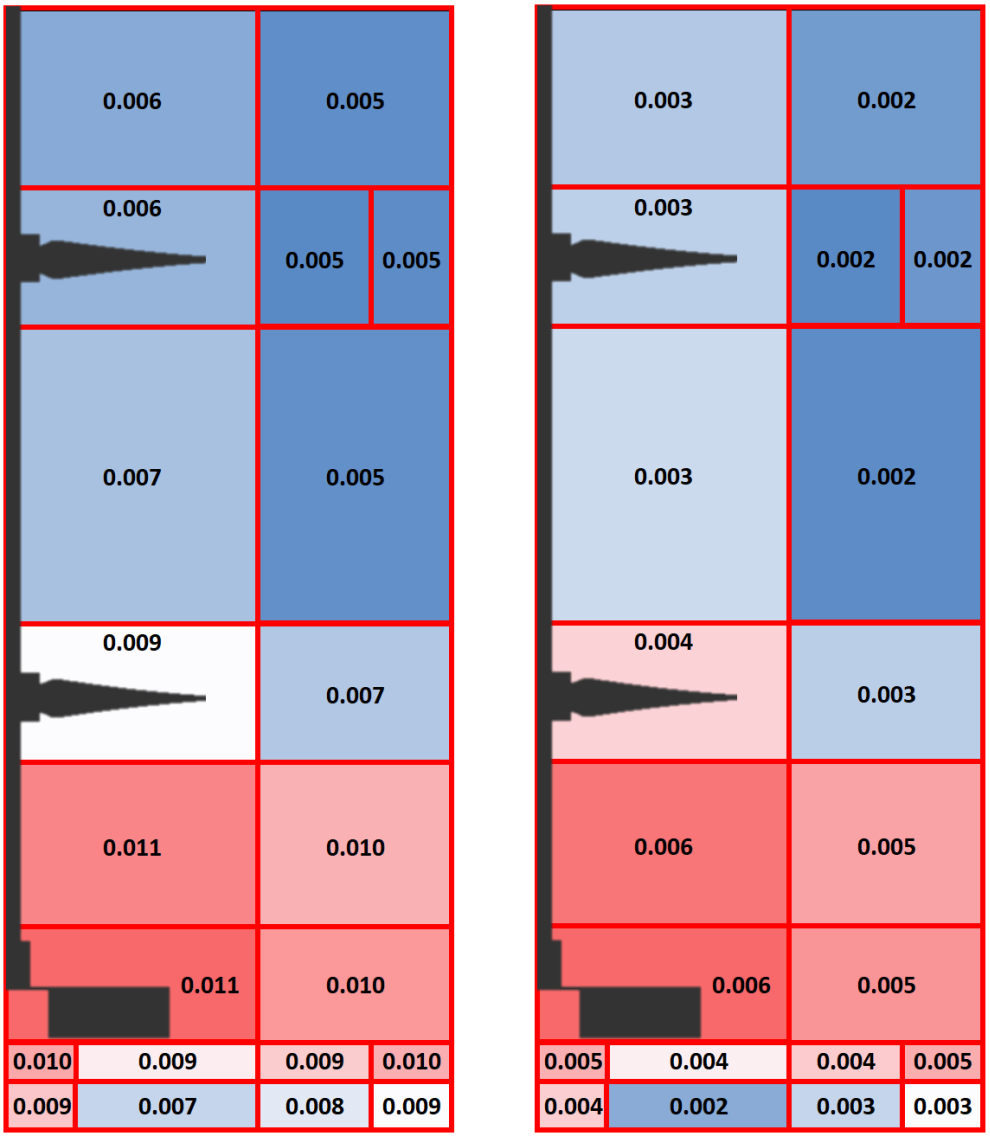

Figure 4.21: Distribution of dissolved oxygen concentrations in the $800\,\mathrm{m^3}$ bioreactor without (on left) and with (on right) oxygen control at the probe point. Color scale were adapted to specific range of values.

4.6 Chapter conclusions

This chapter has presented the different steps in the development of a hydrokinetic model of a bioleaching reactor, from the simulation of a gas-liquid CFD model to its reduction into a compartmental model.

First, a CFD model of a stirred reactor was developed to determine the gas-liquid flow induced by the considered geometry. From this model and the experimental results previously obtained, it was shown that the $k_{\mathrm{L}}a$ model of Danckwerts was the best to represent the experimental gas-liquid mass transfer.

Subsequently, a kinetic model was developed to simulate the bioleaching kinetics in "ideal" hydrodynamic conditions. This model was validated using the experimental data obtained on Chapter 2 and showed a good match for the various kinetics involved, such as chemical dissolution and biological oxidations. From the results obtained, oxygen dissolution model and maximal consumption rate could also be validated.

In a third part, the CFD gas-liquid model was simplified to a compartmental model using the simulated velocity fields. Liquid and gas exchanges between the compartments were then defined by mass balances at their interfaces as well as by their homogeneous content, such as $k_{\mathrm{L}}a$, turbulent dissipation rate or pressure. Lastly, this model was completed using ordinary differential equation to represent oxygen dissolution and consumption and was validated through a gassing-in gassing-out experiment.

On the last section of this chapter, an original scaling-up study was performed using the compartmental model to predict the oxygen distribution with the bioreactor evolution from the pilot- to the industrial-scale. It was shown that scaling of the bioreactor resulted in a better oxygen concentration overall for higher scales due to pressure increase but also promoted the appearance of strong gradients within the tank. Adaptive rules for oxygen control were also suggested for industrial-scale STR.

Bibliography

[1] J. B. Joshi. Computational flow modelling and design of bubble column reactors. *Chemical Engineering Science*, 56(21):5893–5933, November 2001.

[2] F. Scargiali, A. D'Orazio, F. Grisafi, and A. Brucato. Modelling and Simulation of Gas–Liquid Hydrodynamics in Mechanically Stirred Tanks. *Chemical Engineering Research and Design*, 85(5):637–646, January 2007.

[3] L. Schiller. A Drag Coefficient Correlation. *Zeit. Ver. Deutsch. Ing.*, 77:318–320, 1933.

[4] J. Morchain, J.-C. Gabelle, and A. Cockx. A coupled population balance model and CFD approach for the simulation of mixing issues in lab-scale and industrial bioreactors. *AIChE Journal*, 60(1):27–40, 2014.

[5] J. Abrahamson. Fluent Theory Guide. page 962, 2019.

[6] T. T. Devi and B. Kumar. Mass transfer and power characteristics of stirred tank with Rushton and curved blade impeller. *Engineering Science and Technology, an International Journal*, 20(2):730–737, April 2017.

[7] R. Higbie. The rate of absorption of a pure gas into a still liquid during short periods of exposure. *Trans. AIChE*, 31:365–389, 1935.

[8] P. Danckwerts. Significance of liquid-film coefficients in gas absorption. *Industrial & Engineering Chemistry*, 43(6):1460–1467, 1951.

[9] P. Calderbank. Physical rate processes in industrial fermentation. Part II—Mass transfer coefficients in gas–liquid contacting with and without mechanical agitation. *Trans. Inst. Chem. Eng*, 37:173–185, 1959.

[10] M. Laakkonen, P. Moilanen, V. Alopaeus, and J. Aittamaa. Modelling Local Gas–Liquid Mass Transfer in Agitated Vessels. *Chemical Engineering Research and Design*, 85(5):665–675, January 2007.

[11] J. Gimbun, C. D. Rielly, and Z. K. Nagy. Modelling of mass transfer in gas–liquid stirred tanks agitated by Rushton turbine and CD-6 impeller: A scale-up study. *Chemical Engineering Research and Design*, 87(4):437–451, April 2009.

[12] G. R. Kasat, A. B. Pandit, and V. V. Ranade. CFD Simulation of Gas-Liquid Flows in a Reactor Stirred by Dual Rushton Turbines. *International Journal of Chemical Reactor Engineering*, 6(1), 2008.

[13] P. H. Calderbank. Gas absorption from bubbles. *The Chemical Engineer*, pages CE209–CE233, 1967.

[14] B. Murthy, R. Ghadge, and J. Joshi. CFD simulations of gas–liquid–solid stirred reactor: Prediction of critical impeller speed for solid suspension. *Chemical Engineering Science*, 62(24):7184–7195, December 2007.

[15] R. Panneerselvam, S. Savithri, and G. D. Surender. CFD modeling of gas–liquid–solid mechanically agitated contactor. *Chemical Engineering Research and Design*, 86(12):1331–1344, December 2008.

[16] A. R. Khopkar, G. R. Kasat, A. B. Pandit, and V. V. Ranade. Computational Fluid Dynamics Simulation of the Solid Suspension in a Stirred Slurry Reactor. *Industrial & Engineering Chemistry Research*, 45(12):4416–4428, June 2006.

[17] D. Chapple, S. M. Kresta, A. Wall, and A. Afacan. The Effect of Impeller and Tank Geometry on Power Number for a Pitched Blade Turbine. *Chemical Engineering Research and Design*, 80(4):364–372, May 2002.

[18] A. R. Khopkar and P. A. Tanguy. CFD simulation of gas–liquid flows in stirred vessel equipped with dual rushton turbines: Influence of parallel, merging and diverging flow configurations. *Chemical Engineering Science*, 63(14):3810–3820, July 2008.

[19] N. Midoux, A. Laurent, and J. C. Charpentier. Limits of the chemical method for the determination of physical mass transfer parameters in mechanically agitated gas-liquid reactors. *AIChE Journal*, 26(1):157–162, 1980.

[20] S. Bouffard. *Understanding the Heap Biooxidation of Sulfidic Refractory Gold Ores*. PhD thesis, University of British Columbia, 2003.

[21] M. J. Nicol. The role of electrochemistry in hydrometallurgy. In *Nicol, M.J. <http://researchrepository.murdoch.edu.au/view/author/Nicol, Mike.Html> (1993) The Role of Electrochemistry in Hydrometallurgy. In: 4th International Symposium on Hydrometallurgy, 1 - 5 August 1993, Salt Lake City, UTAH*, Salt Lake City, UTAH, 1993.

[22] S. C. Bouffard and D. G. Dixon. Modeling pyrite bioleaching in isothermal test columns with the HeapSim model. *Hydrometallurgy*, 95(3):215–226, February 2009.

[23] A. Ahmadi, M. Ranjbar, M. Schaffie, and J. Petersen. Kinetic modeling of bioleaching of copper sulfide concentrates in conventional and electrochemically controlled systems. *Hydrometallurgy*, 127-128(Supplement C):16–23, October 2012.

[24] J. Gimbun, S. Y. Liew, Z. K. Nagy, and C. D. Rielly. Three-Way Coupling Simulation of a Gas-Liquid Stirred Tank using a Multi-Compartment Population Balance Model. *Chemical Product and Process Modeling*, 11(3), January 2016.

Conclusion

The aim of the present work of thesis was to model and simulate the effect of transport phenomena on the bacterial microenvironment through the development of a coupled bioleaching STR hydrokinetic model. All along this PhD work, key features on possible impacts of hydrodynamics on the operation of bioleaching STR were investigated such as particle suspension and stress or oxygen dissolution and transport. From a general point of view, this demonstrated that the development and use of new modelling tools to address the underlying scientific questions of bioleaching reactor scale-up are clearly worthwhile. This work has answered some of the scientific questions identified by descriptive modelling of a 2-liter laboratory-scale and a 800-liter pilot-scale bioreactor and offered some insights for their operation improvement but also by a predictive modelling of industrial scales, as summarized by Fig. 4.22.

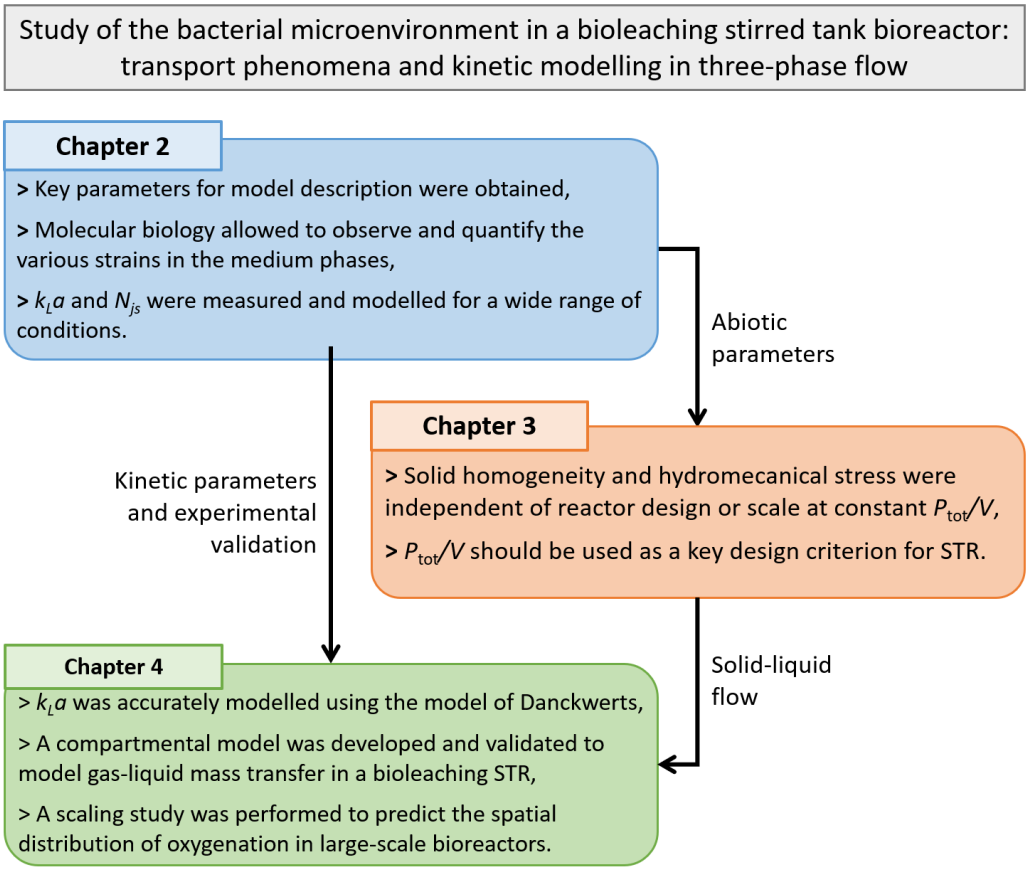

Figure 4.22: Main results of this work.

Concluding results

Experimental characterization of bioleaching conditions in STR

In order to obtain validation data for the models but also to propose sizing rules of particle suspension and mass transfer, a complete description of a laboratory-scale bioleaching stirred tank reactor was obtained through biotic and abiotic experiments.

Bioleaching experiments dedicated to kinetics determination
Bioleaching experiments were conducted to obtain key parameters: sulphide mineral dissolution kinetics, bacterial oxidation kinetics, bacterial growth and dissolved oxygen kinetics. In addition to the bacterial growth kinetics, a molecular biology study was performed to highlight the distribution of the different bacterial species in the medium. The expected BRGM-KCC bacterial strains were identified, namely *L. ferriphilum*, *At. caldus* and *Sb. thermosulfidooxidans*. It was also found that *L. ferriphilum* acted as the main iron-oxidizer and *At. caldus* as the main sulfur-oxidizer. Furthermore, qPCR allowed to define their respective attachment to the solid or their suspension in the liquid. Lastly, a relationship between cell count and the gene copy number was established.

Abiotic experiments dedicated to hydrodynamics study
In addition to the previous study, abiotic parameters were defined to quantify the hydrodynamics of the considered STR. The just-suspended speed N_{js} and gas-liquid mass transfer were measured for 120 and 72 different operating conditions respectively, including solid fraction, solid concentration, impeller configuration and gas flow rate. Supplementary studies were done to model the just-suspended speed using the Zwietering correlation and a new correlation to represent the impact of the presence of a gas phase. Similarly, the gas-liquid mass transfer was modeled using a power law with a common power superscript for all results.

Modelling of particles suspension and hydromechanical stress

The second part of this thesis presented the impact of impeller design and solid concentration on particles suspension and hydromechanical stress for a laboratory- and a pilot-scale bioreactors. These parameters were determined through CFD numerical simulations and theoretical models of particle distribution and stress.

Study of the suspension quality
The suspension quality H_s was determined for different operating conditions including geometrical parameters (tank scale, impeller design), solid concentration and agitation speed. On one hand, varying the impeller design or the tank scale showed no

significant impact on particle suspension at a given dissipated power per unit volume. On the other hand, increasing the solid concentration had a negative impact on solid dispersion as a significant rise of power consumption per unit volume was needed to achieve a given suspension quality.

Parameters affecting particle hydromechanical stress
The hydromechanical stress quantified by the sheared fraction of particles SF was also obtained varying the same conditions as for the suspension quality. The variation of SF with the power consumption per unit volume showed similar results than the suspension quality as no impact of the reactor design was observed. Both parameters, SF and the suspension quality $H_{\mathrm{s,adj}}$, were compared for the considered parameter of design and solid concentration and were related for all the conditions tested except a negligible, positive impact of the solid concentration. Lastly, it was also shown that this comparison could represent a way to obtain the just-suspended criterion.

The power consumption per unit volume: an effective design criterion
To sum up the previous results, the power consumption per unit volume could be used as a design criterion due to the independence of most parameters considered on the suspension quality and the hydromechanical stress on particles. However, for bioleaching processes, it should be noted that a similar generalized modelling should be applied to gas-liquid mass transfer to definitively confirm this scale-up rule proposal.

Development of a hydro-kinetic compartment model

The last part focused on the development of a hydro-kinetic compartment model that consisted in a CFD-based gas-liquid compartmental model and its coupling with a kinetic model.

Modelling gas-liquid mass transfer using a compartment-based approach
The gas-liquid model of the bioleaching STR was obtained using CFD simulations and used to determine the optimal mass transfer coefficient model. It was found that the model of Danckwerts offered the best fit and could predict the experimental mass transfer coefficient within a 4% margin for the laboratory-scale tank and 10% for the pilot-scale tank. The CFD gas-liquid model was then divided into homogeneous compartments based on velocity field data. Critical parameters such as phases fraction, turbulent energy dissipation, pressure and $k_{\mathrm{l}}a$ were extracted from volume averaged data of each compartments. The compartment model was validated through gassing in gassing out experiments and establish the first CFD-based compartmental model of a bioleaching reactor in literature.

Hydrokinetic coupling of the models and prediction of large-scale bioreactor oxygenation
The gas-liquid compartmental approach was enriched with kinetic information resulting from a dedicated kinetic model validated by the experiments of chapter 2. From the experimental and modelled data, the maximal oxygen demand, which imposes critical operating conditions in terms of agitation and aeration, was extracted and implement in the compartmental approach. Using dedicated scale-up rules of the bioreactor, it was shown that the compartmental approach could be then used to predict the spatial distribution of oxygenation.

Future works

Bioleaching process characterization and modelling doubtless need further investigation to decipher the couplings between biological phase and the multiphase transport of substrates. A non-exhaustive list of perspectives to this PhD work is proposed below.

- *Solid composition:*
  For development purpose, this work focused on pyrite as substrate, being the most common sulphide mineral. This choice made it possible to have as many comparative studies as possible. However, a recurrent aspect of bioleaching processes is the wide range of resources encountered [1–3]. These resources react differently depending on the environment and the metal they contain will therefore be more or less difficult to extract. Therefore, **a short-term development of the model would be to adapt its functioning for most metal sulphides**, allowing a better versatility.

- *Microbial population dynamics modelling:*
  The operation of bioleaching process comes from the observation of acid mine drainage for which microorganisms naturally assist the dissolution process. A wide variety of microorganisms was observed, most of the time functioning as consortia [4, 5]. The characterization of this diversity for modelling purposes is extremely complex due to a lack of precise knowledge on the microorganisms involved [6]. This work considered a two-bacteria system consisting of one iron-oxidizing and one sulfur-oxidizing bacteria. The **development of a model considering on all bacterial species of a given consortium, their inner interactions and distributions on the solids and in the liquid phase could allow a predictive adaptation of the model to the local biochemical environment** which should effectively represent more accurately experimental observations. The transposition of microbial population balance modelling coupled with CFD simulations from one pure strain culture is clearly an interesting option that should be considered in the near future [7].

- *Carbon dioxide impact on growth:*
  As for oxygen, carbon dioxide plays an important role in bioleaching processes as its supplementation in air sparging assists microorganisms growth with a non negligible impact [8, 9]. Currently, no growth model taking into account local CO_2 concentrations are available for bioleaching process. Thus, it could be interesting to **consider an implementation of carbon dioxide in Monod's growth equation** but also to consider its solubilization in the compartmental approach.

- *Impact of geometry on gas dispersion:*
  As developed in this study, tank and impellers geometries have a critical impact on solid dispersion and hydromechanical stress. Furthermore, it is well-known that dissolved oxygen plays an important role in bioleaching processes and is linked to the system efficiency for gas-liquid mass transfer [10, 11]. Although the literature has focused on the study of gas dispersion and the impact of a given geometry on this parameter, few studies have addressed the issues encountered in bioleaching. For that, it would be interesting to **study the coupling of the gas dispersion to the solid suspension and to the particle hydromecanical stress, and this for different tank and impeller geometries**.

- *Implementation of the biological model in the compartmental approach*
  The implementation of a complete biological model to a compartmental approach is far from being trivial and relies on a complex knowledge that could not be developed in the present work. Whereas the compartmental approach is expected to predict with a good accuracy the distribution of mass fluxes, the modelling of biological response to potentially fluctuating concentrations along the microorganism path needs intense experimental studies. For instance, depending on the substrate or on the microorganism, the biological response may be adaptive, related to the mean value of substrate concentration along the microorganism path or to its instantaneous value [12]. It is therefore strongly encouraged to **collect biological data allowing to characterize the microbial response to these potentially fluctuating environments**. Such "scale-down" studies are indeed now routinely performed in pure strain cultures [13].

Bibliography

[1] J. Cui and L. Zhang. Metallurgical recovery of metals from electronic waste: A review. *Journal of Hazardous Materials*, 158(2):228–256, October 2008.

[2] A. Ahmadi, M. Ranjbar, M. Schaffie, and J. Petersen. Kinetic modeling of bioleaching of copper sulfide concentrates in conventional and electrochemically controlled systems. *Hydrometallurgy*, 127-128(Supplement C):16–23, October 2012.

[3] A. H. Kaksonen, X. Deng, T. Bohu, L. Zea, H. N. Khaleque, Y. Gumulya, N. J. Boxall, C. Morris, and K. Y. Cheng. Prospective directions for biohydrometallurgy. *Hydrometallurgy*, 195:105376, August 2020.

[4] H. Watling. Microbiological Advances in Biohydrometallurgy. *Minerals*, 6(2):49, June 2016.

[5] A. H. Kaksonen, N. J. Boxall, Y. Gumulya, H. N. Khaleque, C. Morris, T. Bohu, K. Y. Cheng, K. M. Usher, and A.-M. Lakaniemi. Recent progress in biohydrometallurgy and microbial characterisation. *Hydrometallurgy*, 180:7–25, September 2018.

[6] S. C. Bouffard and D. G. Dixon. Modeling pyrite bioleaching in isothermal test columns with the HeapSim model. *Hydrometallurgy*, 95(3):215–226, February 2009.

[7] J. Morchain, J.-C. Gabelle, and A. Cockx. A coupled population balance model and CFD approach for the simulation of mixing issues in lab-scale and industrial bioreactors. *AIChE Journal*, 60(1):27–40, 2014.

[8] C. G. Bryan, C. S. Davis-Belmar, N. van Wyk, M. K. Fraser, D. Dew, G. F. Rautenbach, and S. T. L. Harrison. The effect of CO2 availability on the growth, iron oxidation and CO2-fixation rates of pure cultures of Leptospirillum ferriphilum and Acidithiobacillus ferrooxidans. *Biotechnology and Bioengineering*, 109(7):1693–1703, 2012.

[9] A.-G. Guezennec, C. Joulian, C. Delort, F. Bodénan, S. Hedrich, and P. D'hugues. CO2 mass transfer in bioleaching reactors: CO2 enrichment applied to a complex copper concentrate. *Hydrometallurgy*, 180:277–286, September 2018.

[10] T. Y. See, A. A. A. Raman, R. S. S. R. E. Shah, S. Ibrahim, and M. I. M. Nor. Study of sparger location on solid suspension in a triple-impeller stirred vessel. *Asia-Pacific Journal of Chemical Engineering*, 11(2):229–236, 2016.

[11] A.-G. Guezennec, C. Joulian, J. Jacob, A. Archane, D. Ibarra, R. de Buyer, F. Bodénan, and P. d'Hugues. Influence of dissolved oxygen on the bioleaching efficiency under oxygen enriched atmosphere. *Minerals Engineering*, 106:64–70, May 2017.

[12] C. Haringa. From industrial fermentor to CFD-guided downscaling – What have we learned ? *Biochemical Engineering Journal*, page 15, 2018.

[13] P. Neubauer and S. Junne. Scale-down simulators for metabolic analysis of large-

scale bioprocesses. *Current Opinion in Biotechnology*, 21(1):114–121, February 2010.

Chapter 5

Résumé du travail de thèse

5.1 Introduction

La biolixiviation est un procédé d'extraction qui a été mise en œuvre avec succès au cours des dernières décennies pour récupérer les métaux provenant de ressources sulfurées en utilisant des procédés à grande échelle (statiques ou dynamiques). Ce procédé a connu un grand nombre d'améliorations de ses mécanismes réactionnels et des consortia microbiens impliqués suite à un nombre important de travaux scientifiques dédiés. Compte-tenu des continuels progrès de la modélisation et des outils de calcul, l'évolution digitale de la biolixiviation est attendue et doit s'intensifier dans les années à venir afin de proposer des règles améliorées de conduite et d'extrapolation en évitant notamment la multiplication d'applications expérimentales coûteuses. Globalement, la plupart de ces apports en terme de modélisation se sont concentrés sur les procédés statiques en tas ; les études relatives à la modélisation des applications dynamiques en bioréacteurs ont été pour la majorité interrompues, bien qu'il s'agisse de l'une des applications d'hydrométallurgie les plus prometteuses pour faire face au problème mondial à venir concernant l'épuisement des ressources. Ce travail de thèse s'inscrit dans le projet Intercarnot **MODELIX**, qui vise à modéliser l'hydrodynamique local d'un réacteur de biolixiviation, la construction d'un modèle compartimental basé sur ces études hydrodynamiques et une première proposition de couplage de l'hydrodynamique aux cinétiques de biolixiviation.

Ainsi, la recherche d'un outil complet adaptable à de multiples échelles, qui couple cinétique et hydrodynamique en réacteur agité de biolixiviation afin d'établir des critères de conduite et / ou d'optimisation de ces réacteurs a été le fil conducteur de ce travail de thèse. Pour cela, une première phase expérimentale a été effectuée dans le but de décrire le comportement d'un procédé de biolixiviation à l'échelle laboratoire, permettant l'obtention d'un ensemble complet de données, cinétiques et hydrodynamiques, nécessaires à la calibration des différents modèles utilisés dans ce projet. Le développement du modèle complet s'est orienté sur l'analyse de mécanismes clés de l'optimisation "physique" d'un réacteur de biolixiviation, à savoir l'homogénéisation des composants ainsi que le transfert de masse gaz-liquide dans le réacteur. Pour cela, le développement des modèles a débuté par la description d'un modèle de mécanique des fluides numérique (MFN) multi-échelle solide-liquide. L'objectif de ce premier modèle était de décrire l'impact de différents paramètres sur l'homogénéité du solide et la contrainte mécanique perçue par les particules. Par la suite, la description des phénomènes de transfert de masse gaz-liquide a été réalisée au travers de l'utilisation d'un modèle MFN décrivant l'écoulement gaz-liquide. En parallèle, un modèle décrivant les cinétiques de dissolution chimique, d'oxidations biologiques et de transfert de masse gaz-liquide a été développé et validé par les résultats expérimentaux précédemment établis. Ce dernier a été utilisé pour valider les modèles de transfert de masse gaz-liquide. Enfin, par simplification du modèle MFN gaz-liquide et injection des résultats de cinétique de

transfert et de consommation d'oxygène, un modèle compartimenté a été obtenu puis utilisé dans une étude d'extrapolation pour établir des codes de conduite permettant d'optimiser l'oxygénation des procédés à l'échelle industrielle.

5.2 Etat de l'art

5.2.1 La biolixiviation : une solution face à l'appauvrissement des ressources minérales

Vers l'exploitations de ressources nouvelles

Au cours des dernières décennies, la demande en métaux a rapidement augmenté en raison des besoins croissants de la société moderne. Ces besoins reflètent l'importance des métaux, qui sont devenus une ressource de base essentielle à la fabrication et le fonctionnement de la plupart des produits de la vie quotidienne, et ce en raison de leurs propriétés particulières. Cette consommation importance a accru la pression sur les ressources naturelles suivant l'intensification de l'exploitation minière, ce qui a provoqué (i) une diminution des réserves de ressources récupérables [1] et (ii) une baisse constante de la teneur moyenne des minerais [2].

Dans une logique d'optimisation de la rentabilité, l'industrie minière s'est majoritairement concentrée sur les gisements les plus riches. Néanmoins, ces gisements s'amenuisent, forçant l'exploitation de gisements de moindre valeur pour couvrir la demande croissante en matériaux. Malgré une optimisation toujours plus poussée des procédés d'extractions, l'augmentation des coûts d'exploitation (OPEX) demeure supérieure à l'augmentation des rendements d'extractions [3]. De plus, préoccupations croissantes concernant l'impact écologique de l'exploitation minière a entraîné une révision de la chaîne de valeur économique des métaux. À cet égard, de nouvelles façons d'extraire les ressources ont été développées dans le monde entier afin de maintenir un approvisionnement suffisant en ressources critiques. Ces améliorations se sont notamment tournées vers l'exploitation de la mine urbaine, représentée par des ressources provenant de produits finis et comportant des métaux précieux en quantité non négligeables, ce qui est le cas des cartes électroniques.

Généralités sur le procédé de biolixiviation

Parmi les différents procédés liés à l'extraction des métaux, cette étude s'est concentrée sur la biolixiviation en raison de sa polyvalence et de son potentiel pour l'extraction des métaux provenant des ressources de demain (mine urbaine, faible teneur en métaux, forte teneur en soufre, etc.). La biolixiviation est un procédé hydrométallurgique qui utilise des solutions aqueuses et des microorganismes pour l'extraction des métaux. Son principe repose sur deux étapes :

- Une étape de lixiviation permettant la libération ou la solubilisation du métal via l'utilisation de milieux acide et oxydant. Par exemple pour l'oxydation de la pyrite (FeS_2) :

$$FeS_2 + 14\,Fe^{3+} + 8\,H_2O \longrightarrow 15\,Fe^{2+} + 2\,{SO_4}^{2-} + 16\,H^+ \tag{5.1}$$

- Une étape de régénération de l'oxydant afin d'entretenir l'étape lixiviante. Contrairement aux procédés abiotiques qui emploient une régénération chimique, la biolixiviation utilise des micro-organismes permettant une régénération biologique de l'oxydant. Cet oxydant sera le plus souvent du fer ferrique (Fe^{3+}) en raison de sa régénération possible par des bactéries ferro-oxydantes. En reprenant notre exemple précédent, on obtient donc cette équation :

$$14\,Fe^{2+} + 3.5\,O_2 + 14\,H^+ \longrightarrow 14\,Fe^{3+} + 7\,H_2O \tag{5.2}$$

On note également une étape d'oxydation du soufre élémentaire, qui s'accumule en surface des particules de minerai, bloquant alors la dissolution et donc la libération des métaux. Pour cela, des bactéries sulfo-oxydantes prennent en charge le soufre élémentaire pour empêcher la formation de cette couche, comme montrée par l'éq. 5.3. Cette étape participe aussi à l'acidification du milieu, indispensable à la réaction de dissolution mais aussi à la limitation de réactions secondaires de précipitations.

$$S_0 + 1.5\,O_2 + 2\,H^+ \longrightarrow H_2SO_4 \tag{5.3}$$

L'utilisation de microorganismes dans les procédés d'extraction offre comme avantages une diminution des coûts d'exploitation en raison des températures de conduites plus faibles, une diminution des composants nécessaires à la pérennisation de la réaction de dissolution et enfin une durabilité du procédé grâce à des méthodes plus respectueuses de l'environnement. Depuis sa première mise en place à l'échelle industrielle, la technologie a été continuellement étudiée et affinée pour une meilleure compréhension de ses mécanismes physiques, biochimiques et microbiens. Aujourd'hui, cette technologie est utilisée dans des dizaines de procédés à grande échelle pour la récupération de métaux et est encore en cours de développement pour élargir son utilisation à de nouvelles ressources [4, 5]. Néanmoins, les applications commerciales de la biolixiviation ont été principalement ciblées sur les minerais sulfurés, qui sont les minerais les plus courants dans la nature, et ont donc fait l'objet de ce travail.

Développement des applications en bioréacteur

Industriellement, deux techniques principales de biolixiviation sont utilisées : la méthode statique (percolation) et la méthode dynamique (agitation) [6]. La lixiviation par

percolation est centrée sur l'irrigation d'un tas de matériaux sulfurés avec une solution acide chargée de micro-organismes. Cette méthode est essentiellement utilisée pour les minerais à faible teneur, tels que les sulfures de cuivre. En outre, le processus est lent (plusieurs mois, voire années) avec un faible rendement, mais il est intéressant en raison de ses faibles coûts opérationnels (OPEX) [7].

La méthode dynamique utilise des réacteurs agités en combinaison avec des micro-organismes pour la solubilisation ou la libération des métaux. Compte tenu des ressources utilisées, elle s'oppose à la méthode statique en raison des coûts d'investissement (CAPEX) et des OPEX élevés. Pour cette raison, les bioréacteurs sont surtout utilisés pour les minerais et les concentrés de haute valeur, contenant des métaux tels que l'or, le nickel ou le cobalt. Cependant, le processus d'extraction est rapide (plusieurs jours) et le rendement global est généralement important (plus de 90%) [8]. L'intérêt principal du procédé de biolixiviation en cuve agitée est la possibilité de contrôler précisément les différents paramètres opératoires tels que les paramètres physico-chimiques (température, pH, aération, agitation), les paramètres biologiques (consortium microbien) et la géométrie de la cuve, notamment les mobiles d'agitation, le sparger et les chicanes [9, 10].

Si la biolixiviation en tas a été jusqu'à présent la méthode préférentielle pour le traitement des déchets miniers, elle n'est pas toujours la meilleure solution. Les principales raisons qui s'opposent au traitement en tas sont la composition des matériaux à traiter (présence de carbonate ou de fortes concentrations en sulfures) et le manque d'espace suffisant, en particulier dans les zones densément peuplées comme en Europe. Des optimisations techniques sont donc encore nécessaires pour que cette technologie atteigne une viabilité économique pour toutes ressources. Néanmoins, des avancées récentes ont montré qu'il s'agit d'une technologie appropriée pour répondre aux préoccupations écologiques liées à l'extraction des ressources.

5.2.2 Amélioration de la compréhension du procédé de biolixiviation par la modélisation

La révolution numérique offre désormais des outils puissants pour aider l'industrie minière à optimiser ses procédés d'extraction, tels que la modélisation des écoulements, les méthodes reliées à l'intelligence artificielle et l'apprentissage automatique. Ces outils ont le potentiel d'utiliser les connaissances d'une technologie afin d'optimiser ses procédés, limitant grandement la nécessité de campagnes expérimentales longues et coûteuses.

La biolixiviation a été étudiée parmi les procédés de biohydrométallurgie à l'aide

d'outils de modélisation pour améliorer certains aspects de son fonctionnement. En tant que processus d'ingénierie biochimique, les modèles existants ont été modifiés et appliqués pour représenter des phénomènes tels que la croissance microbienne, le transfert d'oxygène, l'oxydation du minerai, les bilans énergétiques et les phénomènes de transport [11, 12]. Ces modèles ont été ajustés pour tenir compte de leur corrélation avec les paramètres physico-chimiques du système considéré, comme examiné par Mahmoud et al. (2017) [13]. Dans notre cas d'étude de la biolixiviation en cuve agitée, les interrelations entre les facteurs microbiens, minéralogiques, physico-chimiques et géométriques doivent être pris en compte pour optimiser la conception et l'efficacité du procédé (Fig. 5.1).

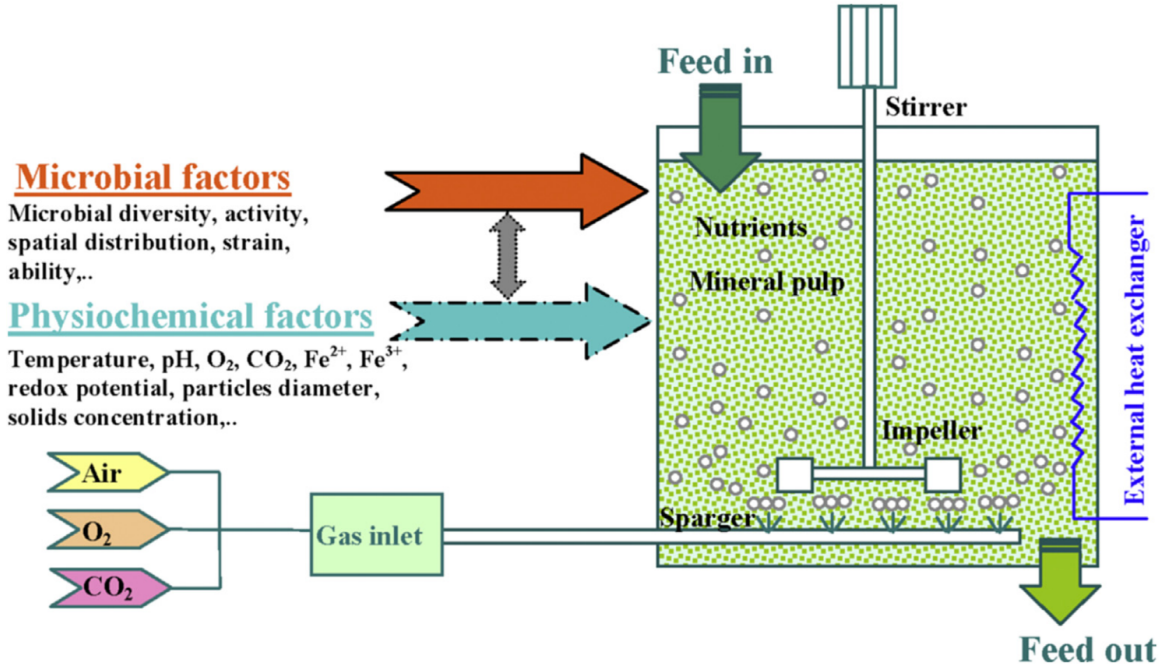

Figure 5.1: Facteurs influençant la biolixiviation en cuve agitée. Figure reproduite de Mahmoud et al. 2017 [13].

Modélisation des cinétiques biologiques et chimiques

Il est possible de modéliser une partie des réactions chimiques et biochimiques à l'aide de modèles cinétiques. En particulier, il est nécessaire de décrire les cinétiques chimiques (dissolution du minerai) et biologiques (oxydations par les microorganismes).

Dans le mécanisme de lixiviation, la dissolution du minerai sulfuré est une réaction d'oxydo-réduction. Ainsi, la cinétique de la dissolution est liée aux conditions chimiques et électrochimiques de l'environnement [14]. De plus, en raison de la nature particulaire du minerai sulfuré dans les processus de biolixiviation, la variation de la taille des particules pendant la dissolution joue un rôle important. Compte tenu de ces facteurs,

Bouffard et al. (2006) ont représenté la vitesse de dissolution d'un minéral sulfuré r_s comme fonction de 3 facteurs [15] :

$$r_s = G_s \cdot \frac{dX_{c,s}}{dt} = G_s \cdot K(T) \cdot f(C) \cdot g(d_{p,0}, X_{c,s}) \tag{5.4}$$

avec G_s la teneur initiale en minéraux sulfurés, $X_{c,s}$ le taux de conversion du minerai, $K(T)$ une constante de vitesse dépendante de la température, $f(C)$ une fonction chimique dépendant de la composition du milieu et $g(d_{p,0}, X_{c,s})$ une fonction topologique représentant la variation de taille d'une particule sulfurée de taille initiale $d_{p,0}$.

Ce premier mécanisme est assisté des réactions d'oxydations biologiques du fer ferreux ainsi que du soufre élémentaire, réalisées par différentes bactéries. Ces dernières s'obtiennent à partir de la croissance microbienne, usuellement représentée par des modèles qui la décrive en fonction d'un ou plusieurs substrats limitants et en considérant ou non des inhibitions provenant de sources variées. Le modèle le plus courant est la loi de Monod, qui est un modèle empirique simple se basant sur un substrat limitant sans inhibition [16]. Ce modèle est néanmoins insuffisant pour représenter complètement la croissance. Dans le cas de la biolixiviation, un modèle à double substrat limitant est usuellement utilisé, se basant sur le substrat principale de l'oxydation (Fe_2^+ ou S_0) ainsi que sur l'oxygène en tant qu'accepteur final des électrons dans la réaction d'oxydation [17, 18]. Par exemple pour la croissance des bactéries ferro-oxydantes :

$$\mu = \mu_{max} \cdot \frac{\left[Fe_2^+\right]}{K_{Fe_2^+} + \left[Fe_2^+\right]} \cdot \frac{[O_2]}{K_{O_2} + [O_2]} \tag{5.5}$$

avec μ le taux de croissance, $\left[Fe_2^+\right]$ la concentration en fer ferreux, $[O_2]$ la concentration en oxygène et $K_{Fe_2^+}$ et K_{O_2} les constantes de demi-saturation respective du fer ferreux et de l'oxygène.

La croissance des bactéries sulfo-oxydantes s'obtient de manière similaire en remplaçant la concentration en fer ferreux par la concentration en soufre élémentaire. Des modifications additionnelles peuvent être apportées à ces équations pour prendre en compte l'effet de facteurs physico-chimiques additionnels tels que la température ou encore le pH.

La grande difficulté de l'utilisation de telles équations est l'obtention des constantes cinétiques associées. Ces dernières sont dépendantes de la souche bactérienne considérée et, compte tenu de la grande diversité de microorganismes utilisés en biolixiviation, il est souvent difficile d'avoir ces données pour tous les constituants d'un consortium malgré les nombreuses études existantes. De plus, en raison de la variété des consortia existants, une même bactérie peut présenter différentes constantes selon le milieu dans lequel elle évolue.

Modélisation de l'hydrodynamique des réacteurs de biolixiviation

Les modèles cinétiques présentés précédemment n'intègrent de base pas les effets de l'hydrodynamique du bioréacteur sur la distribution spatiale des concentrations en substrats. Cette hypothèse est presque satisfaite pour les systèmes à petite échelle tels que les installations de laboratoire, mais elle est probablement rarement atteinte lorsqu'on considère les processus de biolixiviation habituels à l'échelle industrielle. Les processus dynamiques sont souvent réalisés dans de multiples cuves dont la taille peut atteindre $1000\,\mathrm{m}^3$. De ce fait, les phénomènes de transport peuvent jouer un rôle important sur l'efficacité du procédé.

La plupart des modèles cinétiques pour les approches en cuve agitée proviennent des modèles existants pour les procédés statiques, car les constantes cinétiques dépendent principalement des substrats et des micro-organismes utilisés. De plus, des modèles théoriques classiques de transfert de masse gaz-liquide peuvent être utilisés pour représenter le transfert de masse de l'oxygène dans le milieu de culture [19]. Cependant, les phénomènes de transport diffèrent fortement des processus statiques car le système est mélangé mécaniquement. Divers paramètres se sont avérés avoir une influence sur la distribution des scalaires transportés par l'écoulement, comme le montre la Fig. 5.2. Un meilleur contrôle de ces paramètres devrait donc améliorer l'efficacité du processus [20].

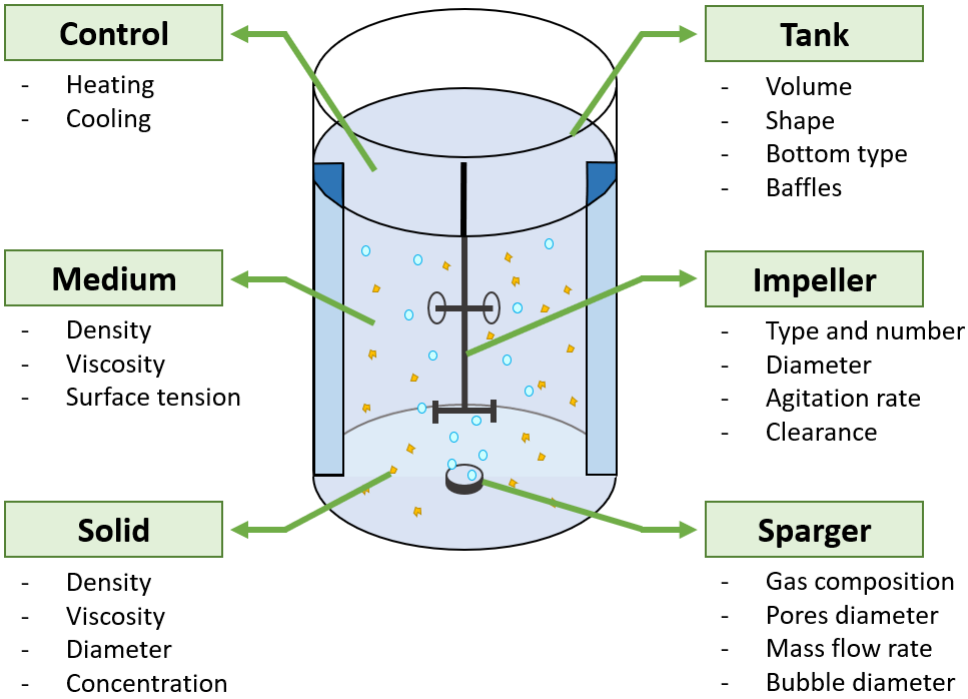

Figure 5.2: Représentation d'une cuve agitée solide-liquide-gaz de biolixiviation et des composants influençant le transport des scalaires.

Actuellement, des représentations expérimentales de l'efficacité du mélange du solide

en cuve agitée existent [20]. De plus, quelques études récentes ont utilisé la modélisation MFN pour représenter l'hydrodynamique triphasique d'un réacteur agité de bio-oxydation [21, 22]. Cependant, malgré la disponibilité d'études cinétiques et hydrodynamiques, aucun modèle ne représente pleinement le couplage de ces méthodes en cuve agitée, ce qui est critique compte tenu de la complexité et de la taille des réacteurs industriels de biolixiviation.

5.3 Description expérimentale d'un réacteur de biolixiviation

5.3.1 Etude en présence de microorganismes

Comme mentionné précédemment dans l'état de l'art, la modélisation des procédés de biolixiviation a permis un certain nombre d'améliorations de la méthode au travers d'augmentations de productivité. Néanmoins, ces modèles se sont surtout concentrés sur la méthode en tas et les données disponibles pour les méthodes dynamiques restent insuffisantes pour représenter complètement un réacteur agité de biolixiviation. Pour cela, cette partie s'est concentrée sur la description d'un réacteur de biolixiviation à l'échelle laboratoire au travers d'une étude expérimentale complète. Les expériences ont été réalisées au travers de 10 réacteurs fermés (batch) de 2 litres, partageant les mêmes conditions opératoires. Toutes les expériences ont été effectuées en utilisant le consortium BRGM KCC sur milieu 0Km et un minerai sulfuré majoritairement composé de pyrite cobaltifère. Des résultats détaillés ont été obtenus au cours du temps via analyse des métaux (Fe, Co, Cu), des composants majeurs et des gaz.

Pour tous les essais, la cinétique de dissolution de la pyrite a été représentée par deux phases. Une première phase de lancement, représentée par une activité bactérienne faible car la biomasse contenue dans l'inoculum n'est pas encore fixée au matériau sulfuré. Durant cette phase, on observe une lente augmentation de la concentration en cobalt dans le milieu qui traduit la dissolution de la pyrite. A partir du troisième jour, on entre progressivement dans une seconde phase, marquée par une croissance exponentielle des microorganismes qui est représentée par une augmentation importante du potentiel électrochimique en raison de la régénération importante du fer ferrique. De plus, le taux de régénération du fer ferrique devenant supérieur à sa consommation par la dissolution chimique, on observe une lente augmentation du rapport $\left[Fe^{3+}\right] / \left[Fe^{2+}\right]$. Cette phase est également marquée par une diminution rapide du pH en raison de l'oxydation du soufre élémentaire S^0 en H_2SO_4 par les bactéries sulfo-oxydantes. En fin de cette phase exponentielle, la population bactérienne se stabilise car sa croissance est limitée par la formation de Fe^{2+} et S^0. À ce stade, vers le cinquième jour, la vitesse maximale instantanée de dissolution de la pyrite a été calculée à $434 \pm 75\ \mathrm{mg\,l^{-1}\,h^{-1}}$. Il a

été montré qu'après 10 jours d'expérience, le taux de dissolution de la pyrite atteignait 99% de la pyrite initiale.

Des analyses de gaz ont également été réalisées au long des expériences et utilisées pour observer le taux de consommation d'oxygène (OUR) par la biomasse. Il a été montré que la tendance de l'OUR suivait celle de la dissolution de la pyrite et atteignait un OUR maximum de 396 ± 116 mg l^{-1} h^{-1}, ce qui concorde avec les données précédemment obtenues du taux de dissolution de la pyrite. Après ce maximum observé vers 5 jours, la valeur diminue lentement en raison de l'épuisement de la pyrite accessible. Ceci est marqué par une diminution de la croissance et de l'activité microbienne.

La cinétique biologique a également été observée en utilisant le comptage de la biomasse et des méthodes de biologie moléculaire. Dans un premier temps, une analyse des séquences ADN des échantillons par PCR spécifique et SSCP ont permis de valider la présence des souches bactériennes attendues pour le consortium BRGM-KCC utilisé, à savoir *Leptospirillum ferriphilum*, *Acidithiobacillus caldus*, *Sulfobacillus thermosulfidooxidans*. A noter que *Sulfobacillus benefaciens*, normalement présente dans ce consortium, n'a pas été détectée, ce qui n'est pas anormal compte tenu des conditions expérimentales choisies.

Dans un second temps, l'influence de la localisation sur la distribution de la biomasse a été évaluée par qPCR des échantillons précédents. L'observation de ces résultats indique que plus de 99% de la biomasse se trouvait dans le liquide. Cependant, ces résultats peuvent être discutés compte tenu des inconvénients de la méthode de séparation utilisée, qui se base sur la gravité. Les abondances relatives des souches ont également été déterminées dans la pulpe, le solide et le liquide, comme le montre la figure 5.3. Les résultats montrent que *L. ferriphilum* était principalement en suspension dans le liquide tandis que *At. caldus* et *Sb. thermosulfidooxidans* se trouvaient plutôt fixées sur le solide. En examinant l'évolution de ces ratios dans le temps, *At. caldus* et *Sb. thermosulfidooxidans* ont montré une meilleure croissance que le *L. ferriphilum* pendant les deux premiers jours, avec *L. ferriphilum* ne représentant que 15% de la biomasse en comparaison des 50% de l'inoculum. Considérant l'importance de l'élimination de la couche de soufre à la surface du minerai et du fait que *At. caldus* est la principale bactérie sulfo-oxydante, la dissolution du minerai est limitée par la fixation et la croissance de *At. caldus*. Comme *Sb. thermosulfidooxidans* est à la fois sulfo-oxydante et ferro-oxydante, elle assiste le processus d'élimination du soufre tout en permettant au fer ferreux d'être réoxydé en fer ferrique. Après les premiers jours, la tendance à la croissance du consortium s'inverse rapidement, car *L. ferriphilum* devient la principal bactérie ferro-oxydante, représentant 45% de la biomasse. Cela entraîne également une diminution relative de *Sb. thermosulfidooxidans* jusqu'à 3% de la biomasse car moins efficace pour convertir le fer ferreux. Enfin, *At. caldus* était la sulfo-oxydante principale, comme le montre son ratio de 55% de la biomasse totale en fin d'expérience.

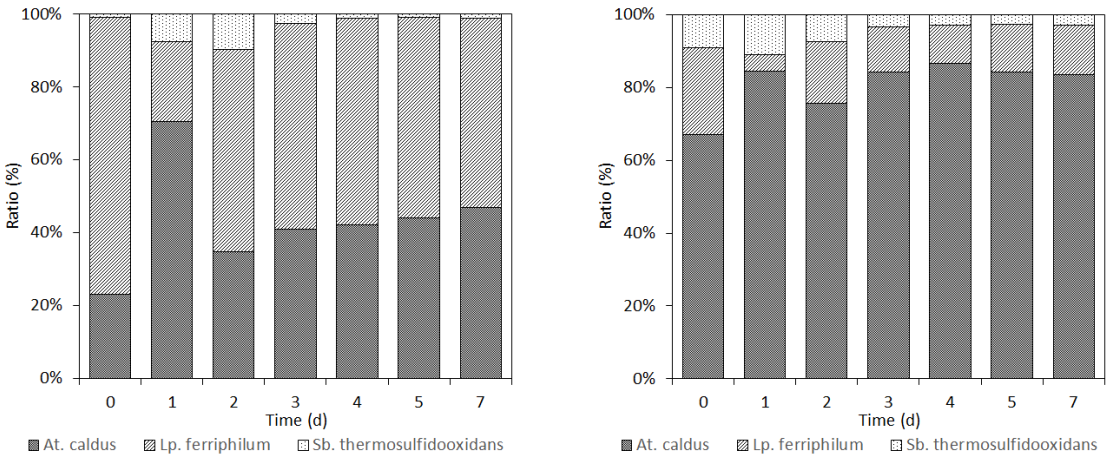

(a) Liquid ratio

(b) Solid ratio

Figure 5.3: Abondance relative des différentes souches microbiennes dans le réacteur.

5.3.2 Etude abiotique d'un réacteur de biolixiviation

Une étude abiotique a également été réalisée pour caractériser la capacité de la cuve agitée à homogénéiser le solide, le liquide et les gaz. Ceci a été fait en déterminant deux paramètres différents : la vitesse minimale de mise en suspension du solide et le coefficient de transfert de masse gaz-liquide. Les deux paramètres ont été obtenus pour une large gamme de conditions telles que la taille de particule, la concentration solide, la configuration du système d'agitation et le débit de gaz.

Les vitesses minimales de mise en suspension du solide ont été modélisées en l'absence de gaz via la corrélation de Zwietering et déterminées pour deux configurations différentes du système d'agitation. Il a été constaté que tous les résultats pouvaient être modélisés à l'aide de la corrélation avec une erreur quadratique moyenne de moins de 20% de différence entre les valeurs expérimentales et modélisées. Similairement, en présence de gaz, la corrélation de Zwietering a été adaptée pour prendre en compte le débit de gaz : en utilisant modèle additif $N_{\mathrm{jsg,add}}$ ou un modèle adimensionnel $N_{\mathrm{jsg,na}}$, qui se base sur le nombre d'aération (comme montré Fig. 5.4). Il a été constaté que $N_{\mathrm{js,add}}$ offrait un bon ajustement aux valeurs expérimentales, avec une erreur d'approximation moyenne de 4,0% pour les constantes déterminées. Concernant le second modèle $N_{\mathrm{js,na}}$, les résultats ont montré une excellente corrélation entre les résultats expérimentaux et le modèle, représenté par un $R^2 = 0.95$. Ces deux modèles peuvent donc aisément être utilisés dans la gamme de paramètres employés par cette étude pour estimer la vitesse de suspension minimale, avec ou sans aération.

Le coefficient de transfert de masse gaz-liquide $k_{\mathrm{l}}a$ a aussi été déterminé pour des conditions variées, proches de celles utilisées pour les expériences de biolixiviation. Il a été montré que l'utilisation d'une configuration avec deux turbines Rushton offrait un meilleur $k_{\mathrm{l}}a$ que la configuration avec une turbine Rushton et une hélice A310, et ce pour toutes les conditions testées. Aussi, considérant la concentration en solide, son

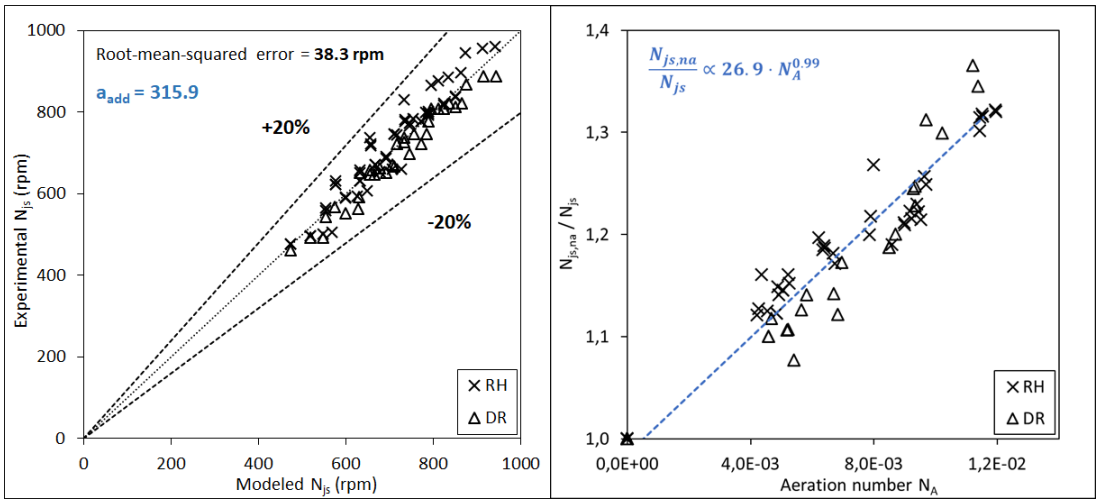

Figure 5.4: Comparaison des modèles de N_{jsg} en présence de gaz pour plusieurs configurations d'agitation. Deux modèles ont été étudiés, le modèle additif $N_{\text{jsg,add}}$ (gauche) et le modèle adimensionnel $N_{\text{jsg,na}}$ (droite).

augmentation a provoqué un effet positif sur le $k_{\text{l}}a$, ce qui peut être due à l'interaction entre les particules solides et les bulles. Enfin, la corrélation des résultats avec une loi puissance s'est avérée satisfaisante avec un coefficient de corrélation $R^2 > 0.90$ pour toutes les conditions testées.

5.4 Modélisation de la suspension des particules et des contraintes hydromécaniques dans un réacteur de bi-olixiviation

Ce chapitre s'est concentré sur l'impact de divers paramètres sur la suspension des particules et sur la contrainte hydromécanique, connus comme des paramètres critiques pour l'optimisation des conditions de réaction. Pour cela, deux modèles de mécanique des fluides numériques (MFN) de réacteurs multi-étagés solide-liquide, un à l'échelle laboratoire et l'autre à l'échelle pilote, ont été simulés. Ces deux modèles ont été validés en utilisant les boucles d'écoulement du liquide et les nombres de puissance des mobiles d'agitation utilisés. L'impact de la géométrie du mobile d'agitation inférieur et de la concentration solide a été évalué sur la puissance nécessaire, l'efficacité du mélange et la contrainte hydromécanique perçue par les particules.

5.4.1 Impact de la géométrie et de la concentration en solide sur la dispersion du solide

Afin de décrire le comportement des particules en suspension, la qualité de la suspension H_{s} a été estimée. Elle a été calculée comme la moyenne volumique de la différence

entre la concentration locale et la concentration moyenne en particules solides [23]. Dans le but de déterminer des règles de conduite robustes, la variation de la qualité de la suspension $H_{\mathrm{s,adj}}$ a été déterminée en fonction de la puissance dissipée par unité de volume P_{tot}/V (Fig. 5.5a).

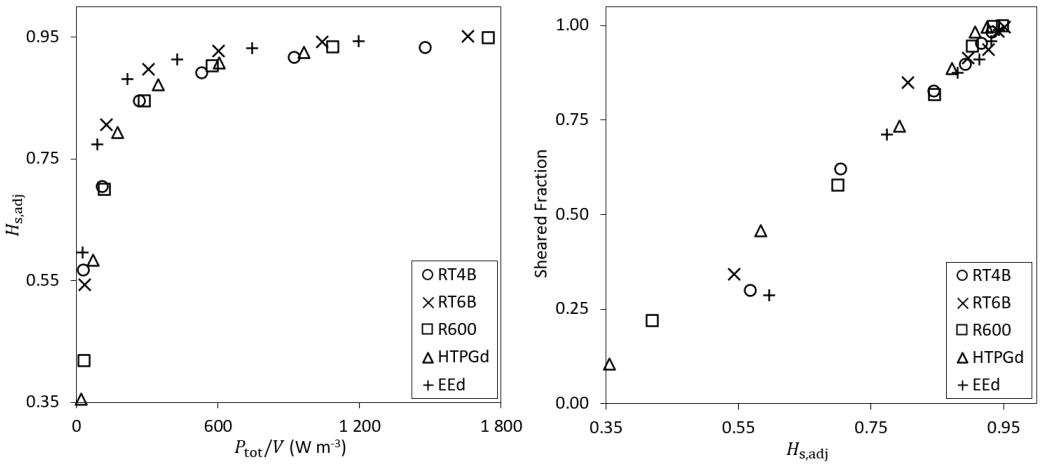

Figure 5.5: Impact du mobile d'agitation sur qualité du mélange $H_{\mathrm{s,adj}}$ (gauche) et sur la fraction cisaillée SF (droite). Concentration solide : 10% w/w.

La variation de $H_{\mathrm{s,adj}}$ se divise en deux zones distinctes. Pour P_{tot}/V inférieure à 600 W m^{-3}, $H_{\mathrm{s,adj}}$ a rapidement augmenté jusqu'à une valeur d'environ 0.90 ; concernant la distribution des particules obtenue pour cette gamme de puissance dissipée, seule une suspension partielle a été observée. Pour P_{tot}/V supérieur à 600 W m^{-3}, la valeur de $H_{\mathrm{s,adj}}$ a lentement augmenté jusqu'à environ 0.95, indiquant une homogénéisation progressive des particules au-delà de l'état de juste-suspension. Ainsi, une augmentation substantielle de la consommation d'énergie mécanique est nécessaire pour obtenir une amélioration mineure de l'homogénéisation des particules. De plus, il a également été démontré que l'homogénéité totale ($H_{\mathrm{s,adj}} = 1.0$) n'est pas réalisable car toutes les conditions testées stagnent en dessous de $H_{\mathrm{s,adj}} = 0.95$. Ceci pourrait s'expliquer par le fait que, même pour une forte dissipation de puissance par unité de volume, une petite région proche de la surface est restée libre ou peu concentrée en particules [24]. Enfin, il est intéressant de noter que, pour une dissipation de puissance par unité de volume donnée, les variations de $H_{\mathrm{s,adj}}$ étaient approximativement indépendantes de la conception du réacteur, ce qui signifie que la dissipation de puissance par unité de volume pourrait être utilisée non seulement comme paramètre d'échelle pour la détermination de l'état de particules juste-suspendues mais aussi pour prédire la qualité de l'homogénéisation.

L'impact de la concentration solide a également été considéré pour deux échelles de réacteur différentes, comme le montre la Fig. 5.6. Les résultats des simulations MFN ont confirmé que l'augmentation de la concentration en solide entraînait une élévation de P_{tot}/V pour atteindre une homogénéisation donnée. De plus, il a également

été mis en évidence que la valeur asymptotique de $H_{s,adj}$ obtenue, pour la valeur la plus élevée de P_{tot}/V considérée dans cette étude, se réduisait progressivement avec l'augmentation de concentration du solide. Par exemple pour l'échelle laboratoire, la puissance nécessaire pour atteindre $H_{s,adj} = 0.90$ avec la turbine Rushton était de $(P_{tot}/V)_{26\%} \simeq 2 \cdot (P_{tot}/V)_{18\%} \simeq 6 \cdot (P_{tot}/V)_{10\%}$. En ce qui concerne l'échelle pilote, les résultats ont montré une augmentation logarithmique allant de 38 à 99%, proche des résultats obtenus à l'échelle laboratoire. Néanmoins, un $H_{s,adj}$ maximum plus élevé a été observé à cette échelle, ce qui pourrait s'expliquer par (i) une plus faible hauteur du mobile d'agitation inférieur ($(C/T)_{2l} = 0.42$ comparé à $(C/T)_{800l} = 0.12$) et (ii) une configuration tri-étagée de l'agitation, permettant une meilleure homogénéisation de la surface du réacteur. Néanmoins, la valeur maximale de $H_{s,adj}$ pour chaque configuration est atteinte pour une valeur de P_{tot}/V équivalente, ce qui valide l'hypothèse selon laquelle ce paramètre pourrait être utilisé pour l'optimisation de la conception du réacteur et le scale-up du procédé.

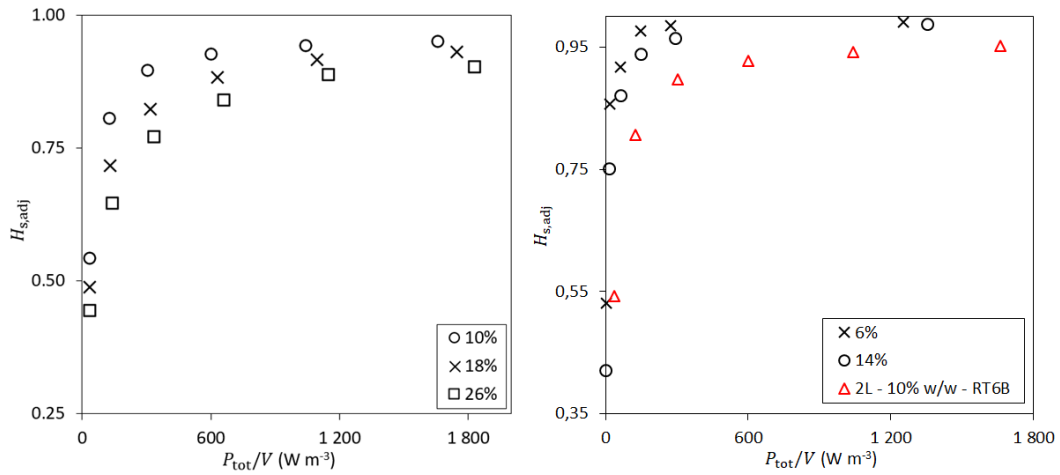

Figure 5.6: Impact de la concentration en solide sur la qualité du mélange à l'échelle laboratoire avec une turbine Rushton inférieure (gauche) et à l'échelle pilote (droite).

5.4.2 Impact de la géométrie et de la concentration en solide sur le stress hydromécanique

En dehors de la détermination de l'efficacité du mélange, ce chapitre a également considéré l'impact de la contrainte hydromécanique perçue par les particules. Selon la littérature, les contraintes hydromécaniques agissant sur les particules lorsqu'elles sont en suspension dans la cuve doivent être déterminées localement et en considérant le rapport de la taille des particules d_p sur l'échelle de longueur de Kolmogorov l_K. Ainsi, ce paramètre a été affirmé en calculant la fraction cisaillée SF, représentant le pourcentage du volume des particules en conditions cisaillées, à savoir dans les zones présentant des échelles de Kolmogorov inférieures au diamètre des particules ($l_K < d_p$).

La variation de la fraction cisaillée SF avec la qualité de la suspension $H_{s,adj}$ a été rapportée dans la Fig. 5.5 et 5.7. Comme on pouvait s'y attendre, la contrainte sur les particules a augmenté avec la qualité de la suspension pour le réacteur laboratoire comme pour le réacteur pilote. Cependant, les résultats à l'échelle pilote ont montré que l'évolution n'était pas strictement linéaire comme observé à l'échelle laboratoire, pouvant être attribué à une hauteur plus faible du mobile d'agitation inférieur, qui favoriserait alors la dispersion du solide à des P_{tot}/V faibles pour lesquelles la fraction cisaillée est moindre. Dans le cas du réacteur à l'échelle laboratoire, il a également été montré que toutes les configurations de mobiles d'agitation présentaient la même évolution linéaire de SF, ce qui signifie que toutes les configurations génèrent une contrainte similaire sur les particules pour une qualité de suspension donnée. Il est également intéressant de noter que l'obtention d'une homogénéisation quasi-consistante des particules implique que presque toutes les particules rencontrent des tourbillons turbulents potentiellement endommageant, qui pourraient favoriser le détachement du biofilm dans le cas d'une expérience contenant de la biomasse. En conclusion, bien que chaque configuration et échelle de bioréacteur aient généré des champs de dissipation turbulente différents, le lien physique entre la vitesse d'écoulement, la dissipation turbulente et les concentrations de particules a conduit à des relations uniques entre la fraction cisaillée des particules et la qualité de la suspension.

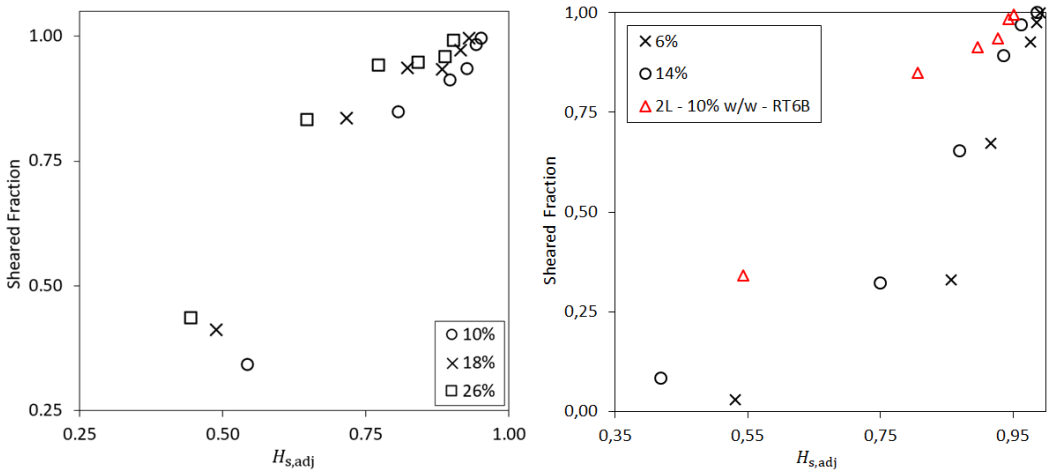

Figure 5.7: Impact de la concentration en solide sur la fraction cisaillée à l'échelle laboratoire avec une turbine Rushton inférieure (gauche) et à l'échelle pilote (droite).

L'impact de la concentration en solide sur la fraction cisaillée a également été considéré aux deux échelles, comme le montre la Fig. 5.7. Il a été montré que, pour un $H_{s,adj}$ donné, une fraction plus élevée de particules était transportée dans le sous-domaine inertiel à des concentrations solides plus élevées, entraînant un SF plus important. Cependant, pour toutes les concentrations en solide considérées, le paramètre SF a atteint une valeur proche de 1 pour les degrés d'homogénéisation les plus élevés.

5.5 Développement d'un modèle compartimenté d'un réacteur de biolixiviation multi-échelles

Dans ce chapitre, le développement du modèle de biolixiviation en réacteur agité a été complété par l'implémentation de la phase gazeuse et l'ajout de modèles cinétiques. Pour cela, l'impact du gaz sur l'hydrodynamique d'un réacteur de biolixiviation a été introduit par simulations MFN gaz-liquide à plusieurs échelles (2 et 800 litres). En parallèle, une étude cinétique, validée experimentalement, a permis de valider les modèles de transfert de masse gaz-liquide d'oxygène en présence de bactérie. Une simplification du modèle MFN a ensuite été effectué et validée par modélisation d'expérience de $k_{\mathrm{L}}a$ en méthode statique. Enfin, ce modèle a été utilisé dans une étude de montée en échelle afin de déterminer des critères de conduite de réacteurs allant de l'échelle pilotes à industrielle.

5.5.1 Modélisation du coefficient de transfert de masse gaz-liquide

Modélisation MFN gaz-liquide des réacteurs de 2 et 800 litres

Les écoulements gaz-liquide ont été simulés par MFN et le coefficient de transfert de masse $k_{\mathrm{L}}a$ a été calculé en utilisant la théorie de la pénétration d'Higbie et les approches de Danckwerts et Calderbank (Tableau 5.1). Ces résultats ont été comparés aux mesures expérimentales, à savoir les résultats présentés au chapitre 2 pour le réacteur à l'échelle du laboratoire et les données du BRGM pour le réacteur à l'échelle pilote.

Table 5.1: Coefficients de transfert de masse pour le modèle à l'échelle laboratoire et à l'échelle pilote.

$k_{\mathrm{L}}a$ (s^{-1})		**MFN**		**Expérimental**
	Higbie	**Danckwerts**	**Calderbank**	**-**
Réacteur 2 l	0.066	0.024	0.006	0.025
Réacteur 800 l	0.077	0.027	0.018	0.030

Les résultats ont montré que tous les modèles présentent un $k_{\mathrm{L}}a$ du même ordre de grandeur que les résultats expérimentaux. La théorie de la pénétration de Higbie a indiqué une valeur de $k_{\mathrm{L}}a$ plus élevée que les résultats expérimentaux (164% pour le 2 litres et 157% pour le 800 litres). Le modèle de Calderbank a montré un meilleur ajustement que la théorie de la pénétration, en particulier en considérant le réacteur à l'échelle pilote, mais a prédit des valeurs inférieures aux résultats expérimentaux (76% pour le 2 litres et 40% pour le 800 litres). Enfin, le modèle de Danckwerts a affiché les meilleures prédictions pour les deux configurations, avec une erreur de seulement 4% pour le réacteur de 2 litres et 10% pour celui de 800 litres. En comparant les trois

modèles, le modèle de Danckwerts se montre le plus adapté mais le modèle de Calderbank pourrait aussi être utilisé dans le cas du réacteur à l'échelle pilote.

Modélisation cinétique d'un réacteur de biolixiviation

En parallèle de l'étude précédente, un modèle cinétique de biolixiviation a été développé, en l'absence d'hydrodynamique. Ce dernier intègre les équation cinétiques représentant la dissolution chimique de minerais sulfurés, les oxydations biologique de fer et de soufre, et le transfert de masse gaz-liquide de l'oxygène. Le bon fonctionnement du modèle cinétique ainsi que la validité des paramètres cinétiques choisis ont été atestés par utilisation des résultats expérimentaux obtenus dans le chapitre 2.

L'évolution des paramètres principaux de biolixiviation ont été observés, notamment via l'observation du taux de conversion du matériau sulfuré et de l'évolution de la concentration en biomasse au cours du temps. La comparaison du taux de conversion modélisé avec celui obtenu expérimentalement a montré un très bon ajustement avec une erreur relative inférieure à 10% pour la durée de l'expérience. Des observations similaires ont été faites par observation de l'évolution de la concentration de la biomasse et du taux de consommation de l'oxygène (OUR) (montré sur la figure 5.8). Cependant, une vitesse maximale de consommation d'oxygène plus faible a été atteinte, avec $OUR_{mod} = 291\,\mathrm{mg\,l^{-1}\,h^{-1}}$ contre les $396\,\mathrm{mg\,l^{-1}\,h^{-1}}$ obtenus expérimentalement. Sachant que des hypothèses ont dû être formulées pour obtenir l'OUR expérimental au cours du temps, la valeur maximale observée expérimentalement pourrait éventuellement être surestimée. Ces résultats montrent que le modèle cinétique a représenté, avec une erreur acceptable, ce qui s'est passé pendant les expériences. Le modèle peut être utilisé pour prédire l'évolution des différents composants d'un réacteur de biolixiviation.

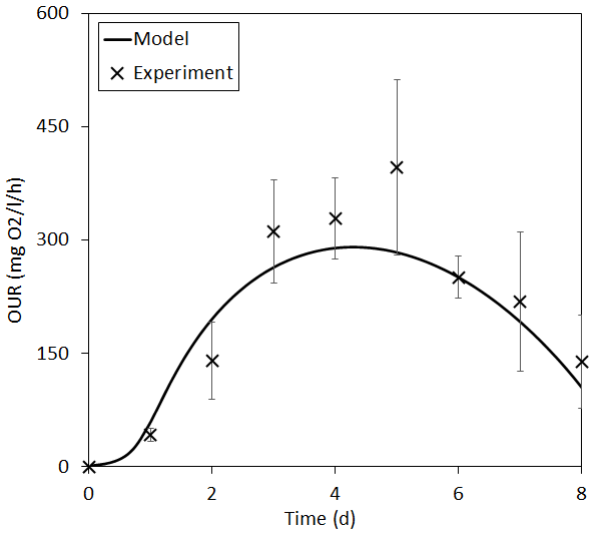

Figure 5.8: Comparaison du taux de conversion expérimental et modélisé pour le réacteur à l'échelle laboratoire.

5.5.2 Modélisation et prédiction de l'oxygénation d'un bioréacteur de l'échelle laboratoire à industrielle

Développement d'un modèle compartimenté de transfert, transport et consommation d'oxygène

Le modèle MFN gaz-liquide précédemment établi a été simplifié par une approche compartimentée afin de permettre son utilisation plus rapide et à plus grande échelle. La division des modèles en compartiments s'est basée sur les données du champ de vitesse (liquide et gaz) des simulations MFN réalisées précédemment. Selon ces critères, le réacteur de 2 l a été divisé en 17 compartiments et celui de 800 l en 21 compartiments. La connexion entre les différents compartiments est représentée par un débit massique de liquide ou de gaz à travers l'interface entre chaque compartiment. Chaque compartiment a été considéré comme homogène en termes de fraction gazeuse α_{g}, de dissipation turbulente ε, de pression et de coefficient de transfert de masse $k_{\mathrm{L}}a$. Pour cela, la valeur moyenne de ces paramètres a été calculée par moyenne volumique sur l'ensemble des cellules du compartiment.

Le modèle compartimenté a été simulé à l'aide du code commercial MATLAB R2017a pour représenter la méthode statique de désoxygénation-réoxygénation utilisée expérimentalement. L'évolution de la concentration en oxygène dissous a été observée dans chaque compartiment. Le résultat de cette expérience est montré sur la Fig. 5.9, avec le compartiment 8 sélectionné comme donnée modèle.

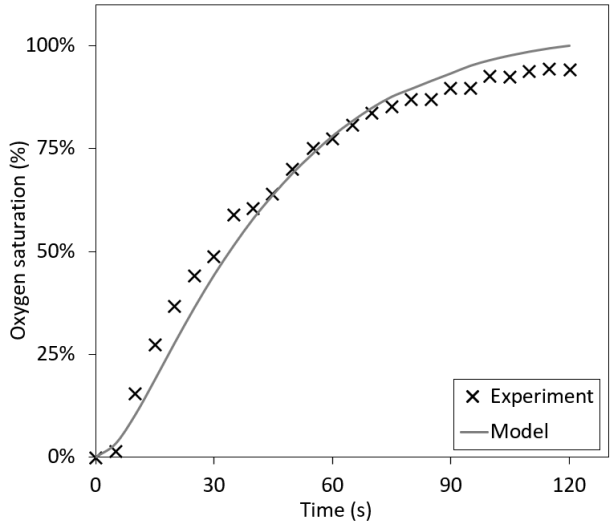

Figure 5.9: Évolution de la saturation en oxygène dissous au cours du temps dans une expérience de désoxygénation-réoxygénation et comparaison avec les valeurs modélisées.

Les résultats ont montré que le modèle était représentatif des mesures expérimentales, démontré par un coefficient de détermination $R^2 = 0.99$. La légère variation observée dans l'évolution et la valeur maximale pourrait être due à l'hypothèse de modélisation utilisée dans la simulation CFD et le modèle de compartiment. Bien que les données modélisées soient présentées pour le compartiment 8, il a été constaté que peu ou pas de différences ont été observées entre les compartiments, avec une variation standard maximale de $0.05\,\mathrm{mg\,l^{-1}}$ pour la concentration d'oxygène dissous.

Montée en échelle du modèle compartimenté afin établir des règles de conduite

Dans cette dernière étude, une extrapolation du réacteur de 800 l a été effectué en se basant sur les données du modèle compartimenté précédemment établi. Pour cela, une méthode basée sur des similarités géométriques entre deux échelles a été appliquée, se basant sur le rapport de taille K_L entre deux points similaires de chaque réacteur.

A partir de cette méthode, le réacteur a pu être extrapolé à plusieurs échelles : 8, 80, 800 et $2000\,\mathrm{m^3}$. Les différents modèles ainsi obtenus ont été utilisés dans des expériences d'oxygénation supposant un terme de consommation bactérienne constant en tout point du réacteur. Dans notre cas, le taux de consommation maximum de $360\,\mathrm{mg\,l^{-1}\,h^{-1}}$ observé expérimentalement a été utilisé. Les résultats, présentés en Fig. 5.10, montrent que plus l'échelle du réacteur est importante et plus la concentration globale moyenne en oxygène augmente dans le milieu. Cela s'explique par l'augmentation de la hauteur de liquide qui permet l'accroissement de la saturation en oxygène. Néanmoins, l'écart standard de concentration en oxygène dissous entre deux compartiments augmente aussi avec l'échelle. En effet, on observe seulement 2 % de différence entre les compartiments pour le réacteur de 800 l mais plus de 29 % pour celui de $2000\,\mathrm{m^3}$.

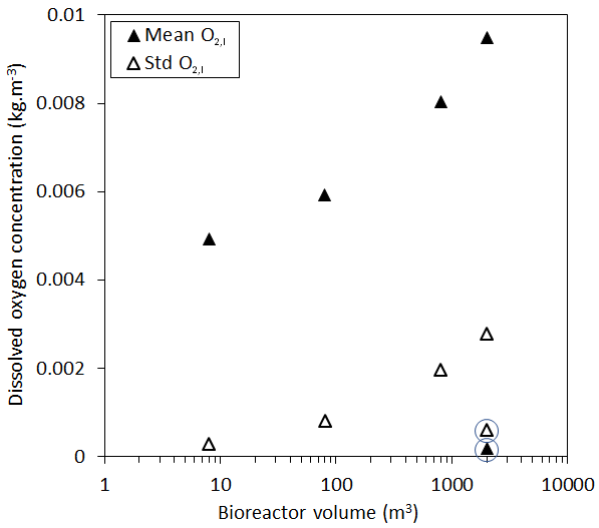

Figure 5.10: Variation de la moyenne et de l'écart type en concentration en oxygène dissous dans le réacteur. Les données entourées correspondent à $V = 2000\,\mathrm{m}^3$ et $r_{O2} = 1800\,\mathrm{mg\,l^{-1}\,h^{-1}}$.

Une seconde stratégie a été menée en ajoutant une consigne sur la concentration en oxygène dissous dans le réacteur pour chaque échelle, représentée par un compartiment donné. Cette consigne a été fixée à 50 % de la saturation en oxygène d'un air à pression atmosphérique ($O_{2,l} \simeq 5\,\mathrm{mg\,l^{-1}}$) et agissait sur la fraction d'oxygène injectée par le sparger afin de représenter son impact avec les données disponibles. Ces résultats se sont avérés satisfaisant pour le 800 l où la consigne a permis de maintenir une concentration en oxygène dissous constante partout dans le réacteur. Néanmoins, des différences importantes ont été observées pour le réacteur de $2000\,\mathrm{m}^3$, influencées par la position de la sonde. Ces résultats suggèrent qu'à l'échelle industrielle, (i) une modélisation compartimentée devrait être effectuée en amont de la conception du procédé afin de déterminer la position optimale de la sonde permettant la régulation d'oxygène et (ii) la consigne doit être reconsidérée à la hausse pour permettre que chaque zone du réacteur soit suffisamment aérée.

5.6 Conclusion et perspectives

L'objectif du présent travail de thèse était de modéliser et de simuler l'effet des phénomènes de transport sur le microenvironnement bactérien à travers le développement d'un modèle hydrocinétique couplé de biolixiviation en réacteur agité. Comme expliqué dans ce manuscrit, l'hydrodynamique a un impact critique sur l'efficacité des réactions de biolixiviation.

Une description complète d'un réacteur de biolixiviation a été effectuée au travers d'une campagne expérimentale approfondie. Cette campagne a permis d'obtenir un certain nombre de paramètres cinétiques (dissolution de la matière sulfurée, oxydations biologiques, transfert de masse gaz-liquide de l'oxygène) nécessaires à la validation des modèles établis dans ce travail. De même, des paramètres abiotiques ont été déterminés (N_{js}, $k_{\mathrm{L}}a$) pour quantifier l'hydrodynamique du réacteur. Suite à cette campagne, un premier modèle MFN solide-liquide a été établi pour présenter l'impact de la géométrie de l'agitation et de la concentration en solide sur la suspension des particules solides et sur le stress hydromécanique perçu par les particules. Ensuite, un second modèle MFN gaz-liquide a été décrit et utilisé pour représenter le transfert de masse gaz-liquide de l'oxygène. Ce modèle a ensuite été simplifié en utilisant une approche compartimentée puis utilisé avec succès pour représenter l'évolution de l'oxygène au cours du temps dans le réacteur. Une extrapolation des modèles de l'approche compartimenté a été effectué avec succès pour établir des critères de conduite de réacteurs allant de l'échelle laboratoire (2 l) à l'échelle industrielle (jusqu'à 2000 m^3).

En perspectives pour ce travail, des ajouts seraient appréciables pour le modèle afin de permettre sa généralisation. Dans notre cas, l'étude complète a été réalisée sur deux échelles, à 2 et 800 l et l'étude à plus haute échelle s'est effectuée sur le transfert de masse gaz-liquide seul. Une étude élargissant l'extrapolation à la suspension des particules et aux cinétiques biologiques et chimique serait intéressante. De plus, cette étude pourrait aussi prendre en compte l'impact de la géométrie sur la dispersion du gaz et la suspension du solide car cruciale dans le procédé de biolixiviation. Enfin, considérant le modèle cinétique, seuls un seul type de solide et une bactérie de chaque type (ferro-oxydante et sulfo-oxydante) ont été considérés. L'ajout de la plupart des solides ainsi que des bactéries communément utilisées en biolixiviation en réacteur élargirait le champ d'utilisation du modèle. Le modèle de base ainsi que ces améliorations offriraient alors un outil modulable d'optimisation d'un réacteur de biolixiviation, peu importe l'échelle considérée.

Bibliography

[1] L. D. Meinert, G. R. Robinson, and N. T. Nassar. Mineral Resources: Reserves, Peak Production and the Future. *Resources*, 5(1):14, March 2016.

[2] G. M. Mudd. *The Sustainability of Mining in Australia: Key Production Trends and Environmental Implications*. Monash University, Department of Civil Engineering, Clayton, 2009.

[3] G. Calvo, G. Mudd, A. Valero, and A. Valero. Decreasing Ore Grades in Global Metallic Mining: A Theoretical Issue or a Global Reality? *Resources*, 5(4):36, December 2016.

[4] C. A. du Plessis, J. D. Batty, and D. W. Dew. Commercial Applications of Thermophile Bioleaching. In D. E. Rawlings and D. B. Johnson, editors, *Biomining*, pages 57–80. Springer, Berlin, Heidelberg, 2007.

[5] C. Joulian, V. Fonti, S. Chapron, C. G. Bryan, and A.-G. Guezennec. Bioleaching of pyritic coal wastes: Bioprospecting and efficiency of selected consortia. *Research in Microbiology*, September 2020.

[6] H. L. Ehrlich. Past, present and future of biohydrometallurgy. *Hydrometallurgy*, 59(2):127–134, February 2001.

[7] J. Petersen. Heap leaching as a key technology for recovery of values from low-grade ores – A brief overview. *Hydrometallurgy*, 165:206–212, October 2016.

[8] D. E. Rawlings, D. Dew, and C. du Plessis. Biomineralization of metal-containing ores and concentrates. *Trends in Biotechnology*, 21(1):38–44, January 2003.

[9] C. S. Gahan, H. Srichandan, D.-J. Kim, and A. Akcil. Biohydrometallurgy and Biomineral Processing Technology: A Review on its Past, Present and Future. 1:15, 2012.

[10] D. E. Rawlings and D. B. Johnson. The microbiology of biomining: Development and optimization of mineral-oxidizing microbial consortia. *Microbiology*, 153(2):315–324, February 2007.

[11] S. C. Bouffard and D. G. Dixon. Investigative study into the hydrodynamics of heap leaching processes. *Metallurgical and Materials Transactions B*, 32(5):763–776, October 2001.

[12] J. Petersen. Modelling of bioleach processes: Connection between science and engineering. *Hydrometallurgy*, 104(3):404–409, October 2010.

[13] A. Mahmoud, P. Cézac, A. F. A. Hoadley, F. Contamine, and P. D'Hugues. A review of sulfide minerals microbially assisted leaching in stirred tank reactors. *International Biodeterioration & Biodegradation*, 119:118–146, April 2017.

[14] P. R. Holmes and F. K. Crundwell. The kinetics of the oxidation of pyrite by ferric ions and dissolved oxygen: An electrochemical study. *Geochimica et Cosmochimica Acta*, 64(2):263–274, January 2000.

[15] S. C. Bouffard, B. F. Rivera-Vasquez, and D. G. Dixon. Leaching kinetics and

stoichiometry of pyrite oxidation from a pyrite–marcasite concentrate in acid ferric sulfate media. *Hydrometallurgy*, 84(3):225–238, November 2006.

[16] D. G. MacDonald and R. H. Clark. The oxidation of aqueous ferrous sulphate by thiobacillus ferrooxidans. *The Canadian Journal of Chemical Engineering*, 48(6):669–676, 1970.

[17] T. V. Ojumu, J. Petersen, G. E. Searby, and G. S. Hansford. A review of rate equations proposed for microbial ferrous-iron oxidation with a view to application to heap bioleaching. *Hydrometallurgy*, 83(1):21–28, September 2006.

[18] S. C. Bouffard and D. G. Dixon. Modeling pyrite bioleaching in isothermal test columns with the HeapSim model. *Hydrometallurgy*, 95(3):215–226, February 2009.

[19] A.-G. Guezennec, C. Joulian, J. Jacob, A. Archane, D. Ibarra, R. de Buyer, F. Bodénan, and P. d'Hugues. Influence of dissolved oxygen on the bioleaching efficiency under oxygen enriched atmosphere. *Minerals Engineering*, 106:64–70, May 2017.

[20] S. Harrison, A. Kotsiopoulos, R. Stevenson, and J. Cilliers. Mixing indices allow scale-up of stirred tank slurry reactor conditions for equivalent homogeneity. *Chemical Engineering Research and Design*, 153:865–874, January 2020.

[21] C. Zheng, J. Guo, C. Wang, Y. Chen, H. Zheng, Z. Yan, and Q. Chen. Experimental study and simulation of a three-phase flow stirred bioreactor. *Chinese Journal of Chemical Engineering*, June 2018.

[22] C. Zheng, Y. Huang, J. Guo, R. Cai, H. Zheng, C. Lin, and Q. Chen. Investigation of cleaner sulfide mineral oxidation technology: Simulation and evaluation of stirred bioreactors for gold-bioleaching process. *Journal of Cleaner Production*, 192:364–375, August 2018.

[23] S. Hosseini, D. Patel, F. Ein-Mozaffari, and M. Mehrvar. Study of Solid-Liquid Mixing in Agitated Tanks through Computational Fluid Dynamics Modeling. *Industrial & Engineering Chemistry Research*, 49(9):4426–4435, May 2010.

[24] A. Delafosse, C. Loubière, S. Calvo, D. Toye, and E. Olmos. Solid-liquid suspension of microcarriers in stirred tank bioreactor – Experimental and numerical analysis. *Chemical Engineering Science*, 180:52–63, April 2018.

List of communications and publications

Publications

Chéron, J., Loubière, C., Delaunay, S., Guezennec, A. G., Olmos, E. (2020). CFD numerical simulation of particle suspension and hydromechanical stress in various designs of multi-stage bioleaching reactors. *Hydrometallurgy*, 197, 105490.

Oral communications

Chéron J., Ménard Y., Delaunay S., Loubière C., Guezennec A.G., Olmos E. (2019). Study of the bacterial microenvironment in a bioleaching stirred tank bioreactor: transport phenomena and kinetic modelling in three-phase flow. *GDR Prométhée*, le 27 Novembre 2019, Nancy, France.

Olmos E., Chéron J., Loubière C., Delaunay S., Guezennec A.G. (2018). Hydrodynamic modelling of bioleaching reactors. *3rd Promethee Workshop*, le 10 Octobre 2018, Orléans, France.

Poster communications

Chéron J., Loubière C., Delaunay S., Ménard Y., Guezennec A.G., Olmos E. (2019). CFD numerical simulation of multiphase flow in a bioleaching stirred tank reactor: Effects of impeller geometry on pyrite suspension reactor. *23rd International Biohydrometallurgy Symposium (IBS)*, du 20-23 Octobre 2019, Fukuoka, Japon.

Chéron J., Loubière C., Delaunay S., Ménard Y., Guezennec A.G., Olmos E. (2019). Modélisation cinétique du procédé de biolixiviation. *17ème Congrès de la Société Française de Génie des Procédés (SFGP)*, du 15-17 Octobre 2019, Nantes, France.

Abstract

Extractive bioleaching is a range of technologies aiming at recovering metals contained in mineral resources using biological means. It was successfully implemented at the industrial scale and used either in the form of dump or heap treatments, or by using large-scale stirred tank reactors (STR). Recently, bioleaching is evolving towards the exploitation of unusual resources (very low-grades, complex mineralogy, or high sulphur content) caused by the declining trend in mean ore grades. Bioleaching STR have proven to be more efficient than the dump or heap treatments for the treatment of high-value resources (such as refractory gold ores) mainly thanks to the better control over the process. However, it still needs further technical optimization to reach economic viability in the case of unconventional resources. In this PhD work, a coupled bioleaching STR hydrokinetic model was developed to model and simulate the bacterial microenvironment / response to the local heterogeneities of the tank in order to establish optimization criteria. First, an experimental study was performed at laboratory-scale to obtain the data necessary for the calibration of the various models. This includes bioleaching tests in STR to gather kinetics parameters and abiotic studies to determine essential hydrodynamics parameters (N_{js}, $k_{l}a$). On a second study, a multi-scale solid-liquid CFD model was developed and simulated using various conditions of impeller geometries, solid concentrations, and agitation rates. The impact of these conditions on solid homogeneity and particle stress was assessed and basic sizing rules were extrapolated from the results. Lastly, a hydro-kinetic model of a multi-scale bioleaching STR was developed. For this, a CFD model describing the gas-liquid flow was developed and simplified using a compartment approach. This approach was modelled on MatLab and combined with previous results on kinetic and solid-liquid models. Finally, the compartment hydro-kinetic model was used to characterize the kinetics of bioleaching and was compared with experimental data.

Résumé

La biolixiviation extractive est un ensemble de technologies visant à récupérer les métaux contenus dans les ressources minérales via l'assistance de microorganismes. Ces technologies ont été mises en œuvre avec succès à l'échelle industrielle et utilisées, soit sous la forme de traitements en tas, soit en utilisant des réacteurs à cuve agitée à grande échelle. Récemment, la biolixiviation a évolué vers l'exploitation de ressources non communes (très faibles teneurs, minéralogie complexe ou forte teneur en soufre) causée par la tendance à la baisse des teneurs moyennes en métaux contenus dans les minerais. La biolixiviation en cuve agitée s'est avérée plus efficace que les traitements en décharge ou en tas pour le traitement des ressources de grande valeur (comme les minerais d'or réfractaire), principalement grâce à un meilleur contrôle du processus. Cependant, ce traitement doit encore être optimisé sur le plan technique pour atteindre une viabilité économique dans le cas des ressources non conventionnelles. Dans ce travail de thèse, un modèle couplé hydrocinétique de biolixiviation en réacteur a été développé pour modéliser et simuler le microenvironnement bactérien et sa réponse aux hétérogénéités locales du réacteur afin d'établir des critères d'optimisation. Pour cela, une étude expérimentale a été réalisée à l'échelle laboratoire afin d'obtenir les données nécessaires à la calibration des différents modèles. Cette étude comprenait des tests de biolixiviation en cuve agitée pour recueillir les paramètres cinétiques, et des études abiotiques pour déterminer les paramètres hydrodynamiques essentiels (N_{js}, k_la). Dans une seconde étude, un modèle CFD multi-échelle solide-liquide a été développé et simulé en utilisant différentes conditions de géométries de mobiles d'agitation, de concentrations en solide et de vitesses d'agitation. L'impact de ces conditions sur l'homogénéité du solide et la contrainte mécanique perçue par les particules a été évalué et des règles de base de dimensionnement ont été extrapolées à partir des résultats. Enfin, un modèle hydrocinétique d'un réacteur de biolixiviation multi-échelle a été développé. Pour cela, un modèle CFD décrivant l'écoulement gaz-liquide a été formulé et simplifié en utilisant une approche par compartiments. Cette approche a été modélisée sur MatLab et combinée avec les résultats précédents sur les modèles cinétiques et d'hydrodynamique solide-liquide. Enfin, le modèle hydrocinétique compartimenté a été utilisé pour caractériser la cinétique de biolixiviation puis comparé aux données expérimentales.